3D Emission & Physical Chemistry Simulations of the Io Plasma Torus

by

Edward Gregory Nerney

B.A., University of Colorado Boulder, 2015

M.S., University of Colorado Boulder, 2019

A thesis submitted to the

Faculty of the Graduate School of the

University of Colorado in partial fulfillment

of the requirements for the degree of

Doctor of Philosophy

Department of Physics

2022

Committee Members:

Mihály Horányi, Chair

Fran Bagenal

Nicholas M. Schneider

Dmitri A. Uzdensky

Tobin L. Munsat

Nerney, Edward Gregory (Ph.D., Physics)

3D Emission & Physical Chemistry Simulations of the Io Plasma Torus

Thesis directed by Prof. Fran Bagenal

The Galilean moon Io emits volcanic gases into space at a rate of about a ton per second. The gases become ionized and trapped in Jupiter's strong magnetic field, forming a torus of plasma that emits 2 terawatts of UV emissions. After reanalyzing UV emissions observed by Voyager, Galileo, & Cassini, this work found that the Voyager plasma conditions were consistent with a physical chemistry model with a neutral source of dissociated sulfur dioxide from Io. The Voyager analysis of Shemansky (1988)[121] found an O/S ratio of the neutral source of 4 required to match UV observations whereas we find it to be 2 consistent with dissociation of SO_2. There are plenty of ways I could see it being less than 2 when also including sources from SO, S_2, and other sulfur compounds but it is much harder to explain it being larger than 2.

By using a double Maxwellian distribution where both the core thermal electrons as well as supra-thermal "hot" electron population are assumed to be Maxwellians I have modeled the emission in the UV using the CHIANTI atomic database. This double Maxwellian model of UV emission spectra when compared with a spectrum from CASSIN UVIS at 6 R_J does not well constrain the fraction of hot electrons. Additional physics from energy constraints from physical chemistry modeling allows me to determine that for nominal warm torus plasma parameters the fraction of hot electrons is about 0.25% at 6 R_J. This research determined the mass and energy budget and dominant chemical pathways in the Io plasma torus. This result is particularly important due to the abundance of recent spectral analyses of UV data from JAXA's Hisaki satellite. Spectral analysis of the Hisaki observations has found fractions of hot electrons on the order of a few percent (Yoshioka et al. (2014); Tsuchiya et al. (2015)) [163] [150] inconsistent with our model and previous results.

ESA's JUICE mission and NASA's Europa Clipper are sending UVS instruments to the

Jupiter system that will view the Io plasma torus. In anticipation of these missions, I have built a 3D Io plasma torus emission model in order to simulate what we would expect to see from both UVS instruments looking at the Io plasma torus. In addition, our model allows for observation planning to predict if particular torus stare scenarios will produce sufficient signal to determine plasma conditions. The Colorado Io Torus Emission Package 2 (CITEP 2) calculates the line of sight given the position and pointing of the spacecraft and produces a synthetic spectrum given plasma densities and temperatures along the line of sight using the CHIANTI atomic database version 9 to compute volume emission rates.

I have adapted and built upon a 3D model of the physical chemistry (Copper et al. (2016))[33] while varying the neutral source rate and diffusion coefficient in order to model the warm torus, ribbon, and cold torus self-consistently. I have corroborated Copper's results and adapted the model for my own purposes. I have moved the model in from the warm torus to simulate the cold torus, gap region, ribbon, and warm torus. I am able to produce the ribbon and a peak in flux-tube content at L=5.7 by applying a discontinuity in the diffusion coefficient in that region consistent with a change in flux-tube interchange processes. By applying the "notched" D_{LL} profile that Taylor (1996) [142] used for a few model runs I was able to produce a cold torus peak and gap region by fixing the neutral density profiles to the Koga et al. (2018b) [79] scaled up by a factor of 1.5 but with a fast power law fall of +20 and cutting it off inside 5.65 R_J. I found that if I didn't have the neutral densities fall off much steeper than the Koga et al. (2018b) [79] implied power law of +12 inside 5.7 than my electron and ion temperatures would stay far too high due to pickup energy. This implies that inside the peak in neutral density at 5.7 R_J Koga et al. (2018b) [79] was overestimating densities due to line of sight projection effects.

I investigate the tipping point of inflow versus outflow of mass and energy and quantify the transport timescales given the diffusion coefficient profile and flux tube content radial profiles. I found radial transport timescales ranging between tens of days to hundreds of days in the warm torus depending on the method used and many hundreds of days to a thousand days in cold torus. I found a separable transient solution to the radial Fokker-Planck equation I have never seen

applied to Jupiter for flux-tube interchange motion. I found an e-folding timescale for the transient separable solution exactly the same as what is used as a radial transport timescale in the literature and found similar values for this e-folding timescale to match the torus profiles as is found using the integrated transport timescale formulation. I performed a numerical experiment to determine the time for a perturbation to move through the warm torus. By taking our nominal steady-state output in the warm torus and perturbing the solution at L=6 we find shorter timescales for the perturbation to reach L=10 of about 30 days as opposed to around 100 days for the integrated transport timescale.

The output of our 3D physical chemistry model produces a 3D model of densities and temperatures which can be used in conjunction with CITEP 2 to simulate corresponding emission profiles for a given viewing geometry.

Dedication

To my father Steve, my mother Myra, and brother Daniel.

Acknowledgements

I want to thank my advisor Fran Bagenal for her encouragement, patience, invaluable expertise, and knowledge of the magnetosphere of Jupiter. Additionally, I would like to thank Mihály Horányi for agreeing to be my titular advisor as Fran does not have a physics faculty appointment this was necessary. I would like to thank Andrew Steffl, Nick Schneider, and Carl Schmidt for their help in simulating UV spectra. Thanks to Peter Delamere and Drew Coffin for helping me to model the physical chemistry of the Io plasma torus. Thanks goes to Randy Gladstone and Kurt Retherford for funding my research. Thanks to Vincent Dols, Rob Wilson, and Frank Crary who as a part of our weekly research group meetings helped me to progress to where I am now.

To my parents Steve Nerney and Myra Tuckerman, and my brother Daniel Nerney thank you for all your love and support over the years. Special thanks to my father for working tirelessly over years to help to teach me the math, physics, and astronomy responsible for where I am today. I am forever grateful for his patience and perseverance.

This work was supported at the University of Colorado as a part of NASA's Juno mission, Nasa's Europa Clipper mission, and ESA's JUICE mission supported by NASA. This work utilized the CHIANTI atomic database. CHIANTI is a collaborative project involving George Mason University, the University of Michigan (USA), University of Cambridge (UK) and NASA Goddard Space Flight Center (USA). This work utilized the Summit supercomputer, which is supported by the National Science Foundation (awards ACI-1532235 and ACI-1532236), the University of Colorado Boulder, and Colorado State University. The Summit supercomputer is a joint effort of the University of Colorado Boulder and Colorado State University.

Contents

Chapter

Tables

Table

Figures

Figure

Chapter 1

Introduction

The following introduction includes material from the introductions of my papers Nerney, Bagenal, & Steffl (2017) [96] as well as Nerney & Bagenal (2020) [95].

The Galilean moon Io is the ultimate source of the majority of the plasma that fills up the giant magnetosphere of Jupiter. Kupo et al. (1976) [81] first detected via ground-based observations the S^+ emission surrounding the orbit of Io and Brown and Yung (1976) [26] identified this optical emission as coming from a cold, dense plasma. Io's volcanism was discovered in 1979 (Morabito et al., 1979; Peale et al., 1979) [100]. During the Voyager 1 and 2 flybys of Jupiter the Voyager Plasma Science instrument (PLS) (Bridge et al., 1979) [18] took in-situ plasma measurements and found a dense plasma torus (T_e = 5 eV, n_e = 2000 cm^{-3}) that was strongly emitting in the ultraviolet (UV) that was observed via remote observations from Voyager Ultraviolet Spectrometer (UVS) (Broadfoot et al., 1979) [19].

Io's volcanic source of predominantly neutral SO_2 is the origin of the Io plasma torus. Material is removed from Io's atmosphere via the local plasma interaction which includes ion/neutral charge-exchanges, electron-impact molecular dissociation and molecular ion dissociative recombination which result in a distribution of neutrals ejected out of Io's atmosphere to form an extended neutral cloud that is shaped via charge exchange, electron impact ionization, and gravity (Bagenal & Dols) [7]. Neutral ejection from Io has also been explained via sputtering off the exobase by Burger (2003)[28]. This extended source of neutral atomic sulfur and oxygen is ionized into sulfur and oxygen ions (S^+, S^{++}, S^{+++}, O^+, and O^{++}). These ions are picked up by Jupiter's intense

magnetic field and brought up to corotation velocity via mega amp currents via $\boldsymbol{J} \times \boldsymbol{B}$ forces that transfer angular momentum to the plasma near the orbit of Io (5.91 R_J) by coupling it to the ionosphere (See figures 23.5 & 23.6 from Thomas et al. 2004 for a description of the pickup process) [143]. In figure 1.1 we show a schematic view of the Io-Europa Space Environment and major components from Bagenal & Dols (2020) [7].

This corotating plasma is excited to higher energy states via electron impact excitation, and then via spontaneous emission of forbidden transitions, it decays back to a lower energy state emitting UV light which is diagnostic of plasma conditions (Steffl et al. (2004b); Osterbrock et al. (2006); Bagenal et al. (1992)).[137][99][3] This UV light has been studied by spacecraft we have sent to Jupiter such as Voyager UVS (Broadfoot et al., 1979, 1981;Sandel et al., 1979) [19] [108], Galileo UVS, Cassini UVIS (Esposito et al., 2004; Steffl et al., 2004a, 2004b) [50] [138] [137] and by Earth-orbiting satellites, International Ultraviolet Explorer (IUE) (Moos et al., 1983) [89], Hopkins Ultraviolet Telescope (HUT) (Moos et al., 1991) [90], Extreme Ultraviolet Explorer (EUVE) (Gladstone & Hall, 1998) [56], Hubble Space Telescope (HST) (Herbert et al., 2003; McGrath et al., 1993) [67] [84], Far Ultraviolet Spectroscopic Explorer (FUSE) (Feldman et al., 2001, 2004) [52] [53], and Hisaki (Yoshikawa et al., 2014, 2016) [162] [161].

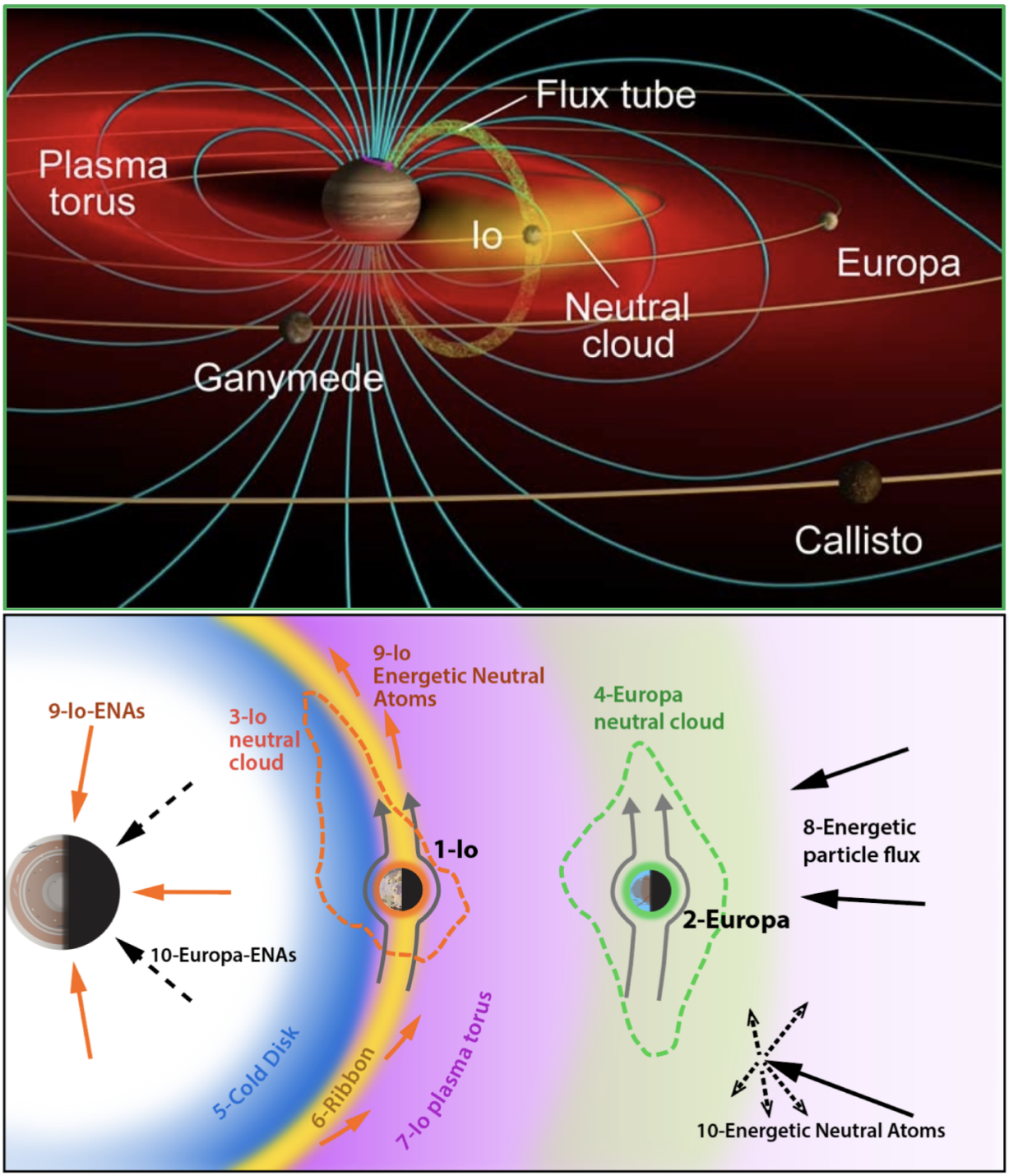

Figure 1.1: The Io-Europa Space Environment (from Bagenal & Dols (2020)[7]) and the 10 major components. Io and Europa orbit Jupiter at 5.9 and 9.4 RJ, with 1 R_J being the radius of Jupiter = 71,492 km. (Credit: top: John Spencer, SwRI; bottom: Steve Bartlett).

The primary ions in the Io plasma torus are S^+, S^{2+}, S^{3+}, O^+, and O^{2+}, with an additional 10% protons [Bagenal, 1994] [5]. 1 R_J or 1 Jupiter radii is defined for our work to be exactly 71,492 km and is the relevant length scale to work with. In the cold torus (<5.7 R_J) SO_2^+ ions have also been detected at the 1% level [Bagenal, 1985] [4]. Minor amounts of S^{4+} [Steffl et al., 2004b] [137], Na+ [Hall et al., 1994] [60], Cl^+, Cl^{2+} [Feldman et al., 2001] [52], and K^{2+} [McNutt, 1993] [86] have also been detected. The relative abundances of S^+, S^{2+}, and S^{3+} are well determined by the relative strengths of their multiple emission lines across the UV spectrum as measured by Voyager [Broadfoot et al., 1979, 1981; Sandel et al., 1979] [19] [108], IUE [Moos et al., 1983] [89], HUT [Moos et al., 1991] [90], EUVE [Gladstone and Hall, 1998] [56], HST [McGrath et al., 1993; Herbert et al., 2003] [84] [67], FUSE [Feldman et al., 2001, 2004] [53], Cassini Ultraviolet Imaging Spectrograph (UVIS) [Steffl et al., 2004a, 2004b] [138] [137], and Hisaki [Yoshioka et al., 2014] [163]. Extensive observations by the latter two have quantified the modulation of the S^{n+} emissions with longitude (Systems III and IV), local time, and epoch [Steffl et al., 2006, 2008; Tsuchiya et al., 2015] [135] [136] [150].

The Io plasma torus ion latitudinal distribution along magnetic field lines can be approximated as a Gaussian scale height distribution $\left(n_i \propto e^{-z^2/H_i^2}\right)$ for small distances z about the centrifugal equator depending on the equatorial ion temperatures, ion mass, and angular velocity (Hill & Michel (1976); Bagenal et al. (1981), (1994))[72] [8][5].

There are essentially four distinct radial regions within the Io plasma torus. The first is the "warm" torus which constitutes the majority of the mass (90%) (Bagenal & Dols 2020) [7] (hence doughnut-shaped). The warm torus is the outer region outside the orbit of Io which is predominantly circular in cross-section ($H_i \approx 1R_J$) with 60 -100 eV ion temperatures. The second region moving radially inward is the "ribbon" which is traditionally given by the location of the peak of the S^+ visible emission profile. The location of the ribbon is just inside Io's orbit and is between about 5.6 and 5.8 R_J from Jupiter where the scale height decreases rapidly in a narrow region moving radially inward to the "cold" torus. Between the ribbon and cold torus there is the "gap" region where emission and density plummet before coming back up in the cold torus. The

fourth and final region within the Io plasma torus is the cold torus which is inside the ribbon. This region is between about 5 and 5.5 R_J from Jupiter and resembles a thin disk or washer. These radially defined regions vary with local time by up to 0.3 R_J (Herbert et al. 2007)[66]. This cold torus has much lower ion and electron temperatures of a few eV and therefore the scale height is smaller ($H_i \approx 0.2 R_J$) resulting in the plasma being confined to the equatorial region.

The plasma is primarily confined to the equator and experiences centrifugal forces which drive the transport of the plasma outwards away from Jupiter to larger radial values. Hill et al. (1981) [70] described the radial plasma transport via centrifugally driven flux tube interchange which can be thought of as an analog to the Rayleigh–Taylor instability. Full flux tubes move outwards and are replaced with empty or less massive flux tubes leading to radial transportation of mass. Outward transport is strongly favored over inwards as the centrifugal acceleration at Io is about 1 g (9.8 m/s^2) pointing away from the rotation axis which dominates over the approximately $\frac{GM_J}{r_{Io}^2}$=0.7 m/s^2 (where G is the gravitational constant, M_J is the mass of Jupiter, and r_{Io} is the orbital distance of Io from Jupiter) that gravity contributes inwards towards Jupiter. The Boltzmann equation describes how the plasma distribution function evolves in time. Due to flux tube interchange motions, the plasma will diffuse with radially outward, favored over inwards. The relevant version of this is the Fokker-Planck equation which describes radial transport via a diffusion equation which is reviewed in Thomas et al. (2004) [143].

Via what is known as "diffusive equilibrium" the distribution of plasma along a dipole magnetic field given by an anisotropic Maxwellian is found by considering the multi-fluid Navier-Stokes momentum equation in the rotating frame non-inertial frame including the plasma pressure, the centrifugal force, the ambipolar electric field, and neglecting gravity along a dipole magnetic field line (Bagenal et al. (1981), (1994); Dougherty et al. (2017); Delamere et al. (2005) [8][5][47][40]). By integrating each ion momentum equation along a field line from S_0 to S the distribution along a magnetic field line is given by

$$n(S)_i = n(S_0)_i \exp\left[\left(1 - \frac{T_{\perp i}}{T_{\parallel i}}\right)\log\left(\frac{B(S)}{B(S_0)}\right) + \frac{m_i\Omega^2}{2T_{\parallel i}}\left(\rho^2(S) - \rho^2(S_0)\right) - \frac{Z_i e}{T_{\parallel i}}\left(\Phi(S) - \Phi(S_0)\right)\right] \tag{1.1}$$

S_0 is the reference point along the field line, S is the desired point along the field, n_i is the ion number density (ions/cm^3), m_i is the ion mass, $T_{\parallel i}$ and $T_{\perp i}$ are the parallel and perpendicular ion temperatures, B is the magnetic field strength, Ω is the angular velocity of the corotating plasma, ρ is the perpendicular distance to the spin axis, Z_i is the charge number, e is the elementary charge, and Φ is the ambipolar electric potential. If we included gravity there would be 1 extra term in the exponential given by $\frac{1}{T_{\parallel i}}\left(\frac{GM_J m_i}{r(S)} - \frac{GM_J m_i}{r(S_0)}\right)$. This term is not important near the torus but on field lines close to Jupiter it becomes important.

The ion and electron velocity distributions in the Io plasma torus are approximately Maxwellians at low energies. Which, in an approximately dipolar magnetic field the latitudinal diffusive equilibrium distribution for a single ion species, can be approximated as a Gaussian scale height distribution $\left(n_i \propto e^{-z^2/H_i^2}\right)$ about the centrifugal equator depending on the equatorial ion temperatures, ion mass, and angular velocity (Hill & Michel (1976); Bagenal et al. (1981), (1994))[72] [8][5]. For a Maxwellian in a dipole magnetic field, the temperature is constant along a field line. Typical ion scale heights are about 1 R_J in the warm torus and 0.2 R_J in the cold torus.

While sulfur ion abundances are well determined, the total amount of oxygen and the relative abundances of O^+ and O^{2+} remain a major issue. Two unfortunate quirks of nature frustrate our determination of composition: (i) O^+ and S^{++} share a mass/charge ratio of 16 which means that they are not separated by in situ plasma instruments that measure energy/charge and (ii) the strongest EUV emission lines of O+ and O^{2+} are right next to each other at 833 and 834 Å. The initial Voyager UVS papers only mentioned O^{++} [Broadfoot et al., 1979; Sandel et al., 1979] [19] [108]. Shemansky [1980a] [120] argued that the lack of emission at 539 Å from O^+ implied that the strong emission in the 833–834 Å region had to be from O^{++}. Furthermore, he wanted a high electron temperature so he argued that the 833–834 multiplet had to be O^{++}. This inference was

contradicted by Durrance et al. [1983] [49] who reported on a 1981 rocket flight of a UV instrument that showed a lack of O^{++} emission at 1664 Å (as well as emissions from neutral O and S consistent with O/S=2 from dissociation of SO_2 escaping from Io's atmosphere).

A major contribution to the difficulty in analyzing these early observations was the lack of reliable atomic data on efficiencies for radiation at these EUV wavelengths. Strobel and Davis [1980] [141] accessed different atomic data (to that used by the Voyager team) at the Naval Research Laboratory and modeled the Voyager UVS spectra with a composition of $O^+/O^{++} \approx 2$ (but with total sulfur ions dominating over oxygen) and invoked the need for a hot electron population. Shemansky and Smith [1981] [123] and Broadfoot et al. [1981] [21] maintained that their analysis of the Voyager UVS spectra was consistent with $O^+/O^{++} < 15\%$.

In the meantime, modelers were trying to match the various ground-based optical and space-based UV emissions, plus in situ Voyager plasma measurements with equilibrium calculations of electron impact ionization of neutral O and S, heating via ion pickup and cooling via radiation [Shemansky and Sandel, 1982; Brown and Shemansky, 1982] [122][24]. Brown et al. [1983] [25] noted the lack of O^{++} emission at 5007 Å and suggested that perhaps the process of charge exchange, with reaction cross sections recently calculated by Johnson and Strobel [1982] [75], could be removing O^{++} ions. Such "neutral cloud theory" modeling efforts proceeded, starting with relatively simple models [Smyth and Shemansky, 1983; Moreno et al., 1985; Shemansky, 1987] [134] [125] [91]. With a remarkably comprehensive model of the torus (that calculated the velocity distribution of ions resulting from ionization, charge exchange, Coulomb collisions, and radiation) Smith and Strobel [1985] [132] pointed out the difficulty in producing Broadfoot et al.'s [1979] [19] reported UV brightness for a torus powered by just ion pickup. Later models recognized this need to add energy to the system via an ad hoc source of hot electrons [Barbosa and Moreno, 1988; Shemansky, 1988; Smith et al., 1988] [11] [121] [131] and incorporated new charge exchange cross sections as they became available [McGrath and Johnson, 1989] [85]. While Thorne [1981] [147] proposed that auroral secondary electrons could be powering the torus, Smith et al. [1988] [131] argue for hot ions moving inward from the outer magnetosphere. Current ideas support an external

source of hot electrons either associated with fluxtube interchange transport [Hess et al., 2011] [68] or waves [Yoshioka et al., 2014; Tsuchiya et al., 2015] [163][150].

The Voyager in situ plasma measurements from the Plasma Science (PLS) instrument provided key measurements of electron density and temperature, including evidence of a suprathermal component [Scudder et al., 1981; Sittler and Strobel, 1987] [118] [128]. The Voyager PLS ion measurements provided good composition in the inner torus (<5.6 R_J) where high Mach flow produces separate peaks in energy/charge spectra for mass/charge=8, 16, 32, and 64 ions, but in the warm torus the ions produced overlapping peaks preventing unique determination of composition [Bagenal and Sullivan, 1981; Bagenal, 1985] [8][4]. A relatively small fraction (10%) of the iogenic material moves inward from Io's orbit, and the composition is likely affected by the neutral clouds that extend inward (see review by Thomas et al. [2004] [143]). It is probably unwise, therefore, to apply the cold, inner torus composition to the warm, outer torus. Bagenal [1994] [5] relied on analysis of UV emissions (specifically Shemansky [1987] [125]) for warm torus composition to construct an empirical model of the Io plasma torus for the Voyager era.

In the post-Voyager era, further space-based UV observations provided valuable clues about the ion composition, particularly the abundance of oxygen species, but their analysis continued to be frustrated by uncertainties in the atomic data. McGrath et al. [1993] [84] used HST to look at the torus and detected O+ emission at 2471 Å. EUVE detection of O+ emission at 539 Å indicated O+ to be not just greater in abundance than O^{++} but, in fact, the dominant ion species [Hall et al., 1994; Gladstone and Hall, 1998; Herbert and Hall, 1998] [60] [56] [63]. Herbert et al. [2001, 2003] [62] [67] further analyzed EUVE and HST data, looking for evidence of temporal variations while Galileo was orbiting Jupiter (1996–2003). Within this time frame a new atomic database was being developed, primarily for analyzing solar data, called CHIANTI [Dere et al., 1997] [43]. Herbert et al. [2001, 2003] [62] [67] found factors of 2 variations in abundances depending on whether the original Collisional and Radiative Equilibrium (COREQ) (from Don Shemansky) or the CHIANTI database is applied (see discussion in section 2.2). Similarly, physical chemistry models produced varying results depending on the input atomic data [Shemansky, 1988; Barbosa,

1994; Schreier et al., 1998; Lichtenberg et al., 2001] [121] [10] [117] [82]. Delamere and Bagenal [2003] [39] developed a physical chemistry model to explore the sensitivity of torus conditions to changes in radial transport as well as sources of neutrals and hot electrons, comparing their model with these previous studies. They found that it was necessary to have a neutral atomic source with O/S 4 in order to match their model to the Voyager conditions from Shemansky [1987] [125] and Bagenal [1994] [5].

In late 2000 the Cassini spacecraft approached Jupiter to get a gravity assist to its primary destination, Saturn. The Cassini UVIS instrument [Esposito et al., 2004] [50] obtained high-resolution spectra of the torus from 561 Å and 1913 Å. Steffl et al. [2004a] [138] present an overview of several months of Cassini UVIS observations of the torus. Steffl et al. [2004b] analyze a radial scan of the torus obtained in January 2001. This radial profile was modeled by Delamere et al. [2005] [40] who found that they could match the Cassini torus composition in a physical chemistry model having a neutral atomic source with O/S ≈ 2, consistent with dissociation of SO_2, Io's main atmospheric constituent. Provoked by a thousandfold increase in dust from Io observed by Krüger et al. [2003] [80], Delamere et al. [2004] [41] explored the temporal variability of the Cassini UVIS emissions which they modeled with just a factor of 3–5 increase in atomic O and S from Io, suggesting that the gases escaping from Io are less variable with volcanic eruptions than the dust. Steffl et al. [2006] [135] presented an analysis of torus emission variations with Systems III and IV longitudinal which they modeled with a static System III longitudinal modulation of hot electrons, modulated by a second hot electron population that drifted with System IV period [Steffl et al., 2008] [136]. Recently, Copper et al. [2016] [33] have combined the radial model of Delamere et al. [2005] [40] with the azimuthal model of Steffl et al. [2008] [136] to produce a two-dimensional model of torus variability driven by changes in the small fraction ($< 0.5\%$) of hot electrons. Continuing with Copper's model Coffin et al. (2017) [31] showed that using an L-shell dependent subcorotation profile consistent with observations of Brown (1994) [23] and Thomas et al. (2001) [146] in addition to a System III hot electron modulation could reproduce the System IV periodicity.

As Jupiter rotates with a period of 9.925 hours so do its magnetic field lines and the corotating plasma. This defines what is known as System III longitude. System IV is periodicity that drifts at a few percent slower than System III (Bagenal & Dols 2020) [7]. There have been observed modulations in torus brightness due to volcanic eruptions such as in October 2000 as viewed by Cassini (Delamere et al. 2004 ; Bagenal & Dols 2020)[41][7] and by Hisaki during 2015 (Hikida et al. 2020) [69]. The brightness of torus emissions has a dawn-dusk asymmetry and a radial shift in emissions due to an east-west electric field from Iogenic plasma flowing down the tail of the magnetosphere which gives a $-\boldsymbol{v} \times \boldsymbol{B}$ convection electric field (Barbosa & Kivelson 1983) [13].

Due to a 10° offset between the magnetic equator and Joviagraphic (rotational) equator centrifugal forces confine the plasma to what is known as the centrifugal equator which is defined as the farthest point from the spin axis along a magnetic flux-tube (Phipps & Bagenal 2021) [102]. For an offset titled dipole this is 2/3 of this difference ($\approx 7^{\circ}$ from rotational). Io and its neutral clouds orbit in the rotational equator. This tilted torus corotating with Jupiter's magnetic field as viewed from Earth then appears to wobble at $\pm 7^{\circ}$ as the plasma rotates. The geometry of these 3 equators is shown in figure 1.2 from Dougherty et al. (2017)[47].

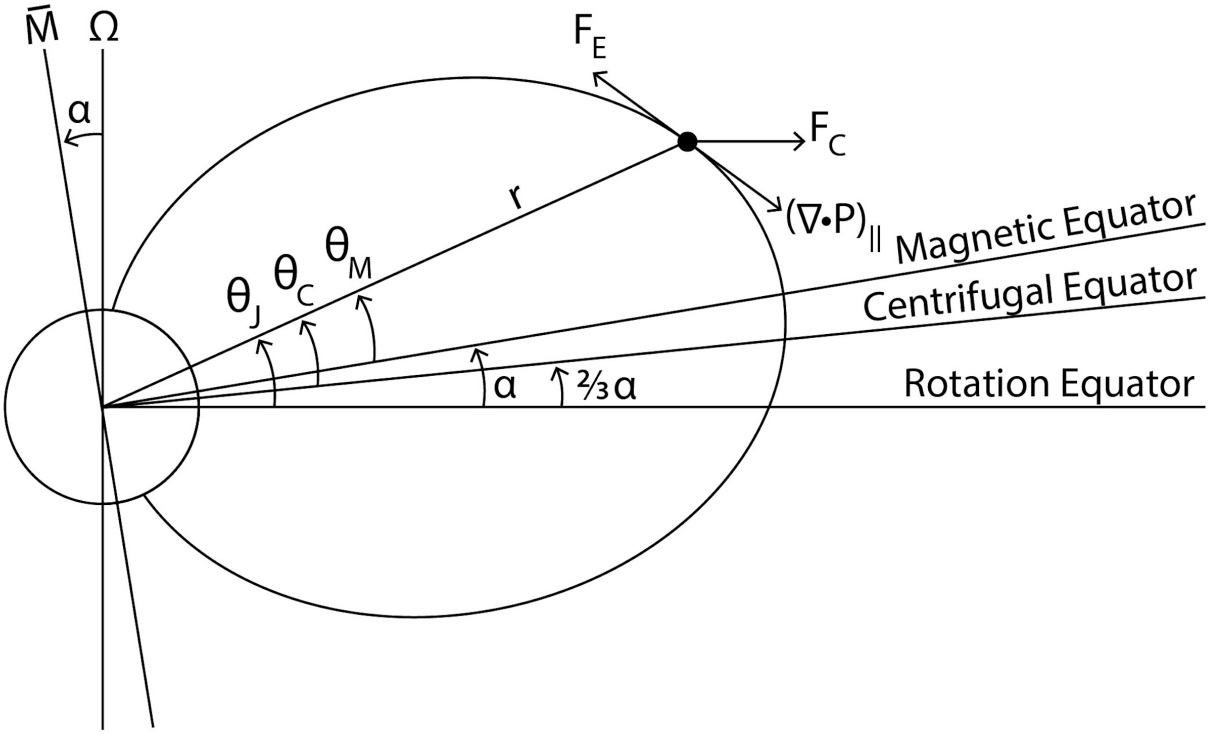

Figure 1.2: Geometry of a dipole magnetic field with magnetic moment ($\boldsymbol{M}$) tilted by an angle (α) from the planet's spin axis ($\boldsymbol{\Omega}$). The peak in the plasma density is found at the centrifugal equator, the farthest point from the spin axis along a given magnetic field line (Dougherty et al. 2017)[47].

In the Io plasma torus the plasma is magnetic pressure dominated. At the orbit of Io, Jupiter's magnetic field strength is about 2×10^{-6} Tesla and typical ion temperatures are around 100 eV. This gives a plasma β of about 0.001 which is the ratio of the plasma pressure (nkT) to the magnetic pressure $\left(B^2/2\mu_0\right)$. The typical Debye length is about 33 cm. In my work, I deal with typical scales of 0.05 R_J =3574.6 km at the minimum, so the quasi-neutrality condition holds. At Io the electron plasma frequency is about 2.7×10^6 rads/s, the electron plasma timescale is 2.4×10^{-6} seconds, ion gyro-radii are between 2-10 km, the sound speed is 10^6 m/s, and the Alfvén

speed is about 200 km/s. In our work thus the spatial scales we care about are much larger than any of these lengths. The local interaction with Io is on the timescale of minutes, ionization/charge exchange timescales on the order of hours, and radial transport timescales on the order of days. The timesteps we use in our modeling are at a minimum 10 seconds (due to numerical instabilities). Again much larger than the plasma oscillation timescale of about a μs.

In chapter 2, I present my analysis of the warm Io plasma torus Voyager, Galileo, & Cassini YV spectra and determined ion composition. In Chapter 3, I show that by using spectral analysis alone I am unable to determine the fraction of hot electrons (non-thermal component) in the warm torus uniquely. By combining UV spectra and physical chemistry modeling I can constrain the fraction of hot electrons. In chapter 4, I describe in detail the model used to simulate an Io plasma torus emission spectrum and how I integrate this over the line of sight using the Colorado Io Torus Emission Package 2 (CITEP 2). I apply the model to various density models and compare them with observations. I predict emissions in the visible as well as in the UV as a future mission planning tool and to determine a nominal torus emission model. In chapter 5, I describe the components of our physical chemistry model including the cubic cm model, latitudinal averaging scheme, longitudinal model, and radial transport model. I describe our self-consistent 3D IPT physical chemistry model incorporating the cold torus, gap region, ribbon, and warm torus and I have determined the tipping point for inwards vs outwards radial diffusion and implied plasma transport timescales. In chapter 6, I summarize my results, future work to be done, and open questions about the Io plasma torus. In appendix A, I present an analytic solution to the radial transport equation for the steady state without source and loss terms and show that for general source and loss terms what the contribution would look like to the steady state. I also present a separable solution to the transient radial transport equation (in the absence of sources or losses) and find a transient timescale or e-folding time reminiscent of the transport timescales generally used in the literature to describe transport.

Chapter 2

Io Plasma Torus Ion Composition: Voyager, Galileo, Cassini

2.1 Introduction

The following Chapter is from my paper Nerney, Bagenal, & Steffl (2017) [96].

With Japan Aerospace Exploration Agency's (JAXA) Hisaki spacecraft in orbit around Earth gathering information on the Io plasma torus [Yoshikawa et al., 2014] [162] and the Juno mission measuring plasma conditions in the Jovian magnetosphere [Bagenal et al., 2017] [1], the time is ripe for a reevaluation of earlier observations of the plasma torus to assess evidence for temporal variations. In particular, we are interested in exploring the ion composition of the torus and whether there is evidence that the volcanic gasses from Io (the ultimate source of the ions) have deviated from SO_2.

Previous reviews of the composition of the plasma torus [e.g., Strobel, 1989; Delamere and Bagenal, 2003; Thomas et al., 2004; Steffl et al., 2004b] [140] [39] [143][137] have shown significant changes in reported composition since the early detections by Voyager [Broadfoot et al., 1979; Sandel et al., 1979] [19] [108]. The issue is the extent to which these changes are real variations in composition versus "essentially a function of our learning curve" [Strobel, 1989] [140]. In particular, estimates of the radiation efficiencies of the relevant sulfur and oxygen ions have changed dramatically over the past 40 years and are still being updated.

In this chapter we return to the UV spectra of the torus obtained by Voyager, Galileo, and Cassini, which we analyze with the latest version of the CHIANTI atomic database, to test if there is evidence of the torus ion composition varying between these epochs. In section 2.2 we describe

our analysis method, section 2.3 shows the results, we discuss these results in relation to past other observations in section 2.4, and we summarize our conclusions in section 2.5.

2.2 Method

The data analyzed in this paper come from UV spectrometers aboard the Voyager, Galileo, and Cassini spacecraft as they flew close to Jupiter. The Voyager UV Spectrometer (Voy-UVS) covered the wavelength range 50–170 nm (500–1700 Å) with a resolution of 3.0 nm (30 Å) [Broadfoot et al., 1977] [20]. The initial analysis of Io torus spectra is presented in Broadfoot et al. [1979] [19] and Sandel et al. [1979] [108]. The Galileo (GLL) ultraviolet spectrometer comprised two instruments: a UVS that was pointed on the scan platform of the three-axis stabilized part of the spacecraft and the EUVS instrument that was on the spinning part of the spacecraft. The EUVS was the only instrument to obtain torus data. Hord et al. [1992] [74] report that GLL-EUVS spanned 54–128 nm (540–1280 Å) with a spectral resolution of 0.7 (below 190 nm) to 1.3 nm (7–13 Å). Given the fact that the EUVS spectrometer only had the torus in the field of view for a few seconds per spin, it is perhaps not surprising that the quality of the torus observations is quite poor. Esposito et al. [2004] [50] report that the Cassini Ultraviolet Imaging Spectrograph (UVIS) has a spectral range of 56.1–118.1 nm (561–1181 Å) in the EUV and 114–191.3 nm (1140–1913 Å) in the FUV, with a spectral resolution of 0.3 nm (3 Å).

Figure 2.1 shows a comparison of spectra taken by these three instruments of the Io plasma torus. The Voyager spectrum shown is from Donald Shemansky as published in Bagenal et al. [1992] [3]. The Voyager 1 UVS instrument scanned the Jovian system for 30 days beginning 15 March 1979, and the 30 days of data were binned in steps of 0.5 R_J. The spectrum shown is from 5.75 R_J. The spectrum was converted from counts per channel to Rayleighs per angstrom using the pre-Jupiter encounter calibration curve (see section 2.11) that was provided by Jay Holberg (personal communication, 2015). The error bars on the spectrum are calculated using Poisson statistics on the original spectral bins.

The Galileo EUVS spectrum and the calibration curve were provided by Wayne Prior (private

communication, 2014). We examined 1326 Galileo EUVS spectra but only found a few from June 1996 that had significant signal-to-noise for compositional analysis. The Galileo data shown in Figure 2.1 are from the midnight ansa. We took 17 spectra over days 171–174 of 1996 and median combined the spectra to derive the median counts for each channel. The error bars shown in Figure 2.1 are derived using Poisson statistics on these counts.

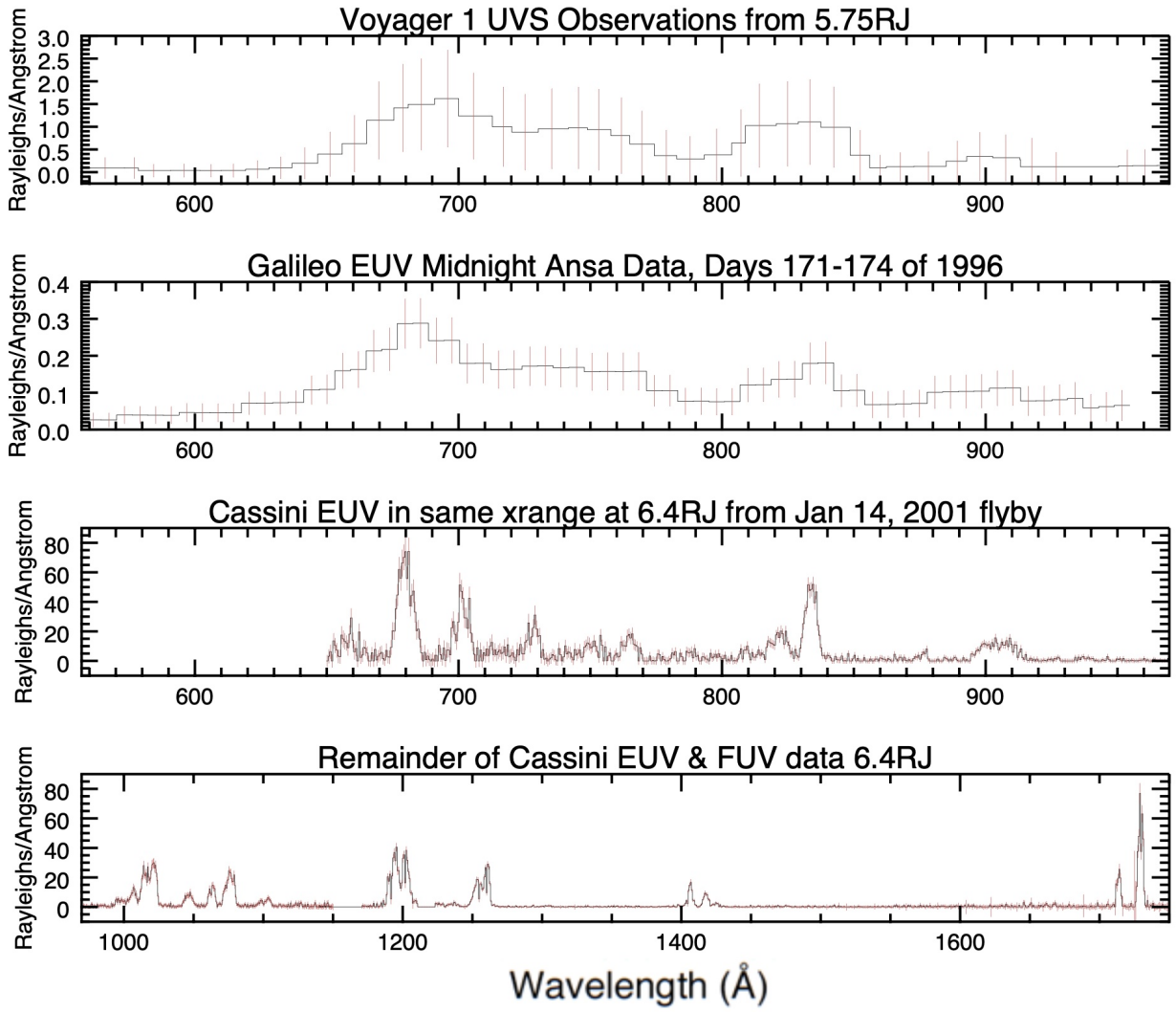

Figure 2.1: Ultraviolet emissions observed by Voyager, Galileo, and Cassini. The error bars reflect Poisson statistics on the raw counts.

The Cassini UVIS observations of the Io plasma torus are summarized in Steffl et al. [2004a] [137]. Figure 2.1 of that paper shows the calibration curve that we use in this paper. For this paper we take the UVIS data obtained on 14 January 2001 as a radial scan across the torus [Steffl et al., 2004b] [137].

2.3 Spectral Emission Model

We use a "cubic centimeter emission model" to calculate the volume emission rate which we integrate over a line of sight to produce the total emission at a given wavelength in units of Rayleighs (=10^{-6} photons cm^{-2} s^{-1} sr^{-1}). This is the same technique used by Steffl et al. [2004a] [138] and similar to that used by Shemansky [1980a] [120] and Shemansky and Smith [1981] [123]. This approach ignores the vertical scale height distribution and assumes the brightest emission is from the equator. The brightness, B, of a given spectral line is given by

$$B = 10^{-6} \int A_{ji} f_j n_{ion} dL \quad \text{Rayleighs} \tag{2.1}$$

The constant A_{ji} is the Einstein coefficient for spontaneous emission, otherwise known as the radiative decay rate from the upper emitting state j to the lower state i. The function f_j is the fraction of ions in the upper emitting state j which varies with the local temperature and density of the electron population. We assume a Maxwellian electron velocity distribution with an electron temperature T_e, electron number density n_e, and n_{ion} is the number density of the ion species responsible for the emission.

In order to do the line integral in equation 2.1, we must assume the spatial variation of the electron distribution function over the line of sight. Because the observed brightness of the torus falls off sharply with radial distance, we take the electron density to be uniform over an effective scale length along the line of sight.

With this last assumption of a uniform electron distribution function over the line of sight, we have

$$B = 10^{-6} A_{ji} f_j N_{ion} \quad \text{Rayleighs} \tag{2.2}$$

$$N_{ion} = \int n_{ion} dL \tag{2.3}$$

where N_{ion} is the ion species column density (in units # cm^{-2}), the integrated local number density (# cm^{-3}) over the line of sight. We refer to the approximate path length or line of sight as

$$\frac{N_{ion}}{n_{ion}} = L \tag{2.4}$$

Using an atomic database of differential cross sections and radiative decay values, we can calculate $A_{ji}\ f_j(T_e, n_e)$ and then we multiply by $10^{-6}\ N_{ion}$ to have the model output in Rayleighs at each discrete wavelength in the range of interest. To simulate a spectrum observed by a specific instrument with a spectral resolution, we divide the predicted brightness by the bin size to obtain emission in Rayleighs per angstrom. We then treat each discrete emission as a normalized Gaussian (at the full width half maximum (FWHM) resolution of the instrument) and add up emissions due to each different ion species to create a synthetic continuous spectrum to compare with an observation.

Figure 2.2 shows a sample spectrum from Cassini UVIS [Steffl et al., 2004b] [137] which shows the multiple lines that contribute to the torus emissions from the five dominant ions.

2.4 Atomic Databases

When Voyager first detected UV emissions from the Io plasma torus in 1979, the data on emission rates of sulfur and oxygen ions in the EUV were limited. Initial analyses [Broadfoot et al., 1979; Sandel et al., 1979] [19] [108] used what was available in the literature at the time. Donald Shemansky developed a database (Collisional and Radiative Equilibrium, COREQ) that he used to analyze the Voyager UVS data [e.g., Shemansky, 1980a, 1980b, 1987, 1988] [120] [119] [125] [121] and made available to the community. In 1997 a group of UV astronomers put together a database of UV emissions in the CHIANTI database [Dere et al., 1997] [43]. This public database has been

updated periodically, the most recent being CHIANTI 8.0 [Del Zanna et al., 2015; Del Zanna and Badnell, 2016] [38] [37].

Steffl et al. [2004b] [137] used the CHIANTI 4.2 for their data analysis of the Cassini UVIS spectra. There are no significant changes in the EUV emissions predicted by CHAINTI versions 4.2 to 7.0, but for version 8.0 Del Zanna and Badnell [2016] [37] report substantial differences in S^{+} and S^{++} emissions, especially in the EUV. These differences stem from updated atomic cross sections and radiative decay values from recent experimental work [Del Zanna and Badnell, 2016] [37]. Furthermore, the method for computing the differential cross section has also changed. To illustrate the differences between the Io torus emissions predicted by changing atomic data, we compare in Figure 2.3 the emissions predicted by CHIANTI 7.0 and 8.0 for the same typical torus conditions at the resolution of the Cassini UVIS instrument. While the changes in emissions from O^{++} and S^{+++} did not change, there are significant changes to S^{+}, S^{++}, and O^{+} emissions.

To illustrate the differences between the current CHIANTI 8.0 and earlier analyses of Voyager data, we have taken values of the radiative cooling coefficients (versus electron temperature) for the different relevant sulfur and oxygen ions of the torus from Shemansky [1988] [121]. In Figure 2.4 and 2.5 we compare these Shemansky [1988] [121] values (shown as symbols) with the output of CHIANTI 8.0 (shown as continuous lines). We have used the same units as Shemansky [1988] [121], essentially the power per ion density per electron density per volume being emitted in photons by the torus, 1 ergs s^{-1} cm^{3} = 10^{-13} Watts m^{3}. Given an electron temperature and density, the CHIANTI program produces A_{ji} $f_{j}(T_{e}, n_{e})$ for each discrete emission line in units of photons/s for a given ion. Multiplying this by $\frac{hc}{\lambda}$ in cgs gives ergs/s, and then dividing the result by the electron density gives us the radiated power in ergs s^{-1} cm^{3}. We then sum up all of the discrete emission in the spectral range of the CHIANTI database version 8.0 (1–600,000 Å) to obtain radiative cooling coefficients for the different ions in Figure 2.4 and 2.5. We held n_{e} and then varied the electron temperature to create the plot above. Recalculating for a more realistic electron density for the center of the torus of 2000 cm^{-3} produced curves that were negligibly different.

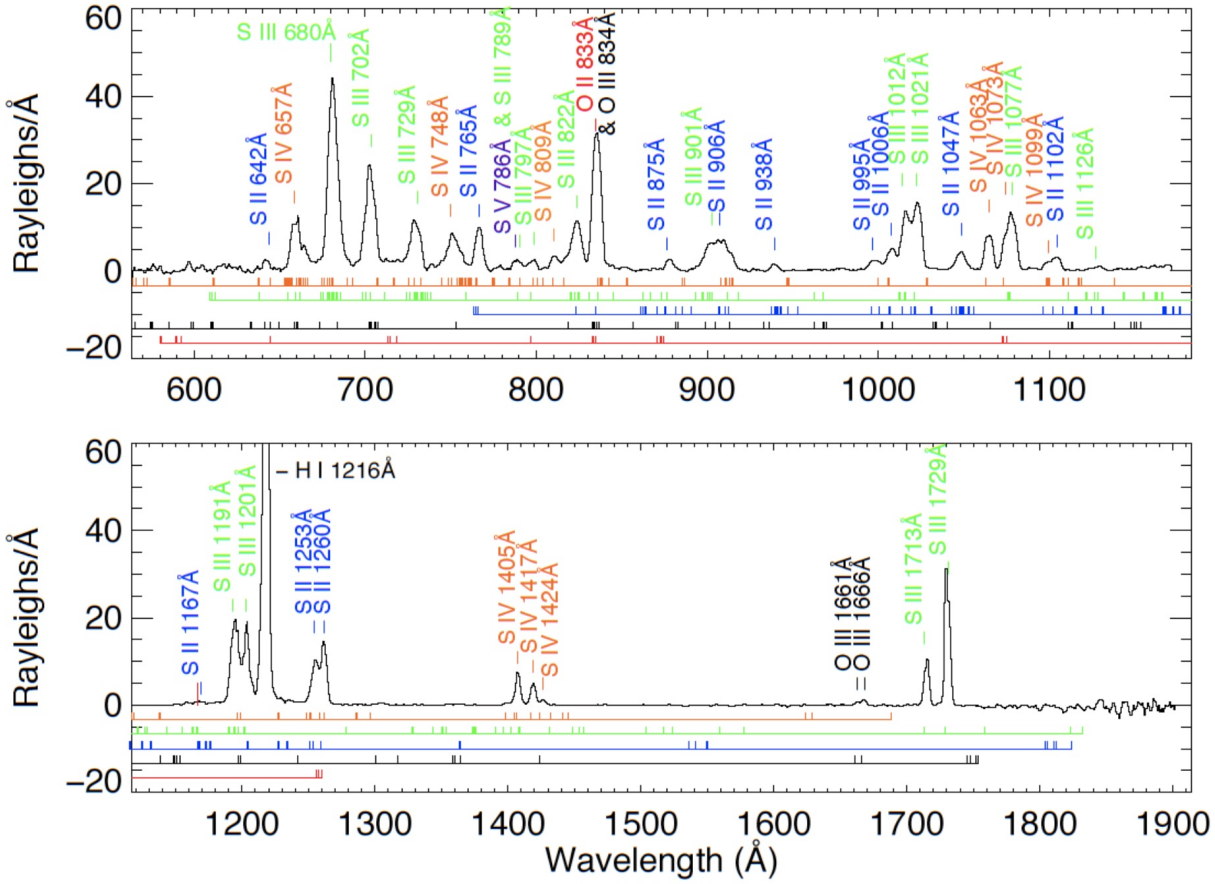

Figure 2.2: Composite spectrum of the Io plasma torus from 561–1913 Å. The spectral features are labeled and color-coded by the ion species that makes the dominant contribution to the feature. Locations (as contained in the CHIANTI database) of the individual spectral lines of the five major ion species in the torus are plotted beneath the spectrum [from Steffl et al., 2004b] [137].

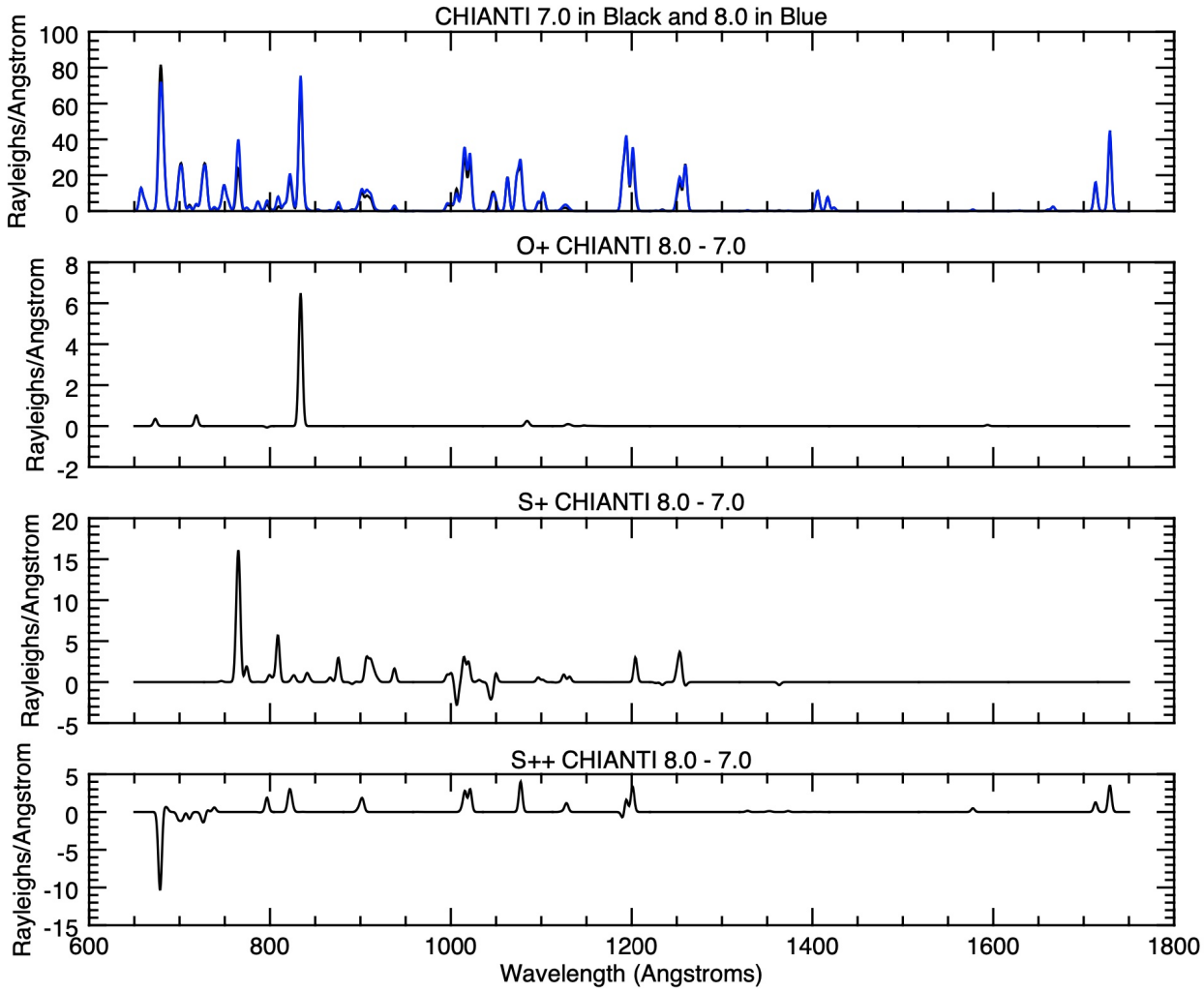

Figure 2.3: Differences in emissions predicted by CHIANTI 8.0 and 7.0 for typical parameter conditions shown at the UVIS resolution. The differences in S^{+++} and O^{++} emissions between CHIANTI 8.0 and 7.0 are negligible.

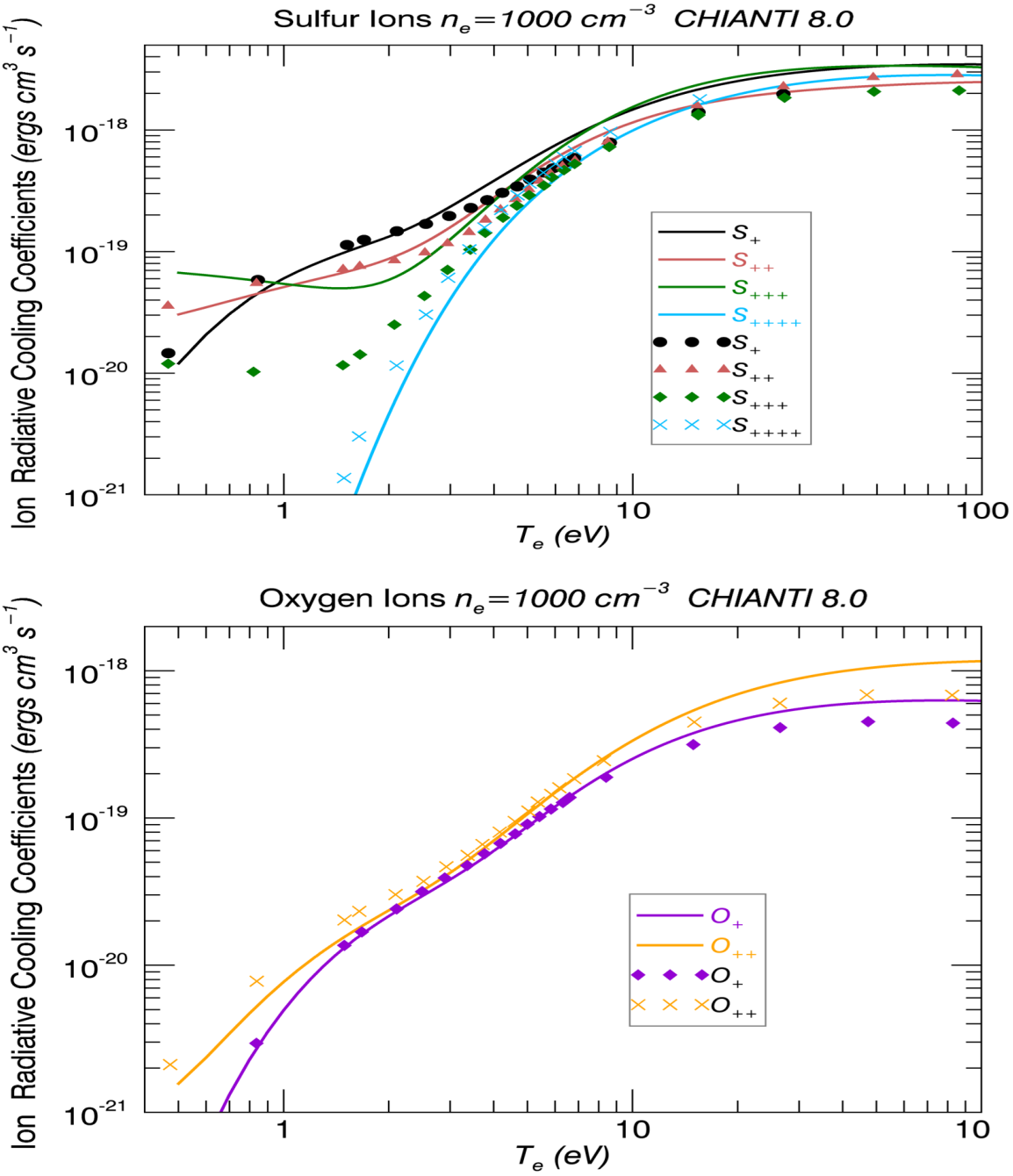

Figure 2.4: Net emission from (top) sulfur and (bottom) oxygen ions versus electron temperature as predicted by (lines) CHIANTI 8.0 compared with (symbols) Shemansky [1988] [121].

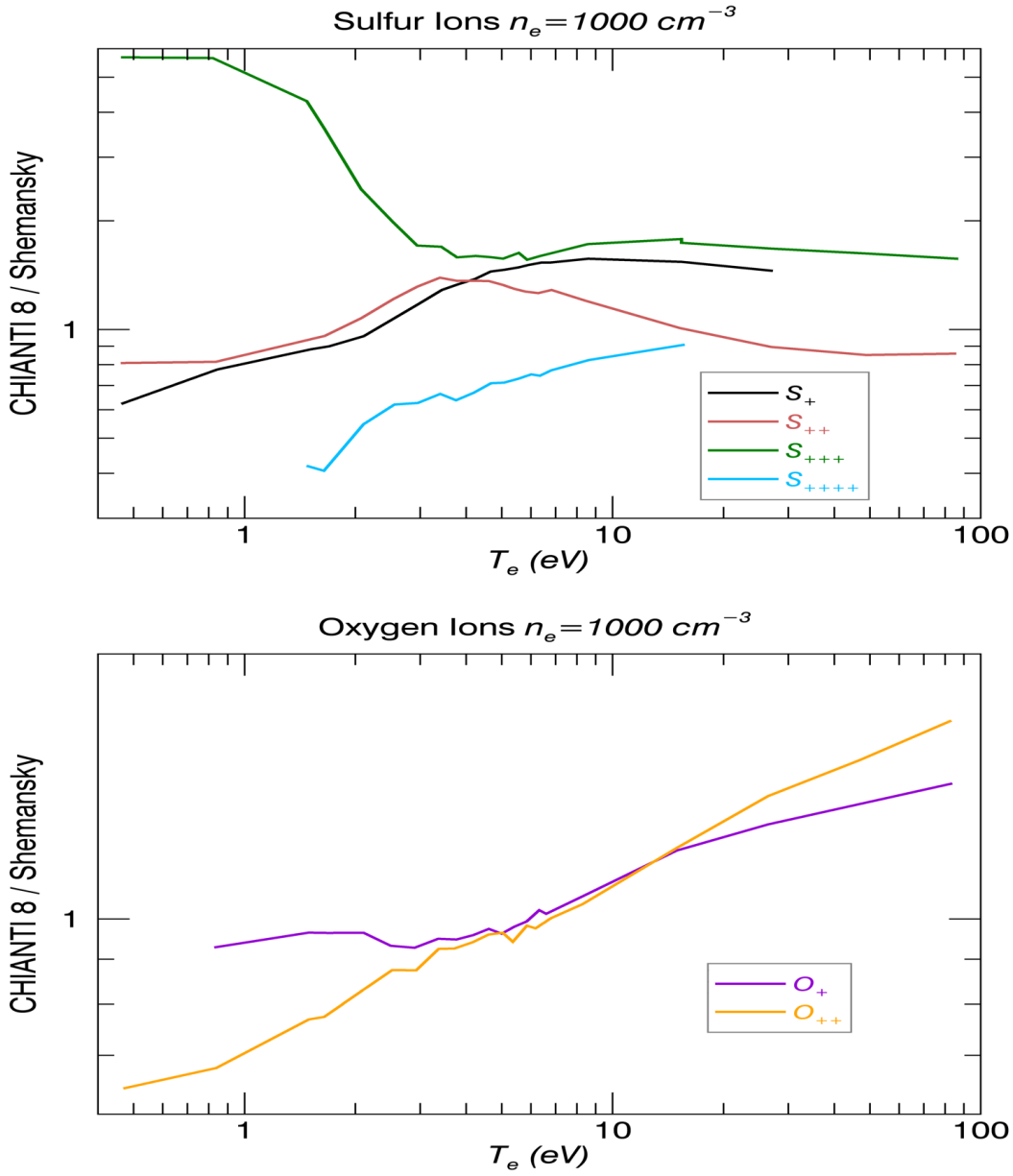

Figure 2.5: The CHIANTI 8.0 predictions divided by the values calculated by Shemansky (1988) [121].

Figure 2.4 and 2.5 shows the largest changes in S^{+++} emissions which CHIANTI 8.0 suggests radiate as much as 6 times more efficiently at electron temperatures below $\approx$ 3 eV. For analysis of torus data (where temperatures of 4–10 eV are more typical) the 50% increases in efficiency of radiation by S^{+} and S^{++} as well as O^{+} and O^{++} (particularly for any suprathermal electrons above 10 eV) are more important.

2.5 Fitting Procedure

With a forward model (using CHIANTI 8.0) that calculates a spectrum as a function of electron density, electron temperature, and ion composition, we can compare the model spectrum with different UV data sets. While we use a single Maxwellian electron distribution in our modeling, we note that in situ measurements of the electron distribution in the Io plasma torus made by the Voyager and Galileo spacecraft suggest that the electron distribution function in the Io torus has a suprathermal tail [Sittler and Strobel, 1987; Frank and Paterson, 2000] [128] [54]. Addition of a small amount (≈0.2–0.5%) of hot (20–100 eV) electrons is key for physical chemistry models of the torus [Barbosa, 1994; Shemansky, 1988; Delamere and Bagenal, 2003] [10] [121] [39]. However, Steffl et al. [2004b] [137] showed that including such a suprathermal electron component made little difference to analysis of the Cassini UVIS spectrum.

For analysis of the Voyager and Cassini UV data of emissions at different radial cuts through the torus we use the profile from Steffl et al. [2004b] [137]:

$$n_e = 2200 \left(\frac{r}{6}\right)^{-5.4} \text{ cm}^{-3},\ r < 7.81\ R_J \tag{2.5}$$

$$n_e = 400 \left(\frac{r}{6}\right)^{-12} \text{ cm}^{-3},\ r > 7.81\ R_J \tag{2.6}$$

For analysis of Galileo UVS data, we use a constant electron density of $n_e = 2000\ cm^{-3}$. We assume that the ion composition comprises S^{+}, S^{++}, and S^{+++} sulfur ions (adding S4+ for Cassini) and O^{+} and O^{2+} oxygen ions. For analysis of the Cassini UVIS data we follow Steffl et al. [2004b] [137] in using the FUV features at 1661 and 1666 Å to constrain the O^{++} abundance and

hence separate the O+ and O++ contributions to the 833–834 Å feature. This yields an abundance ratio of O^+/O^{++} that varies between about 8 at 6 R_J to about 2 at 9 R_J. While fitting the Galileo data, we kept the value of O^+/O^{++} fixed at 5 because these data were averaged over time and not confined to any particular radial distance in the torus.

Assuming charge neutrality, we set the electron charge column density equal to the sum of the ion charge densities. With the addition of 10% protons [Bagenal, 1994] [5], we have a total electron column density of

$$N_e = \left(N_{S^+} + N_{O^+} + 2\left(N_{S^{++}} + N_{O^{++}}\right) + 3N_{S^{3+}} + 4N_{S^{4+}}\right)/0.9 \tag{2.7}$$

We fit the spectral data with the different ion column densities as parameters. By specifying n_e and the calculation of N_e from charge neutrality (at the end of fitting), we have an implied line of sight path length for the observation from the $\frac{N_e}{n_e}$ ratio.

We apply the code MPFIT (Levenberg-Marquardt technique) to apply a nonlinear least squares minimization to find the best fit of the model to an observed spectrum. We then compute the curvature matrix at the best fit to find the associated uncertainties in the fit parameters [Wilson, 2015] [155].

2.6 Cassini UVIS Data Results

To investigate the implications of changes in the atomic data from CHIANTI 4.2 (as used by Steffl et al. [2004b] [137]) to CHIANTI 8.0, we fit the Cassini UVIS spectra for torus ansa distances of 6.4 R_J and at 7.85 R_J as shown in Figure 2.6 and 2.7. When forward fitting the spectra, we need to assume a full width half maximum (FWHM) spread of each emission line. A FWHM of 3 Å is quoted by Steffl et al. [2004a] [138], while a value of 4.7 Å was used by Yoshioka et al. [2011] [164]. We found 3 Å to be too narrow and that a FWHM of 4.47 Å produced the best fit to the spectrum.

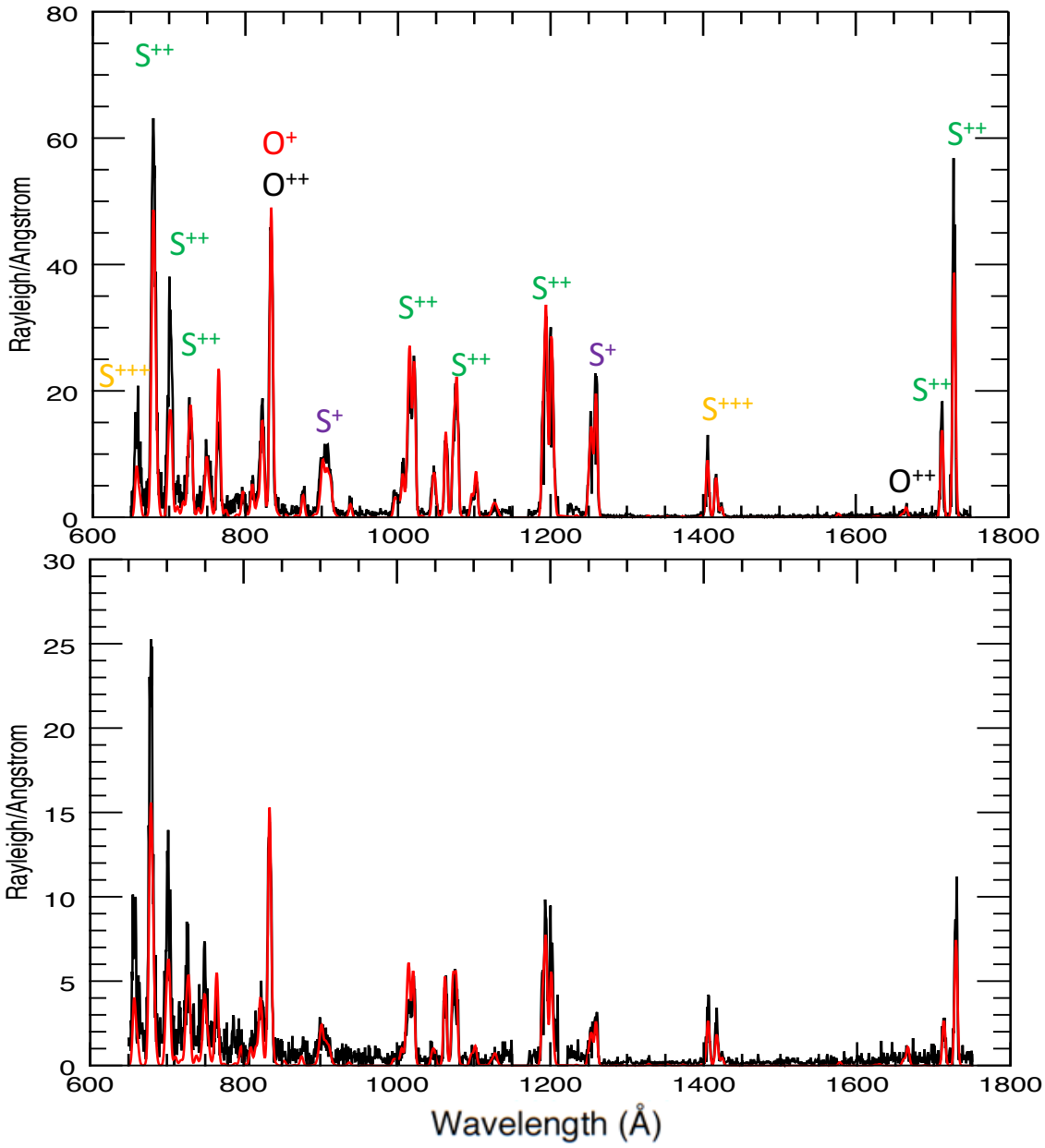

Figure 2.6: Fit to Cassini UVIS spectra for 6.4 R_J (top) and 7.85 R_J (bottom) using the CHIANTI 8.0 atomic database.

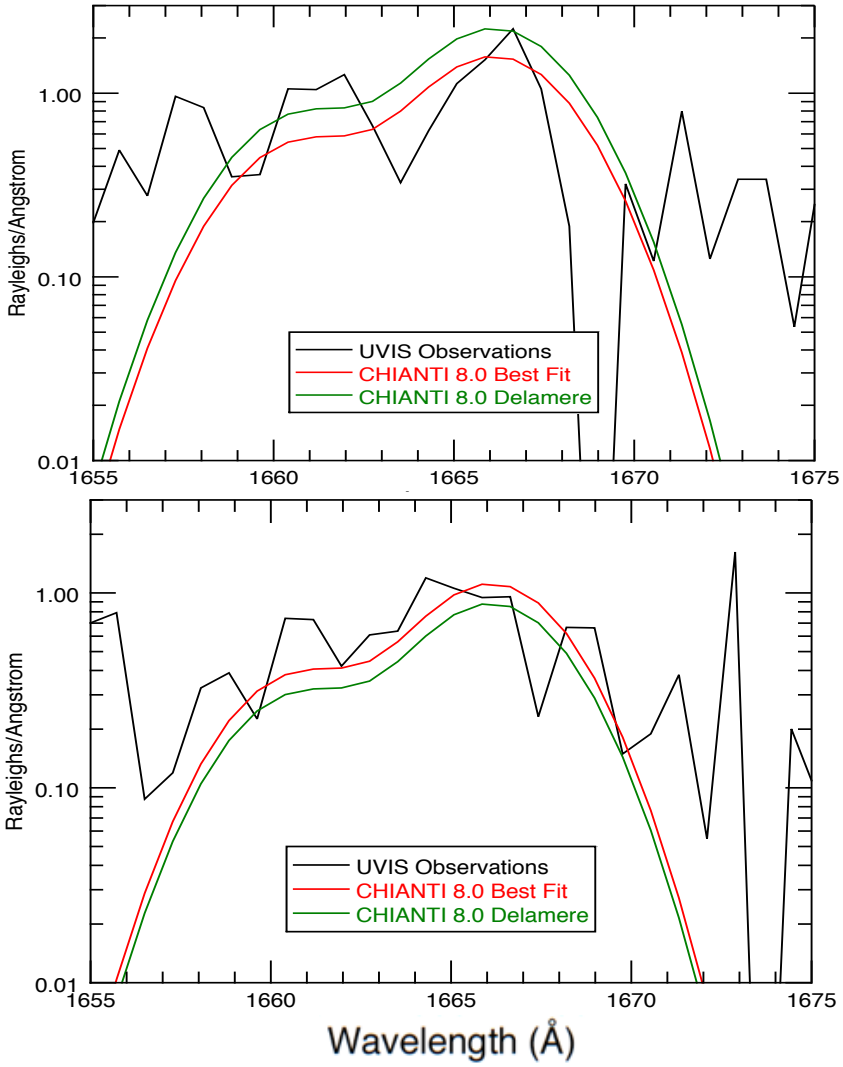

Figure 2.7: Part of the Cassini UVIS spectrum (black) in the FUV includes the location of two O III (O^{++}) lines at 1661 and 1665 Å. The best CHIANTI 8 fit to the data for these two lines is shown in red, while the amount of O^{++} predicted by the Delamere [40] model is shown in green.

Overall, we are able to find a reasonably good fit to the spectrum but a few S^{++} features are under fit. Specifically, model emissions for S III 680, 702, and 1729 are noticeable below values in the observed spectrum. The quality of the fit is similar to that shown in Figure 4 of Steffl et al. [2004b] [137]. It is not clear if the quality of the fit is limited by calibration, averaging of the emissions over a line of sight, the atomic data, or, most likely, some combination thereof. New atomic data for S IV (S^{+++}) [Del Zanna and Badnell, 2016] [37] will be added to the next version of CHIANTI that may help the overall match to the data.

Ratio of Column Densities	*Steffl* [2004b] 6.4 R_J	CHIANTI 8 6.4 R_J	*Steffl* [2004b] 7.85 R_J	CHIANTI 8 7.85 R_J
N_{S+}/N_e	0.060 ± 0.003	0.064 ± 0.001	0.031 ± 0.007	0.035 ± 0.002
N_{S++}/N_e	0.21 ± 0.006	0.21 ± 0.004	0.16 ± 0.03	0.19 ± 0.01
N_{S+++}/N_e	0.034 ± 0.001	0.037 ± 0.001	0.041 ± 0.008	0.049 ± 0.003
N_{O+}/N_e	0.24 ± 0.02	0.26 ± 0.05	0.14 ± 0.07	0.18 ± 0.01
N_{O++}/N_e	0.033 ± 0.01	0.025 ± 0.004	0.13 ± 0.07	0.082 ± 0.02
$\Sigma O^{n+}/\Sigma S^{n+}$	0.90 ± 0.07	0.92 ± 0.2	1.2 ± 0.4	0.96 ± 0.09
$<M>$ (amu)	24.4 ± 1	24.3 ± 2	23.4 ± 5	24.2 ± 1.3
$<Z>$	1.5 ± 0.08	1.5 ± 0.2	1.7 ± 0.5	1.7 ± 0.1

Table 2.1: Comparison of ion composition derived from Cassini UVIS spectra using the CHIANTI 8 atomic database compared with that derived by Steffl et al. [2004b] [137] Using CHIANTI 4.2

The determination of the composition of the oxygen species is complicated by the fact that the 833–834 Å feature is a combination of O^+ and O^{++} emission. The FUV component of the Cassini UVIS spectrum includes a couple lines of O^{++} emission at 1661 and 1665 Å. While these lines are weak, they allow at least an upper limit to be set on the abundance of O^{++} (Figure 2.7).

To improve the signal to noise of the O^{++} signature, we do a five-bin running average of the UVIS, effectively over a radial distance of about 1 R_J. We start by fitting the whole spectrum to determine electron temperature and sulfur ion column densities while holding the electron density fixed (according to the profile described above) and not fitting the oxygen line. We then hold the electron temperature and sulfur composition constant at these best fit values and fit the O^{++} feature at 1661/1666 Å to find an upper limit on the amount of O^{++}. We then hold everything

except O^+ fixed at the best fits just found while we fit the 833/834 blended feature. This allows us to constrain the O^{++} so the least squares fitting procedure does not get lost in parameter space.

Table 2.1 shows the mixing ratios of the sulfur and oxygen species for our analysis using CHIANTI 8.0 and the process described above compared with what Steffl et al. [2004b] [137] found. The ion composition is basically the same derived by both versions of CHIANTI for both spectra. Both analyses show 12% increase in charge state but little change in the total O/S content with radial distance.

In a recent paper which focuses on the torus emissions observed by the Cassini UVIS at the distance of Europa's orbit (9.4 RJ), Shemansky et al. [2014] [124] find a very different composition (very high O^{++}) to both Steffl's papers and the original Shemansky [1988] [121] analysis of the Voyager data. Until the flat field, calibration, and atomic data used in the Shemansky et al. [2014] [124] study are published, it is difficult to compare with the current analysis.

2.7 Voyager UVS Data Results

Having calibrated our spectral fitting technique on the Cassini UVIS data, we turn to the Voyager UVS spectrum to determine what ion composition we find best matches the data using the CHIANTI 8 atomic database. Figure 2.8 shows Voyager UVS spectra obtained at the torus ansa distances of 5.75 and 8.25 R_J. These are two spectra analyzed by Donald Shemansky and published in Bagenal et al. [1992] [3]. The analysis of these spectra is discussed in Shemansky [1988] [121]. In this study we used the Voyager 1 pre-Jupiter encounter calibration curve provided by Jay Holberg (private communication) to convert counts per channel to Rayleighs per angstrom. The original figure and calibration curve are shown in the Appendix A.

Using the Cassini data as a guide, we fit the two Voyager spectra with the electron density profile above and a fixed O^+/O^{++} ratio of 8 at 5.75 R_J and of 2 at 8.25 R_J to obtain our best fit ion composition. We also show the results of using CHIANTI 8 to show the predicted emissions for the ion composition derived from these spectra by Shemansky [1988] [121] and from the Cassini UVIS data for these distances by Steffl et al. [2004b] [137]. In Table 2.2, we compare our best fit

of the UVS observations using the CHIANTI 8.0 database with these previous analyses.

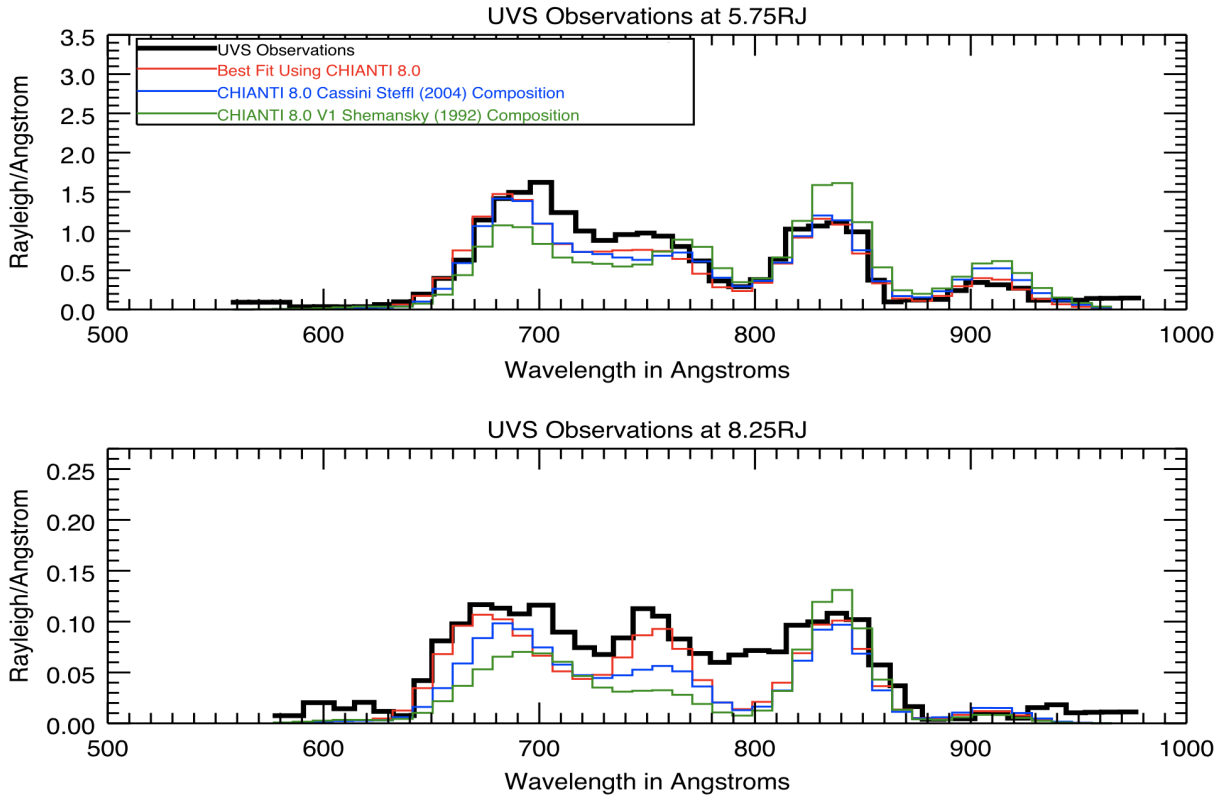

Figure 2.8: Voyager UVS spectra (black) for (top) 5.75 $R_J$and (bottom) 8.25 R_J with the best fit (red), with composition from Shemansky [1988] [121] (green) and from Steffl et al. [2004b] [137] (blue), all using the CHIANTI 8.0 atomic database.

At 5.75 R_J we are able to obtain a reasonable match to the data with a composition that is very similar to the Cassini-based composition of Steffl et al. [2004b] [137]. In his earlier analysis of the Voyager spectrum Shemansky [1988] [121] derived a substantially higher oxygen abundance. We take the Shemansky [1988] [121] composition and use the CHIANTI 8 emission rates to produce a synthetic Voyager UVS spectrum for comparison in Figure 2.8. The Shemansky [1988] [121] composition overestimates the emission in the 833–834 Å feature. Similarly, the sulfur features (650–750 Å) are underestimated by the Shemansky [1988] [121] composition. Table 2.2 also shows

the composition from Steffl et al. [2004b] [137] for comparison. The composition from our analysis of the Voyager spectrum is more consistent with the analysis of Cassini UVIS data by Steffl et al. [2004b] [137] than with Shemansky [1988] [121]. It is interesting to note that our reanalysis of the Voyager data also quite closely matches the composition derived from the Voyager data by Smith and Strobel [1985] [132].

Ratio of Column Densities	Voyager UVS Shemansky 5.75 R_J	Voyager UVS CHIANTI 8 5.75 R_J	Cassini UVIS Steffl 6.16 R_J	Voyager UVS Shemansky 8.25 R_J	Voyager UVS CHIANTI 8 8.25 R_J	Cassini UVIS Steffl 8.14 R_J
N_{S+}/N_e	0.13	0.044 ± 0.02	0.065 ± 0.002	0.012	0.019 ± 0.02	0.027 ± 0.004
N_{S++}/N_e	0.18	0.21 ± 0.04	0.22 ± 0.006	0.081	0.12 ± 0.03	0.16 ± 0.02
N_{S+++}/N_e	0.021	0.061 ± 0.02	0.032 ± 0.001	0.032	0.10 ± 0.02	0.045 ± 0.006
N_{O+}/N_e	0.42	0.20 ± 0.08	0.22 ± 0.001	0.23	0.17 ± 0.07	0.17 ± 0.003
N_{O++}/N_e	0.015	0.026 ± 0.008	0.034 ± 0.02	0.26	0.086 ± 0.03	0.12 ± 0.04
$\Sigma\, O^{n+}/\Sigma\, S^{n+}$	1.3	0.72 ± 0.3	0.80 ± 0.05	3.9	1.1 ± 0.4	1.3 ± 0.2
$<M>$ (amu)	22.9	25.3 ± 4	24.9 ± 0.7	19.3	23.7 ± 4	23.1 ± 2
$<Z>$	1.3	1.7 ± 0.4	1.6 ± 0.07	1.7	1.8 ± 0.4	1.7 ± 0.2

Table 2.2: Comparison of Ion composition derived from Voyager UVS spectra using the CHIANTI 8.0 atomic database compared with that derived by Shemansky [1988] [121] and from the Cassini UVIS data by Steffl et al. [2004b] [137]

Figure 4.4 shows a summary bar chart of the different abundances of the five major ions in the torus (6 R_J) derived from Voyager 1 data by Smith and Strobel [1985] [132], Shemansky [1988] [121], Herbert and Sandel [2001] [62], and this study (using CHIANTI 8). We also include Steffl et al.'s [2004b] [137] analysis of Cassini UVIS data for comparison.

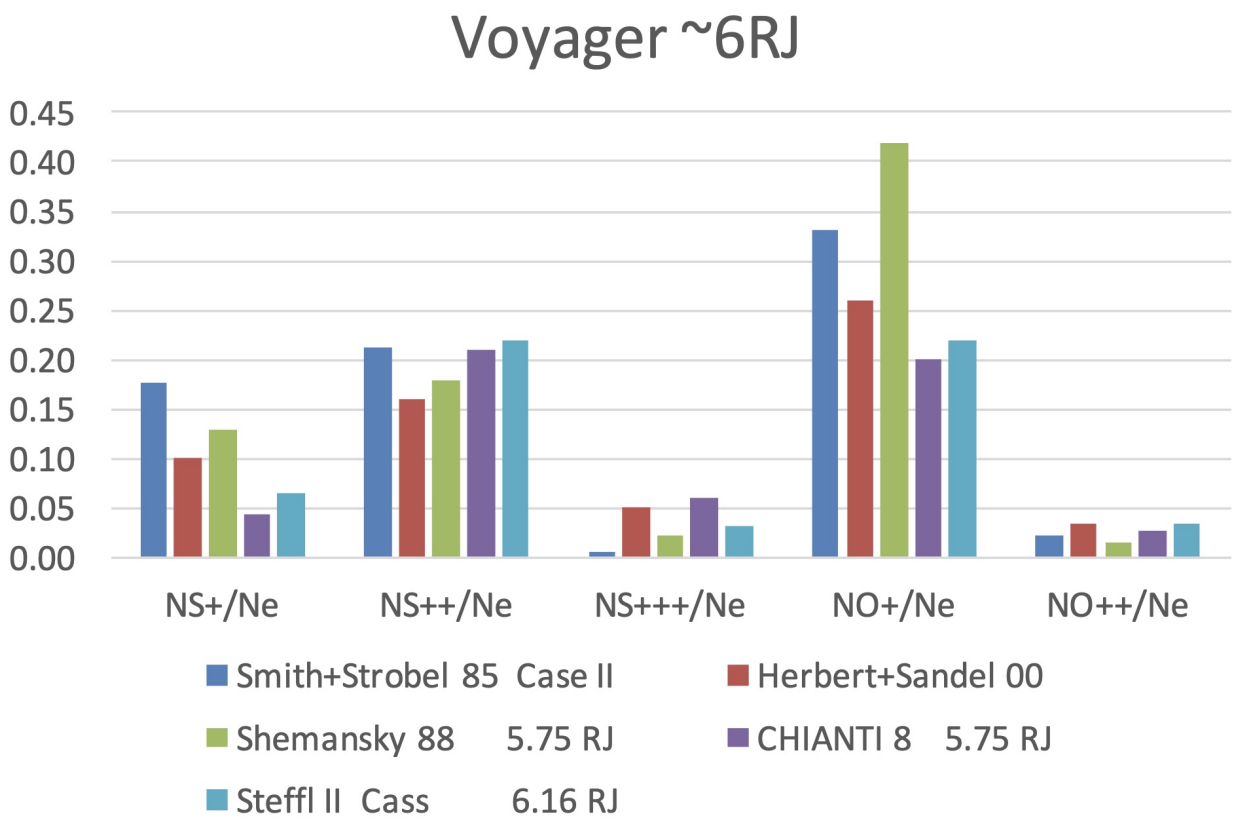

Figure 2.9: Ion composition near Io's orbit as modeled to fit the Voyager 1 UVS data by Smith and Strobel [1985] [132], Herbert and Sandel [2001] [62], Shemansky [1988] [121], and this study using CHIANTI 8. Steffl et al.'s [2004b] [137] analysis of the Cassini UVIS observations is shown for comparison.

We found it much harder to find a good match to the Voyager spectrum at 8.25 R_J, particularly at around 800 Å where there are no strong lines expected (Figure 2.3). Again, the Shemansky [1988] [121] composition (using the CHIANTI 8.0 atomic data) overestimates the oxygen emission at 833–834 Å and underestimates the sulfur emissions. The Cassini composition derived using CHIANTI 8.0 suggests a similar amount of oxygen ions to that derived by Steffl et al. [2004b] [137] and from our analysis of the Voyager spectra, but less sulfur ions than Voyager at 8.25 R_J. Our analysis

using the CHIANTI 8.0 database finds a slightly better match to the 8.25 R_J Voyager spectrum but with a composition that is closer to the Steffl et al.'s [2004b] [137] analysis of Cassini data than the Shemansky [1988] [121] composition. Specifically, we find less oxygen, less of a change in ionization state with radial distance, and overall, the ionization state of sulfur is higher than found by Shemansky [1988] [121].

2.8 Galileo EUVS Data Results

The Galileo EUVS data were initially in units of counts over variable integration times (mostly in 47–95 s range). We then summed the spectra over the spatial direction, limiting the spectral range to wavelengths short of 950 Å. We subtracted the background signal, divided by the appropriate integration time, and used the calibration curve and bin sizes from Hord et al. [1992] [74] to put the GLL-EUVS data in units of Rayleighs/Angstrom. The spectrum shown is from combining the median values of the counts in each spectral bin from data obtained between days of year 171 and 174 in June 1996.

The quality of the Galileo UVS data does not allow detailed analysis, but we have taken the ion composition and electron properties consistent with the Cassini UVIS data [Steffl et al., 2004b] [137] and used CHIANTI 8.0 to produce a synthetic spectrum for comparison. Figure 4.5 shows the data plus synthetic spectrum using Cassini composition as well as a best fit to the data. The lower emission in the 833/834 Å region suggests a lower abundance of oxygen during the Galileo epoch (1996) than at the time of Cassini flyby (2000). A better match is found by decreasing the amount of oxygen to 10%. The composition from our fit to the Galileo EUVS spectrum from June 1996 is shown in Table 2.3. Note the relatively large uncertainties in the derived ion abundances, especially the oxygen species.

We looked at other times where there seemed to be a reasonable fit and compared the total counts in the 833 Å region of oxygen emission to the total count in the 680 Å region of S^{++} emission. We found that in the above June 1996 data the oxygen:sulfur line ratio was 70% of the more typical values found in 28 October to 1 November 1996, 10–14 December 1996, and 9–16 June

2000.

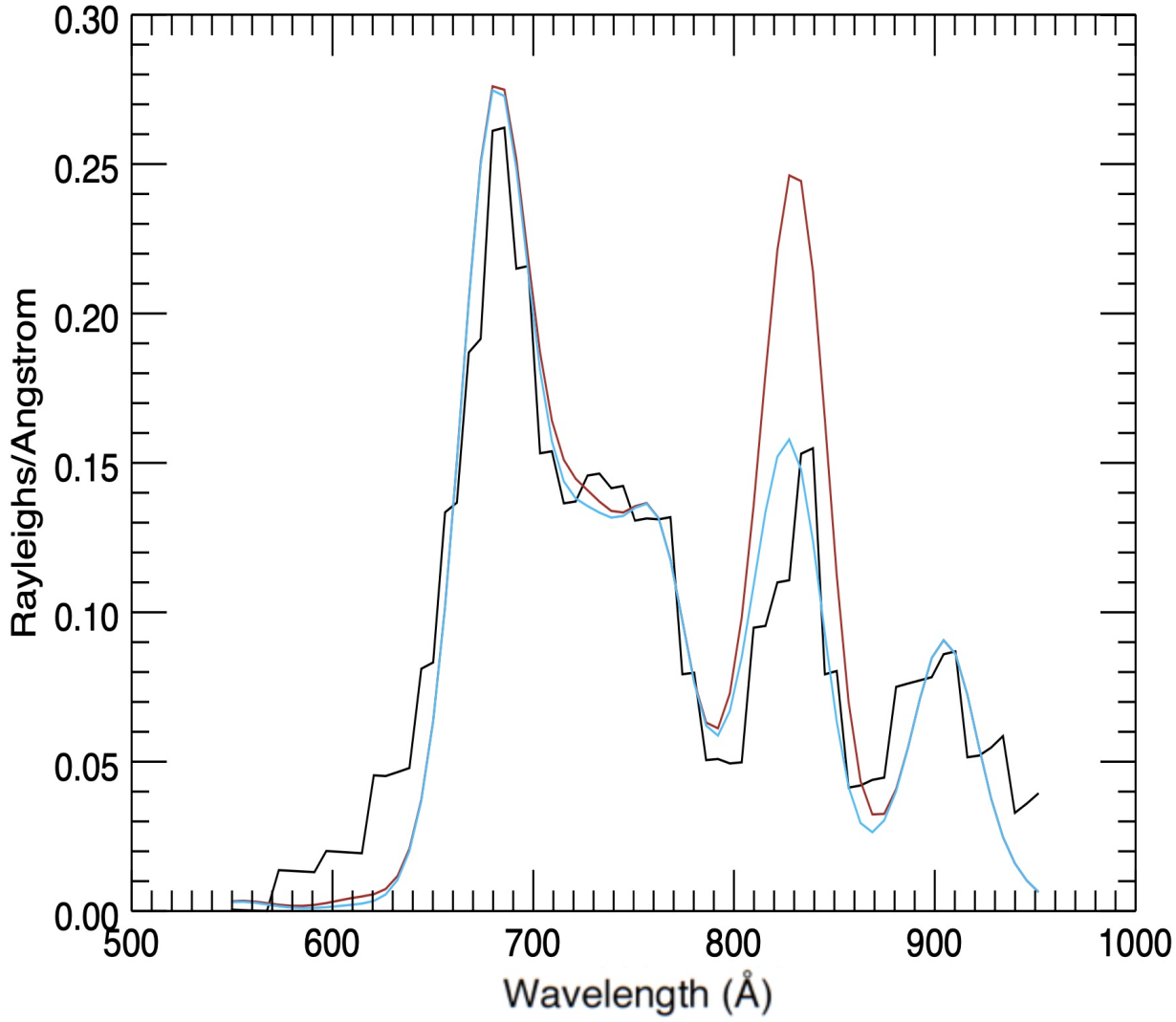

Figure 2.10: Galileo UVS spectra (in black) with the Cassini composition (in red with O^+/S^{++} = 1.2) put through the CHIANTI 8.0 atomic database to predict emissions and with the best fit (in blue with $O^+/S^{++} = 0.5$).

Table 2.3 shows the composition at 6.4 RJ from Steffl et al. [2004b] [137] as well as the best fit to the Galileo data using CHIANTI 8.0. We compare these compositions with those derived

during the same Galileo epoch derived from ground-based optical telescope observations by Thomas et al. [2001] [146] and from the EUVE telescope by Herbert et al. [2001] [62]. Thomas et al. [2001] [146] also report a low oxygen abundance in the October 1999 observations but state (conclusion 9) that ground-based (optical) measurements consistently show lower O^+ abundance. Herbert et al.'s [2001] [62] analysis of EUVE data produced a consistently higher O^{n+}/S^{n+} ratio, perhaps related to their use of COREQ atomic database. But they also report a 70% drop in the oxygen abundance in 19–20 June 1996 (the same time as the 70% drop in oxygen:sulfur lines measured by Galileo EUVS) compared with EUVE observations in October 1999. It might be worthwhile to reanalyze the EUVE data with the latest CHIANTI.

2.9 Discussion

Figure 2.12 shows radial profiles of ion composition derived from our analysis of the Cassini UVIS spectra using CHIANTI 8.0 compared with the Steffl et al. [2004b] [137] analysis as well as with the physical chemistry model of Delamere et al. [2005] [40]. The update in atomic data from CHIANTI 4.2 to 8.0 does not make much difference in the derived composition. The largest uncertainties are in the abundance of O^{++} which is detectable in the 1661/1665 Å feature of the Cassini spectrum in the denser, inner part of the torus, but beyond about 8 R_J the signal is weak, and the last three points in the black curve in Figure 2.12 represent an upper limit on O^{++} and hence the corresponding O+ values are lower limits.

The physical chemistry model of Delamere et al. [2005] [40] indicates that collisions (hence chemical reactions) basically cease beyond about 8 R_J (compared with radial transport that is picking up at the outer edge of the torus) and the ion composition is frozen in for > 8 R_J. Recent reanalysis of the Voyager PLS data (Bagenal et al. 2017 ; Dougherty et al. 2017 ; Bodisch et al. 2017) [2] [47] [16] in the middle magnetosphere using physical chemistry models (Delamere et al. 2005)[40] to constrain the composition in regions of warm plasma. They found that the net charge density and ion temperatures are similar to the previous analysis but could match the data in the warm torus using constraints from physical chemistry models where individual ion peaks were not

well resolved and to sort out O^+ and S^{++} ambiguity due to both having the same m/q or mass to charge ratio. They also found cold plasma with varying compositions found in the plasma sheet. A summary of their results are shown in figure 2.11 which comes from Figure 1 of Dougherty et al. (2017)[47].

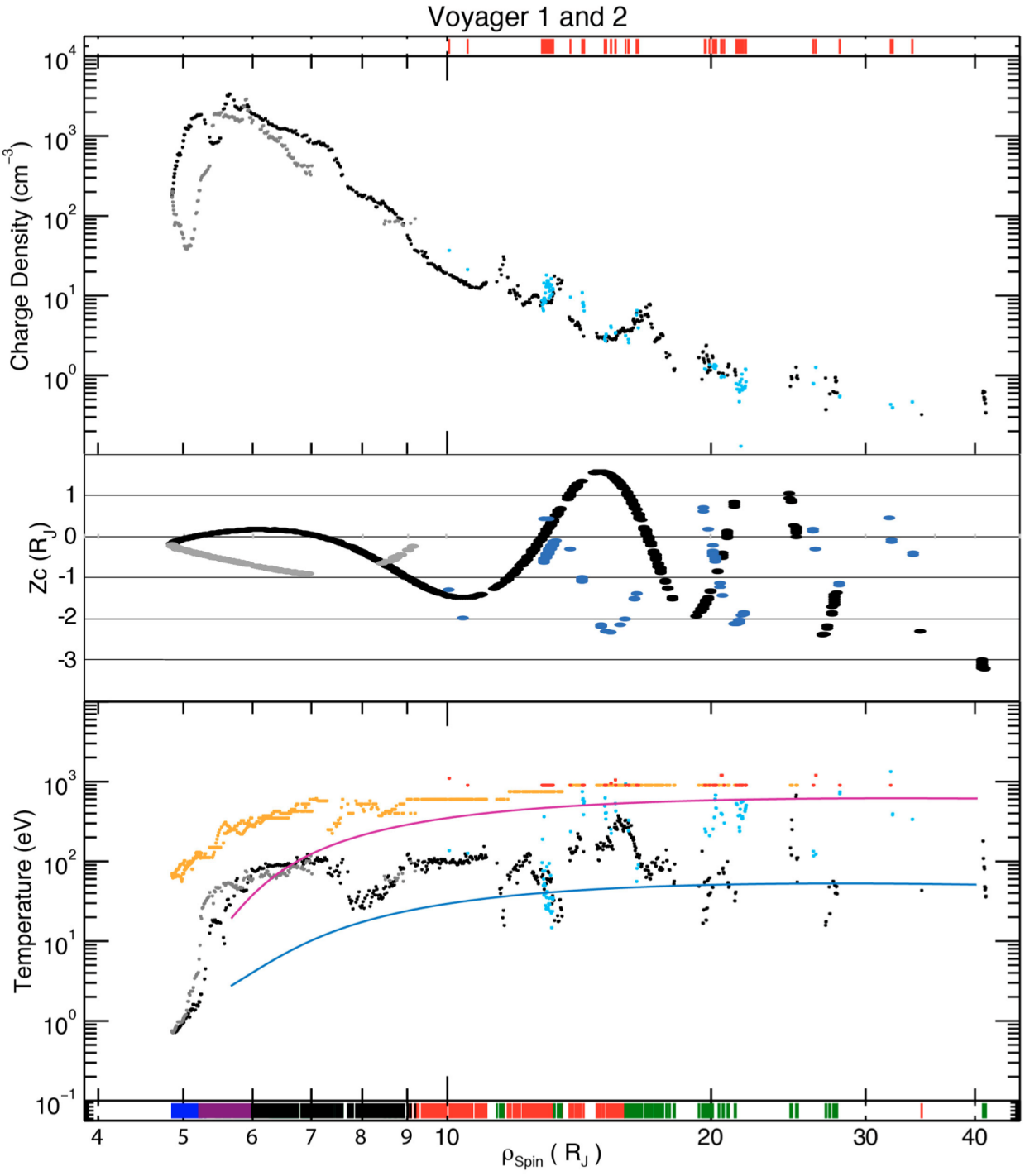

Figure 2.11: Figure 1 from Dougherty et al. (2017)[47] reanalysis of Voyager PLS data. Radial profiles of in situ (top) density and (bottom) temperature from Voyager 1 (inbound black and outbound gray) and Voyager 2 (blue). (middle) The vertical distance (Z_C) of the spacecraft from the centrifugal equator.

Ratio of Column Densities	Cassini UVIS Steffl 6.4 R_J	Galileo EUVS June 1996	Ground-Based *Thomas* [2001]	EUVE 96 *Herbert* [2001]	EUVE 99 *Herbert* [2001]
N_{S+}/N_e	0.06 ± 0.003	0.06 ± 0.04	0.13	0.11 ± 0.01	0.12 ± 0.02
N_{S++}/N_e	0.21 ± 0.006	0.20 ± 0.1	0.14	0.13 ± 0.01	0.10 ± 0.01
N_{S+++}/N_e	0.03 ± 0.001	0.04 ± 0.04		0.06 ± 0.01	0.05 ± 0.01
N_{O+}/N_e	0.24 ± 0.02	0.10 ± 0.2	0.15	0.32 ± 0.02	0.43 ± 0.02
N_{O++}/N_e	0.03 ± 0.01	0.03 ± 0.2	<0.011	0.07 ± 0.01	0.07 ± 0.01
$\Sigma O^{n+}/\Sigma S^{n+}$	0.90 ± 0.07	0.42 ± 0.9		1.30 ± 0.1	1.88 ± 0.2
$<M>$ (amu)	24.4 ± 0.9	27.3 ± 17.5		23.0 ± 1.1	21.5 ± 1.3
$<Z>$	1.54 ± 0.08	1.72 ± 1.68		1.46 ± 0.09	1.33 ± 0.09

Table 2.3: Composition of ions in the Io torus derived by Steffl et al. [2004b] [137] from Cassini data at 6.4 R_J compared with the composition derived from a June 1996 Galileo spectrum and with ground-based observations (taken in October 1999) by Thomas et al. [2001] [146] as well as EUVE observations by Herbert et al. [2001] [62]

In Figure 4.7 we compare ion composition derived from our CHIANTI 8.0 analysis of Cassini UVIS spectra with ion composition derived from Voyager UVS spectra by Shemansky [1988] [121]. We also include our reanalysis of the Voyager spectra using CHIANTI 8.0 at 5.75 and 8.25 R_J. Particularly noticeable is the high O+ abundance found by Shemansky [1988] [121] throughout the torus and the dramatic increase in O^{++} (by a factor of 10) across the torus. Our analysis of the same Voyager spectra produced a significantly higher ionization state for sulfur. We deduce a higher (lower) amount of S^{+++} (S^{+}) than Shemansky [1988] [121]. But we also find a little higher ionization state than the Cassini UVIS data and the Delamere et al. [2005] [40] physical chemistry model. This is consistent with the higher electron temperature measured in situ the outer torus by the Voyager PLS instrument [Sittler and Strobel, 1987] [128] as shown in the top left panel of Figure 2.12, compared with electron temperature derived from analysis of the Cassini UVIS data.

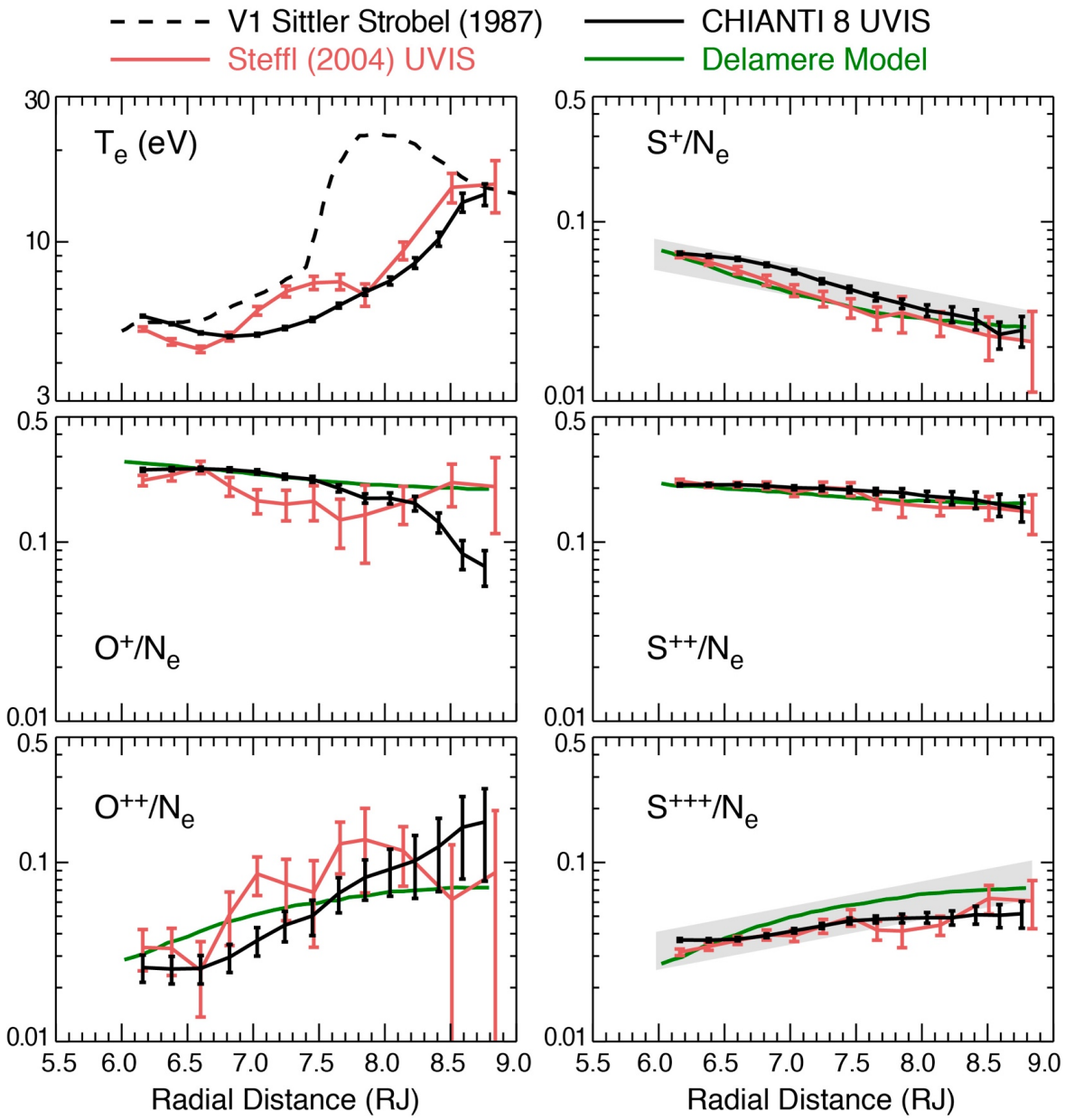

Figure 2.12: Radial profiles of electron temperature and ion composition derived from fits to Cassini UVIS, compared with that of Delamere et al. [2005] [40]. The grey shaded regions show the maximum (anticorrelated) ranges in S+ and S^{+++} composition modulation in longitude reported

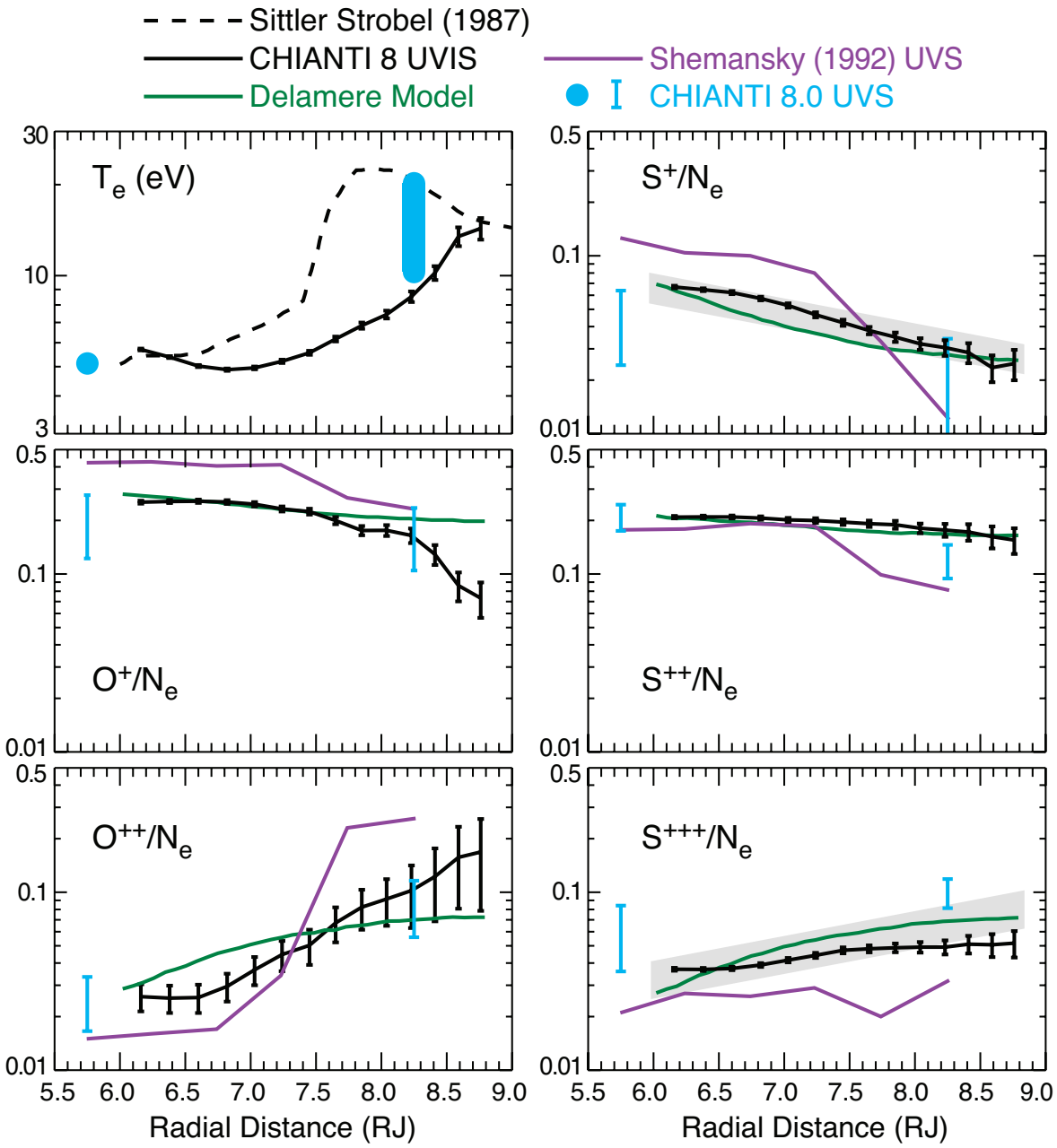

Figure 2.13: Radial profiles compared with the composition derived from Voyager UVS data.

Figure 2.8 also shows (in gray areas) the variations in sulfur ions observed in the UV emissions from S^+ and S^{+++} ions in the Io plasma torus associated with Jupiter's System III longitude. Steffl et al. [2006] [135] analyzed 6 weeks of Cassini UVIS data and found systematic variations (of about 25%) in the UV emissions with longitude. Modeling these variations by modeling the hot electron population Steffl et al. [2008] [136] showed that a 30% modulation of hot (55 eV) electrons that form only 0.2% of the total electron density are able to produce the observed modulation of UV emissions. Figure 2.12 shows that the observed composition derived from our reanalysis of the Cassini UVIS data remains pretty much within this range of variability, while our reanalysis of the Voyager UVS spectra using CHIANTI 8.0 suggests the S^+ (S^{+++}) abundances are lower (higher) than the range observed during the Cassini epoch.

Since the first detection of the Io plasma torus, a primary scientific goal has been to understand how variable volcanic activity on Io might change the torus properties. One problem with monitoring torus emissions for comparison with volcanic infrared outbursts from Io is that the S^+ species which is easiest to observe (e.g., see review of ground-based observations by Thomas [1992] [144]) is a relatively minor ion in the central torus. Brown and Bouchez [1997] [22] monitored both neutral Na and S^+ emissions for 6 months from December 1991 to June 1992 and found an approximately month-long enhancement in Na emission preceded an approximately month-long variation in S^+ emission by about 20 days. Short-term (few days to weeks) temporal variability in torus emissions has been observed [Delamere et al., 2004; Nozawa et al., 2004; Yoneda et al., 2010, 2015] [41] [97][158][157], but the changes seem to be mostly in electron density. The Cassini UVIS data obtained on approach to Jupiter showed declining total emission from the torus [Steffl et al., 2004a] [138] that was consistent with an eruption (strongly indicated by dust measurements reported by Krüger et al. [2003] [80]) occurring the month before in September 2000. Analysis of the ion composition measured by Cassini on approximately October 1st suggests that the oxygen ion abundance was about 87% of that in January 2001, consistent with a neutral cloud of O/S $\approx$ 1.7 [Delamere et al., 2004] [41].

While the UV emissions from the torus include several species, it is hard to obtain long

observing periods on space telescopes and their analysis has been plagued by the historical variation in atomic data (discussed in section 2.2). Gladstone and Hall [1998] [56] report an exception when the EUVE satellite looked at the torus between 1993 and 1996, including 83 consecutive orbits in June 1996. Hall et al. [1995] [59] and Herbert and Hall [1998] [63] also used EUVE to explore temporal variability over the period when Comet Shoemaker-Levy-9 passed through the system in 1994. Unfortunately, at the time of the June 1996 EUVE observations, Io's volcanoes were not cooperating, there were no volcanic outbursts, and the torus showed little variability [Gladstone and Hall, 1998] [56].

Ground-based observations by Nozawa et al. [2004] [97] of S^+ during the Galileo epoch indicated that the emission decreased over four observing periods between fall 1997 and early 2001. Unfortunately, these observations did not overlap with the 1996 Galileo EUV data we analyze in this paper, nor the enhanced UV emission observed by Cassini UVIS in late fall 2000. Nozawa et al. [2005] [98] compared the S+ emission intensity with the in situ electron density inferred from Galileo Plasma Wave observations between 30 and 60 R_J which also showed lower densities at the later periods. It is puzzling why the in situ Galileo Plasma Science data between 6 and 25 R_J did not show such a significant temporal variation [Bagenal et al., 2016] [9] at least in plasma density (the instrument was not able to make good measurements of composition).

While the evidence remains slim, it seems that Io eruptions that increase the torus plasma density tend to decrease the O/S ratio of the source neutral gases and hence the O^{n+}/S^{n+} ratio of the plasma. Smith and Strobel [1985] [132] suggested that the torus might have two states with the higher-density torus being more sulfur rich. Blanco-Cano [2004] [15] reviews the ion cyclotron waves observed near Io by Galileo at frequencies corresponding to ion pickup of recently ionized SO_2^+, SO^+, and S^+ ions. Russell et al. [2003] [107] showed that the relative strengths of these emissions varied for different Galileo flybys of Io, suggesting that the composition of the escaping gases changed.

To fully explore the production (and loss) processes in the torus requires both a physical chemistry model and, most importantly, measurements of all five of the main ionic species in the

torus. In section 2.1 we described the difficulties of determining the abundances of all five major species in the Io plasma torus. We hope that the combination of data from the EXCEED instrument on JAXA's Hisaki Earth-orbiting satellite, NASA's Juno mission in polar orbit around Jupiter, plus ground-based observations will further reveal variability in the Io plasma torus—should Io oblige us with a volcanic eruption in 2017.

2.10 Conclusions

1. When we reanalyze Voyager UVS data from 1979 with the experience of the higher resolution and greater temporal coverage of Cassini UVIS, we find that the ion composition plus the electron density and temperature are essentially consistent with the conditions observed by Cassini in 2000 at the region of brightest emission in the torus (6 R_J). Fractional ion abundances (relative to electron densities) are $S^+/N_e \approx 5\%$, $S^{++}/N_e \approx 20\%$, $S^{+++}/N_e \approx 5\%$, $O^+/N_e \approx 20\%$, $O^{++}/N_e \approx 3\%$, and $\Sigma O^{n+}/\Sigma S^{n+} \approx 0.8$, leaving about 10–15% of the charge as protons and other ions such as Na+ and SO2+. This composition is similar to that derived from Voyager data by Smith and Strobel [1985] [132] and by Herbert and Sandel [2001] [62] but is very different from the Shemansky [1988] [121] analysis that was also reported in the survey of the Io torus by Bagenal [1994] [5].

2. The radial profile of ion composition derived from the UV emissions can be matched with the physical chemistry model of Delamere et al. [2005] [40] that assumes a radial profile of neutral O and S atoms (more radially extended than modeled by Smyth and Marconi [2005]) [133]. As the densities of both neutrals and plasma decrease with distance from Jupiter, the collision rates sharply decrease with distance. Thus, the composition is thought to be basically frozen in outward from ≈8 R_J in the magnetospheric plasma sheet with an ion composition of slightly higher average ionization state and a modest loss of sulfur relative to oxygen: $S^+/N_e \approx$ 2–3%, $S++/N_e \approx$ 12–16%, S^{+++}/N_e 5–10%, O^+/N_e 15–17%, O^{++}/N_e 9–12%, and $\Sigma O^{n+}/\Sigma S^{n+} \approx 1.2$, leaving about 10% of the charge as protons.

3. There seems to be much more similarity in ion composition between torus observations

at the Voyager and Cassini epochs than previously thought. The Galileo observations, however, suggest that the composition in June 1996 may have comprised a lower abundance of oxygen than usual, consistent with observations made at the same time by the EUVE satellite [Herbert et al., 2001] [62] and with a ground-based optical telescope by Thomas et al. [2001] [146].

2.11 Appendix A to Paper 1

The Voyager UVS data used in this analysis (Figure 4.8, left) are two spectra that were published by Bagenal et al. [1992] [3]. These spectra were analyzed by Shemansky [1988] [121] resulting in the composition shown in Figure 4.8 (right). We used the calibration curve in Figure 4.9 from Jay Holberg (private communication) that is also available via the Planetary Data System (http://atmos.nmsu.edu/pdsd/archive/data/vg1-j-uvs-3-rdr-v10/) to convert these spectra to units of Rayleighs per Angstrom (Figure 2.8).

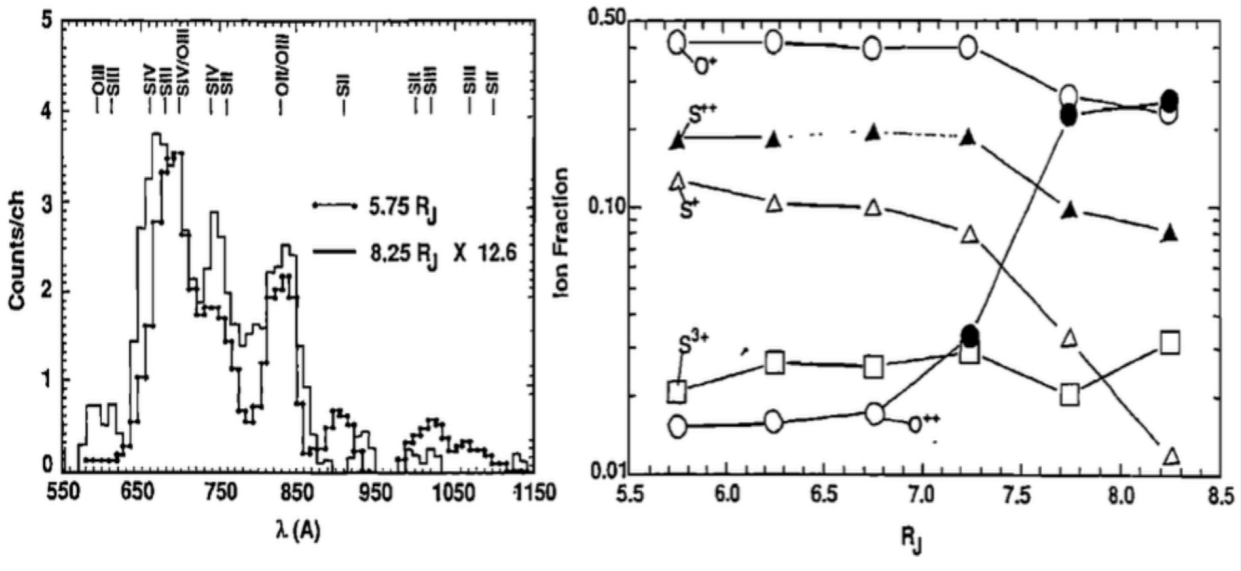

Figure 2.14: Figure 2 of Bagenal et al. [1992] [3] based on analysis by Shemansky [1988] [121]. (left) Spectra from Voyager 1 UVS at 5.75 and 8.25 R_J (normalized 685 Å). Modeled transitions are marked above the figure. (right) Ion partitioning from fits to UVS spectra (except O^{++} open circles which are from model calculations).

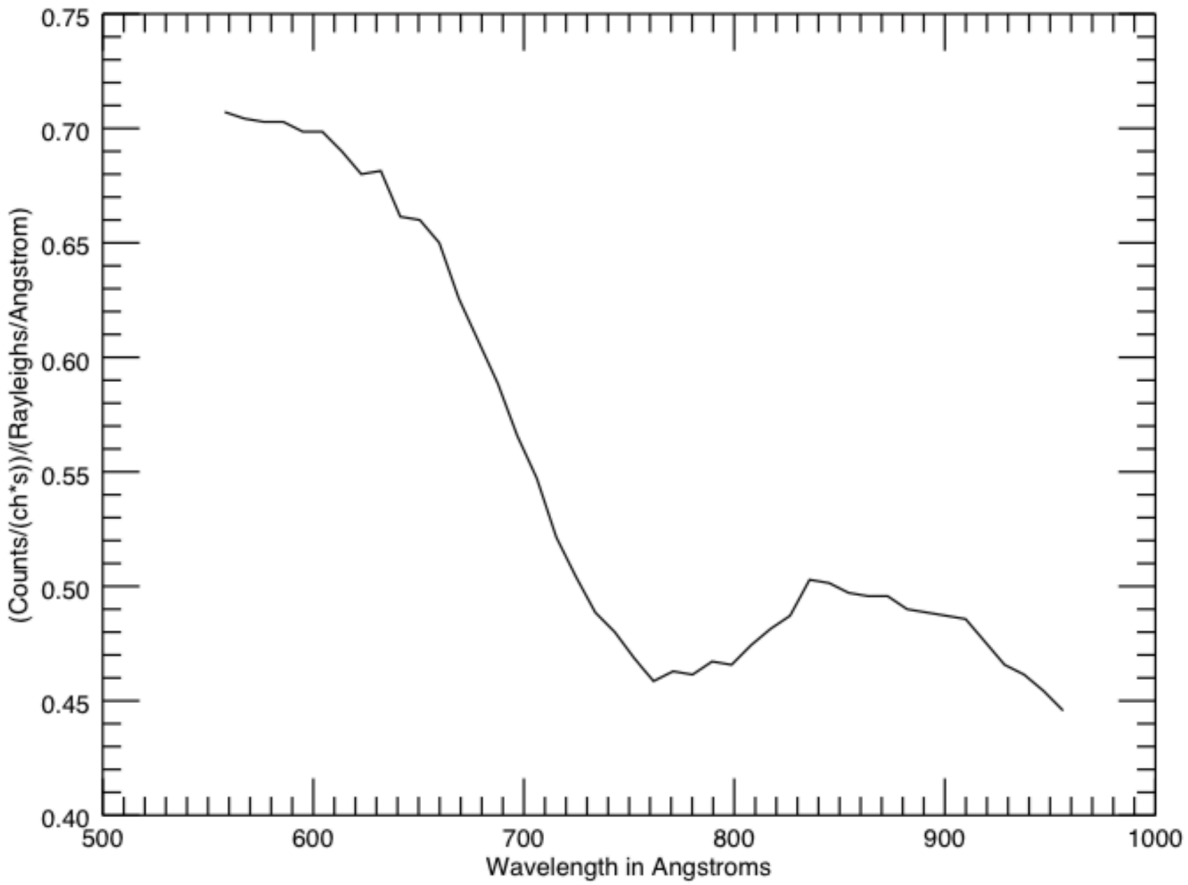

Figure 2.15: The calibration curve for the Voyager 1 UVS instrument provided by Jay Holberg (private communication). We assume a 3.84 s integration time corresponding to the Voyager UVS General Science mode.

Chapter 3

Combining UV Spectra and Physical Chemistry to Constrain the Hot Electron Fraction in the Io Plasma Torus

3.1 Introduction

The following chapter is from my paper Nerney & Bagenal (2020) [95].

We have developed a spectral emission model that is a function of the plasma composition, electron temperature, and electron density using the CHIANTI atomic database version 8 (Dere et al., 1997; Del Zanna & Badnell, 2016) [43] [37]. The lines are excited by electron collisions and spontaneously decay resulting in UV emission that is diagnostic of the plasma conditions.

In 2017 we reanalyzed the Voyager, Galileo, & Cassini UV observations from the Io plasma torus (Nerney et al., 2017). We first used a single Maxwellian distribution to model the spectra. Using our spectral emission model, we simulated a given spectrum as a function of the composition and temperature of the plasma. We found that using updated atomic data (CHIANTI 8) we were able to find that the Voyager and Cassini Epochs could both be explained with neutral oxygen to sulfur ratio consistent with the dissociation of SO_2. We found a lower O/S ratio for the Galileo epoch. This reanalysis of the Cassini observations showed consistency with the results of Steffl et al. (2004b) [137].

Previous physical chemistry models have found the fraction of hot electrons in the Io plasma torus to be a fraction of a percent (Delamere & Bagenal, 2003; Delamere et al., 2005) [39] [40]. In situ observations from Voyager PLS put the fraction of hot electrons at 0.2% at about 300 eV at the orbit of Io (Sittler & Strobel, 1987) [128]. Spectral analysis of the Hisaki observations has

found fractions of hot electrons on the order of a few percent (Yoshioka et al. (2014); Tsuchiya et al. (2015)) [163][150] inconsistent with our model and previous results.

It has been known since the mid 80s that hot electrons are necessary for maintaining the Io plasma torus, but the source mechanism remains unknown. There are two competing ideas for the source of the non-Maxwellian component. The first is that they are produced locally within the fluxtubes connected to the torus (Copper et al., 2016; Hess et al., 2011) [33] [68]. The second theory is that the hot electrons are injected from the outer magnetosphere (Kimura et al., 2018; Tsuchiya et al., 2018, 2019; Yoshikawa et al., 2017) [76] [151] [149] [160]. Beams of supra-thermal electrons produced in the wake of the Io interaction were seen in the Galileo flybys of Io (Frank & Paterson, 2000) [55] but the local spatial extent of this source could not explain hot electrons in the whole torus. However, Voyager and Cassini UV emissions from the torus (Sandel & Broadfoot, 1982a, 1982b; Steffl et al., 2004a, 2004b) [110] [109][138][137] showed no significant Io modulation. JAXA's Earth orbiting satellite Hisaki has recently provided extensive monitoring of the torus and Tsuchiya et al. (2015) [150] reports a 10% modulation of the UV power associated with the phase of Io's orbit.

The Voyager in situ plasma measurements from the Plasma Science (PLS) instrument provided key measurements of electron density and temperature, including evidence of a suprathermal component[118][128]. These in situ measurements of the plasma have implied that the distribution is empirically a Kappa distribution which is modeled well by a core thermal population with a small hot electron component that leads to a core Maxwellian plus a power law tail at higher energies. A 3D isotropic Maxwellian distribution normalized to the number density n is given by, for mass m, and temperature T is given by

$$f(\mathbf{u}) = n4\pi \left(\frac{m}{2\pi kT}\right)^{3/2} u^2 \mathrm{e}^{-\frac{mv^2}{2kT}} \tag{3.1}$$

A kappa velocity distribution is given by (Tsallis et al. (1998))[148]

$$P(u) = \frac{\Gamma(\kappa+1)\left(\frac{u^2}{\theta^2\left(\kappa-\frac{3}{2}\right)}+1\right)^{-\kappa-1}}{\pi^{3/2}\left(\theta^2\left(\kappa-\frac{3}{2}\right)\right)^{3/2}\Gamma\left(\kappa-\frac{1}{2}\right)} \tag{3.2}$$

For $\theta^2 = \frac{2kT}{m}$. A kappa distribution has one extra degree of freedom in addition to the temperature T there is the parameter κ.

A kappa distribution reverts to a Maxwellian for $\kappa \to \infty$. I illustrate this in the following plot for a few different kappa distributions for $T = 1$,$k = 1$,$m = 1$, and $\kappa = 1.6, 2, 5$. The kappa distribution approaches a delta function for $\kappa \to \frac{3}{2}$

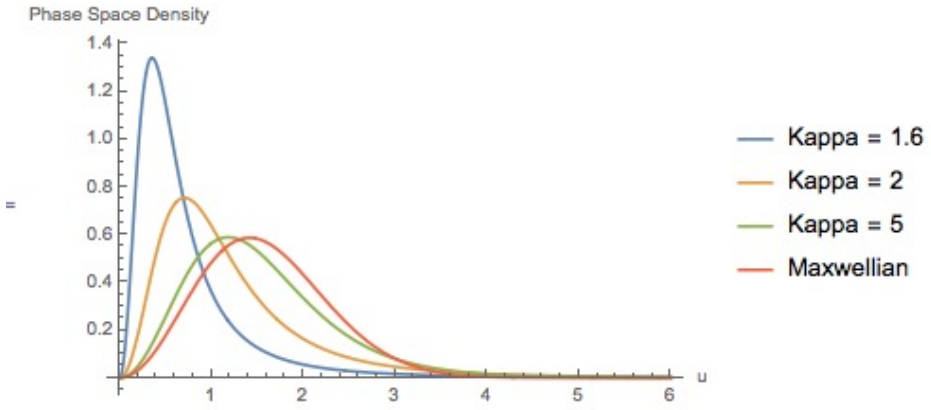

Figure 3.1: Here we see how a kappa distribution reverts back to a Maxwellian for $\kappa \to \infty$

The characteristic temperature in a kappa distribution (T_c) is not the same as the effective temperature (T_e) (Whereas it is for a Maxwellian) which gives the mean energy per particle of the distribution. Instead it is shifted by $T_e = T_c/(\kappa - 3/2)$ (Steffl et al. 2004b)[137].

We now try to determine the fraction of hot electrons using a double Maxwellian distribution where both the core, thermal electrons as well as supra-thermal "hot" electron population are assumed to be Maxwellians. The full electron distribution is approximated as a sum of the two Maxwellian functions, and cross-sections are computed using a weighted sum of the two populations. As we demonstrate below, this double Maxwellian model of UV emission spectra does not well constrain the fraction of hot electrons. Consequently, we turn to models of the physical chemistry

of the Io plasma torus to determine the fraction of hot electrons.

This chapter aims to determine the fraction of hot electrons in the Io plasma torus during the Cassini flyby using a combination of UV spectroscopy and physical chemistry modeling. In section 2 we show that when we fit the Cassini UVIS, spectrum there are large swaths of parameter space with similar chi-squared values, so we are unable to uniquely determine the fraction of hot electrons using only UV spectral modeling. In section 3 we highlight our nominal Cassini solution, showing particle and energy flow diagrams for model runs that match the observed plasma composition and temperatures during the Cassini flyby. In section 4 we show an extensive parameter space search that demonstrates that for fractions of hot electrons above 0.5% there are no solutions that match the plasma composition and temperature implied by the UV emissions. Finally, in section 5 we present a summary and our conclusions.

3.2 Fitting Cassini UV Observations

Using the CHIANTI database, we implement a double-Maxwellian distribution which is a sum of two Maxwellians. One at the core electron temperature and one at the hot electron temperature with a corresponding density given by the fraction of hot electrons (F_{eh}) specified as an input in our spectral emission model. When Steffl et al. (2004b) [137] used a superposition of 5 Maxwellians to approximate a Kappa distribution he found that "The ion composition derived using a kappa distribution of electrons is identical to that derived using a Maxwellian electron distribution; however, the kappa distribution model requires a higher electron column density to match the observed brightness of the spectra". We follow the methods used in Steffl et al. (2004b) [137] to simulate a UV Spectrum as outlined in Nerney et al. (2017). Yoshioka et al. (2011) [164] similarly used a superposition of a core (cold) and a hot Maxwellian population and kept the "mixing ratios for the ions ... to be the same ones that came from the best fit spectra which did include a hot electron component." In our analysis we found that the best fit composition did not change significantly between the single and hot electron spectral emission model like Steffl et al. (2004b) [137] and Yoshioka et al. (2011) [164].

In Nerney et al. (2017) we applied critical atomic data updates for the torus lines in CHIANTI version 8 and used a single Maxwellian electron distribution function. A sum of two Maxwellians matches the core population at low energies, and the power law tail at higher energies. The intermediate section of the spectrum that is underestimated in this approach is only responsible for a minor component of the emission. In this analysis, the temperature of the hot electrons is held constant at 46 eV (consistent with previous work by Delamere et al., 2004) [41] because the emission as a function of temperature flattens out after 40 eV and determining temperatures above such values is not possible from just fitting the spectrum.

In Nerney et al. (2017) we fit UV observations from the Io plasma torus to find best-fit plasma conditions. We use the CHIANTI database (version 8) and the program emiss_calc.pro to simulate volume emission rates. Then we simulate each discrete emission as a normalized Gaussian at the FWHM response of the instrument. We find the best fit using MPFIT, which uses the Levenberg–Marquardt technique to solve the least-squares problem. We previously used a single Maxwellian distribution function for the electrons and found our single Maxwellian best-fit composition at 6.16 RJ to be the values shown in Table 3.1. The uncertainties shown in Table 3.1 were found using MPFIT by numerically computing the curvature matrix around the best fit. This technique assumes the uncertainties are independent and therefore most likely underestimates the uncertainties.

In Table 3.1 The reader can find the best fit inputs for UVIS observations at 6.16 R_J from Steffl et al. (2004b) [137]. By mixing ratio we mean the ion density relative to the total electron density (n_{ion}/n_{etotal}). Where n_{Ion} is the ion number density of a particular species (Ions/cm^3) and n_{etotal} is the total electron number density. The total electron density is determined by charge neutrality. Steffl et al. (2004b)'s [137] electron temperature is about 1 eV cooler than ours and the composition is similar though Steffl et al. (2004b) [137] has less O^+ than we do. Differences in the composition may stem from how we radially averaged over the data set, atomic data (updates included after CHIANTI 8), and fitting algorithms. Yoshioka et al. (2011) [164] quoted their best fit UVIS composition of the Io torus dusk ansa at 5.9 R_J in terms of S^{++} density ratios. Due to

	This study	Steffl et al. (2004b)	Yoshioka et al. (2011)
T_e	6.1 ± 0.2 eV	5.2 ± 0.1 eV	5.6 eV
n_e	1910 ± 50 cm^{-3}	1910 ± 63 cm^{-3}	2400 cm^{-3}
$\frac{N_{S^+}}{N_e}$	$6.4 \pm 0.1\%$	$6.6 \pm 0.32\%$	
$\frac{N_{S^{++}}}{N_e}$	$21 \pm 0.4\%$	$22 \pm 1.1\%$	
$\frac{N_{S^{+++}}}{N_e}$	$3.7 \pm 0.1\%$	$3.2 \pm 0.17\%$	
$\frac{N_{O^+}}{N_e}$	$26 \pm 5\%$	$22.4 \pm 1.8\%$,	
$\frac{N_{O^{++}}}{N_e}$	$2.3 \pm 0.4\%$	$3.2 \pm 0.87\%$.	
$\frac{N_{S^+}}{N_{S^{++}}}$	0.30 ± 0.01	0.30 ± 0.02	0.38
$\frac{N_{S^{+++}}}{N_{S^{++}}}$	0.18 ± 0.01	0.15 ± 0.01	0.13
$\frac{N_{O^+}}{N_{S^{++}}}$	1.24 ± 0.24	1.02 ± 0.1	1.18
$\frac{N_{O^{++}}}{N_{S^{++}}}$	0.11 ± 0.02	0.15 ± 0.04	0.1

Table 3.1: UVIS best fit composition at 6.16 R_J for this study, Steffl et al. (2004b) [137], and Yoshioka et al. (2011) [164] at 5.9 R_J. Best fit composition from the model including hot electrons was found to be the same as in the single Maxwellian model consistent with Steffl et al. (2004b) [137] and Yoshioka et al. (2011) [164]. Error bars for this study are returned via the IDL Algorithm Mpfit which assumes the uncertainties are independent and are calculated via the curvature matrix

issues determining the contribution of O^+ vs. O^{++} to the 833/834 Angstrom feature Yoshioka et al. (2011) [164] fixed $\frac{N_{O^{2+}}}{N_{S^{2+}}} = 0.1$ consistent with previous results (Bagenal, 1994; Herbert & Hall, 1998) [5] [63] and our result of $\frac{N_{O^{2+}}}{N_{S^{2+}}} = 0.11$. Yoshioka et al. (2011) [164] analyzed a Cassini UVIS spectrum at 5.9 R_J and found a lower electron temperature, a similar amount of S^+, less S^{++}, and a similar amount of O^+. They found a hot electron fraction (F_{eh}) of 4.2% inconsistent with our results.

Figure 3.2 shows the reduced χ^2 (logarithmic contours) as a function of the core electron temperature (T_e) and the fraction of hot electrons $F_{eh} = \frac{n_{eh}}{n_{ec} + n_{eh}} = \frac{n_{eh}}{n_{etotal}}$. Where n_{eh} is the number density of the hot electrons, n_{ec} is the number density of the core or cold electron population, and $n_{etotal} = n_{ec} + n_{eh}$ is the total electron density. Using CHIANTI we model UV spectra, applying the electron velocity distribution as a superposition of Maxwellian core and hot populations. We fix the proton to electron ratio to be 0.1 which is consistent with Voyager observations (Bodisch et al., 2017) [16]. We calculate the electron and proton rate coefficients at each temperature, and we calculate a weighted sum of the coefficients to simulate the spectral emission using our modified version of the CHIANTI function emiss_calc.pro. This spectral simulation assumes that the emission is only due to electron and proton collisional excitation. The electron collisional excitation is the dominant contribution, but the proton contribution (3%) is included for completeness.

In Figure 3.2, we have varied the core electron temperature and the fraction of hot electrons and compared the emission predicted by CHIANTI with the Cassini UVIS spectrum. Figure 3.2 shows that the model well determines the core electron temperature and only has a narrow range of values (5.6–6.6 eV) with a similar χ^2 value while the fraction of hot electrons has a large swath of similar χ^2 values. Within the 1.66 contour the value of χ^2 only changes by 10% from the minimum value while F_{eh} varies from 0.1% to 5%. This implies that our analysis does not determine F_{eh} from the spectrum. Three points (labeled A, B, & C) in Figure 3.2 with similar χ^2 values are shown and the corresponding T_{ec} and F_{eh} values are shown in Table 3.2.

We take the three cases (A, B, C) marked on the χ^2 plot in Figure 3.2 with similar values as shown in Table 3.2. Figure 3.3 shows plots of the simulated spectrum over the Cassini UVIS

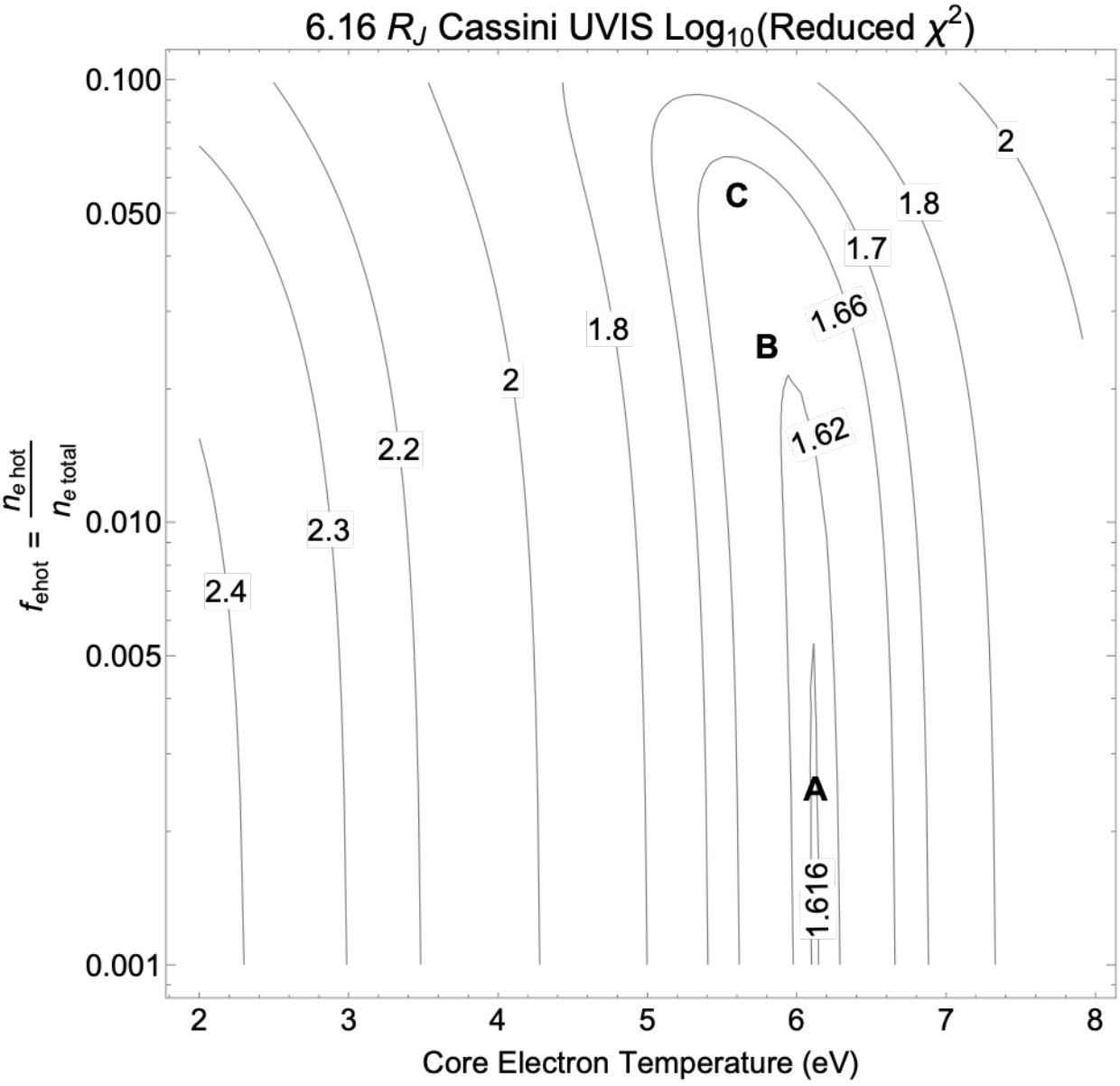

Figure 3.2: Contours of Log10 reduced χ^2 comparing the spectral emission model to a Cassini UVIS spectrum at 6.16 $R_J$from the Cassini flyby of Jupiter on 01/14/2001. The fraction of hot electrons and core electron temperature are varied while holding the hot electron temperature constant at 46 eV. The three labels (A, B, C) represent three solutions with similar χ^2 values with simulated spectra for each shown in Figure 2.2 and associated values given in Table 3.2

spectrum for these three points. We vary the fraction of hot electrons while holding the total electron density (which is a combination of the core and hot population) constant. We also hold the hot electron temperature constant (T_{eh} = 46 eV) and ion composition constant (Table 3.1).

Case	T_e (eV)	F_{eh}
A	6.1	0.25%
B	5.8	2.5%
C	5.6	5.5%

Table 3.2: Case A, B, & C values corresponding to the three labeled points in Figure 3.2. Common hot electron temperature (T_{eh}) of 46 eV assumed

The spectra in Figure 3.3 corresponding to cases A, B, & C, illustrate that varying the fraction of hot electrons (F_{eh}) does not result in a better fit to the spectrum. Some lines are fit better at the expense of others. Increasing the fraction of hot electrons increases the relative intensity of the EUV lines to the FUV lines.

Figures 3.2 and 3.3 show us that our spectral analysis does not accurately determine the fraction of hot electrons (F_{eh}) so we turn to physical chemistry modeling in section 3 to constrain F_{eh} using the energy balance required to match the ion and core electron composition and temperature found via our spectral analysis.

3.3 Mass & Energy Flow Through the Io Plasma Torus

To put tighter constraints on the hot electron in the Io torus, we have adopted a physical chemistry model. We apply a model that has been adapted for exploring the Io plasma torus at different epochs (Delamere & Bagenal, 2003; Delamere et al., 2004; Nerney et al., 2017) [39] [41], to model longitudinal variations (Copper et al., 2016; Steffl et al., 2006, 2008) [135] [136], and radial structure of the torus (Copper et al., 2016; Delamere et al., 2005) [40].

The model starts with a neutral source of atomic oxygen and sulfur at a specified O/S ratio,

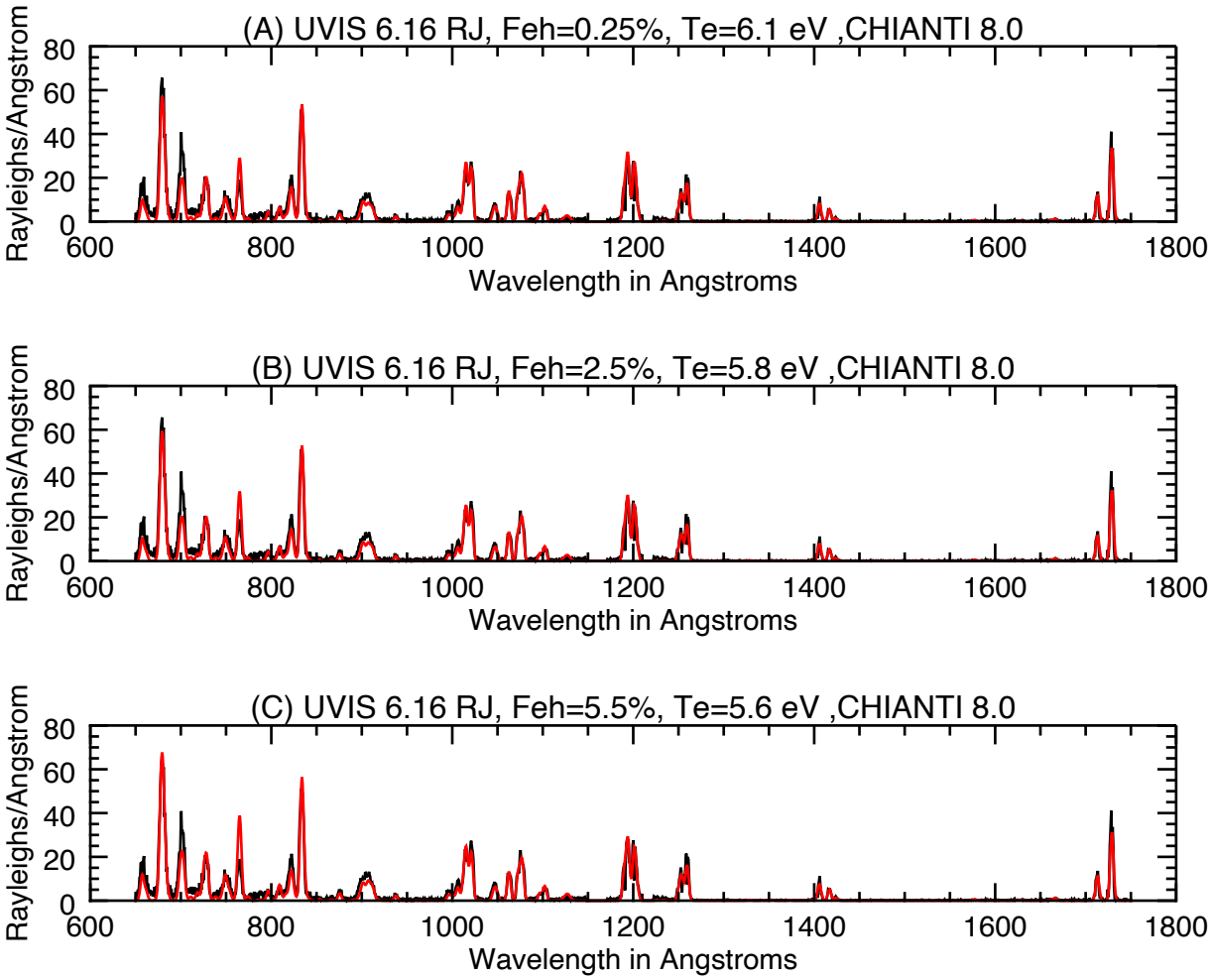

Figure 3.3: Simulated spectra plotted over the Cassini UVIS spectrum at 6.16 R_J from the Cassini flyby of Jupiter on 01/14/2001. The fraction of hot electrons is varied while holding constant the hot electron temperature constant at 46 eV and the plasma composition as listed in Table 3.1.

and we seed the system with a small initial amount of sulfur and oxygen ions. The electron density is given by the quasi-neutrality condition assuming the proton to electron density ratio is 0.1, and a constant fraction (F_{eh}) specifies the density of hot electrons at a specified constant temperature (T_{eh}). The model computes scale heights and, following Delamere et al. (2005) [40], we average over the latitudinal dimension which gives us a latitudinally averaged "cubic-cm" (cm^3) physical chemistry model. The radial transport timescale (τ) describes how the particles and energy are lost from the system due to transport.

The main inputs to the model are radial transport timescale (τ), volumetric neutral source rate (S_n), the O/S ratio of the neutral source, the temperature of the hot electrons (T_{eh}), and the fraction of hot electrons (F_{eh}). Since reaction rates are insensitive to the temperature of the hot electrons above 40 eV (Delamere & Bagenal, 2003) [39], we fix the hot electron temperature to be 46 eV consistent with previous work. In our model we consider, ionization, recombination, charge exchange, radial transport, Coulomb collisions, and energy loss due to radiation.

Our best fit input parameters for the latitudinally averaged "cubic-cm" physical chemistry model are given in Table 3.3. The output parameters to the physical chemistry model are the density & temperatures of the ion and neutral populations in the cubic-cm box. The output from the physical chemistry model is compared with the best fit composition, density, and temperature of the ion and electron populations from the fit to the UVIS spectra (Table 3.1). Varying two of these inputs and holding the rest constant allows us to plot contours of output as a function of these two varying inputs. Fitting the plasma composition derived from the Cassini UVIS spectrum, specifically the numbers in Table 3.1, we find the minimum χ^2 value for the inputs shown in Table 3.3.

In Figures 3.4 and 3.5, we show the flow of particles and energy (respectively) through the system for a "cubic-cm" model with no latitudinal averaging. This is necessary because the latitudinal averaging involves dividing by the scale height for each species to convert between flux tube averaged quantities and local equatorial values (assuming Gaussian scale height distributions) and the scale heights are not the same for all species. This leads to an equatorial source term

for one species not exactly matching the corresponding equatorial loss term for another species, whereas the flux tube averaged source and loss terms are equal. For Figures 3.4 & 3.5 we use the same inputs found in Delamere et al. (2004) [41] for the January 14, 2001 Cassini flyby. These inputs are O/S = 1.9, S_n = 6.4 (10^{-4} cm^{-3} s^{-1}), τ = 64 Days, F_{eh} = 0.25%, and T_{eh} = 46 eV. We find consistent results with Delamere et al. (2004) [41] but go into greater detail by showing the breakdown of source and loss terms species by species.

Case	O/S	τ	S_n	F_{eh}	T_{eh}
Low & Slow	1.9	72 Days	7.8 x 10^{-4} cm^{-3} s^{-1}	0.25%	46 eV
High & Fast	1.9	40 Days	20 x 10^{-4} cm^{-3} s^{-1}	0.25%	46 eV

Table 3.3: Nominal latitudinal averaged "cubic-cm" physical chemistry input parameters

Our model considers recombination, ionization, charge exchange, radial transport, coulomb collisions, and radiation. Each different process is represented by a different colored arrow in Figures 3.4 and 3.5. The sources and losses of particles and energy of each species are computed at each time step, and the model is run to equilibrium at which point the sources balance the losses. Equilibrium is achieved by around, 500 days but for completeness, we ran the model to 5000 days to confirm the system is in a steady state. Using these source and loss terms of particles and energies allows us to create the particle and energy flow through the system. In Figures 3.4 and 3.5 we find the particle and energy flow by taking the inputs for the Cassini flyby of Jupiter from Delamere et al. (2004) [41] and balancing source and loss terms to determine the flow. For example, the ionization of neutral sulfur is a loss term for neutral sulfur but a source term for singly ionized sulfur (S^+) which is why the orange arrow points from neutral sulfur to S^+ in Figure 3.4.

Charge exchange reaction rates come from McGrath and Johnson (1989) [85]. Electron impact ionization reaction rates are from Voronov (1997) [154]. Total electron recombination rates are from the work of Sultana Nahar. For S^+, S^{++}, O^{++}: Nahar (1995 & 1996) [92] [93]. O, O+

from Nahar (1999) [94]. Recombination rates for S and S+++ come from Mazzotta et al. (1998) [83], which provides formulae for the dielectronic recombination rate. The radiative recombination rate comes from Dima Verner's rrfit code (Verner 1995) [153] which for sulfur uses Shull and van Steenberg (1982) [126] and for oxygen uses Péquignot et al. (1991) [101]. Radiation losses are computed using the CHIANTI atomic database version 8 (Del Zanna et al., 2015; Dere et al., 1997) [38] [43]. Coulomb collisional rates are determined using the equations in the NRL plasma formulary page 33 and 34 (Richardson, 2019) [103].

For the flow of particles, a charge exchange reaction involving a sulfur and oxygen species say S^{++} and O^{+} could charge exchange to S^{+} and O^{2+}. There would be a corresponding loss term of particles for S^{++} and O^{+} and a source term for S^{+} and O^{++}. This would be represented by an arrow going between S^{++} and S^{+} and O^{+} and O^{++} but there is no way to change a sulfur species into an oxygen species so there is no arrow for charge exchange pointing between oxygen and sulfur species. Likewise, the energy flow would be between S^{++} and S^{+} and O^{+} and O^{++} not between sulfur species and oxygen species. The only reactions that are included in the model that transfer energy between oxygen and sulfur species are coulomb collisions. The charge exchange arrow pointing between S^{+} and S^{++} for example is a sum of all the charge exchange reactions happening involving S^{+} turning into S^{++} or S^{++} turning into S^{+}. There is more S^{++} turning into S^{+} in the particle flow via charge exchange reactions than S^{+} turning into S^{++} so the arrow points from S^{++} to S^{+} in Figure 3.4.

Arrows not pointing to any other species in the diagram represent loss terms out of the system. The arrows for charge exchange or recombination that are not pointing to other species are due to charge exchange or recombination of ions which result in neutrals that are lost to the system because these are now fast neutrals that no longer feel Jupiter's strong magnetic field and whose speed is greater than the neutral escape velocity so they fly off in whatever direction they were pointed after turning back into neutrals. We expect, therefore, that there are extended neutral clouds of sulfur and oxygen atoms similar to the extended neutral clouds of sodium observed by Mendillo and Flynn (1990) [88] extending beyond 400 R_J. Furthermore, looking at the fast neutral

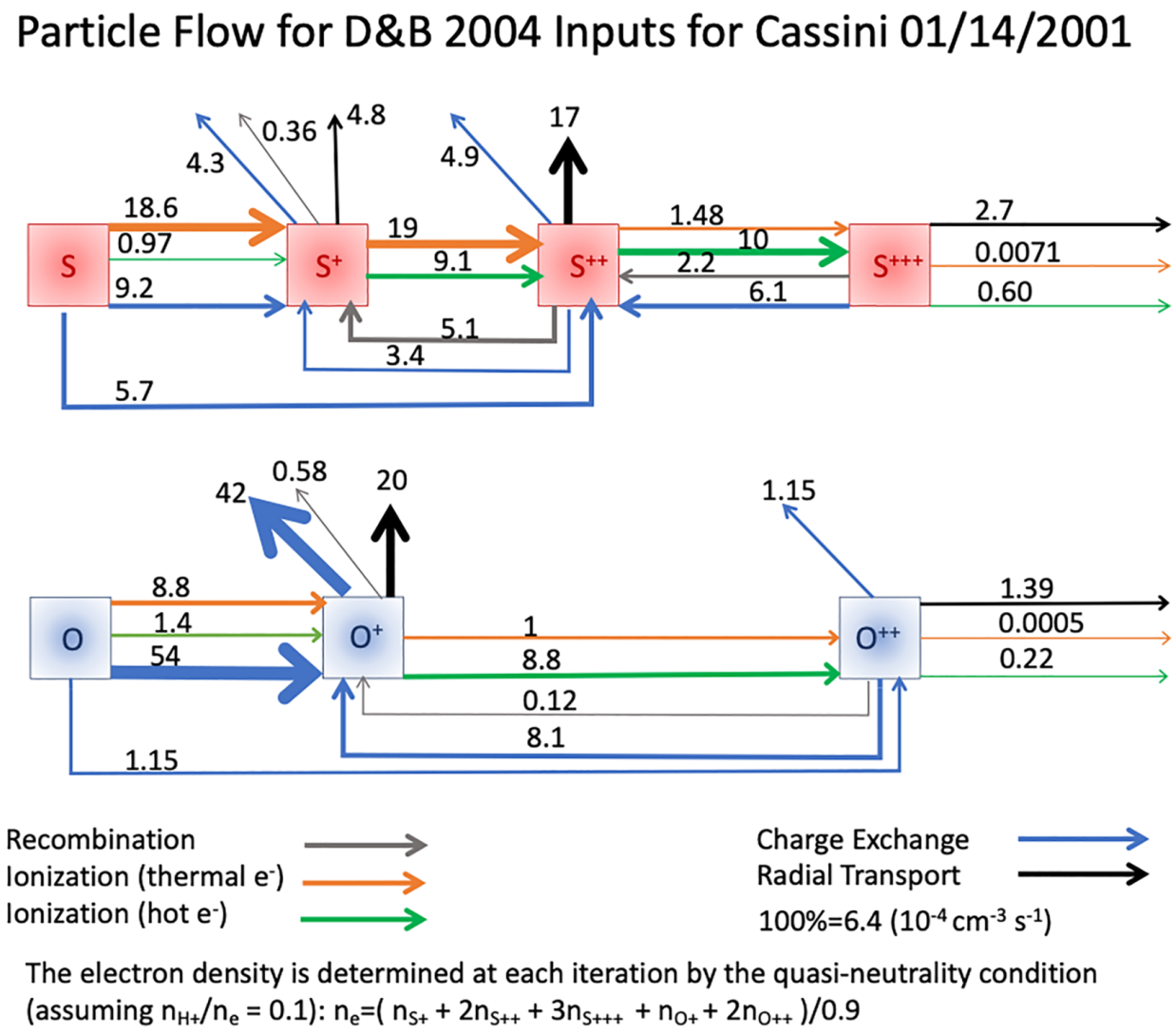

Figure 3.4: The flow of particles through the physical chemistry model at equilibrium for input conditions of O/S = 1.9, τ = 72 days, S_n=7.8 (10^{-4} cm^{-3} s^{-1}), f_{eh}=0.25%, T_{eh} = 46 eV. All numbers next to the arrows are in percentages. The total particle flow into and out of the system adds up to 100%.

loss arrows in Figure 3.4 we would expect there to be about 4.5 times as much neutral oxygen as neutral sulfur in this extended cloud.

The diagrams allow us to distinguish the most important reactions for understanding the system as a whole. The ultimate source of ion particles in Figure 3.4 is from the neutral source of oxygen and sulfur. For S^{+}, S^{+++}, S^{+++} and O^{++} ions the dominant source term is from ionization, but for O^{+} the dominant source term is from charge exchange with neutral O. The largest loss term for S and S^{+} is ionization, the largest loss term for S^{++} is radial transport, and for S^{+++} the dominant loss term is charge exchange taking S^{+++} back to S^{++} the dominant sulfur charge state. For all oxygen species (O, O^{+}, and O^{++}) the dominant loss term for each is due to charge exchange. Charge exchange taking O and O^{++} to O^{+} (the most abundant oxygen charge state) are the dominant loss terms for O and O^{++}. Charge exchange of O^{+} with O resulting in fast neutral O is the largest loss term for O^{+} and the largest single particle loss term of any species in the model.

Charge exchange, radial transport, and recombination can be loss terms from the system. For example, charge exchange of S and O ions can result in fast neutrals lost to the system. Radial transport moves the particles radially outward from 6 R_J which are then lost to the cubic-cm box. The density is too low for recombination to play a major role but can also result in a fast neutral being lost to the cubic-cm box model. Charge exchange accounts for the majority of the total particles lost to the system at about 52% of the total particles lost to the system. Radial transport is the second most important total loss term with about 46% of the total particle flow loss to the system. Ionization to S^{4+} and O^{3+}, two species not tracked by this model in our analysis and thus these reactions are considered as loss terms in our model, and recombination are the least significant loss terms from the system. Due to S^{++} and O^{+} being the dominant charge states the majority of the particles lost to the system are from S++ and O+. As shown by blue arrows in Figure 3.4 we find that about 43% of the total particle outflow from the system is due to fast neutral oxygen (with much less fast neutral sulfur) so we would expect to have an extended cloud of neutral oxygen with about 4.5 times less neutral sulfur. This can be understood by the fact

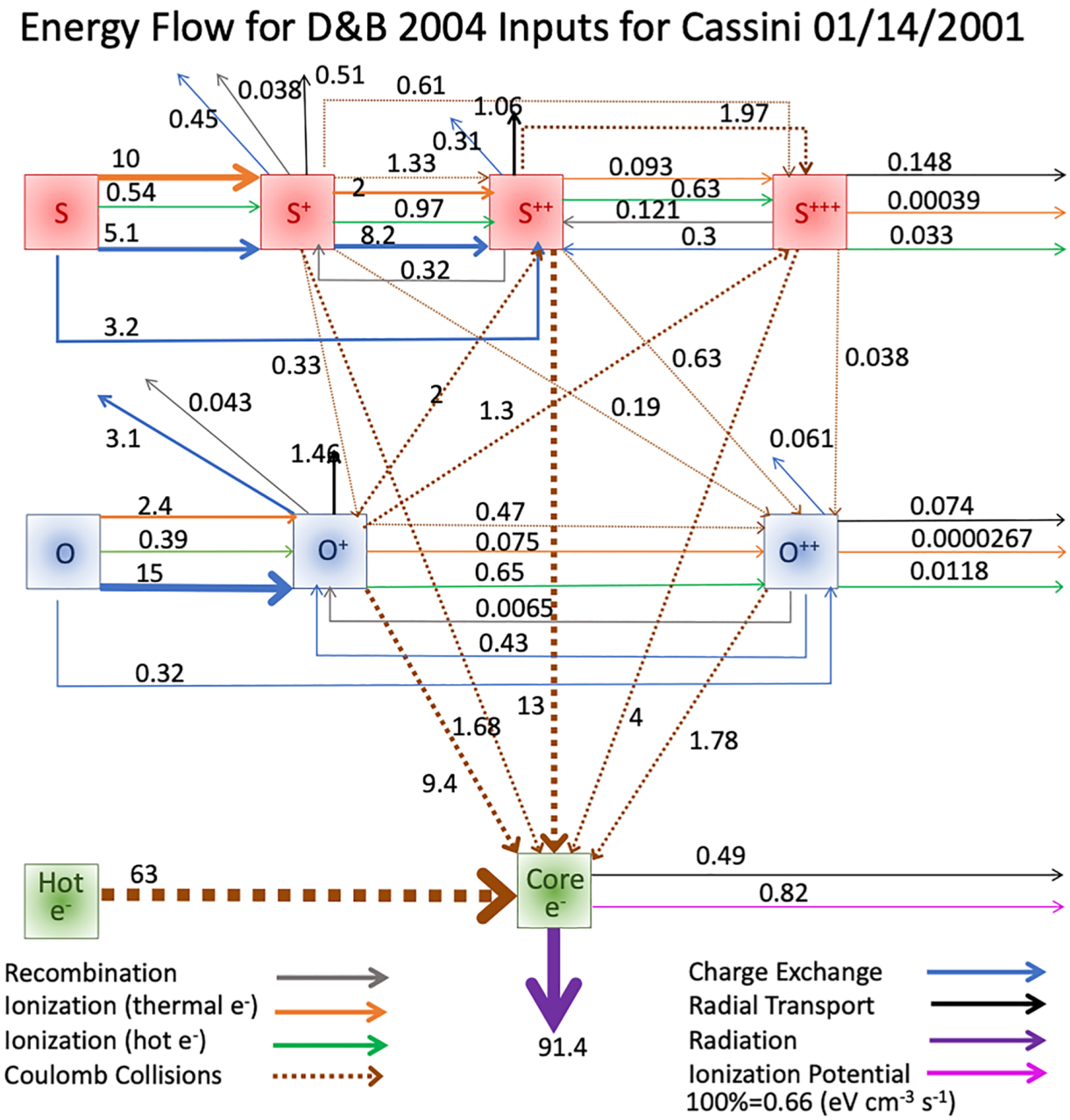

Figure 3.5: Similar to Figure 3.4 for the flow of energy through the system.

that at equilibrium the density of oxygen is about 4.1 times that of sulfur and the loss terms go as the density of both species involved in charge exchange. For S^+ and O^{++} the fast neutral charge exchange efficiencies are smaller than the comparable values for S^+ and O^+. With O^+ having about 4.2 times the density as S^+, this results in the largest single loss term for any species being from O+ charge exchange resulting in fast neutral oxygen.

Figure 3.4 shows us that ionization from the core electron population is important for making the lower charge states S^+, O^+, and S^{++}. The dominant ionization to make S^{+++} and O^{++} is from the hot electron population. This makes sense because to strip each subsequent electron out takes more energy (higher ionization energies) than the last, so higher energy electrons are required to ionize higher charge states.

The energy flow diagram in Figure 3.5 has additional terms due to exchange of energy due to Coulomb collisions and radiation. The net flow channels we discussed above for the mass flow diagram in Figure 3.4 do not necessarily apply to the energy flow for recombination, ionization, charge exchange, and radial transport because we now have more terms to balance.

Figure 3.5 shows the dominant source term for S^+ energy is ionization of S from the core electron population, for S^{++} the major source of energy is from S^+ and S^{++} charge exchange, for S^{+++} it is from Coulomb collisions with S^{++}, for O^+ it is from charge exchange with O, and for O^{++} it is from ionization of O^+ due to the hot electrons. For the thermal electron population, the largest single source term is from Coulomb collisions with the hot electron population. Though the fraction of hot electrons is found only to be 0.25% at 46 eV this is enough to account for 63% of the energy flow into the system due to Coulomb collisions (see Figure 3.5). Early studies pointed out the necessity of adding hot electrons to balance the energy flow in the Io plasma torus (Barbosa, 1994; Shemansky, 1988) [10] [121]. If it were not for this input of energy into the system, the core electron population would cool quickly due to radiation.

In Figure 3.5 we can see that the most significant single loss term for S is ionization due to the core electron population, for S^+ the dominant loss term is charge exchange into S^{++}, and for S^{++} and S^{+++} it is Coulomb collisions that transfers energy to the core electron population. The

largest single loss term for O is charge exchange into O^+, for O^+ and O^{++} the dominant loss term is due to Coulomb collisions sending energy to the core electron population. For the core electron population, the largest single loss term is due to radiation. Via electron impact excitation the ions are excited to higher energy states and then emit the majority of their energy in the UV which is why the electrons are the species losing energy via radiation which stands at 91.4% of the total energy flow out of the system.

Note that the charge exchange reactions used here are calculated here for 60 km/s relative speeds given by (McGrath and Johnson (1989)[85]). This is fine for the neutral/ion reaction at 6 R_J for the warm plasma torus however for the local interaction this is not right. Further, these should not be used for ion/ion charge exchange though in the warm torus these are minor contributions. These particularly should not be applied close to Io for the local ineraction where the flow velocity and ion temperatures are reduced. Dols and Johnson (2022)[45] address this issue and in addition calculate the velocity dependence including molecular chemistry.

3.4 Matching Plasma Conditions From UV Analysis With a Latitudinally Averaged Physical Chemistry Model

The output from the latitudinally averaged physical chemistry model is compared with the best fit composition, density, and electron temperature from the fit to the UVIS spectrum to find the best match of the physical chemistry model to conditions indicated by the UV emission.

Figure 3.6 shows a χ^2 plot for radial transport timescale vs. neutral source rate illustrating the strong anti-correlation of these two parameters as found in previous physical chemistry models (Delamere & Bagenal, 2003; Lichtenberg et al., 2001) [39] [82]. We find similar solutions for a range of timescales between 40–80 days and the neutral source rate between 7.8–20 (10^{-4} cm^{-3} s^{-1}) which implies $\dot{M}$ between about 0.7–1 tons/s. Our nominal solution has a high radial transport timescale and small neutral source rate whereas the Lichtenberg solution (Lichtenberg et al., 2001 [82]) is found for shorter radial transport timescales and a higher neutral source rate (see Table 3.4.). Previous attempts have been made to use the emitted UV power as a constraint (Delamere

& Bagenal, 2003) [39], but we found these contours to be nearly parallel as well and only driven by the electron density (see Figure 3.7) which also follows the same slope as the χ^2 plot shows. Our best fit solution is given by the minimum reduced χ^2.

To convert from the volumetric neutral source rate (S_n) to the total mass source rate ($\dot{M}$) in Table 3.4. we need an effective volume for the torus. Using a density model of the Io plasma torus (Hinton et al., 2019) [73] from a recent reanalysis of the Voyager in-situ plasma measurements (Dougherty et al., 2017) [47] we can integrate the densities from M-shell > 6.0 to get a total torus mass of 1.8 x 10^9 kg (Hinton et al., 2019) [73]. Assuming O/S = 1.9, the mass of the torus above, a typical number density at 6 R_J of 2000 cm^{-3} we find 2.5 x 10^{31} $cm^3 \approx 68$ R_J^3 for our effective typical volume.

In Delamere and Bagenal (2003) [39] the volume is quoted as 1.4 x 10^{31} $cm^3 = 38$ R_J^3 (see their section 3.3) and in Delamere et al. (2004) [41] the volume was up to 3.1 x 10^{31} cm^3. Using our effective volume of 2.5 x 10^{31} cm^3, with the "low & slow" nominal volumetric neutral source rate = 7.8 (10^{-4} cm^{-3} s^{-1}), and O/S = 1.9 we get a net source of about 0.7 tons/s. The "high & fast" case yields a net source of 1.8 tons/s for the same volume which is shown in Table 3.4.

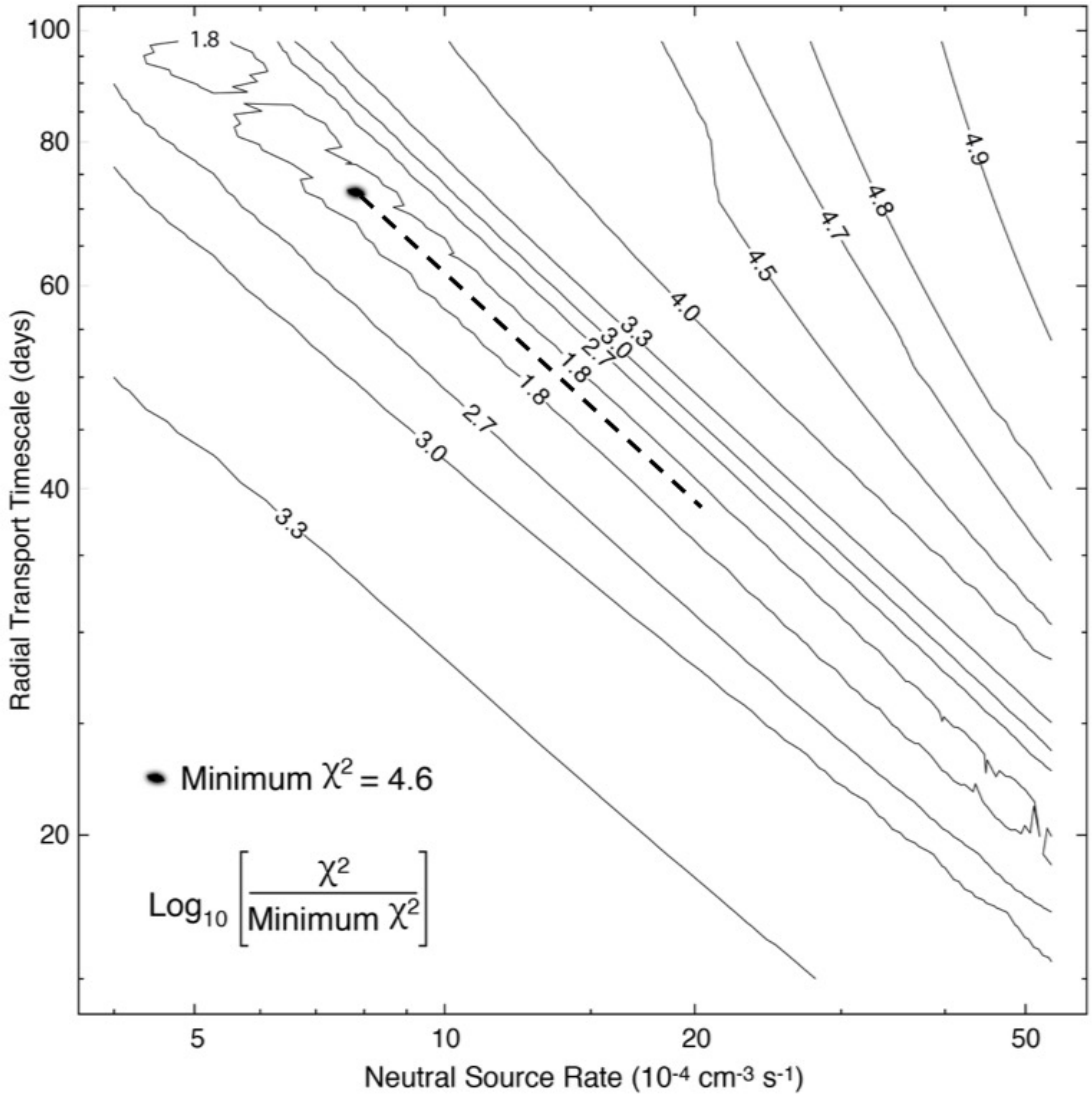

Figure 3.6: Using the latitudinally averaged physical chemistry model we show contours of χ^2 as a function of the radial transport timescale and neutral source rate from fitting the densities found from spectral modeling. The plot shows similar solutions for a range of both parameters.

Model	$\dot{M}$ (Tons/s)	S_n ($10^{-4}\ cm^{-3}\ s^{-1}$)	Torus Volume (10^{31} cm^3)	Transport Timescale τ (Days)
Shemansky et al. 1988	**2.4**	27	N/A	80
Lichtenberg et al. 2001	**2.0**	23	N/A	8
Delamere et al. 2003	*0.4-1.3*	7-30	1.4	23-50
Delamere et al. 2004 Steady Jan 2001 Transient Oct 2000	 *0.7* *1.9*	 6.4 17.2	3.1	 64 27
Delamere et al. 2005	0.6-3	**6.8 - 34**	N/A	14-64
Steffl et al. 2008	**0.87**	9.9	N/A	62
Copper et al. 2016 Steady Transient 2015	<1	**11.3**	N/A	 43 33
Yoshioka et al. 2017	1.3	7.7	5	30
This Study "Low & Slow" "High & Fast"	 0.7 1.8	 7.8 20	2.5	 72 40

Table 3.4: Transport timescales and mass loss rates for various physical chemistry models. Where the volume is not available (N/a) we used Our volume and O/S = 1.9 to calculate bold values from other relevant numbers found in the corresponding reference. Italic values are computed using quoted volume and S_n from the reference to compute $\dot{M}$

Table 3.4 compares different physical chemistry model neutral source rates and radial transport timescales. We list what torus volume was assumed or implied. Different assumptions are made between different models and a wide range of best fit inputs are found as highlighted in Table 3.4.

As shown in Figure 3.6 there are similar solutions along a line of different neutral source rate and radial transport values. If we were to consider the radial transport timescale of 40 days, this corresponds to a volumetric neutral source rate of about 20 ($10^{-4}\ cm^{-3}\ s^{-1}$) which corresponds to a net source of about 1 ton/s.

In Figure 3.7 we plot contours of eight properties of the torus as functions of the radial transport timescale (τ) and the neutral source rate. In Figure 3.7 (Case A) we are able to match

plasma conditions from Cassini UVIS spectral analysis in this physical chemistry input range for $F_{eh} = 0.25\%$ but not for Case B or C. The equivalent of Figure 3.7 for case B is included in the supplementary online material. It can be seen in Figure 3.8 that the electron and ion density contours follow similar slopes which shows there is a range in parameter space with similar solutions. Our nominal solution is shown in Figure 3.7 by a black box plotted over the contours. When we originally fit the UV spectrum at 6.1 R_J using MPFIT (Nerney et al., 2017) we found error bars for the composition and electron temperature. We show these by plotting $\pm 1\sigma$ error bars in gray over the contours to show the range in values due to uncertainty in the UV fits. For $F_{eh} = 0.25\%$ we can match the plasma composition and temperatures from the Cassini UV spectral analysis.

The spectral emission is averaged over the line of sight which biases the electron temperature to a higher value. This is because the electron temperature increases with radial distance. However, the density decreases with radial distance so for density we are biased to the minimum radial distance which is why it is a good assumption in general to treat the density and temperature constant along the line of sight. For the physical chemistry model at 6 R_J there is no line of sight averaging and therefore we would expect the physical chemistry model to find lower electron temperatures for the same set of densities.

In Figure 3.7, away from the best-fit slope, the density changes rapidly, and composition shifts away from the desired solution. In the top left panel of Figure 3.7, the core electron temperature does not change much in this input parameter range, and therefore our solution is much less sensitive to electron temperature. There is a large swath of solutions with core electron temperatures between the reasonable values of 5–7 eV. We only fit the densities in determining our nominal solution, but by inspection, the ion and electron temperatures are reasonably matched as well. In the bottom right panel of Figure 3.7, the PUV contours follow similar slopes as the core electron density and mixing ratios and therefore is not a useful constraint for fixing the anti-correlation issue between the radial transport timescale and the neutral source rate unlike the finding of Delamere and Bagenal (2003) [39]. Each ion species does have a slightly different slope leading to one solution being marginally better than the others.

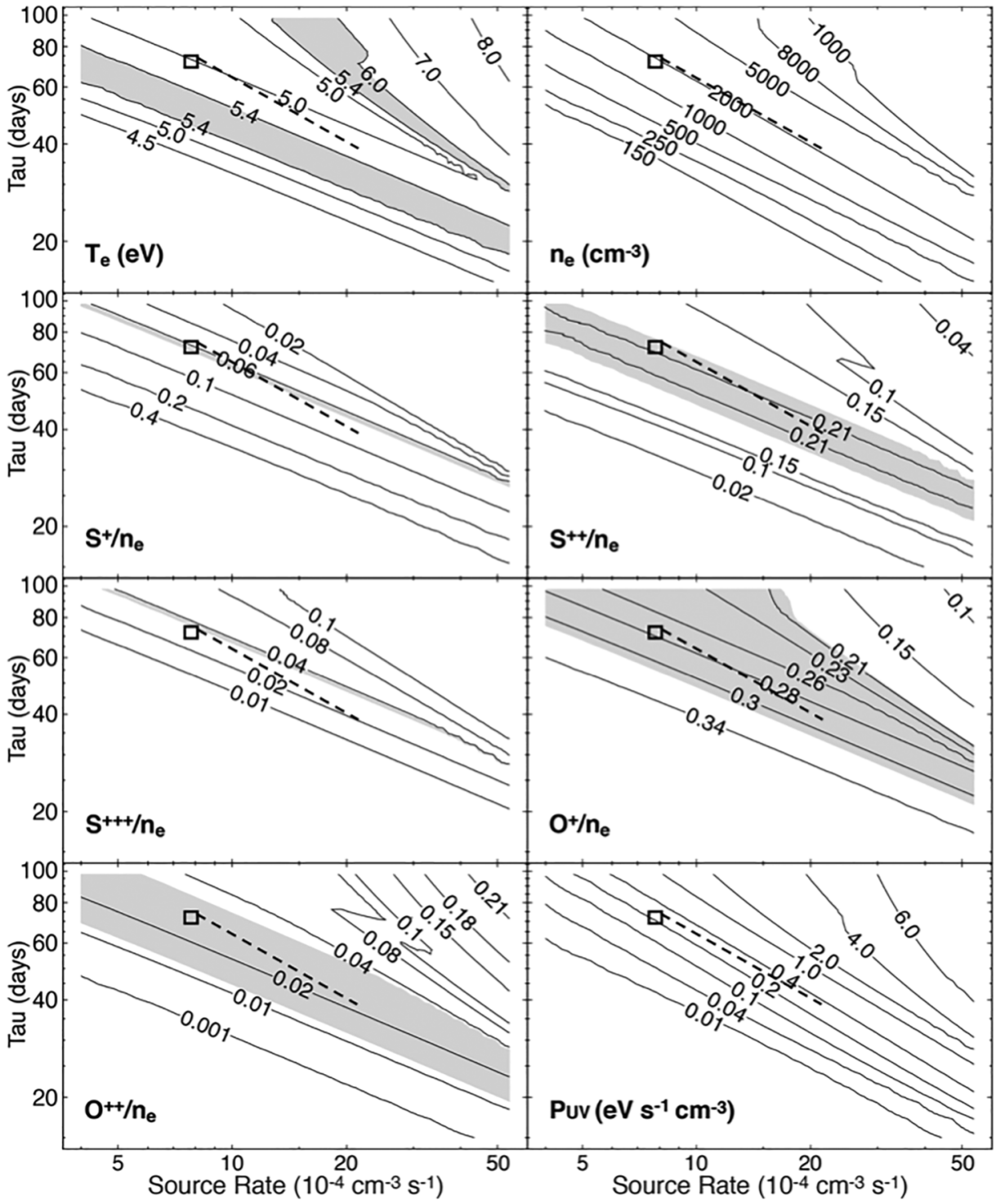

Figure 3.7: (Case A) Physical chemistry model output is shown above. We vary the neutral source rate (S_n) and radial transport timescale (τ) above while holding all other model inputs constant. This is Point A on the χ^2 plot in Figure 3.2 ($\mathbf{F_{eh} = 0.25}\%$, O/S = 1.9, T_{eh} = 46 eV). The square shows our nominal ("low & slow") solution given by the values in Table 3.3. Each shaded region is the $\pm$ uncertainty in that variable derived from the UVIS spectral analysis.

Taking the nominal ("low & slow") solution inputs given in Table 3.3 the physical chemistry outputs a core electron temperature Te = 5 eV,the core electron density $n_e = 1900\ cm^{-3}$, S^+/N_e= 6.1%, S^{++}/N_e= 21%, $S^{3+}/N_e = 3.2\%$, $O^+/N_e = 27\%$, & $O^{++}/N_e = 2.7\%$. Though the contours for the ion temperatures are not shown in Figure 3.7 they are also an important output of the physical chemistry. For the nominal inputs we find $T_{S^+} = 101$ eV, $T_{S^{2+}} = 66$ eV, $T_{S^{3+}} = 63$ eV, $T_{O^+} = 71$ eV, and $T_{O^{2+}} = 61$ eV. These are reasonable values consistent with in-situ plasma measurements from the recent Voyager reanalysis (Dougherty et al., 2017) [47] and modeling (Delamere & Bagenal, 2003) [39]. Contours of ion temperatures vs model inputs are included in the supplementary online material for Case A and B.

Though solutions along the dashed line in Figure 3.6 have a similar goodness of fit the model output and resulting flow of particles and energy is slightly different. We fit the densities in order to compute the chi^2 value which will bias to the total electron density more than the individual mixing ratios. As can be seen in Figure 3.7 the model output contours follow slightly different slopes leading to solutions being slightly different along the dashed line. The equilibrium solution for S_n= 20 ($10^{-4}\ cm^{-3}\ s^{-1}$) and τ= 40 days, the "high & fast" case, has higher singly ionized sulfur and oxygen mixing ratios at 8% and 29%. The other charge states have about the same mixing ratios as our nominal solution. The output electron density and temperature stay essentially the same between the two model runs. Output ion temperatures are about 30–40 eV hotter than for the nominal ("low & slow") solution which increases the ion scale heights that in turn changes the latitudinal averaging.

The mass flow for "high & fast" case is remarkably similar with a slightly lower average ionization state since there is less time to ionize the higher source of neutrals beyond the first ionization state. The energy flow for "high & fast" case requires fewer hot electrons (40% of the energy supply) with the higher neutral source producing more pick-up ions. The ions remain 30–40 eV hotter, carrying more of the energy out of the system with less (73%) being radiated through UV emissions. Looking at differences in the particle budget there is an increased neutral source resulting in a larger total flow of particles in and out of the system. While the total has increased

most of the sources and loss terms in percentages of that total have remained the same. The radial transport timescale was also decreased. The loss rate due to radial transport (RT) for each species goes as $\left(\frac{dn_i}{dt}\right)_{RT} = \frac{n_i}{\tau}$. If the densities all remain about the same we would expect this total loss term to increase because τ is smaller. But the total source is now larger too so along the dashed line in Figure 3.6 the radial transport loss terms stay about the same percentage of the total helping to maintain a similar solution. We mentioned before that there was more S^+ and O^+ in the "high & fast" case than in the nominal solution. This is due to a different balance in the particle flow. In both cases, the loss term due to hot electron ionization to S^{++} and O^{++} has decreased.

As mentioned previously, the output ion temperatures are about 30–40 eV hotter than for the nominal solution so we should expect more differences in the energy budget than we found in the particle budget. The total particle source is higher resulting in a higher total energy source as each freshly ionized neutral is brought up to corotation energy and there is a larger particle source of them so we would expect a larger source of energy too. The radial transport timescale is shorter and the loss rate is larger so the plasma is not sticking around as long which allows it to cool down via collisions. It, therefore, makes sense that the ions are hotter. All ionization loss and associated source energy terms are larger than we found in the nominal solution, again consistent with the larger input of energy allowing for more ionization. Although the source and transport parameters differ by factors of ≈ 2, the solutions are quite similar.

Next, we consider Case B where we increase the fraction of hot electrons to 2.5% (Figure 3.2). We are not able to match plasma conditions from Cassini UVIS spectral analysis in this physical chemistry input range for $F_{eh} = 2.5\%$. Model output contours for Case B are shown in the supplementary online material. The core electron temperatures are too large and densities too low. 6 eV and 2000 cm^3 do not overlap in parameter space. In fact, they are pushed in opposite directions. The core electron temperature around 6 eV is shifted to a lower radial transport timescale and lower neutral source rate pushing our nominal temperature solutions off the plot and showing no reasonable solution can match the core electron temperature for this fraction of hot electrons. The electron density and P_{UV} are pushed to higher transport timescales and higher

neutral source rates pushing the nominal solution for those off the plot to the upper right corner.

The mixing ratios, for Case B (see Table 3.2) follow contours similar in shape to that of the electron temperature contours in the first panel. The nominal plasma composition mixing ratios shown by the gray-shaded regions are no longer overlapping in parameter space for $F_{eh} = 2.5\%$. For S^{+}, S^{3+}, O^{+}, O^{++} we still see part of the gray shaded region in the plot. Each shaded region is the $\pm$ uncertainty in that variable derived from the UVIS spectral analysis. For S^{++}, the dominant sulfur charge state, the solution has been shifted off the plot to the bottom left. At this fraction of hot electrons, the electron density and emitted UV power contours have different slopes than the mixing ratio and temperature contours. For Case C this only gets worse. The electron and ion temperatures are far too high and the nominal plasma composition mixing ratios are even farther from overlapping.

Taking the nominal solution inputs given in Table 3.3 and only changing the fraction of hot electrons (F_{eh}) to 2.5% (trying to match Case B) we find the core electron temperature $T_e =$ 19 eV and the average charge state has increased making S^{++} and O^{+} no longer the dominant species. Ion temperatures are also an important output of the physical chemistry and we find the ion temperatures are 200–300 eV (see section 3.6). These are far higher than measured in the Io plasma torus (Bagenal et al., 2017) [1]. The temperatures for the core electron population and the ions are far higher than we have constrained via observations. Furthermore, at such a high fraction of hot electrons, the dominant charge states are the higher charge states because of the efficiency of ionization from the hot electron population. In fact, S^{4+} & O^{3+} become non-negligible plasma species which is inconsistent with observations. We find S^{4+} is the dominant sulfur charge state when we include it in our model at F_{eh}= 2.5%, inconsistent with Steffl et al. (2004b) [137] which showed between 6-9 R_J that S^{4+}/N_e was less than 1%. When we include S^{4+} for our nominal solution (Feh= 0.25%) we find S^{4+}/N_e= 0.6%.

We explore more of parameter space in Figure 3.8 (τ vs. F_{eh}) and Figure 3.9 (S_n vs. F_{eh}) which show that to match the plasma composition, core electron temperature, and electron density the fraction of hot electrons must be below 0.5%. In Figures 3.8 and 3.9 we only show the critical

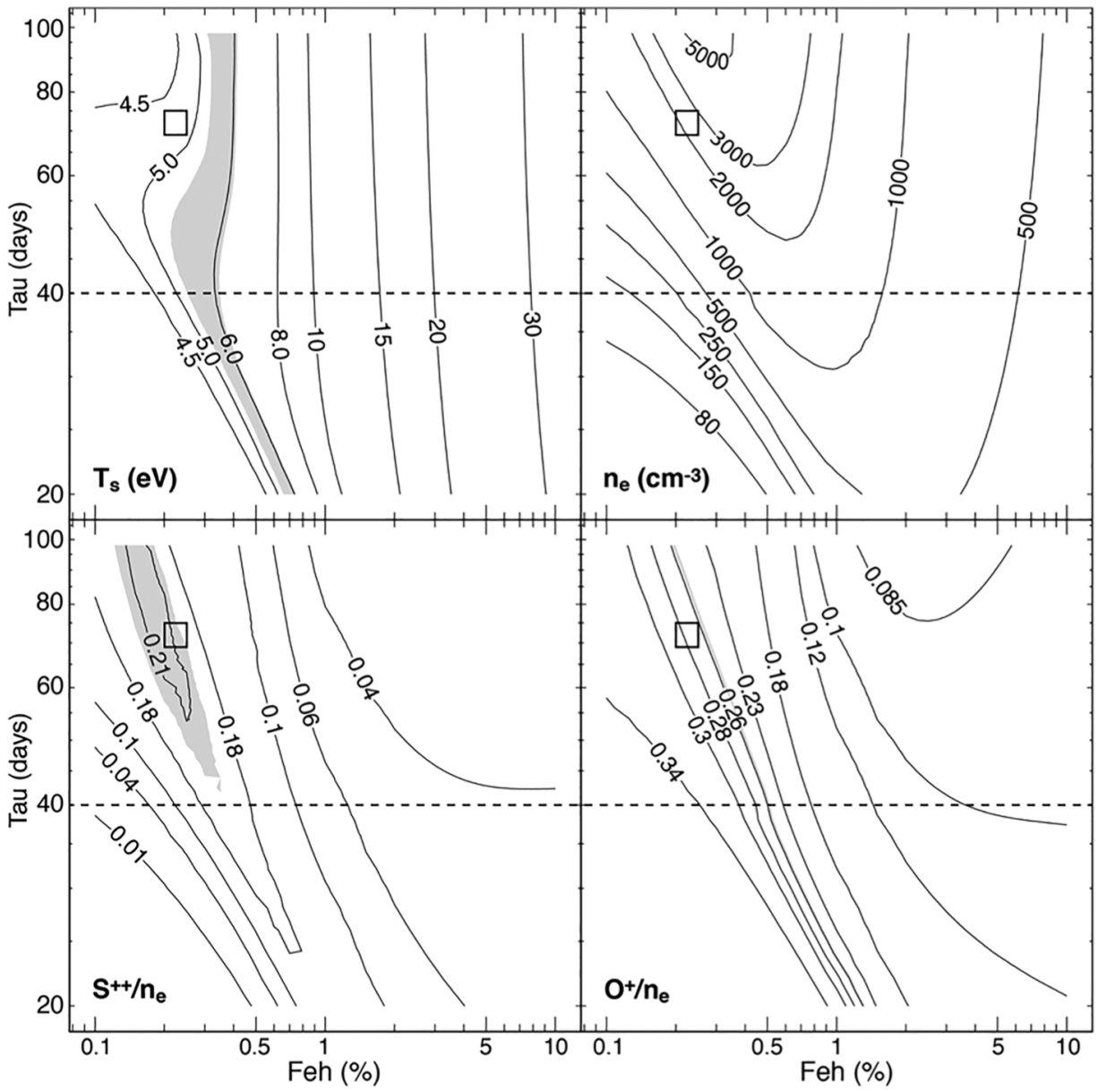

Figure 3.8: Physical chemistry model output for ranges of the fraction of hot electrons (F_{eh}) and radial transport timescale (τ) above while holding all other model inputs constant. (O/S = 1.9, S_n = 7.8 (10^{-4} cm^{-3} s^{-1}), T_{eh} = 46 eV) the dotted line is the lowest value of τ in our range of similar solutions as shown in Figure 3.6. The square shows our nominal solution given by the values in Table 3.3. Each shaded region is the ± uncertainty in that variable derived from the UVIS spectral analysis.

model outputs, specifically core electron temperature, core electron density, and the S^{++} & O^{+} mixing ratios. The electron temperature contours and electron density contours for 5 eV and 2000 cm^{-3} only intersect once in these plots highlighting the strong dependence on fraction of hot electrons. This constrains the fraction of hot electrons to 0.25% via the energy balance requirements. For higher values of F_{eh} the equilibrium core electron temperature would be too high and the density too low.

In Figure 3.8 we plot contours of model output found by varying the fraction of hot electrons and the radial transport timescale. In the first panel on the top left, we see the core electron temperature as a function of the fraction of hot electrons and the radial transport timescale. When the fraction of hot electrons is above 1% the core electron temperature contours go nearly vertical showing almost no radial transport timescale dependence. In the second panel in the top right, we have the core electron density contours which for a given fraction of hot electrons yields one radial timescale value for a given electron density contour. However, for a given radial transport timescale value there are two possible fractions of hot electrons giving the same electron density contour.

In the last two panels, we have S^{++} and O^{+} mixing ratios which have a mixed behavior. The mixing ratio contours have a strong fraction of hot electron dependence. There is only a narrow swath of this parameter space plotted that gives solutions close to S^{++}/N_e=21% and O^{+}/N_e=26%. This strong fraction of hot electron dependence allows us to constrain the fraction of hot electrons.

We plot contours of model output in Figure 3.9 by varying the fraction of hot electrons and the neutral source rate. In Figure 3.9 we plot the same 4 model outputs as we did in Figure 3.8, but we replace the radial transport timescale with the neutral source rate as the other varying quantity. All other inputs are held constant at the nominal values found in Table 3.2.

Again, we find that the fraction of hot electrons drives the electron and ion temperatures and above 1% there is no neutral source rate dependence. Here we also find that core electron temperature and density contours (top right and left panels of Figure 3.9) only intersect once determining the fraction of hot electrons. There is only a narrow swath of parameter space shown in Figure 3.9 that allows for the mixing ratios to match those in Table 3.1. Furthermore, there is

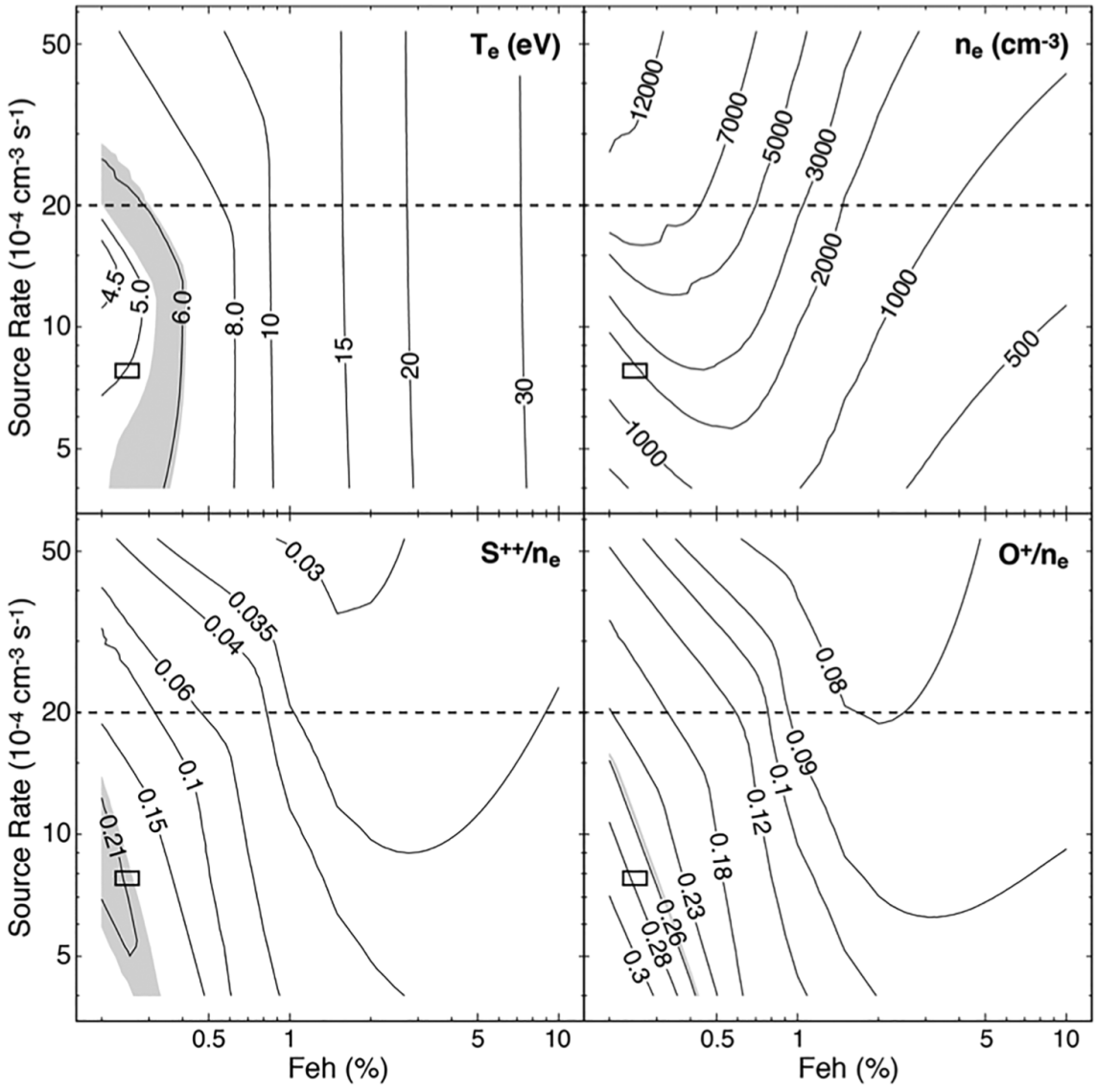

Figure 3.9: Physical chemistry model output for ranges of the fraction of hot electrons (F_{eh}) and neutral source rate (Sn) above while holding all other model inputs constant. (O/S = 1.9, τ =72 days, T_{eh} = 46 eV) the dotted line is the highest value of S_n in our range of similar solutions as shown in Figure 3.6. The square shows our nominal solution given by the values in Table 3.3. Each shaded region is the ± uncertainty in that variable derived from the UVIS spectral analysis.

only one place where these mixing ratios intersect with about 2000 cm^{-3} which also determines the fraction of hot electrons to be 0.25% for our nominal solution. Overall the contour shapes are very similar to what we saw in Figure 3.8 because of the strong fraction of hot electron dependence.

3.5 Summary & Conclusions

Comparing our work with others we find similar plasma composition to Steffl et al. (2004b) [137] and Yoshioka et al. (2011) [164] from spectral analysis for steady state times. Using the latitudinally averaged physical chemistry model for equilibrium conditions we find a higher radial transport timescale and slightly larger neutral source rate than Delamere et al. (2004) [41] found with their model without latitudinal averaging. Yoshioka et al. (2014) [163] and Tsuchiya et al. (2015) [150] have found fractions of hot electrons on the order of a few percent inconsistent with our steady state physical chemistry model. More recent work from Yoshioka et al. (2017) [165] and Hikida et al. (2020) [69] have found values for the fraction of hot electrons (less than 1%) from spectral analysis at the orbit of Io more consistent with our physical chemistry modeling for steady state Io plasma torus conditions. Hikida et al. (2020) [69] in their recent paper shows evidence for an enhancement of the fraction of hot electrons during transient times possibly due to volcanic eruptions on Io.

The goal of this chapter has been to constrain the hot, non-thermal component of the electron population via a combination of spectral analysis and energy balance from physical chemistry modeling. The hot electrons play a critical role in the ionization of the higher charge states and in Coulomb collisions between the hot and core electron population which transfers 54% of the total energy flow from the hot electrons to the core which in turn keeps their temperature near 6 eV. If it were not for these hot electrons supplying energy to the core they would cool down via radiation.

Our spectral modeling found a core electron temperature to be 6.1 eV while our physical chemistry modeling found 5 eV. This is the best we were able to do by only fitting the densities. The spectral emission is a remote sensing observation and our modeling is therefore biased by emission along the line of sight. The physical chemistry model is not averaged over the line of sight

and is therefore not biased to higher temperatures at larger radial distances. More so, the fitting algorithm Mpfit in IDL uses the curvature matrix to compute uncertainties assuming the inputs are independent so in reality, the determined uncertainties values should probably be a bit larger.

Our findings from this study are:

1. Using the spectral emission model to match UV spectra to constrain the fraction of hot electrons leads to a similar "goodness of fit" for a range of values of the core electron temperature (5.6–6.6 eV) and the fraction of hot electrons (0.25% - 5.5%).

2. Constraining F_{eh} with the physical chemistry model shows that to match observed ion and electron densities and temperatures with the "cubic-cm" (0-D) physical chemistry model the fraction of hot electrons must be less than 0.01 or 1%.

3. Adding in additional physics from the energy constraints allows us to determine that for canonical torus plasma parameters the fraction of hot electron is more likely 0.25% than 1% (consistent with Case A and not B or C).

3.6 Supplementary Figures

The following supporting figures are latitudinally averaged cubic-cm physical chemistry model output contours. We vary 2 model inputs for each contour and hold the rest of the inputs constant. Model output trying to match Case B and output temperature contours are shown. For fractions of hot electrons (F_{eh}) above 0.5% the model output is inconsistent with the observed composition and temperatures of the Io plasma torus.

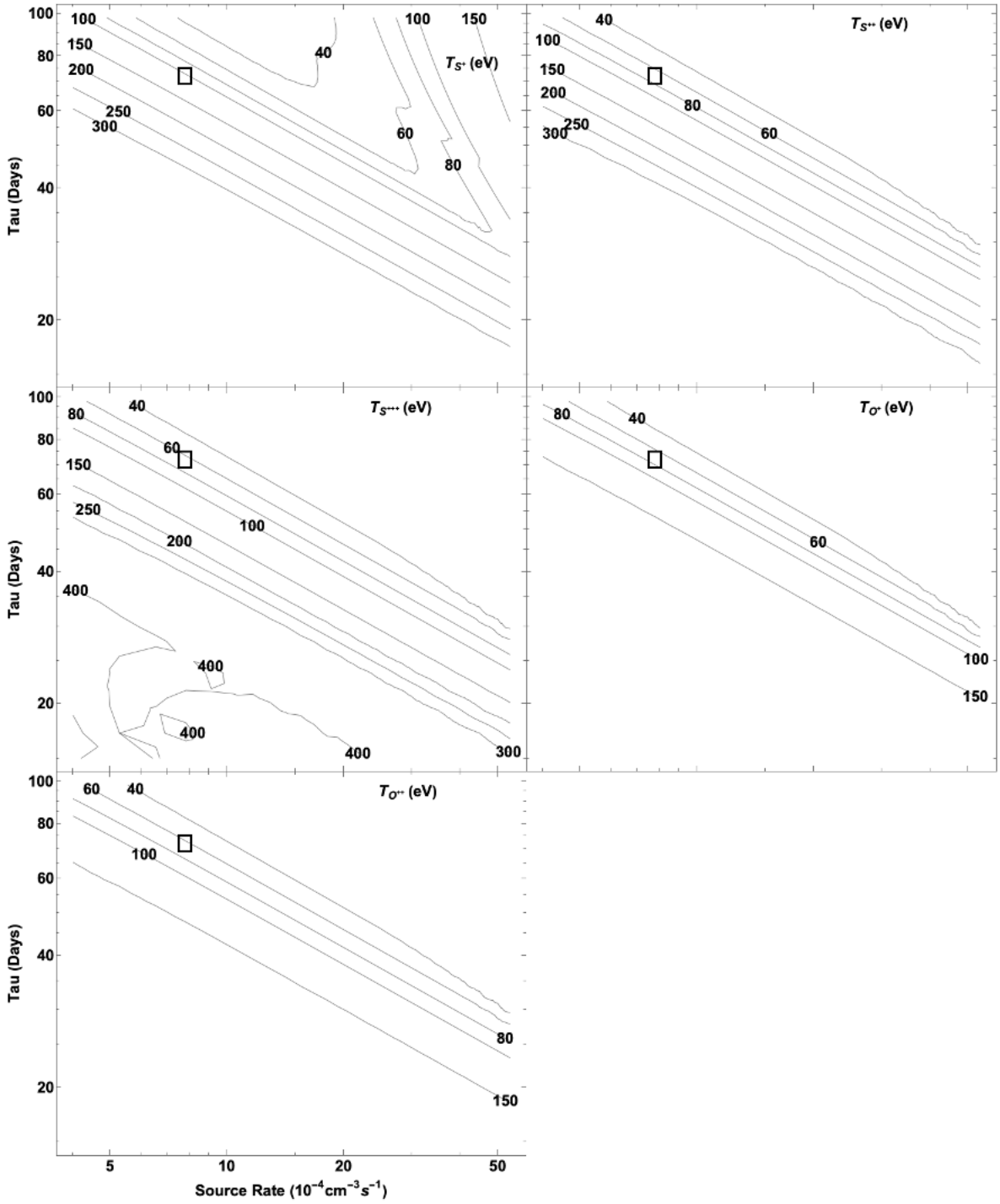

Figure 3.10: (***Case A***) Physical chemistry model output ion temperatures are shown above. We vary the neutral source rate (S_n) and radial transport timescale (τ) above while holding all other model inputs constant. This is Point A on the χ^2 plot in Figure 1 ($\boldsymbol{F_{eh} = 0.25}$%, O/S=1.9, T_{eh}=46 eV). The square shows our nominal ("low slow") solution given by the values in Table 3.

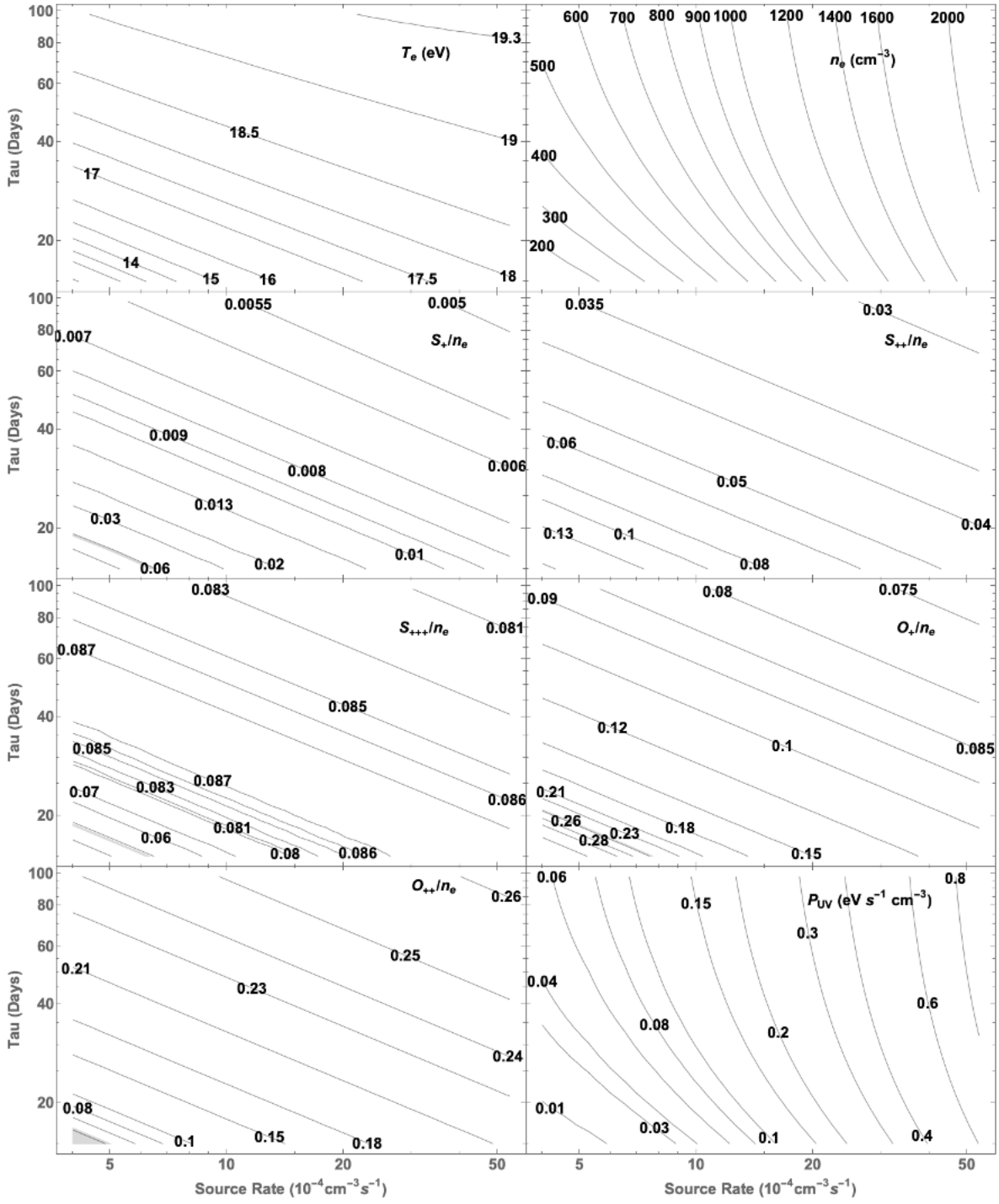

Figure 3.11: (***Case B***) Physical chemistry model output is shown above. We vary the neutral source rate (S_n) and radial transport timescale (τ) above while holding all other model inputs constant. This is Point B on the χ^2 plot in Figure 1 $\boldsymbol{F_{eh} = 2.5}$%, O/S=1.9, T_{eh}=46 eV).

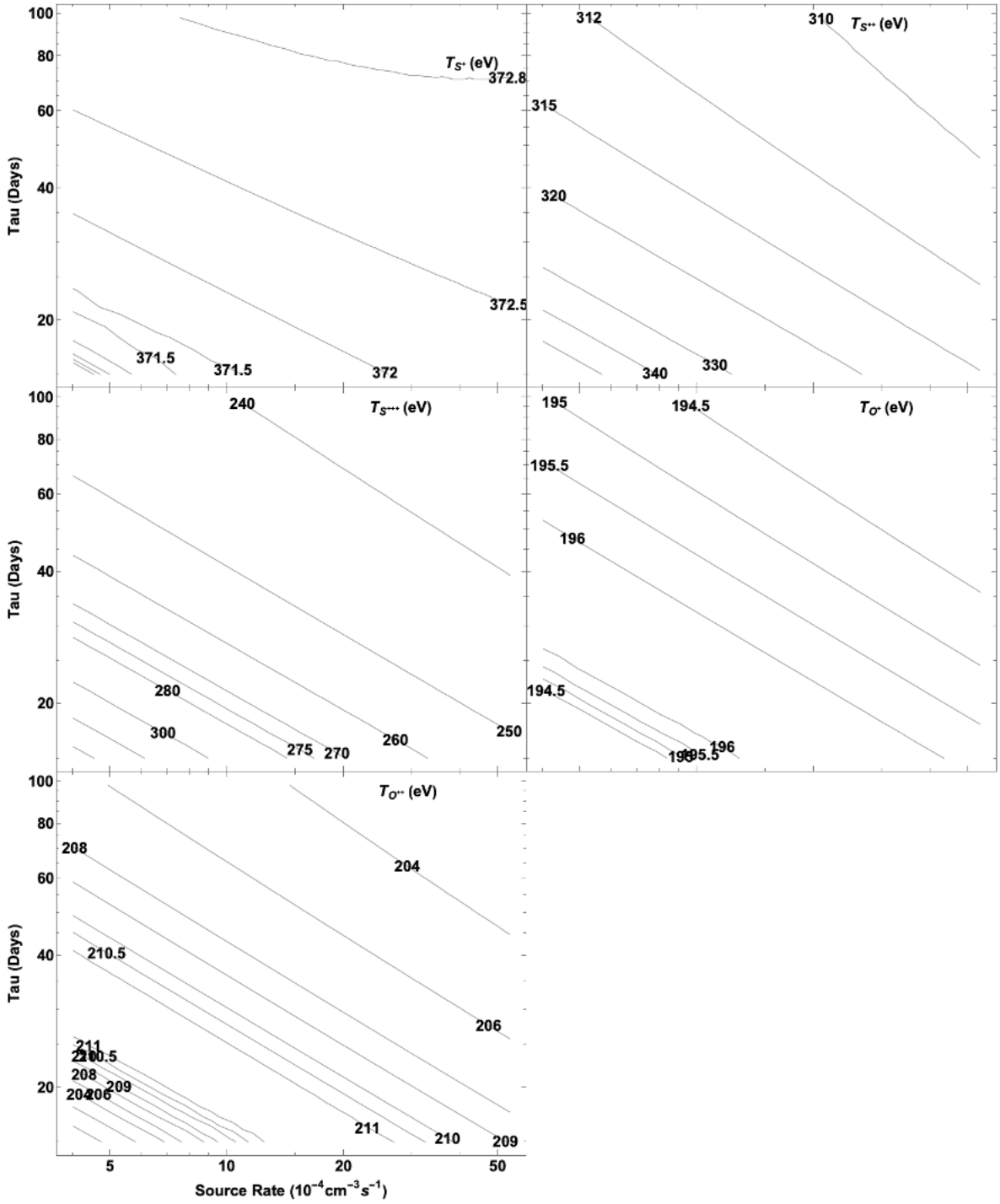

Figure 3.12: (***Case B***) Physical chemistry model output ion temperatures are shown above. We vary the neutral source rate (S_n) and radial transport timescale (τ) above while holding all other model inputs constant. This is Point B on the χ^2 plot in Figure 1 ($\boldsymbol{F_{eh} = 2.5}$%, O/S=1.9, T_{eh}=46 eV).

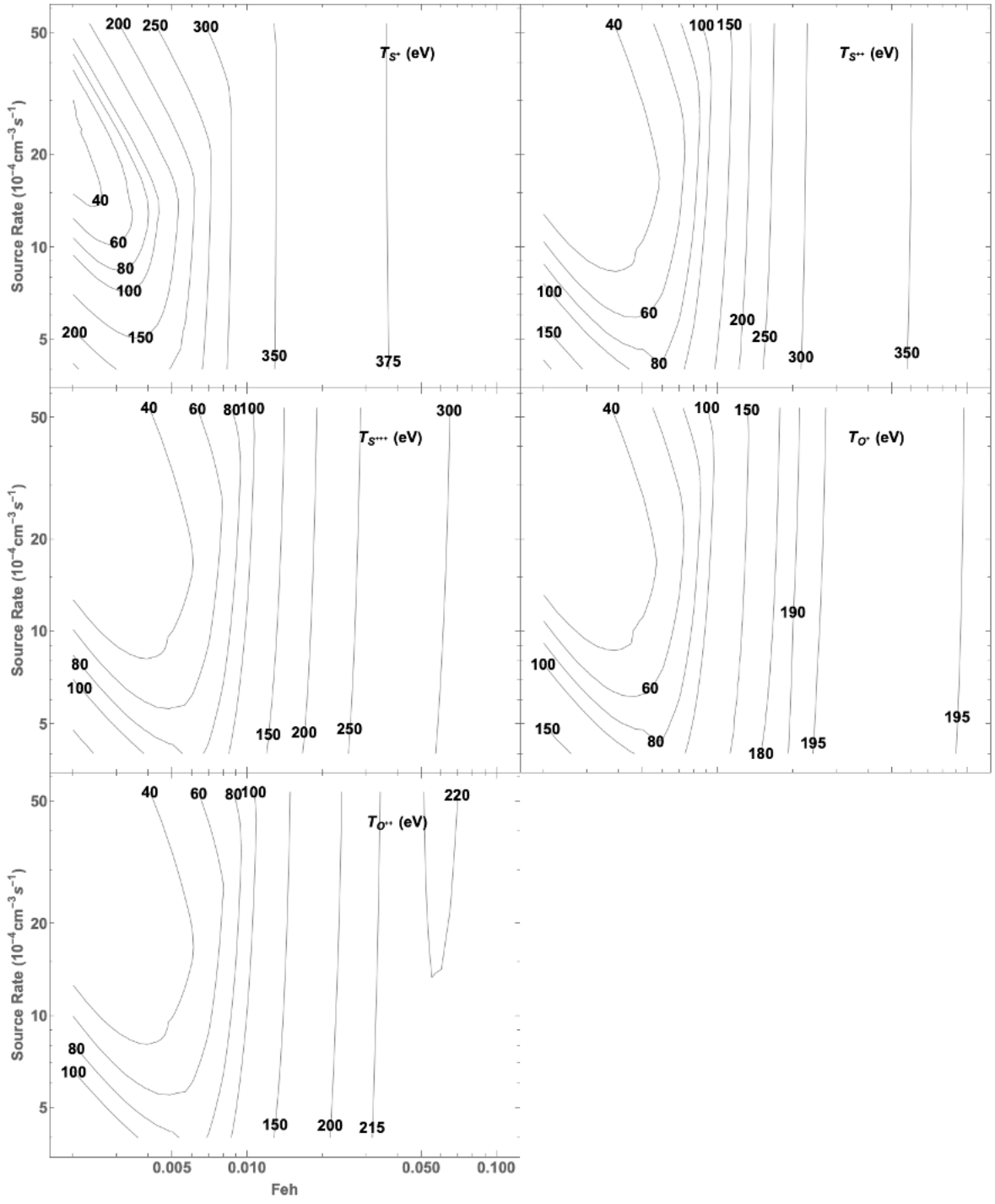

Figure 3.13: Physical chemistry model output ion temperatures for ranges of the fraction of hot electrons (F_{eh}) and neutral source rate (S_n) are shown above while holding all other model inputs constant. (O/S=1.9, τ =72 Days, T_{eh}=46 eV)

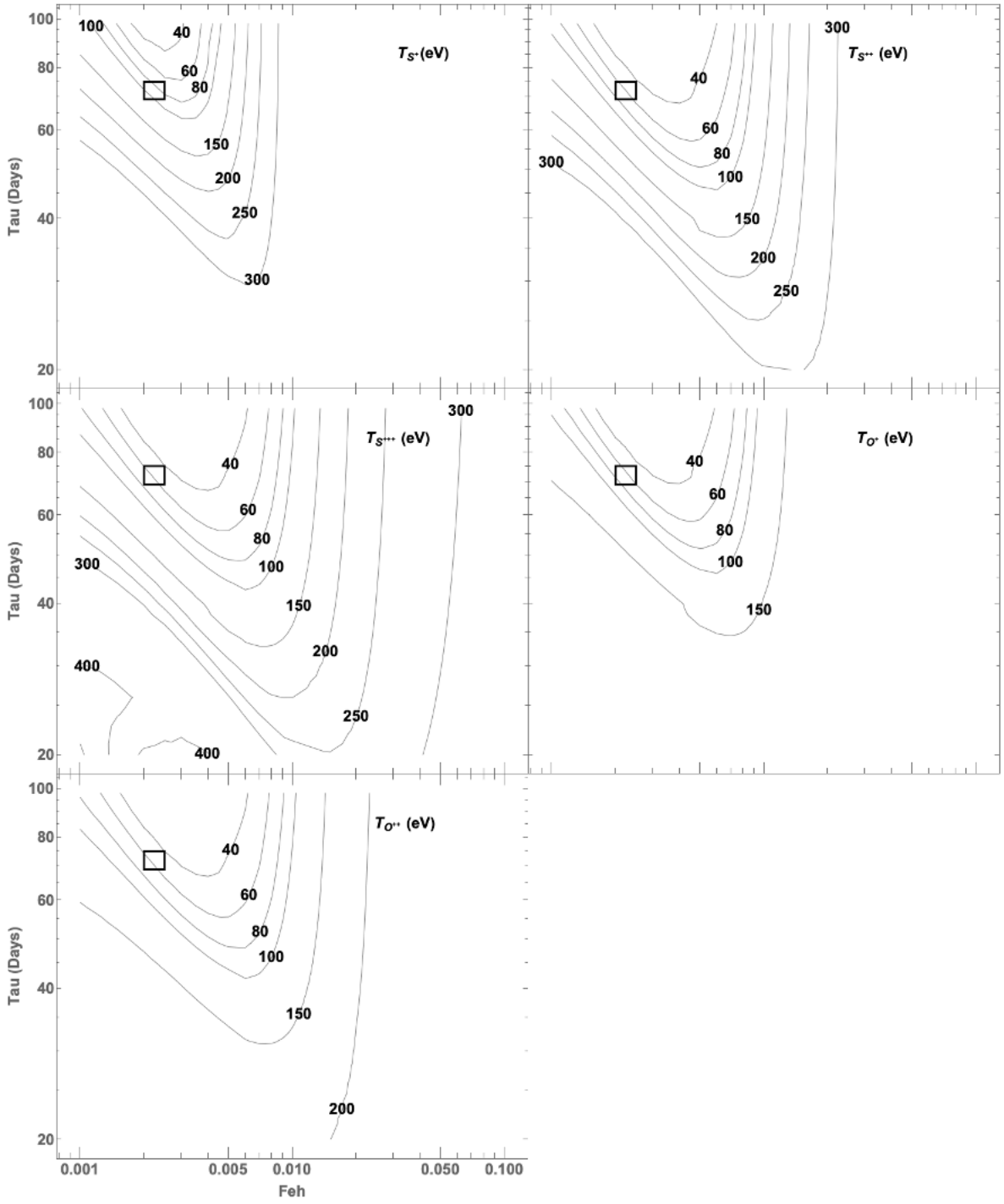

Figure 3.14: Physical chemistry model output ion temperatures for ranges of the fraction of hot electrons (F_{eh}) and the radial transport timescale (τ) are shown above while holding all other model inputs constant. (O/S=1.9, S_n = 7.8 (10^{-4} cm^{-3} s^{-1}), T_{eh}=46 eV)

Chapter 4

Emission Modeling

4.1 Motivation

My work modeling past spectra have shown me the need to develop a more sophisticated spectral emission model to sort out line-of-sight (LOS) effects from real changes in composition and plasma conditions. Specifically for ground-based observations going into the cold torus where emission is coming from a region inside the peak in charge density in the Io plasma torus (IPT). The emission that reaches an observer is due to emission over the entire line of sight not just the region of interest. In these regions projection effects become important and the assumptions made in chapters 2 and 3 using a cubic centimeter spectral emission model fail. By properly integrating over the line of sight and subtracting off the emission coming from outside the region of interest our model will allow us to "peel the onion" and determine the emission due only to that region of interest and subsequently determine the plasma conditions in said region instead of being biased to the region of peak emission and density.

This work will allow us to plan for future missions to Jupiter. My model will for a given spacecraft trajectory, pointing of the spacecraft, integration time, and instrument calibration determine the counts we expect the detector to see. This allows us to determine if said observations will be sufficient to meet project requirements and to receive enough signal to noise in order to properly determine plasma conditions to an acceptable level of certainty. NASA's Europa Clipper is planned to launch in October of 2024 and will arrive in the Jupiter system in April of 2030. Likewise, ESA's JUICE (Jupiter Icy Moons Explorer) mission is scheduled to launch in April of

2023 and will arrive in the Jovian system in July of 2031. Both missions have similar Ultraviolet instruments built by SwRI (Southwest Research Institute). These are Europa UVS and JUICE UVS. These instruments have plans to observe the Io plasma torus and my model is integral to their observation planning and model development.

4.2 Emission Model

The UV emissions from the Io plasma torus are spontaneous emissions resulting from forbidden transitions due to electron impact excitation of sulfur and oxygen ions that make up the torus. The primary ions in the Io plasma torus are S^{+}, S^{2+}, S^{3+}, O^{+}, and O^{++}, with an additional $\approx$ 10% protons [5]. There are also minor amounts of SO_2^{+}, SO^{+}, and possibly O_2^{+} (Bodisch et al. 2017 ; Dols & Johnson 2020) [16][45]. Which we ignore since they are likely confined close to Io.

I simulate a spectrum in the following way. I calculate the brightness of a particular emission line in Rayleighs as [99][96][138][137] [120] [123]

$$B = 10^{-6} \int A_{ji} f_j \left(T_e, n_e\right) n_{ion} dl \tag{4.1}$$

With the integral over the line of sight of the observation with a Rayleigh defined by

$$1 \text{ Rayleigh} = \frac{10^6}{4\pi} \frac{\text{Photons}}{\text{cm}^2 \text{s} \left(\text{str}\right)} \tag{4.2}$$

Which is the photon flux per solid angle.

Then I treat each discrete emission found by equation 4.1 as a normalized Gaussian at the FWHM of the instrument and add them all up to simulate a spectrum. A_{ji} is the Einstein A coefficient for spontaneous emission if state j is at a higher energy than state i and zero otherwise. This is sometimes referred to as the radiative decay rate for the transition. $f_j \left(T_e, n_e\right)$ is the fraction of ions in the upper emitting state j. T_e is the electron temperature, n_e is the electron number density, and n_{ion} is the ion number density (cm^{-3}) of the species causing the emission. Where the integral is over the line of sight of the observer. The level populations (or the fraction of the ions

in the upper emitting state), $f_j\left(T_e, n_e\right)$, are determined by solving the level balance equations for each ion species in the following matrix form (Steffl et al. (2004b))[137]

$$\hat{\boldsymbol{C}}\boldsymbol{f} = \boldsymbol{b} \tag{4.3}$$

Where $\boldsymbol{f}$ is a vector containing the fraction of ions in a particular energy state, relative to the ground state; $\boldsymbol{b}$ is a vector whose elements are all zero except for the first element, which is equal to one; and $\hat{\boldsymbol{C}}$ is a matrix containing the rates for collisional excitation and de-excitation and radiative de-excitation. The elements of this matrix are given by

$$\hat{C}_{ij} = A_{ij} + n_e q_{ij} \tag{4.4}$$

where q_{ij} is the velocity distribution function averaged reaction rate coefficient for collisional excitation (or de-excitation) from state i to state j and is given by

$$q_{ij} = \int_0^\infty 4\pi u^2 P\left(u\right) u \sigma_{ij} du \tag{4.5}$$

Where $P\left(u\right)$is the normalized velocity distribution function, u is the electron velocity, and σ_{ij} is the cross-section for the transition from state i to state j. Once the level balance equations have been solved, the level populations vector, $\boldsymbol{f}$, is re-normalized so that the sum of its elements is equal to one.

To simulate these UV spectra, one must assume an electron velocity distribution to calculate the occupancy of the upper emitting state by solving the level balance equations. The assumption of thermal equilibrium is not valid when the equilibration timescale due to Coulomb collisions is longer than the time scale that the hot electrons are added into the system. In this low density, optically thin environment equilibration is not ensured locally. The Voyager in situ plasma measurements from the Plasma Science (PLS) instrument provided key measurements of electron density and temperature, including evidence of a suprathermal component [118] [128]. These in situ

measurements of the plasma have implied that the distribution is empirically a Kappa distribution which is modeled well by a core thermal population with a small hot electron component that leads to a core Maxwellian plus a power law tail at higher energies which in Nerney et al. (2020) [95] (Chapter 3) we approximated as a core plus a hot component. The kappa distribution was first used to describe an empirical non-thermal velocity distribution by Vasyliunas et al. (1968) [152]. Steffl et al. (2004b) [137] approximated a Kappa as a sum of 5 Maxwellians using CHIANTI and found little difference in the determined composition.

If the electrons are distributed according to Maxwell-Boltzmann statistics then we have the Maxwellian velocity distribution. From non-extensive statistical mechanics and thermodynamics, it can be shown that stationary states out of thermal equilibrium lead to a kappa distribution. One method of deriving the Maxwellian velocity distribution is by following the Gibbs path. This is achieved by maximizing the Boltzmann-Gibbs entropy given the constraints of the Canonical ensemble. The same can be done with the kappa distribution of velocities. The kappa distribution can be obtained by maximizing the generalized entropy of non-extensive statistical mechanics. This is called Tsallis entropy and is parametrized by the q-index [148].

We take the discrete Rayleighs simulated via equation 4.1 and use a Gaussian response function to match the point spread function of the instrument at the given FWHM of the instrument. We produce a synthetic spectrum treating each count at a discrete wavelength as a normalized Gaussian and add up all emissions then integrate the Gaussians over each spectral bin width to determine how many Rayleighs fall into each bin and then divide by bin width to find Rayleighs/Angstrom in each spectral bin.

Instead of actually doing the integral of the Gaussians over each bin each time we take advantage of its known form and use look-up tables for error functions. This is because

A normalized Gaussian as a function of wavelength λ with a standard deviation in wavelength (σ) centered at a discrete wavelength λ_i is given by

$$f(\lambda) = \frac{1}{\sigma\sqrt{2\pi}} \exp\left(-\frac{(\lambda - \lambda_i)^2}{2\sigma^2}\right) \tag{4.6}$$

Converting to full width half maximum (FWHM) we have FWHM $= 2\sqrt{2\ln 2}\sigma$ or $\sigma = \frac{\text{FWHM}}{2\sqrt{2\ln 2}}$

Integrating this over a single bin in wavelength from A to B gives us

$$\frac{1}{\sigma\sqrt{2\pi}} \int_A^B \exp\left(-\frac{(\lambda - \lambda_i)^2}{2\sigma^2}\right) d\lambda \tag{4.7}$$

Making the substitution $x = \lambda - \lambda_i$ then $dx = d\lambda$ and the limits of integration go from p =B - λ_i to q = A - λ_i so we have the following integral to do

$$\left(\frac{c}{\pi}\right)^{1/2} \int_p^q e^{-cx^2} dx = \frac{1}{2}\left(\text{erf}\left(q\sqrt{c}\right) - \text{erf}\left(p\sqrt{c}\right)\right) \tag{4.8}$$

This is done over each bin for each discrete emission and then we sum them all up to find the contribution to each bin.

4.3 "Cubic Centimeter" Emission Model

In Nerney et al. (2017) and (2020) [96] [95] and following from Steffl et al. (2004b) [137] looking at the warm torus emission outside the peak emission and density we made the assumption that the distribution function was constant over the line of sight. This is because finding the value of the integral from equation 4.1 requires knowledge of how the ion and electron density in addition to the electron temperature and thus the electron velocity distribution vary over the line of sight. These quantities are exactly what we are trying to determine via our modeling. The dependence can be used to determine the local torus electron density (Feldman et al., 2001, 2004) [52][53].

The spectral resolution of Cassini UVIS (the highest resolution UV instrument to ever view the IPT) is insufficient to resolve the density-sensitive multiplet structure present in the torus

spectra. Therefore torus spectra are effectively independent of the local electron density. Which lead us to use a "cubic centimeter" spectral emission model. This is why we made the assumption that the electron distribution function of the torus is uniform over the line of sight. The observed brightness gradient of the torus falls off sharply with radial distance outside the orbit of Io (Brown, 1994) [23]. Also, the typical view of the torus from the ansa reduces the path length through the torus and we are biased to the peak emission because this is where the area under the curve or integral is largest.

This assumption breaks down when viewing inside the peak of density and emission. This is why projection effects become extremely important when dealing with emission ribbon and cold torus inwards of the orbit of Io at 5.9 R_J. The assumption of a uniform electron distribution over the line of sight means we are now fitting ion column densities instead of local densities. Equation 4.1 then becomes

$$B = 10^{-6} A_{ji} f_j \left(T_e, n_e\right) \int n_{ion} dl = 10^{-6} A_{ji} f_j \left(T_e, n_e\right) N_{ion} \tag{4.9}$$

With

$$N_{ion} = \int n_{ion} dl \tag{4.10}$$

With N_{ion} in units of cm^{-2} and n_{ion} in units of cm^{-3}. With N_{ion}/n_{ion} being the effective path length of the observation.

4.4 Colorado Io Torus Emission Package 2 (CITEP 2)

We pay homage to the original Colorado Io Torus Emission Package 1 (CITEP 1) written and discussed in Taylor (1996) [142].

The brightness of an emission line is given by (Steffl et al. 2004b) [137]

$$B = 10^{-6} \int A_{ji} f_j \left(T_e, n_e\right) n_{ion} dL \text{ Rayleighs} \tag{4.11}$$

The integral is over the line of sight so we need to know the electron density & temperature as well as the ion density at every point along the line of sight.

In 3d the equation for a line is given by:

$$\begin{bmatrix} x \\ y \\ z \end{bmatrix} = \begin{bmatrix} x_0 \\ y_0 \\ z_0 \end{bmatrix} + s \begin{bmatrix} a \\ b \\ c \end{bmatrix} \tag{4.12}$$

We will work in Joviagraphic Cartesian coordinates which has the origin at the center of Jupiter and the x-y plane rotational equator. Where (x,y,z) are the positions of every point along the line for a line going through the point (x_0, y_0, z_0) that is parallel to the vector with components (a,b,c). The value of s parameterizes where on the line you are. For s>0 you go in the direction the vector (a,b,c) is pointing and opposite that for s<0. If you let $-\infty \leq s \leq \infty$ then you will get all of the line.

A line integral in 3d along a parameterized path $\boldsymbol{r}\left(s\right) = \begin{bmatrix} x\left(s\right) \\ y\left(s\right) \\ z\left(s\right) \end{bmatrix}$ is given by

$$\int f\left(x,y,z\right) dL = \int f\left(x\left(s\right), y\left(s\right), z\left(s\right)\right) \sqrt{\left[\frac{dx}{ds}\right]^2 + \left[\frac{dy}{ds}\right]^2 + \left[\frac{dz}{ds}\right]^2} ds \tag{4.13}$$

For the path along the equation of a line given by equation 2 we have $\sqrt{\left[\frac{dx}{ds}\right]^2 + \left[\frac{dy}{ds}\right]^2 + \left[\frac{dz}{ds}\right]^2} = \sqrt{a^2 + b^2 + c^2}$

Which gives us

$$\int f\left(x,y,z\right) dL = \int f\left(x\left(s\right), y\left(s\right), z\left(s\right)\right) \sqrt{a^2 + b^2 + c^2} ds \tag{4.14}$$

The normal vector to the slit or the pointing will give us the value of (a,b,c). Each spatial pixel on the slit has a central position (x_0, y_0, z_0) that we will approximate the line of sight as going through (as a first step instead of properly averaging for the different line of sights hitting each individual pixel due to the finite slit width).

So for a given pixel position in 3D space and the normal vector of the slit (from the pointing of the spacecraft), we have the (x,y,z) positions of every point along the line of sight. Using these and a model of the electron temperature and electron and Ion density we can now calculate the volume emission rate at every point along the line of sight.

For (a,b,c) being a normalized vector we know $\sqrt{a^2 + b^2 + c^2} = 1$. We will integrate from the slit position (s=0) to the largest s value along the line of sight with as non-zero density and temperature which we will define as s_f or s final. This will define the outer edge of the torus. If the slit is outside the torus, then we do not need to start at s=0 because there will be no contribution till the line of sight intersects the torus. So there will be an s_m or minimum s value along the line of sight with non-zero density and temperatures which will give a non-zero volume emission rate. This will define the inner edge of the torus.

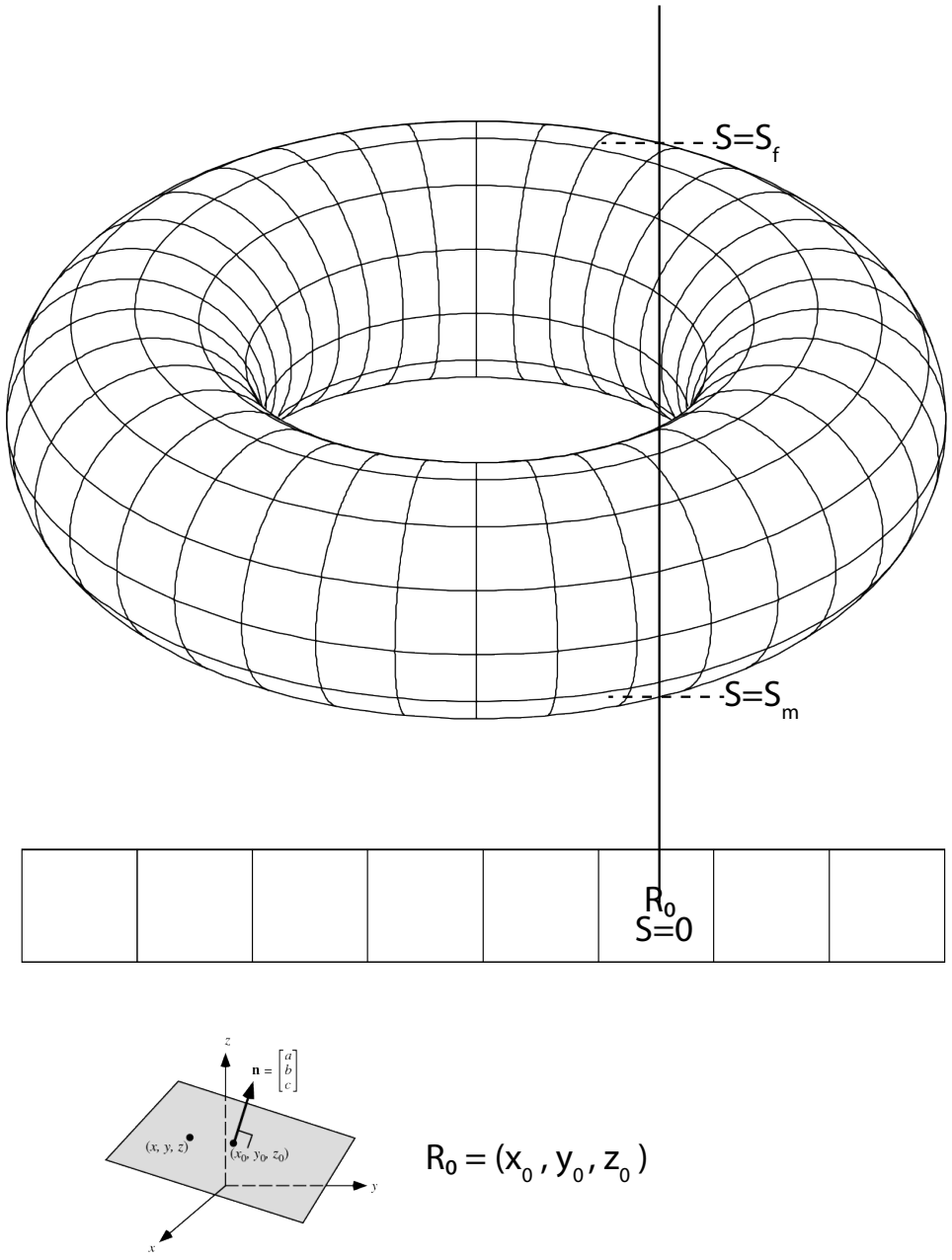

Figure 4.1: CITEP2 Line of Sight (LOS) Diagram

We define the volume emission rate as

$$\epsilon(x,y,z) = \epsilon(x(s), y(s), z(s)) \tag{4.15}$$

$$= 10^{-6} A_{ji} f_j \left(T_e(x(s), y(s), z(s)), n_e(x(s), y(s), z(s))\right) n_{ion}(x(s), y(s), z(s)) \tag{4.16}$$

This gives us the following integral to compute

$$B = \int_{x_m,y_m,z_m}^{x_f,y_f,z_f} \epsilon\left(x,y,z\right) dL = \int_{s=s_m}^{s=s_f} \epsilon\left(x\left(s\right),y\left(s\right),z\left(s\right)\right) ds \text{ Rayleighs} \tag{4.17}$$

Given a density and temperature model in 3d space the program uses an input grid of x, y, and z values and given the position of the slit pixel (x_0, y_0, z_0) and pointing of the slit (a, b, c) it finds the max and min values of s along the line of sight that parameterize the line of sight and determine where on the spatial grid to compute volume emission rates.

$$s_f = \frac{(x_f - x_0)}{a} = \frac{(y_f - y_0)}{b} = \frac{(z_f - z_0)}{c} \tag{4.18}$$

$$s_m = \frac{(x_m - x_0)}{a} = \frac{(y_m - y_0)}{b} = \frac{(z_m - z_0)}{c} \tag{4.19}$$

Once the model calculates the brightness of each spectral line in Rayleighs (at each discrete wavelength center for each transition in the input wavelength range) the model treats each discrete emission as a normalized Gaussian and adds up all the Gaussians to create a simulated spectra at the input full width half max (FWHM) of the response function of the instrument. Then given a wavelength pixel center array and the bin widths of each pixel center the model numerically integrates over the Gaussian representation over each bin to simulate the number of counts due to the Gaussian that fall within each pixel wavelength range. The current number of samples over each bin is 10 for the numerical integral which seems to be sufficient but can be varied as an optional input. After the model determines the number of Rayleigh that fall into each wavelength bin the model divides each wavelength bin by the bin width in Angstrom (Å) which puts the model output in Rayleighs/Å.

4.5 Cassini based 3D Torus Model for CITEP 2

We fit the density and temperatures from Steffl 2004b [137] to find equatorial ion and electron density values as well as electron temperatures. For a first model run we will assume the torus equator is the same as the Joviagrpahic equator. The model will work as long as you provide the densities and temperatures in Joviagraphic coordinates though whatever they may be.

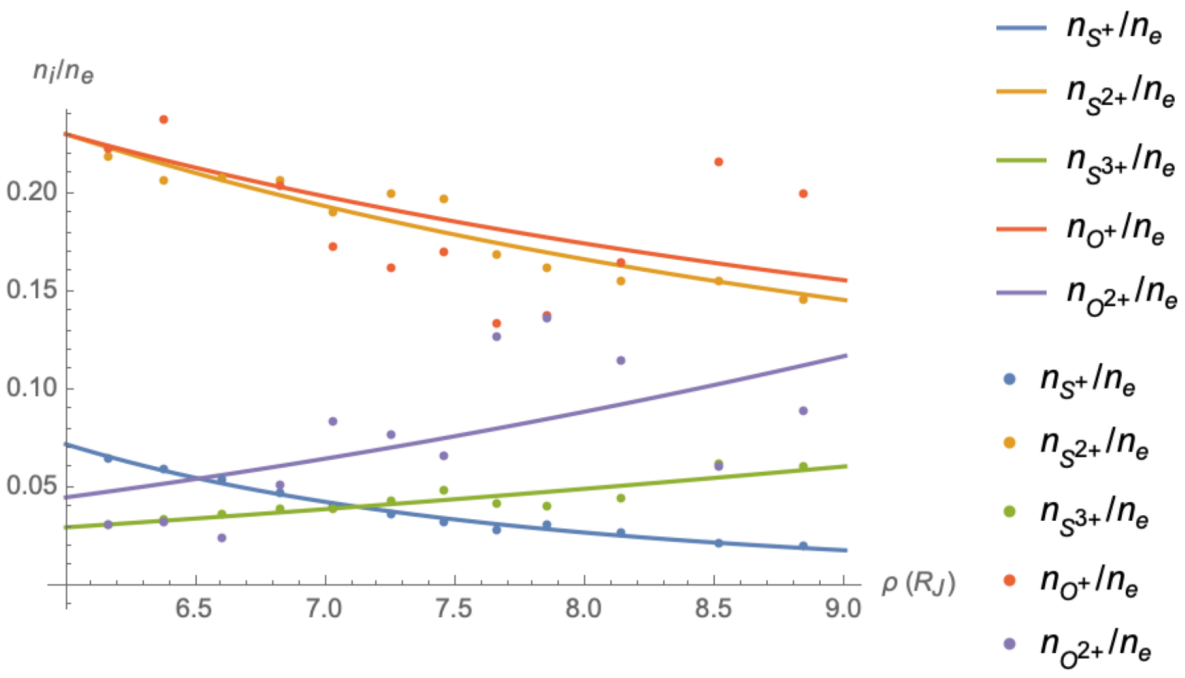

Figure 4.2: Cassini power law fits in solid lines and fit values as points from Steffl et al. (2004b) [137]

We use quasi-neutrality at each spatial bin to find the electron density assuming protons at the 10% level. Taking the ion cylindrical radial temperature profiles from Delamere et al. (2005) [40] we fit them between 6-9 R_J using 4th order polynomials and find the following fits which we extrapolate out to 10 R_J.

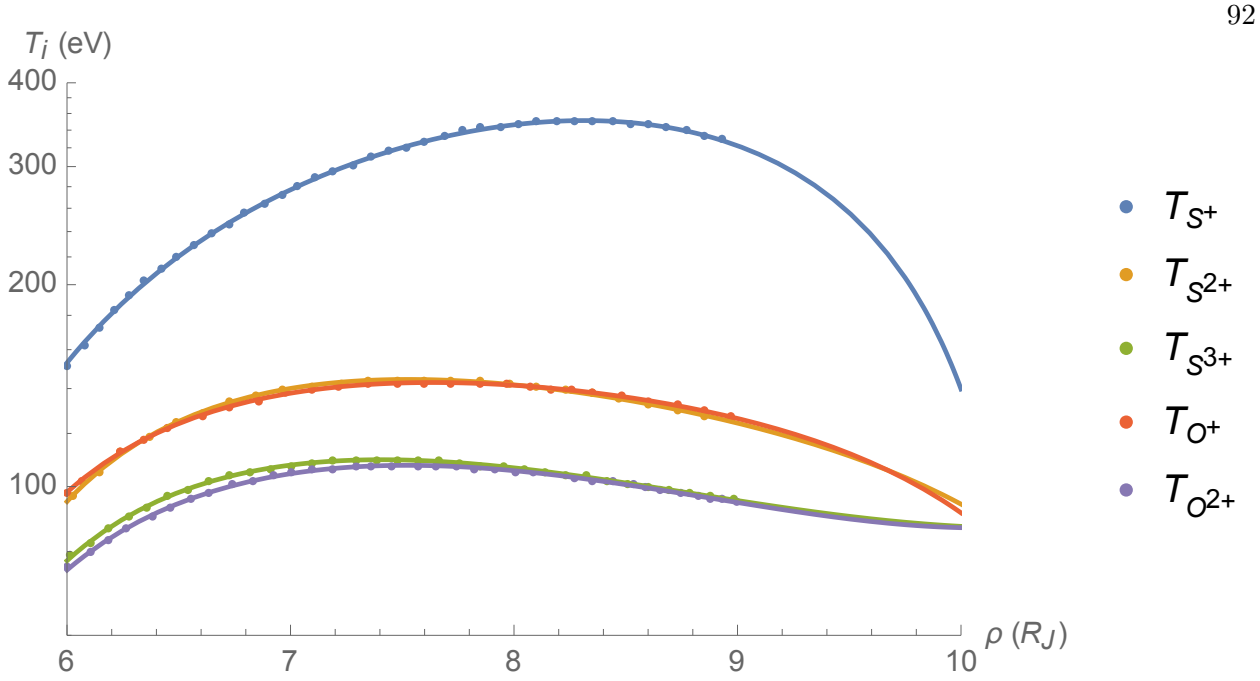

Figure 4.3: Delamere et al. (2005) Radial Temperature Profiles

Using our electron and ion radial temperature profiles and Gaussian scale height equation from pg. 11,049 of Bagenal (1994) [5] we compute the following ion scale heights. Assuming charge neutrality at all z values and assuming a proton mixing ratio of 0.1 we compute the electron scale height.

$$n_{0e}e^{-\left(\frac{z}{H_e}\right)^2} = \frac{\sum_i Z_i n_{0i} e^{-\left(\frac{z}{H_i}\right)^2}}{0.9} \tag{4.20}$$

with $\sum_i Z_i n_{0i} e^{-\left(\frac{z}{H_i}\right)^2}$ summing over all ions for a given charge number Z_i is given by

$$n_{0S^+}e^{-\left(\frac{z}{H_{S^+}}\right)^2} + 2n_{0S^{2+}}e^{-\left(\frac{z}{H_{S^{2+}}}\right)^2} + 3n_{0S^{3+}}e^{-\left(\frac{z}{H_{S^{3+}}}\right)^2} + n_{0O^+}e^{-\left(\frac{z}{H_{O^+}}\right)^2} + 2n_{0O^{2+}}e^{-\left(\frac{z}{H_{O^{2+}}}\right)^2} \tag{4.21}$$

Plugging in $z = 1\ R_J$ and solving for H_e we have

$$H_e = \frac{1}{A^{1/2}} \tag{4.22}$$

With

$$A = -\ln\left(\frac{n_{0S^+}e^{-\left(\frac{1}{H_{S^+}}\right)^2} + 2n_{0S^{++}}e^{-\left(\frac{1}{H_{S^{++}}}\right)^2} + 3n_{0S^{3+}}e^{-\left(\frac{1}{H_{S^{3+}}}\right)^2} + n_{0O^+}e^{-\left(\frac{1}{H_{O^+}}\right)^2} + n_{0O^{++}}e^{-\left(\frac{1}{H_{O^{++}}}\right)^2}}{0.9n_{0e}}\right) \tag{4.23}$$

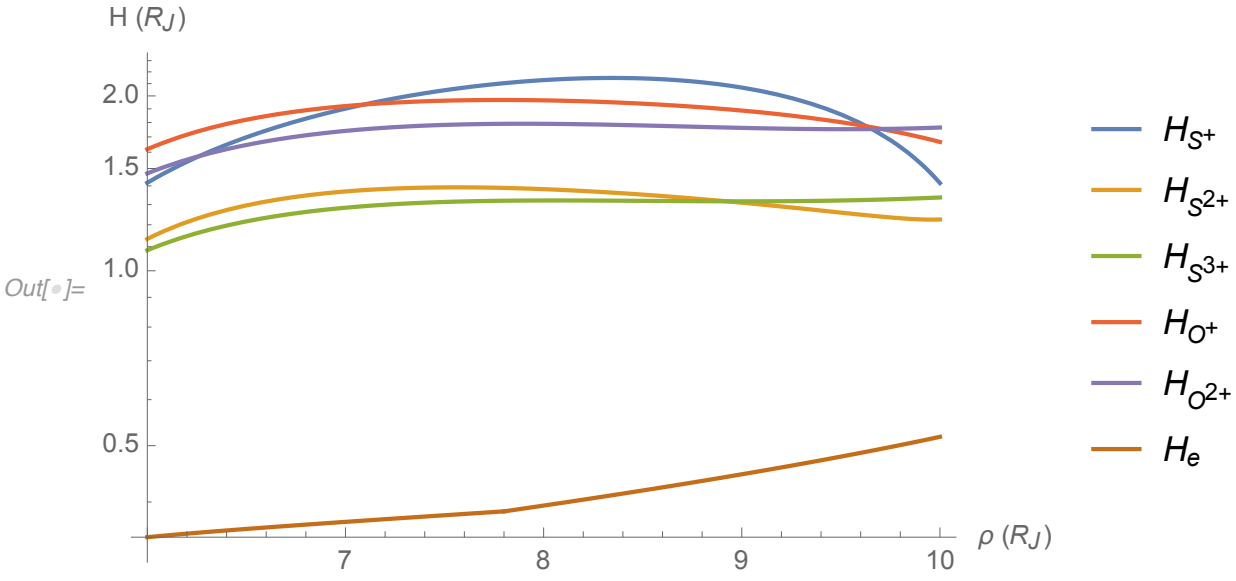

Figure 4.4: Scale heights given by Delamere et al. (2005) Radial Temperature Profiles

Using these power law functional forms for equatorial values of densities, scale height distributions for the distance along the field line, that the temperatures along the field lines are constant (which is true for a Maxwellian), and we are also assuming that the distance along the field line is the same as the z distribution (for a dipole near the equator this is approximately correct) this gives us our 3d model of temperatures densities to integrate over any line of sight (LOS).

Future 3D models will include a cold torus, azimuthal variability, diffusive equilibrium to compute the distribution along the field lines, and will offset the torus equator from the Joviagraphic equator.

4.6 Model Output

4.6.1 1st Model Run

For our first model run we will use $x_0 = 6\ R_J$, $y_0 = -10\ R_J$, and $z_0 = 0\ R_J$. Our normal vector to the slit will $a = 0$, $b = 1$, and $c = 0$ which is pointing in the positive $\hat{\mathbf{y}}$ direction. So our line of sight will be confined to the x-y plane. We will define a numerical grid on -10 to 10 R_J in x and y. For z we will only compute a grid between -4 to 4 R_J as the scale heights are all less than about 2 R_J so the density will rapidly fall off as a function of z. We use a spatial stepsize of 0.1 R_J for the x, y, and z grids.

We will use to Cassini UVIS EUV and FUV spectral resolution (FWHM=3 Å). The EUV channel wavelength range is 550-1150 Å with a bin size of 0.6049 Å. The FUV channel wavelength range is 1150-1800 Å with a bin size of 0.7794 Å. The model is computed for both of these ranges and bin sizes and then artificially put together. Comparing our model output (in red) for viewing a minimum radial value of 6 R_J with a Cassini UVIS spectrum (in black) from 6 R_J we find figure 4.5. Our model (in red) does not match this Cassini UVIS spectrum (in black) from 6 R_J using the Steffl et al. (2004b) [137] radial profiles.

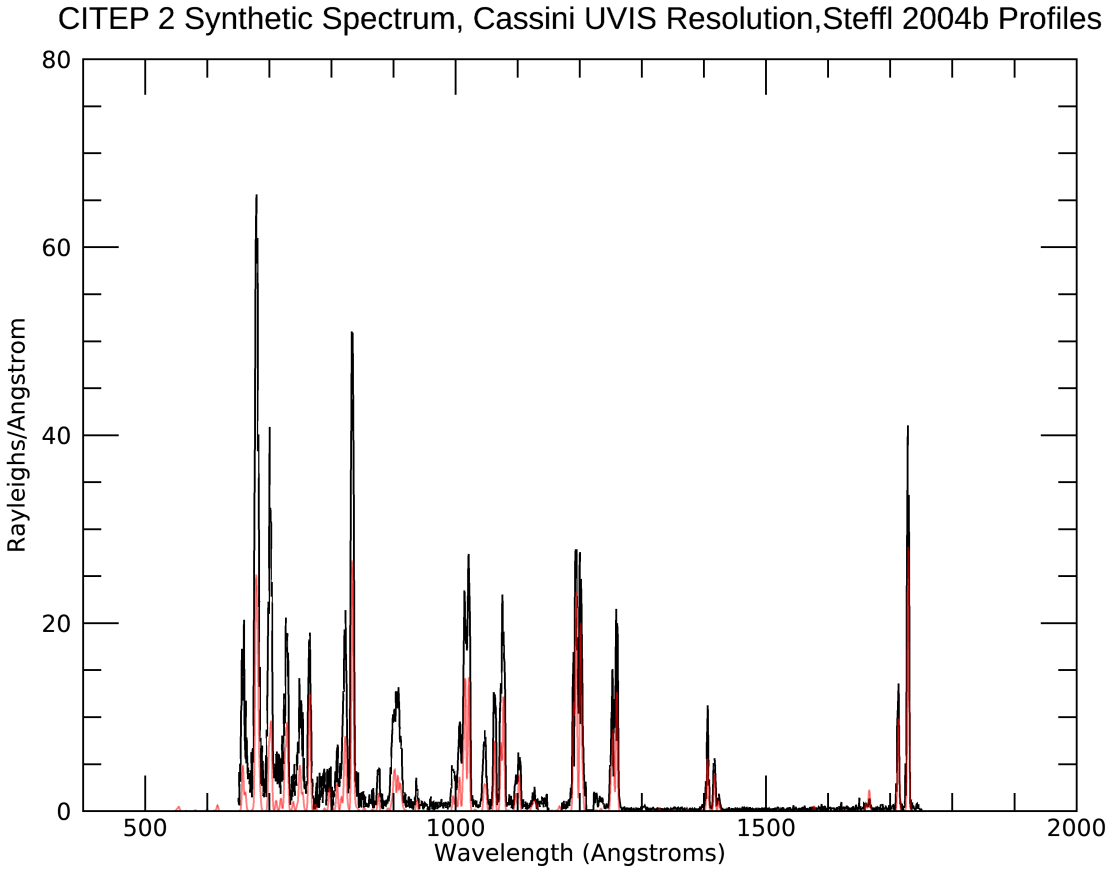

Figure 4.5: Model Output for Cassini UVIS wavelength range and composition from CITEP 2

The total density for our model over the line of sight is clearly too small to match the UVIS spectrum. To fix this we could increase the value at 6 R_J or decrease the steepness of the radial decline. The Steffl et al. (2004b) [137] electron density profile is

$$n_e = 2200(\rho/6)^{-5.4}\ \mathrm{cm}^{-3} \qquad 6\ \mathrm{R}_J \leq \rho \leq 7.8\ \mathrm{R}_J \tag{4.24}$$

$$n_e = 400(\rho/8)^{-12}\ \mathrm{cm}^{-3} \qquad 7.8\ \mathrm{R}_J \leq \rho \leq 10\ \mathrm{R}_J \tag{4.25}$$

This is actually not continuous at $\rho = 7.8\ R_J$ (only a slight jump 542 vs 533.49 cm^{-3}) so instead we use

$$n_e = 2200(\rho/6)^{-5.4}\ \text{cm}^{-3} \qquad 6\ \text{R}_J \leq \rho \leq 7.8\ \text{R}_J \tag{4.26}$$

$$n_e = 533.49(\rho/7.8)^{-12}\ \text{cm}^{-3} \qquad 7.8\ \text{R}_J \leq \rho \leq 10\ \text{R}_J \tag{4.27}$$

Which is continuous at $\rho = 7.8\ R_J$

4.6.2 Increased Density Model Run

We now increase the value of the total electron density at 6 R_J to 3000 cm^{-3} instead of 2200 cm^{-3} and leave the mixing ratios and temperature profiles the same.

$$n_e = 3000(\rho/6)^{-5.4}\ \text{cm}^{-3} \qquad 6\ \text{R}_J \leq \rho \leq 7.8\ \text{R}_J \tag{4.28}$$

$$n_e = 727.49(\rho/7.8)^{-12}\ \text{cm}^{-3} \qquad 7.8\ \text{R}_J \leq \rho \leq 10\ \text{R}_J \tag{4.29}$$

Comparing our model output (in red) for viewing a minimum radial value of 6 R_J with a Cassini UVIS spectrum (in black) from 6 R_J we find figure 4.6. This gives us a better overall intensity match though the exact match in lines is still quite off.

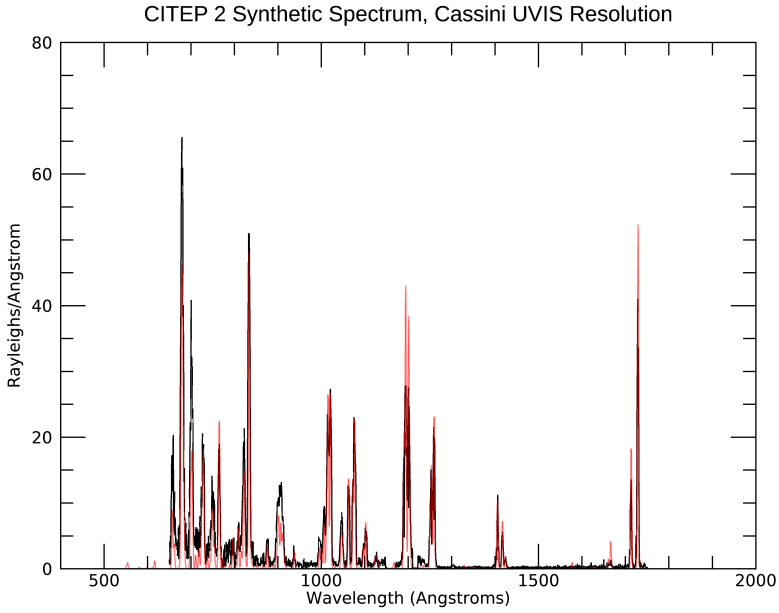

Figure 4.6: Increased density model Output for Cassini UVIS wavelength range and composition from CITEP 2

The model used in Steffl et al. (2004b) [138] is a cubic cm spectral emission model with a geometrically determined line of sight (LOS) for each radial point so the fit composition and temperature values at each radial value are determined independently instead of integrating over the whole line of sight at once. We are using CHIANTI 9 while Steffl et al. (2004b) [138] used CHIANTI 4.3 though Nerney et al. (2017) [96] found similar composition to Steffl et al. (2004b) [137].

4.6.3 Constant Torus Radial Scan

We now define a constant torus between 6-10 R_J. We use $T_e = 5$ eV , $n_e = 2200$ cm^{-3} , $n_{S^+} = 0.06 \times 2200$ cm^{-3}, $n_{S^{2+}} = 0.21 \times 2200$ cm^{-3}, $n_{S^{3+}} = 0.03 \times 2200$ cm^{-3} , $n_{O^+} = 0.26 \times 2200$ cm^{-3}, and $n_{O^{2+}} = 0.03 \times 2200$ cm^{-3}. A wavelength range between 600-1800 Å and a wavelength bin size of 1 Å.

We vary the value of the x position of the center of the slit (x_0) from 4-10 R_J (in increments

of 0.1 R_J consistent with our numerical spatial step size of the spatial grids) and keep the y and z values fixed at ($y_0 = -10$ R$_\mathrm{J}$ and $z_0 = 0$ R$_\mathrm{J}$). We also fix the normal vector or pointing of the slit to always be in the positive $\hat{\mathbf{y}}$ direction. Due to our model being azimuthally symmetric this is equivalent to an equatorial radial view of the constant torus. We then sum the total Rayleighs/Å in the wavelength range and plot this value from x_0 is 4-10 R_J. We find figure 4.7 This is the expected shape and a good check of the constant finite torus model.

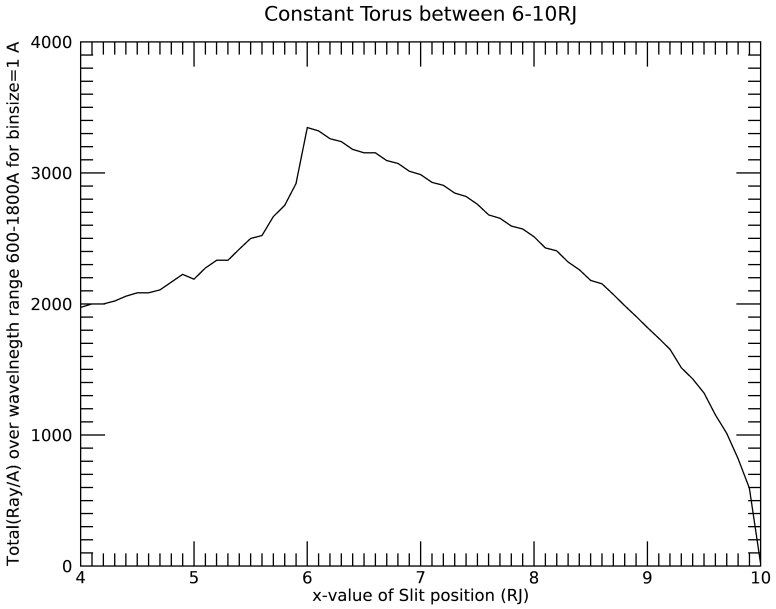

Figure 4.7: Constant torus radial scan test

4.6.4 Increased Density Model Scans

Again using the increased density model from section 3.2 with $n_e = 3000$ cm^{-3} at 6 R_J. We again vary x_0 from 4-10 R_J in increments of 0.1 R_J and keep the y and z values of the slit fixed at ($y_0 = -10$ R$_\mathrm{J}$ and $z_0 = 0$ R$_\mathrm{J}$) with the normal vector or pointing of the slit always in the positive $\hat{\mathbf{y}}$ direction. This is equivalent to a slit aligned parallel to the x-axis of the torus with a spatial pixel bin size of 0.1 R_J. Due to our model being azimuthally symmetric this is equivalent

to an equatorial radial view of the torus. We use a wavelength range between 600-1800 Å and a wavelength bin size of 1 Å. We plot the simulated spectrogram and also sum over the wavelength range to again plot the total Rayleighs/Å as a function of the x value of the slit position across the torus.

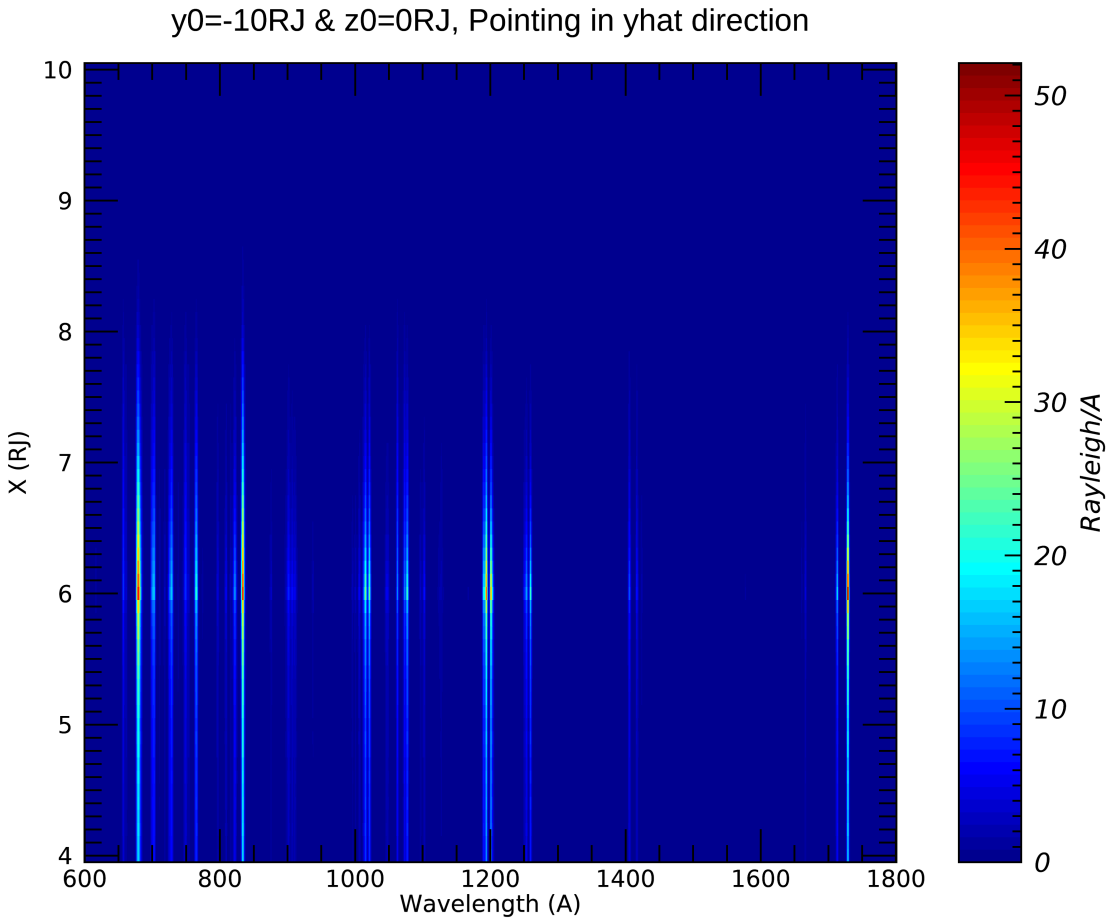

Figure 4.8: 2D spectrogram increased Cassini density model CITEP 2 output

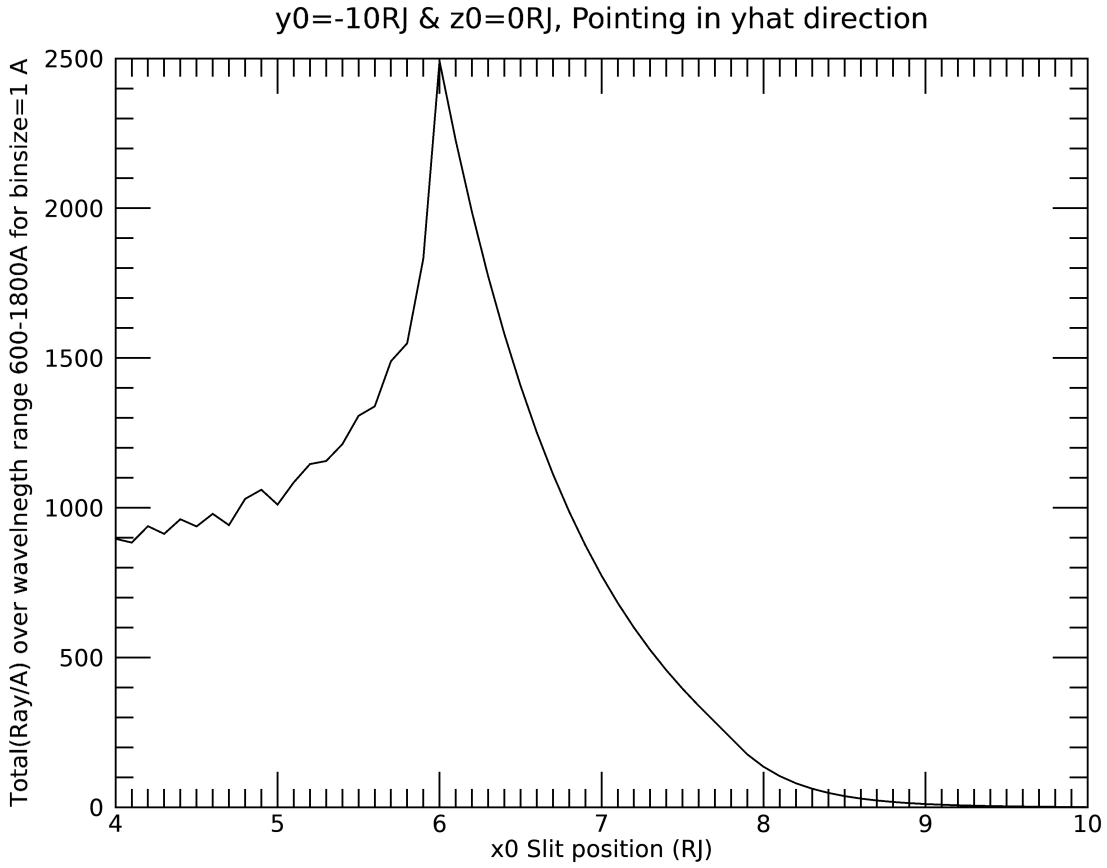

Figure 4.9: Centrifugal equator intensity profile increased density model CITEP 2 Output

Now we do the same for varying z_0 from -4 to 4 R_J while keeping $x_0 = 6\ R_J$ and $y_0 = -10\ R_J$ with the pointing always in the positive $\hat{\boldsymbol{y}}$ direction. This is equivalent to aligning the slit parallel to the z-axis of the torus with its normal in the $\hat{\boldsymbol{y}}$ direction and the center of each spatial pixel having a value of $x_0 = 6\ R_J$ and $y_0 = -10\ R_J$ and spatial pixel bin size of 0.1 R_J. In this case, we are looking at the torus with a side on view.

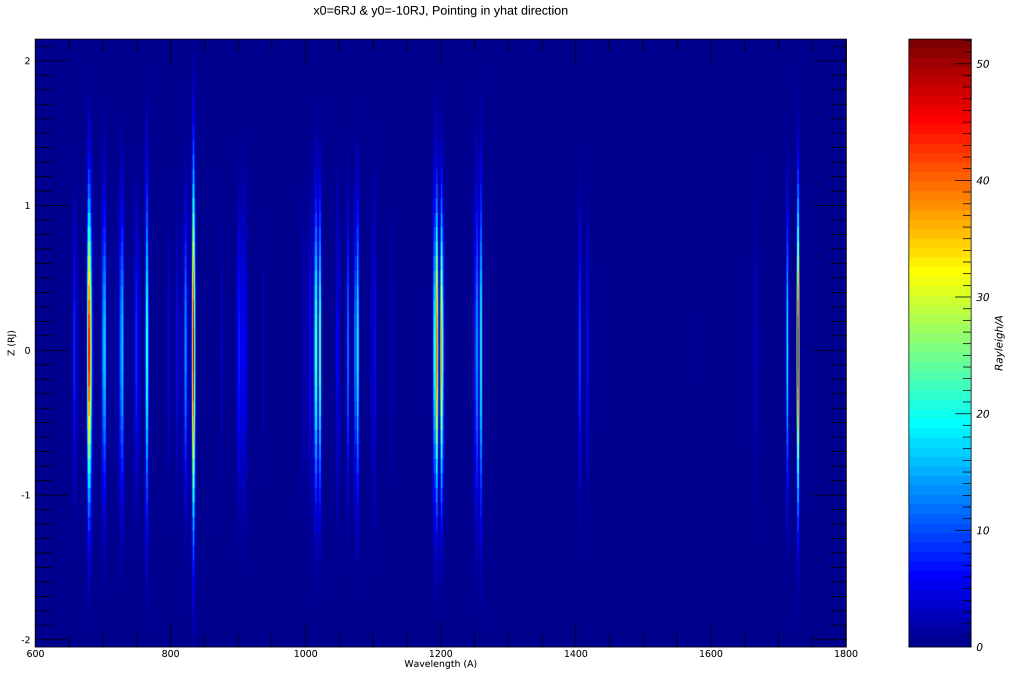

Figure 4.10: 2D spectrogram CITEP 2 Model Output increased density Cassini model vertically aligned slit

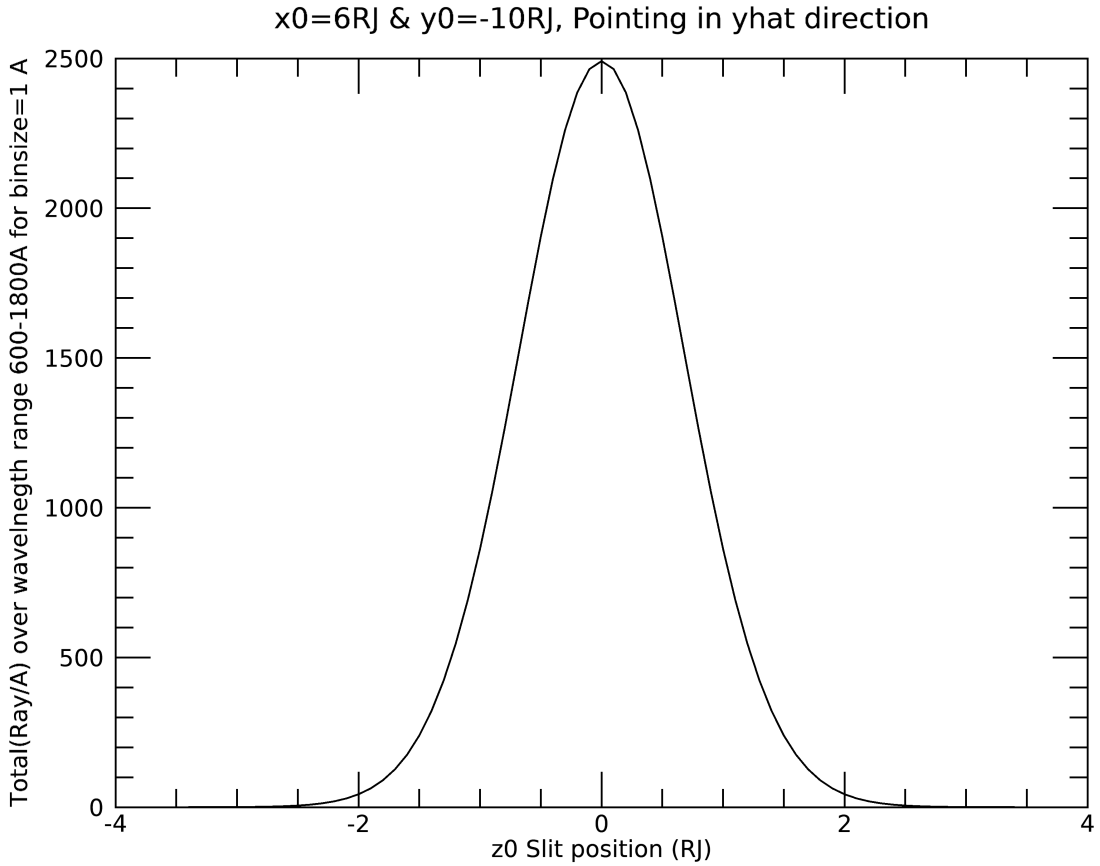

Figure 4.11: Vertical distribution intensity model output Increased density Cassini CITEP 2 Output

Continuing with our Cassini-based model we now explore different geometries for observations. Looking down on torus from above at z=4 R_J, pointing in the -$\hat{z}$ direction for finite Cassini-based azimuthally symmetric torus model for 6 $\leq$ r $\leq$ 10 RJ. We vary x & y position of slit center from -10 to 10 R_J for dx & dy=0.25 R_J and we sum the emission over the wavelengths 550-2100 Å (JUICE/Clipper range). This gives us figure 4.12

The model works for any viewing geometry and 3D distribution of plasma. In the next case in figure 4.12, we are looking down through the torus from 4 R_J above the equator. Summing over all wavelengths gives an intensity view of the torus using a 2D density and temperature model based

on our Cassini reanalysis [96]. We can sum over particular wavelength ranges and for different geometries given and 3d distribution of plasma.

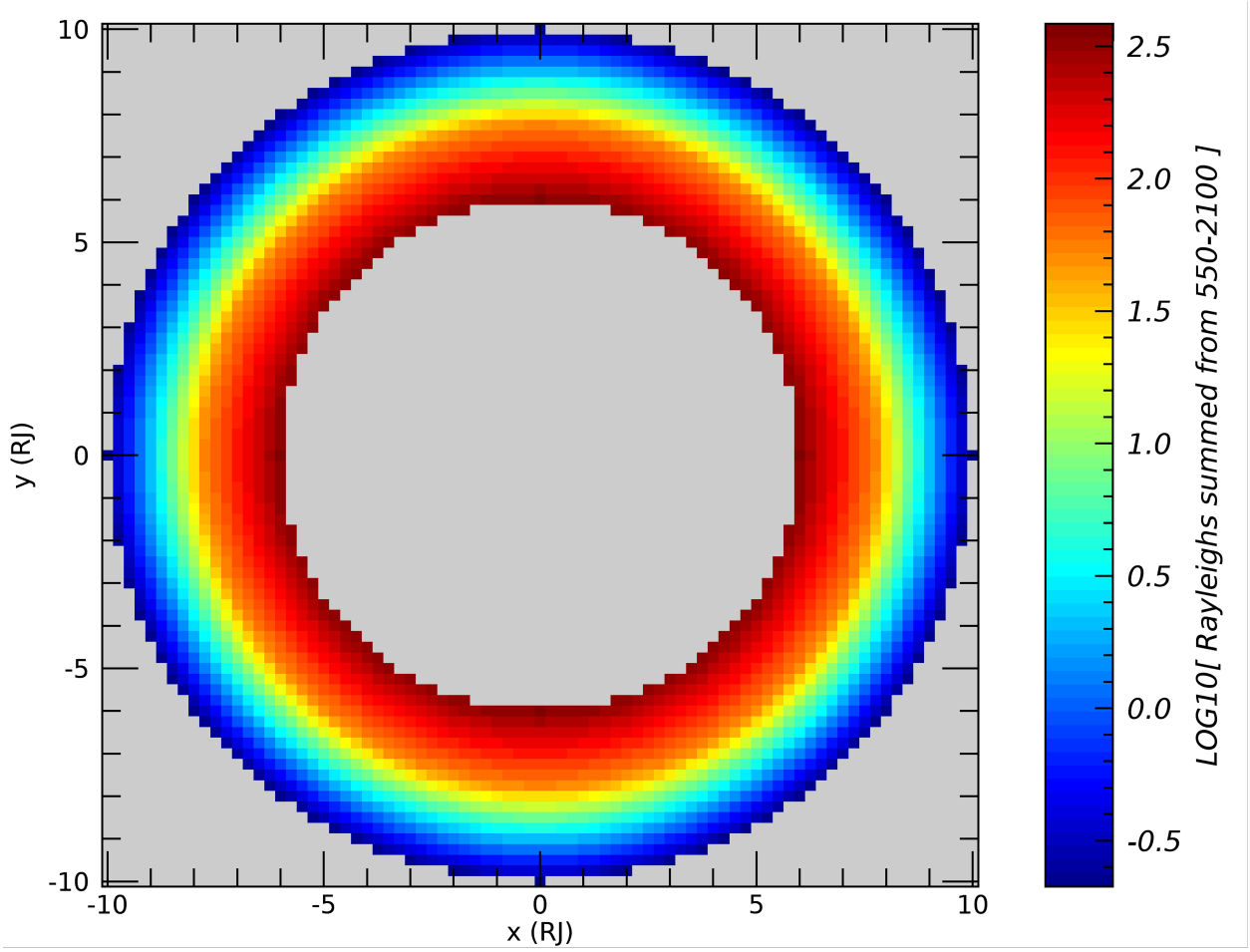

Figure 4.12: Cassini Model CITEP 2 view from 4 R_J above the torus for a 6 to 10 R_J finite torus

In figure 4.13 we view the torus from the side at 10 R_J away from the center of the torus. The observer is at y=-10 R_J and pointing in the $\hat{y}$ direction while we vary x and z for each pixel's view. In figure 4.13 and from here on out for plotting purposes we have assumed that the distance along a dipole magnetic field line is the same as the cartesian z. With maximum scale heights or e-folding distances along a field line for density being about 1 R_J this assumption has little effect on the results because in the region between L= 5 to 10 R_J the field lines are approximately vertical

over $\pm$ 1 R_J as can be seen in figure 4.14. In the warm torus, it is ok to use a tilted dipole due to it being farther from Jupiter the higher order moments falling off faster than the dipoles $1/r^3$. But for the closer in cold torus where the scale height is small, the effects of higher-order complexity would need to be considered (discussed in Bagenal (1994); Bagenal & Dols (2020))[5] [7].

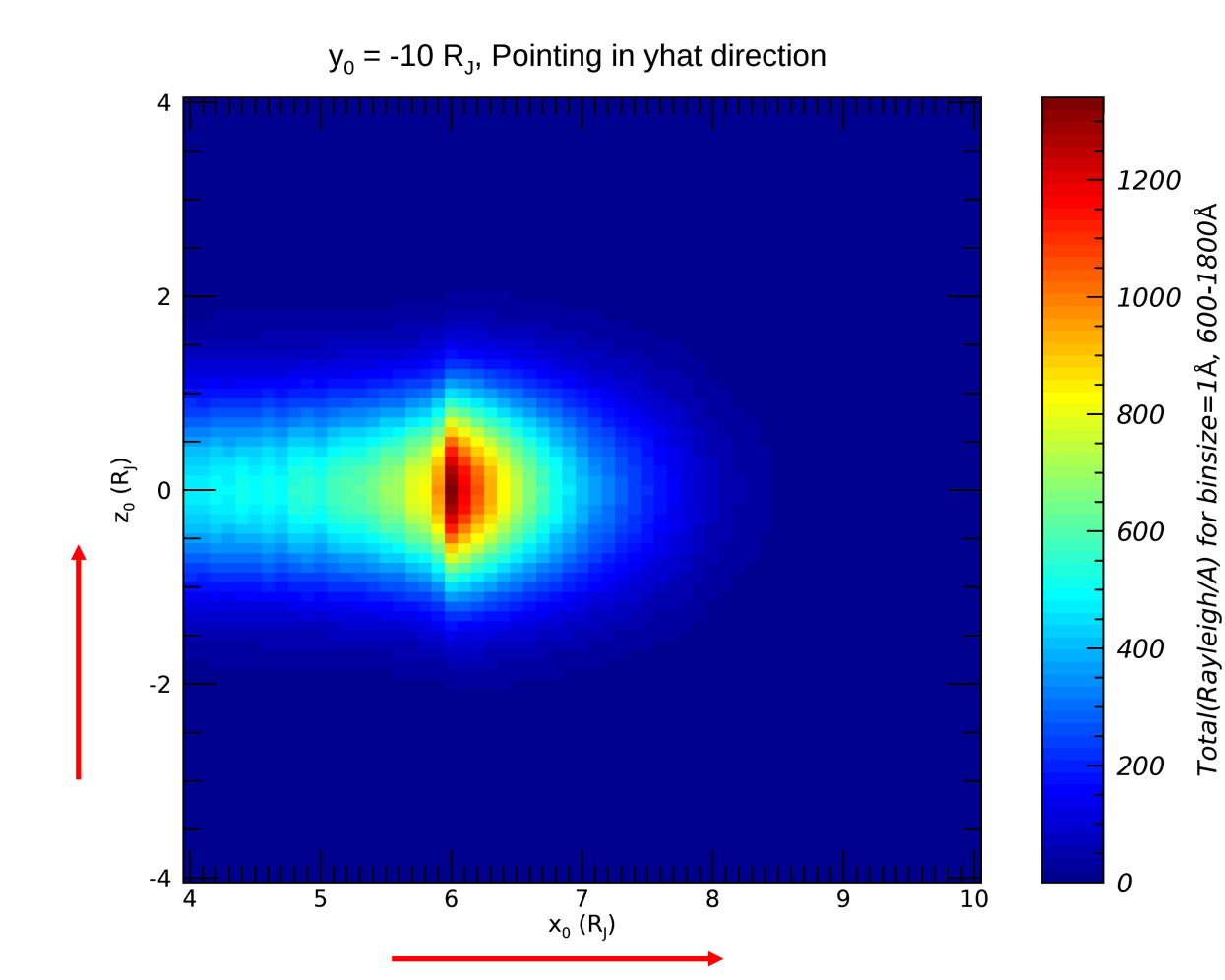

Figure 4.13: Cassini Model CITEP 2 side view of the torus for a 6 to 10 R_J finite torus

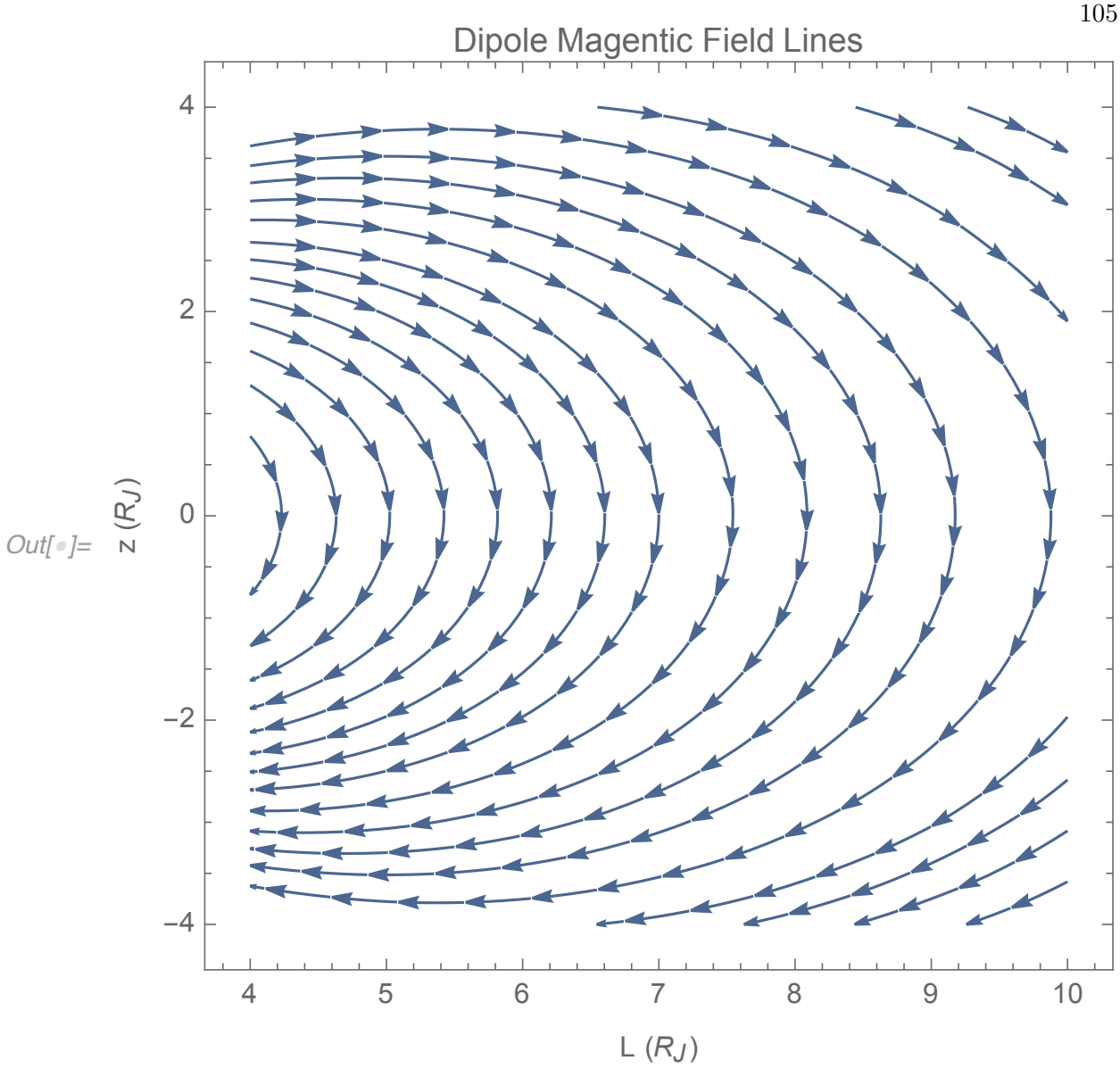

Figure 4.14: Dipole Magnetic fields lines as a function of L and z Cartesian

In figure 4.15 we take our emission to be from the side at z=0 and x=6 (effectively viewing a minimum radial distance of L=6) to compare with the Cassini spectrum from Nerney et al. (2017) and Steffl et al. (2004b) [96] [137]. We take functional power law forms of $A(L/6)^B$ for density and electron temperature and a finite torus between 6-10 R_J to integrate through. We fit sulfur species first along with electron temperature then set an upper limit on the amount of O^{++} from fitting

the feature at 1661/1666 Å. Then holding O^{++} constant at that amount and all sulfur species and electron temperature. Then we fit the remaining discrepancy in the 833/834 Å feature as only O^{+} in a similar manner to [96] but with the proper integration over the line of sight.

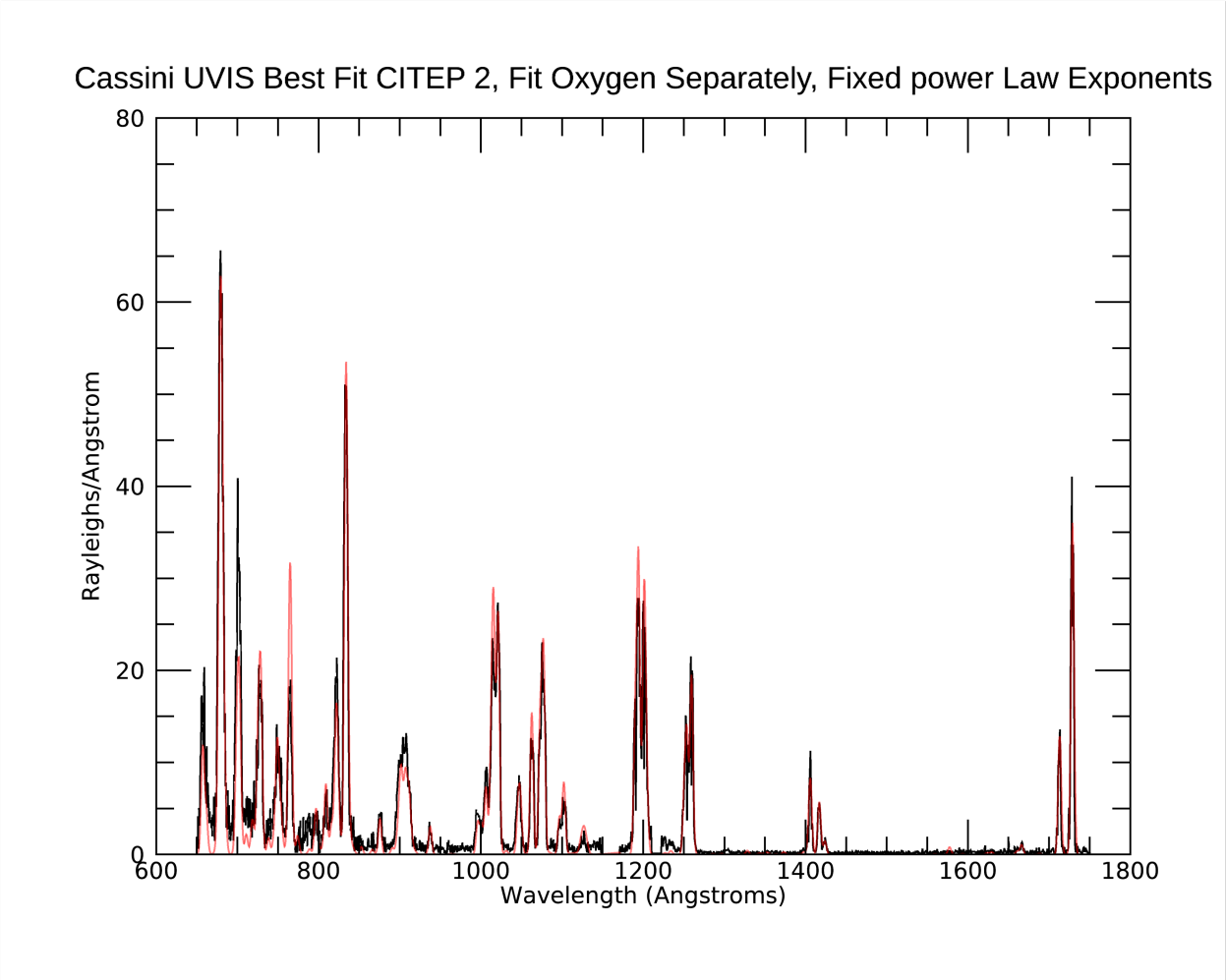

Figure 4.15: Steffl et al. (2004b) [137] Cassini density and Temperature profiles with power law fits as solid lines and Steffl values as dots.

Furthermore, we can go the other direction given a calibration or effective area curve for an instrument and predict counts instead of predicting the number of Rayleighs/Å. We do this by taking observation geometry, pointing, integration time, and a density and temperature model.

In this case, we use a side-on view of the centrifugal equator from outside the torus for the UVS instruments on Nasa's Europa Clipper and Esa's JUICE future missions to Jupiter. We take the number of simulated Rayleighs in each spectral pixel and multiply by the effective area in (cm^2 counts/photon), $\frac{10^6}{4\pi}$, the integration time of 3600 seconds, and the full field of view of the instrument in steradians. We find the following in figure 4.16

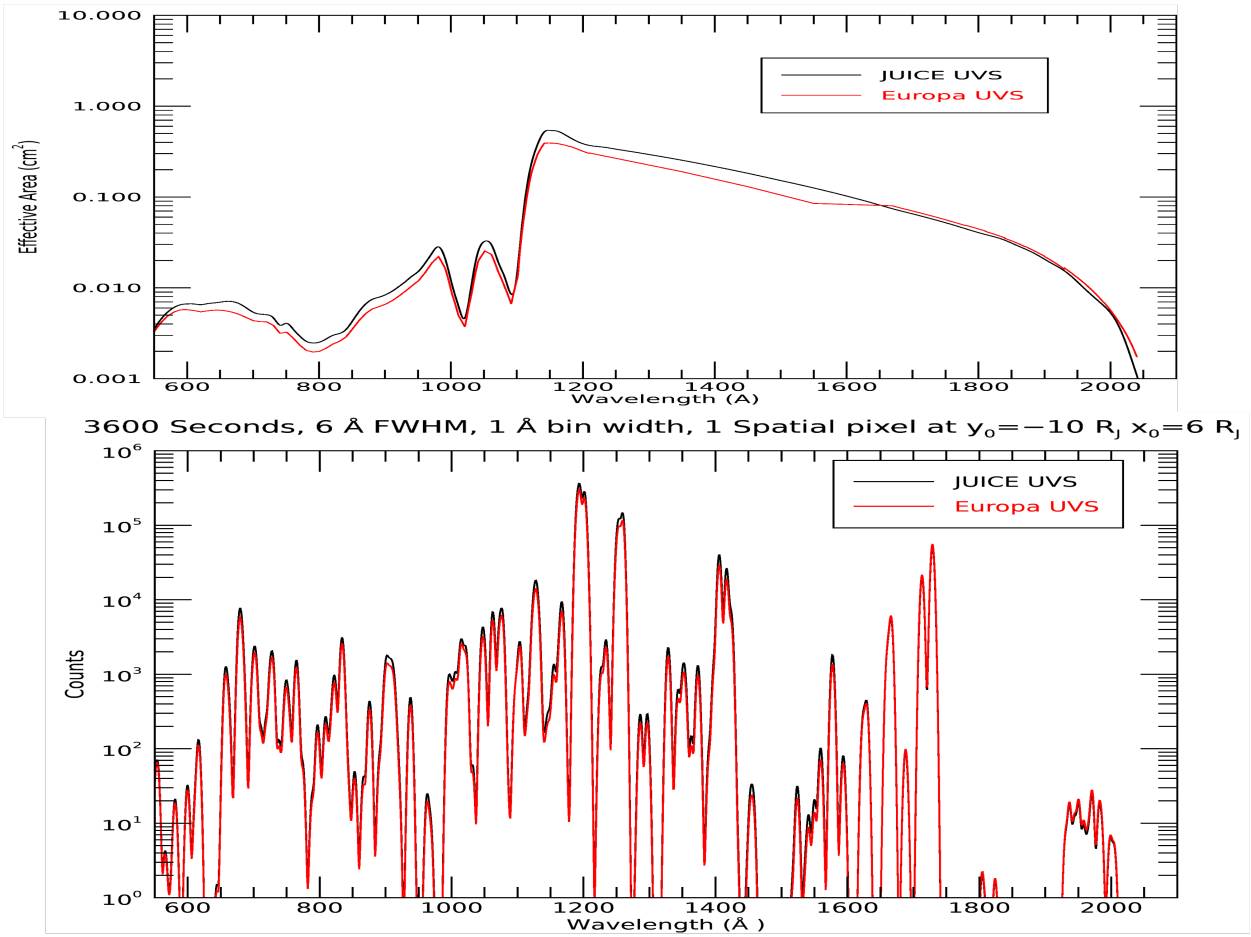

Figure 4.16: JUICE and Clipper effective area cruves from Davis et al. (2020) and (2022) [35] [36] simulation counts CITEP2 for a 3600 second torus stare using an enhanced density Cassini based torus model.

This allows us to plan observations and predict if the signal-to-noise due to Poisson statistics

$\left(\frac{\text{counts}}{\sqrt{\text{counts}}}\right)$ will be high enough for a given observation to match mission objectives. Assuming peak densities and summing over the whole field of view to maximize this we still barely get enough signal in the EUV. Typically one wants at least a signal-to-noise of 10 (over 100 counts) or a 10% uncertainty to have a meaningful signal. As can be seen from the effective area curves the instruments are almost identical. Unlike Cassini, they don't have dedicated EUV and FUV channels. The instrument is designed to observe Auroral FUV features more than EUV features and as a result, the sensitivity below Lyman alpha is limited. This is disappointing as the strongest emission features and the majority of the power are in the EUV region of the emission. Such as the S^{2+} 680 Å and O^{+}/O^{2+} 833/834 Å emission features. Further, the best case scenario for extended source FWHM of the instrument is 6 Å which we assumed in this simulation. This is twice as bad as Cassini and will make the determination of composition from the blended emission features even trickier.

In figure 4.17 we compare our neutral atomic oxygen emission due to electron impact excitation from the CHIANTI atomic database with that due to solar resonant scattering based on the g factor from Barth (1969) and using an atomic neutral O density model based on Smith et al. (2019) [130]. This is done for all neutral O lines in the CHIANTI atomic database for electron impact excitation and the solar resonant scattering just for the 1304 Å emission assuming typical solar conditions as listed in Koga et al. (2018a) [78] using a g factor from Barth et al. (1969) [14], the oscillator strength of 0.047 from Stone and Zipf (1974) [139], emission line profiles from Gladstone et al. (1992) [57], and solar irradiance from Woodman et al. (2005)[156]. Which gives a typical g-factor of 5.35×10^{-7} (photons s^{-1}) for 1304 Å neutral oxygen solar resonant scattering in the Io plasma torus. We do this for Cassini typical conditions and resolution.

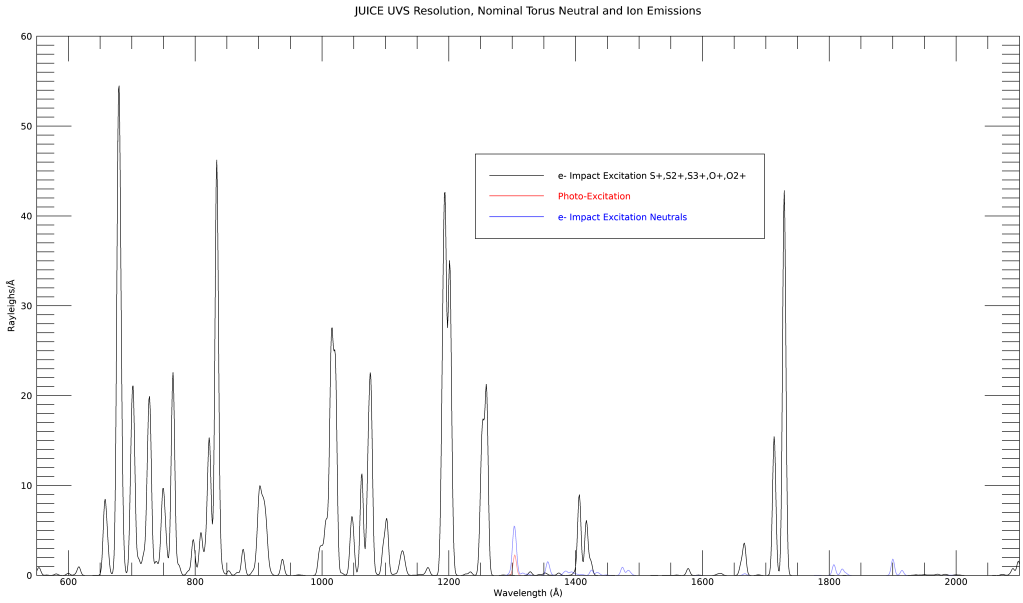

Figure 4.17: Neutral UV Emission CHIANTI compared with Ion emission Cassini resolution

4.6.5 CITEP2 Model Output for Bagenal 1994 Empirical Model

Using Bagenal (1994) [5] as a radial density and temperature model as shown in figure 4.18. This gives us density and temperatures along the line of sight for us to plug into CITEP 2 and find the resulting output. We use interpolate these values to a regular grid with a spatial step-size in all directions of 0.1 R_J for integrating over.

Using Bagenal (1994) 5-10R_J Torus profiles at 0.1RJ resolution for numerical integration assuming Scale Height distribution

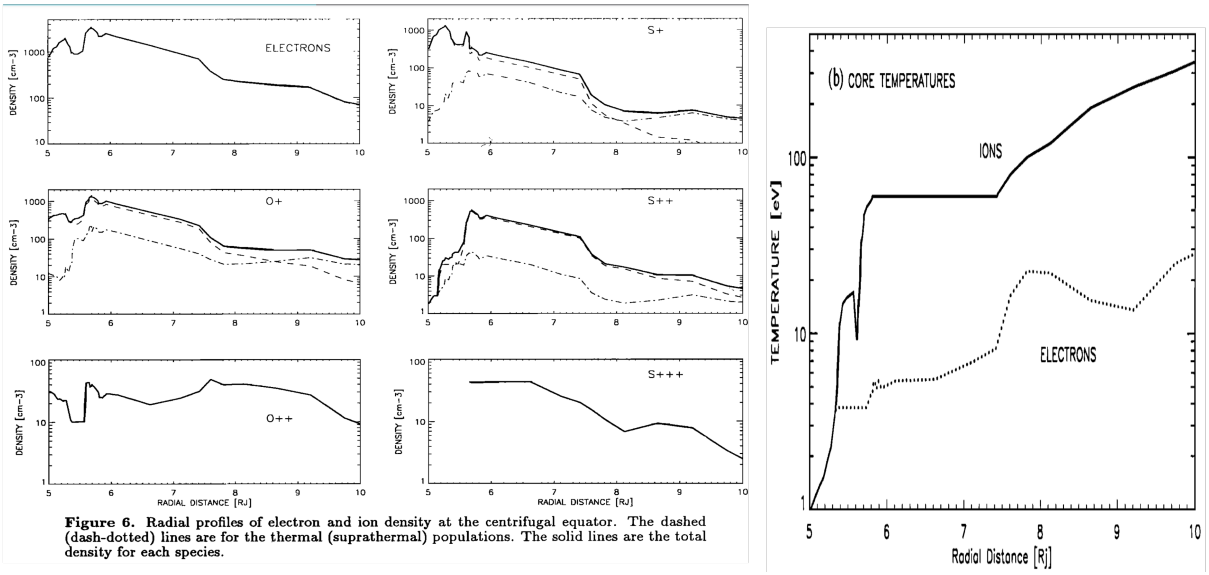

Figure 6. Radial profiles of electron and ion density at the centrifugal equator. The dashed (dash-dotted) lines are for the thermal (suprathermal) populations. The solid lines are the total density for each species.

Figure 4.18: Bagenal (1994) [5] radial profile inputs for CITEP2

Plugging this density and temperature model into CITEP 2 for UV emission and summing over the wavelength range and then taking a radial cut at z=0 and looking at intensity as a function of radius gives us figure 4.19. Again this is a view from the side looking through the torus from y=-10 R_J and with pointing in the $\hat{y}$ direction. We assume a scale height distribution given by the ion temperatures.

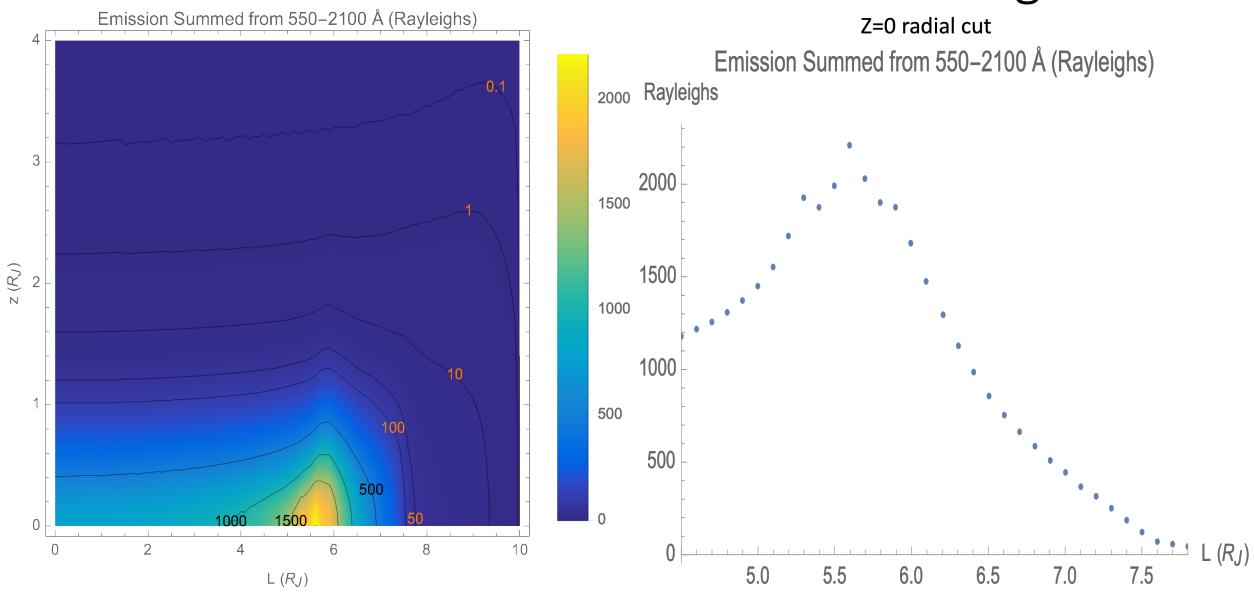

Figure 4.19: Bagenal 1994 Model UV CITEP Simulation

In figure 4.20 we do the same as in figure 4.19 but only for the 680 Å feature allowing us to see the dominant S^{++} emission feature full multi-dimensional structure.

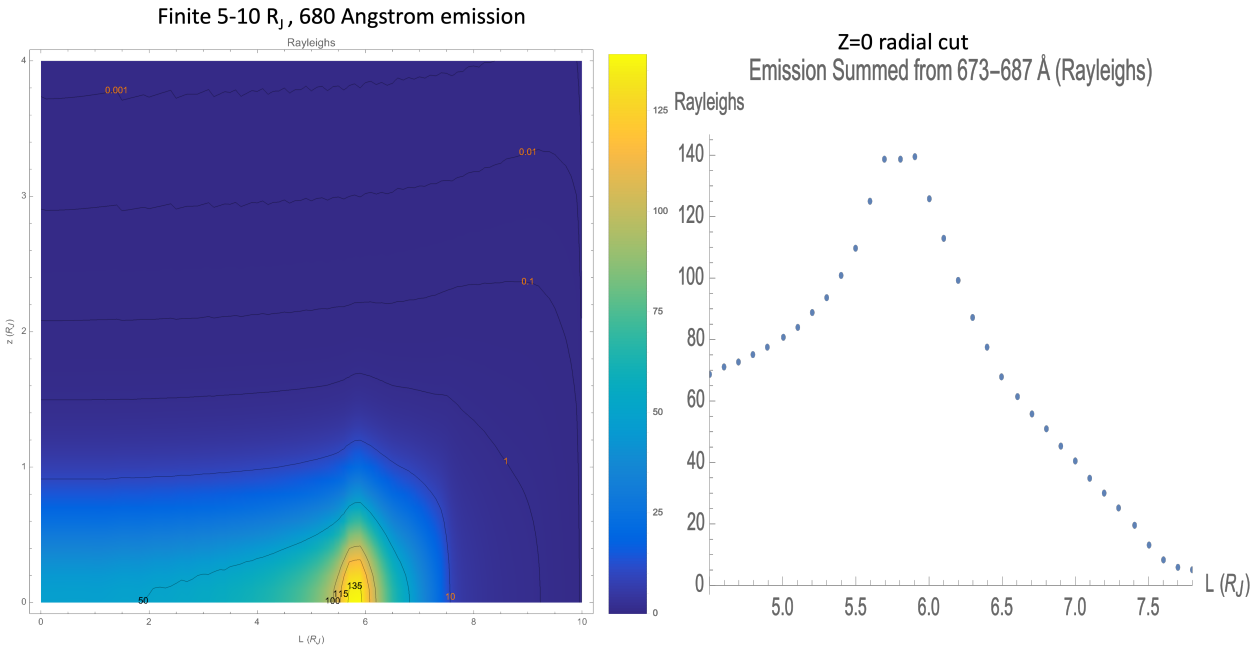

Figure 4.20: Bagenal 1994 Model UV CITEP Simulation S^{++} 680 Å

In figure 4.20 we do the same as in figure 4.19 but only for the 833/834 Å feature allowing us to see the combined O^{+} and O^{2+} emission feature full multi-dimensional structure predicted by our tool for the voyager based Bagenal 1994 empirical model [5].

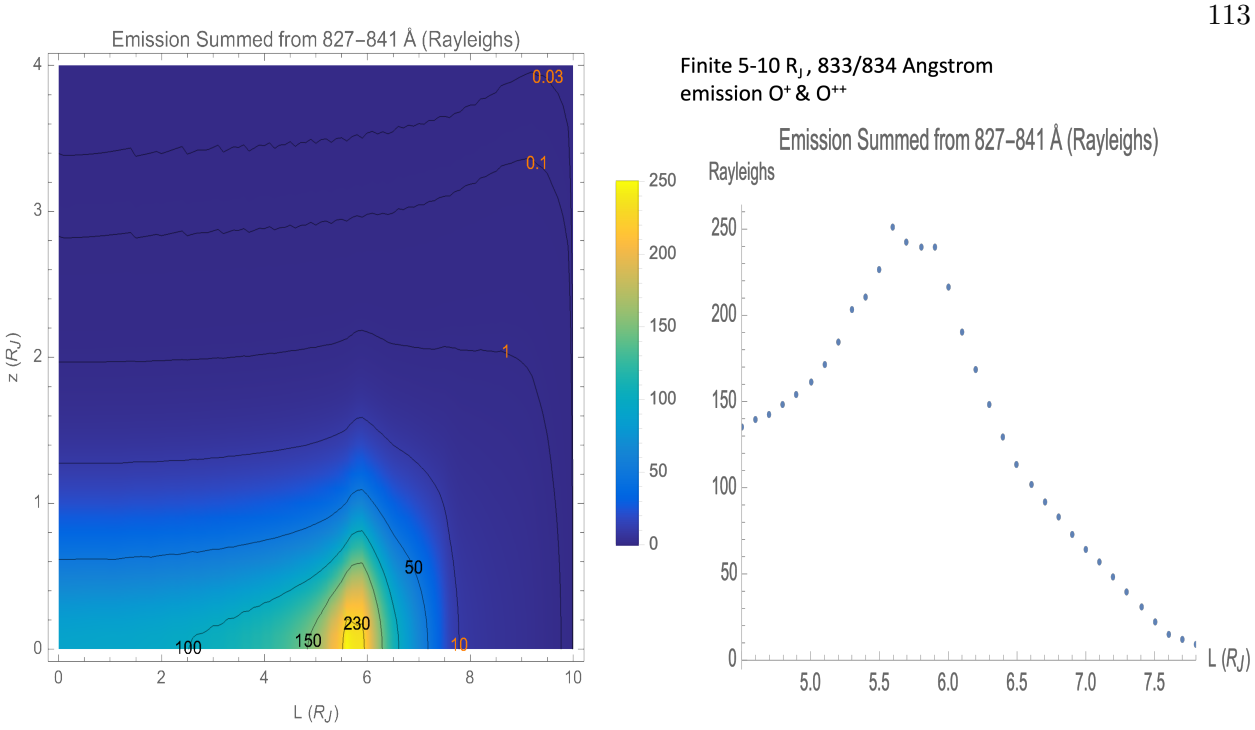

Figure 4.21: Bagenal 1994 Model UV CITEP Simulation O^{+} & O^{++} 833/834 $\AA$

In figure 4.22 we now switch to visible wavelengths with the CHIANTI atomic database and sum over the whole range to find the following.

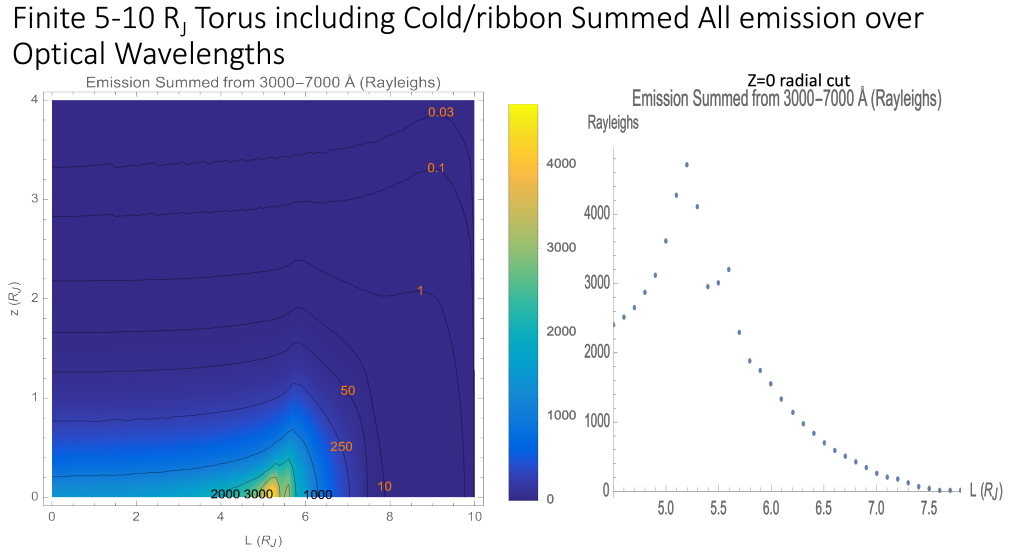

Figure 4.22: Bagenal 1994 Model Visible CITEP2 Simulation

In figure 4.23 we only show emission predicted by CITEP 2 in conjunction with CHIANTI for the same model for just 6731 S^+ emission.

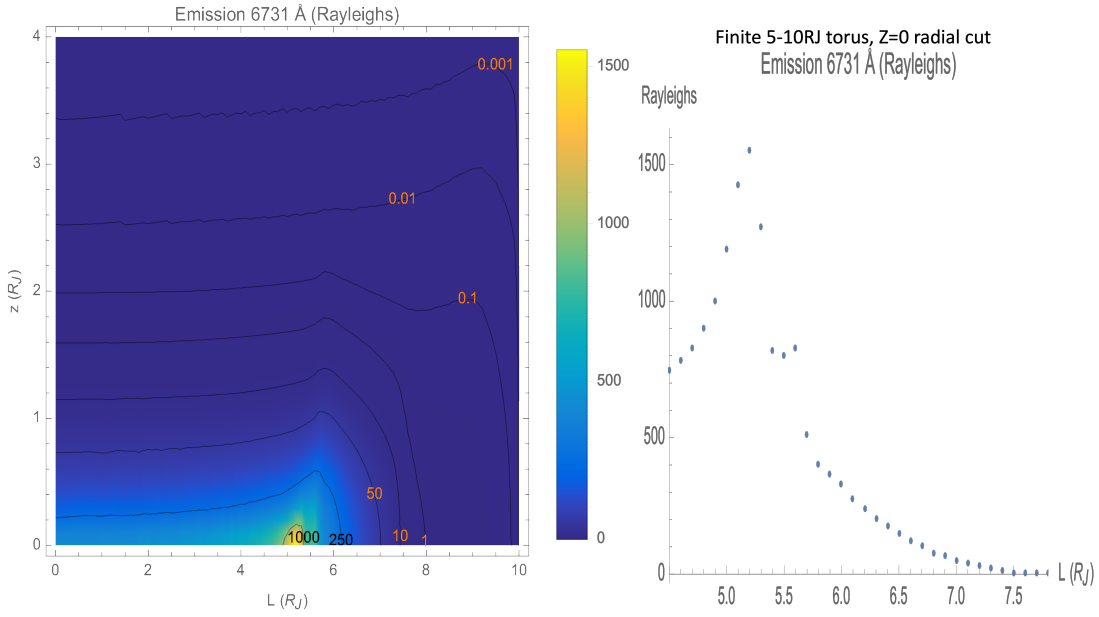

Figure 4.23: Bagenal 1994 Model Visible CITEP2 Simulation 6731Å

In figure 4.23 we show the same for 6716 S^+ emission.

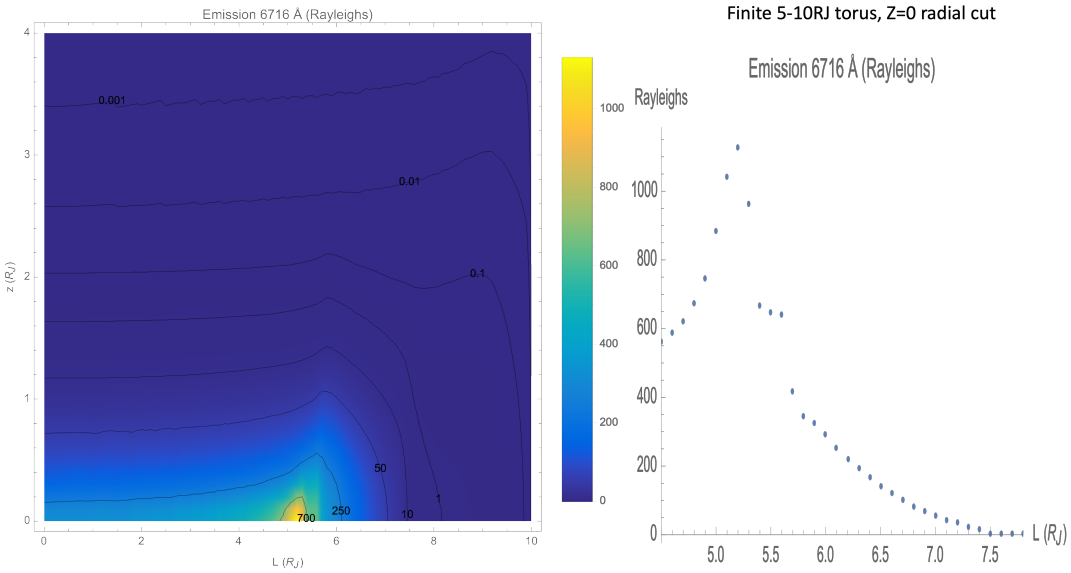

Figure 4.24: Bagenal 1994 Model Visible CITEP2 Simulation 6716Å

Taking the z=0 slice of intensity for all Io torus visible lines we find the following emission in figure 4.25. Comparing this with observations from Apache Point Observatory from Schmidt et al. (2018) [111] finds considerable disagreement. From C. Schmidt (Personal Communication 2022) I show the co-added dawn and dusk APO profiles in figure 4.26. However, some of this may be due to the fact that Voyager 1 sampled the Dusk ansa and due to the East-West electric field due to material flowing down the tail the torus is offset to smaller radial values (Barbosa & Kivelson (1983)) [13]. As well as uncertainties in magnetic field models and extrapolation to the centrifugal equator create additional uncertainties leading to higher densities and emissions. Further, as emission goes as density squared these issues may have been exacerbated. Further work to be done.

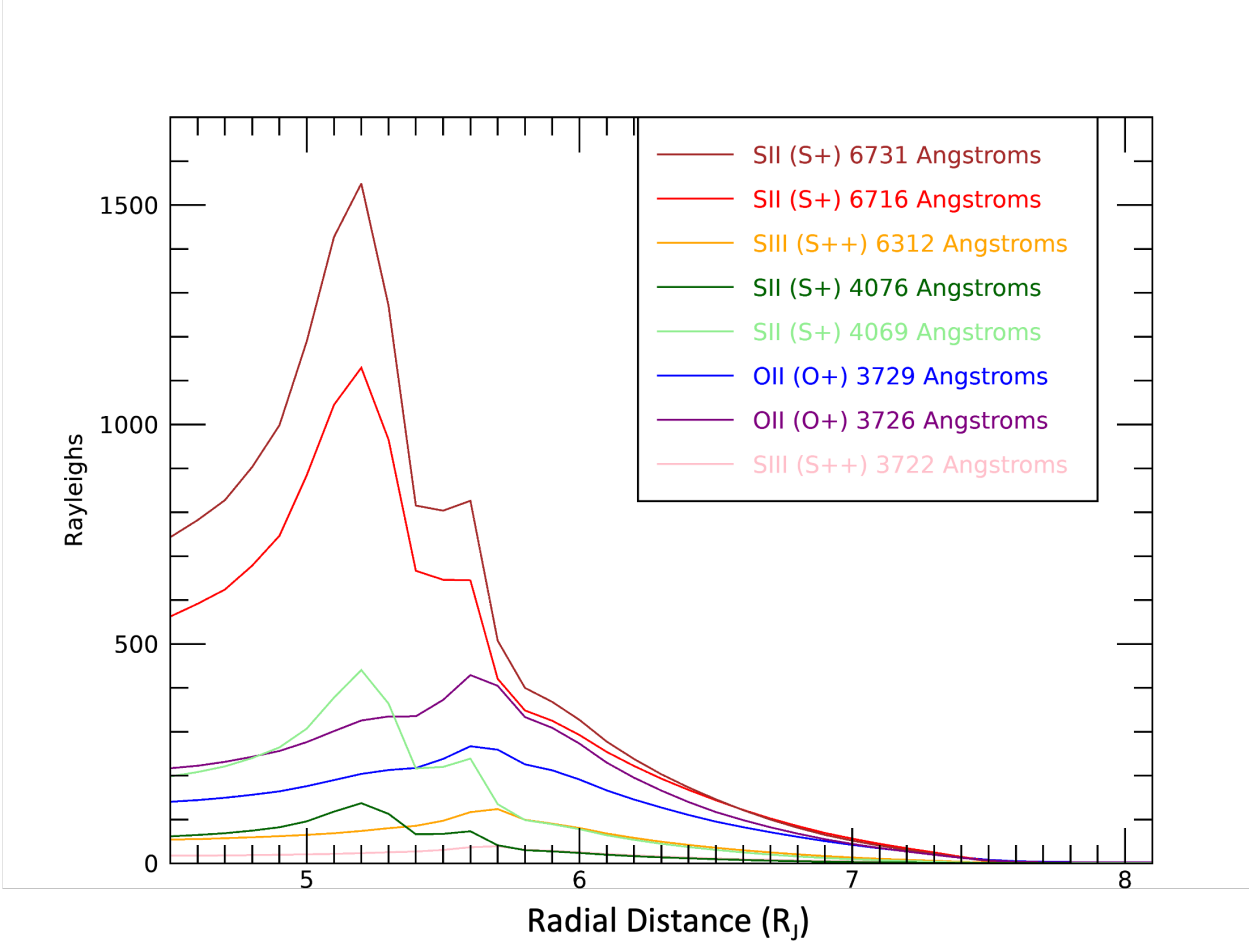

Figure 4.25: Bagenal (1994) [5] density model Ground Based Visible Emission predictions as a function of centrifugal radial distance for a slit aligned with the centrifugal equator

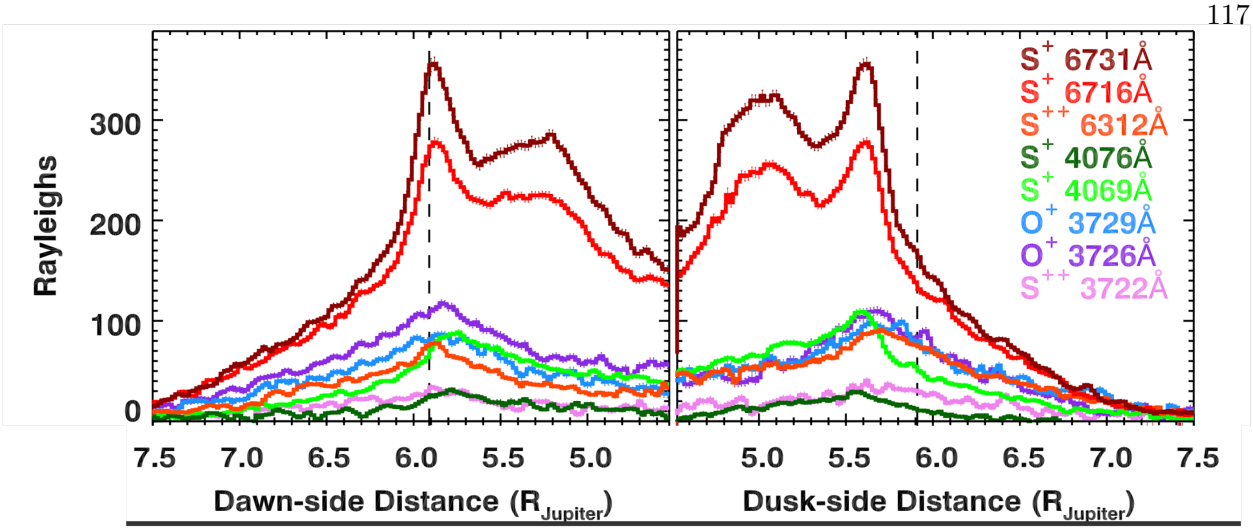

Figure 4.26: From C. Schmidt (Personal Communication 2022), Dawn and Dusk radial profile of Apache Point Observatory Co-added emission. For individual profiles see Schmidt et al. (2018) [111].

4.7 Conclusions

Throughout this section, I have gone over the basics of the emission model I have developed. I started with the physics of determining the brightness of an emission line starting with a cross-section for a transition to occur given the assumed velocity distribution function of the electron population responsible for exciting the ions to upper emitting states. Then I went over the assumptions that go into the "cubic centimeter" emission model which doesn't properly account for how the distribution function varies over the line of sight but doesn't require prior knowledge of the plasma properties over the line of sight and allows us instead to determine average column densities due to the emission. This work developed the Colorado Io torus emission package 2 (CITEP 2) which calculates the line of sight given the position of each spatial pixel and pointing of the spacecraft and produces a synthetic spectrum given plasma densities and temperatures along the line of sight using the CHIANTI atomic database to compute volume emission rates. I then for varying geometries and density models showed our model output and lessons learned.

I learned that model output is highly sensitive to the input model of densities and temperatures and using a proper integration over the line of sight requires larger densities than inferred from the "cubic centimeter" emission model in the UV. I find that projection effects inside the density peak make it extremely difficult to merely apply a "cubic centimeter" emission model and earn anything about the local environment inside peak due to major contributions in emission coming from outside this region. In addition, to properly compare with observations that aren't at the centrifugal equator or in centrifugal coordinates, I need to put the model output in Jovian graphic coordinates. Currently, the z coordinate or vertical distribution is given by a scale height distribution along a field line, but I plotted the model emission output in "z" as if it were just the cartesian z and not the curved distance along a field line. In the cold torus where higher-order non-dipolar magnetic contributions become more significant, we should use the Juno-derived field model to trace field lines along with diffusive equilibrium to take centrifugal equatorial reference densities and temperatures to provide a 3D model taking into account the field line geometry and distribution to compare with observations.

Chapter 5

Physical Chemistry Modeling

5.1 "Cubic Centimeter" Physical Chemistry Model

Our physical chemistry model is based on the work of Delamere et al. (2003, 2004, 2005) [39] [41] [40] and Copper et al. (2016) [33]. A single cubic cm model is at a given radial value dictating the ion pickup velocity and corresponding temperature (assuming equilibration and isotropy).

The relevant equations governing the time evolution of the number density and energy density of all model species are given by a balance of sources, and losses (sinks) of mass and energy [39] [12]. This can be derived from the mass and energy continuity equations with sources and losses (sinks) while working in the plasma frame assuming after the plasma is ionized and it is picked up by the $\boldsymbol{J} \times \boldsymbol{B}$ force density it is corotating in which case in System III which moves with the magnetic field as it rotates around Jupiter in 9.925 hours (Delamere et al. 2005 [40]) it has a 0 velocity so $\boldsymbol{\nabla} \cdot (\rho v) = 0$ (for mass density ρ) and likewise the corresponding divergence term in the energy continuity equation is zero. When subcorotation profiles are applied, this assumption fails while working in System III and then there are effectively source and loss terms between azimuthal bins which I am not considering in my work, but the model is capable of handling (see Copper et al. 2016) [33]. For perfect corotation this gives us

$$\frac{dn_\alpha}{dt} = S_m - L_m \tag{5.1}$$

and

$$\frac{d\left(\frac{3}{2}n_\alpha T_\alpha\right)}{dt} = S_E - L_E \tag{5.2}$$

Where S_m and L_m are the source and loss terms for mass or number density of a given species α and S_E and L_E are the source and loss terms for the number density for each species α.

Note we will henceforth work in units where Boltzmann's constant (k_B) is 1 and temperature and energy will have the same units of eV (with 1 eV = 11,605 Kelvin) but will be different because of the equation of state for a monatomic ideal gas with 3 degrees of freedom. In other words $E_\alpha = \frac{3}{2}T_\alpha$ and the energy density is given by $\frac{3}{2}nT$. Also from here on out we will drop the factor of 3/2 and work in terms of temperature because the model is only interested in calculating the number densities n_α and via the $n_\alpha T_\alpha$ update and previously updated n_α to update the temperatures T_α of given species α.

For mass sources and losses, we consider electron impact ionization due to a thermal Maxwellian electron population and a non-thermal hot electron component. We also include recombination rates due to electrons. As well as charge exchange reactions between ions and ions in addition to ions on neutrals from McGrath and Johnson (1989) [85]. The values used in this study can be found in table 1 of Delamere et al. (2005) [40]. In the simple cubic cm model of Delamere et al. (2003) and Nerney et al. (2020) [39] [95] there is an additional mass and energy loss term due to radial transport that can be appropriately described as an ad hoc loss term given as $\frac{n}{\tau}$ and $\frac{nT}{\tau}$ for a given input radial transport timescale τ. In our more sophisticated model we will not include this term and instead, treat mass and energy loss due to radial transport via numerical solutions to the radial Fokker-Planck equation which will be discussed in section 5.3.

This gives us a mass source term for species α given by

$$S_m = I_{\alpha-} n_{\alpha-} n_e + I^h_{\alpha-} n_{\alpha-} n_{eh} + R_{\alpha+} n_{\alpha+} n_e + \sum_{\gamma,\beta} k_{\gamma,\beta} n_\gamma n_\beta \tag{5.3}$$

and a mass loss term for species α given by

$$L_m = I_\alpha n_\alpha n_e + I^h_\alpha n_\alpha n_{eh} + R_\alpha n_\alpha n_e + \sum_\beta k_{\alpha,\beta} n_\alpha n_\beta \tag{5.4}$$

Where I and I^h are the electron impact ionization rate coefficients for the thermal and hot electron populations respectively, R is the recombination rate, α_- and α_+ are the lower and higher ionization states of species α, and k are the reaction rate coefficients for charge exchange. For example, if α is S^+ then α_- is neutral sulfur and α_+ is S^{2+}. This makes sense because the source of mass for S^+ due to ionization is from S and the source of mass due to recombination is S^{2+} gaining an electron and becoming S^+.

The number density of the core electron population is given by quasi-neutrality condition at each time step and does not have its own mass equation but does have its own energy equation.

For temperature density source and loss terms we have all the same source and loss terms multiplied by the relevant temperatures for each reaction. In addition, we also have source and loss terms due to Coulomb collisions between species. This term is given by thermal equilibration and can be a source or loss term depending on the difference in temperature between species. For simplicity, it was added only to the source term for energy but could be positive or negative.

$$S_E = I_{\alpha-} n_{\alpha-} n_e T_{\alpha-} + I^h_{\alpha-} n_{\alpha-} n_{eh} T_{\alpha-} + R_{\alpha+} n_{\alpha+} T_{\alpha+} n_e + \sum_{\gamma,\beta} k_{\gamma,\beta} n_\gamma n_\beta T_\beta + \sum_{\beta=i,e} \nu^{\alpha/\beta} n_\alpha \left(T_\beta - T_\alpha\right) \tag{5.5}$$

$$L_E = I_\alpha n_\alpha T_\alpha n_e + I^h_\alpha n_\alpha n_{eh} T_\alpha + R_\alpha n_\alpha n_e T_\alpha + \sum_\beta k_{\alpha,\beta} n_\alpha n_\beta T_\alpha \tag{5.6}$$

The collision frequency between species α and β from the 2019 NRL plasma formulary [104] which dictates thermal equilibration in the absence of other reactions is given by

$$\nu^{\alpha\beta} = 1.8 \times 10^{-19} \frac{\left(m_\alpha m_\beta\right)^{1/2} Z^2_\alpha Z^2_\beta n_\beta \lambda_{\alpha\beta}}{m_\alpha T_\beta + m_\beta T_\alpha} \tag{5.7}$$

Where $\lambda_{\alpha\beta} \approx$ 10-20 is the Coulomb logarithm between species α and β.

When a neutral is converted to an ion the freshly ionized or charge exchanged neutral will have a temperature given by the pickup temperature. $\frac{3}{2}T = \frac{1}{2}mv_{rel}^2$ with $v_{rel} = \Omega_J r - \sqrt{\frac{GM_J}{r}}$ which is the relative velocity of corotating plasma with respect to the local Keplerian orbital velocity at a given radial distance from Jupiter. At the orbit of Io $r = 5.91$ and the relative velocity is about 57 km/s and the resulting pickup temperature for sulfur is about 370 eV and for oxygen is 185 eV at the orbit of Io.

The final governing equation is the electron energy density update.

$$\frac{d\left(n_e T_e\right)}{dt} = \sum_{\beta} \nu^{e/\beta} n_e \left(T_\beta - T_e\right) - \frac{2}{3}\sum_{\beta,\gamma} \rho_{\beta,\gamma} n_e n_\beta - \frac{2}{3}\sum_{\alpha} I_\alpha \left(IP\right)_\alpha n_\alpha \tag{5.8}$$

Where in addition to Coulomb collisions we have a loss of energy due to each electron impact ionization and due to radiation. Where IP_α is the ionization potential of each species and $\rho_{\beta,\gamma}$ are the radiative rate coefficients given by summing up the emission from CHIANTI atomic database (between 1-500,000 Å) version 9 (Dere et al. 1997 & 2019) for each species due electron impact excitation [42]. The factors of 2/3 are necessary as the emission rates and ionization potentials are in units of energy not temperature.

The governing equations are solved numerically using a 2nd-order finite difference method. After each ion density is updated, then the core electron density is determined from neutrality. Then after each nT of each species is determined the resulting density times temperature at each iteration is divided by density to get the temperature update for all species including electrons.

5.2 Latitudinal Averaging Scheme using Scale Height Distribution via equatorial Ion Temperatures

Following Delamere et al. (2005) [40] we adopt the following latitudinal averaging scheme assuming Gaussian scale height distribution for each ion. The distribution of plasma along a magnetic flux tube is approximately Gaussian in the Io plasma torus [5] for each species. That is

$n_i(z) = n_{0i}e^{-(z/H_i)^2}$. With

$$H_i = \left(\frac{2T_i\left(1 + Z_iT_e/T_i\right)}{3m\Omega_J^2}\right)^{1/2} \tag{5.9}$$

Where $\Omega_j = 1.76 \times 10^{-6}$ rads/s with n_{0i} the reference point at the centrifugal equator [39].

This applies for small distances about the centrifugal equator and is derived for a Maxwellian which has constant temperatures along a dipole magnetic field line. This only applies for a single-ion plasma. The proper treatment should be given by diffusive equilibrium along a field line given a Juno-derived magnetic field model (ConNerney et al. 2022 [32]). The scale height approximation in the warm torus has been shown to not change output significantly (Delamere et al. 2005 [40]) but the effects of higher order magnetic field contributions in the cold torus and proper diffusive equilibrium treatment should be investigated as in the cold torus Dougherty et al. (2017) [47] showed that the O^{2+} density peaked off the centrifugal equator which cannot be captured by a scale height model which assumes the peak density is at the centrifugal equator. In certain situationsi n the cold torus the lighter ions can be lifted off the centrifugal equator by the ambipolar electric field and can peak off the equator (Bodisch et al. (2017)[16].

The column density along the flux tube is given by

$$N_i = \int_{-\infty}^{\infty} n_{0i}e^{-(z/H_i)^2}dz = \sqrt{\pi}n_{0i}H_i \tag{5.10}$$

This implies that the flux tube averaged source rate for species γ due to a reaction between species ion α and β is given by

$$\frac{\delta N_\gamma}{\delta t} = \int_{-\infty}^{\infty} kn_\alpha(z)\, n_\beta(z)\, dz = kn_{0\alpha}n_{0\beta}\sqrt{\pi}H' \tag{5.11}$$

With $H' = \sqrt{\dfrac{H_\alpha^2 H_\beta^2}{H_\alpha^2 + H_\beta^2}}$

Which allows us to update the equatorial densities via the flux tube averaged update.

Likewise, we can do the same for ion-neutral reactions. We must now take into account the tilt due to the offset between the centrifugal and Joviagrpahic rotational equator which is where the neutrals reside. This is treated as an offset as a function of longitude. In this case we have

$$\frac{\delta N_\gamma}{\delta t} = \int_{-\infty}^{\infty} k n_{i0} n_{n0} e^{-(z/H_i)^2} e^{-(z-z0)^2/H_n^2} dz = k n_{0i} n_{0n} \sqrt{\pi} \sqrt{\frac{\pi}{a}} e^{(b^2-4ac)/4a} \tag{5.12}$$

With $a = \sqrt{\frac{(H_i^2 + H_n^2)}{H_i^2 H_n^2}}$, z0 is the longitude dependent offset, $b = -2z_0/H_n^2$, and $c = z_0^2/H_n^2$.

Likewise, we compute flux-tube averaging for Coulomb collisions and radiation. These are given by numerically determining the following integrals at each iteration.

$$\left\langle \nu^{\alpha/\beta} n_\alpha \right\rangle = \frac{\int \nu^{\alpha/\beta} n_\alpha n_\alpha n_\beta dz}{\int n_\alpha n_\beta dz} \tag{5.13}$$

and

$$\left\langle \sum_\alpha \rho^{\alpha/\gamma} n_\alpha \right\rangle = \frac{\int \sum_\alpha \rho^{\alpha/\gamma} n_\alpha n_e dz}{\int n_e dz} \tag{5.14}$$

5.3 Radial Transport Model

We follow Schreier et al.(1998) [117], Delamere et al. (2005) [39], and Taylor (1996) [142] in using the radial Fokker-Planck equation to describe the radial transport in the Io plasma torus torus. It is essentially a non-linear diffusion equation with a nonlinear diffusion coefficient D_{LL}.

$$L^2 \frac{\partial}{\partial L} \left(\frac{D_{LL}}{L^2} \frac{\partial Y}{\partial L} \right) = \frac{\partial Y}{\partial t} \tag{5.15}$$

Where Y is any quantity conserved as a flux tube moves under interchange motion, L is the magnetic radial coordinate, and D_{LL} is the diffusion coefficient.

A radial Fokker-Planck diffusion equation in terms of the distribution function was derived by Dungey (1965) [48]. This equation was also derived by Falthammar (1968) [51]. This was done

by considering the time evolution of a particle velocity distribution function for radial 1D motion under the violation of the 3rd adiabatic invariant. The first person I can find to have applied this to the Jupiter system was Mead in 1972 [87].

The conserved quantity for mass under flux tube interchange motion is $Y_m = NL^2$ or the total number of ions per unit magnetic flux along a given flux tube.

Following Delamere et al. (2005) [40], and Richardson and Siscoe (1983) [105] we assume that the scale height of the torus is small compared to L such that the effective volume goes as L^3H(rather than L^4), where H is the plasma scale height. This gives us Y_E or our flux tube conserved quantity for energy density given as $Y_E = NL^2TL^2T^{1/3}$. In the warm torus typical ion scale heights are about $1R_J$ and in the cold torus they get as small as $0.1RJ$. The range of our model is between 5-10 R_J so this is a sound assumption.

The flux tube content for a given ion in a dipole magnetic field is given by

$$\left(NL^2\right)_i = 4\pi R_J^3 L^4 \int_{\theta=0}^{\theta_m ax} n_i\left(\theta\right)\cos^7\left(\theta\right)d\theta \tag{5.16}$$

Where

The distance s along a field line is approximately z for small z and is given by

$$dz^2 \approx ds^2 = dr^2 + r^2 d\theta^2 = \left(3\sin^2\theta + 1\right)L^2\cos^2\theta^2 \tag{5.17}$$

We assume the ion particle distributions are isotropic Maxwellians. This is a reasonable assumption as Crary (1998) [34] found there was no systematic anisotropy found in the Io plasma torus during Galileo. For isotropic Maxwellians the temperature of each species is constant along a dipole magnetic field line. Given our scale height distribution along the field line we numerically integrate the local density along the field line to get the flux-tube content. We use the iterative scheme of Newton's method to convert between $\left(NL^2\right)_i$ and the equatorial densities (n_i) for each ion species at each iteration. Then we diffuse $\left(NL^2\right)_i$ and $\left(NL^2TL^2T^{1/3}\right)_i$ then given those we update n_i and T_i.

5.4 Combining all Above into full 3D Physical Chemistry Model using split-step coupling

The numerical split-step method used is highlighted below in figure 5.1

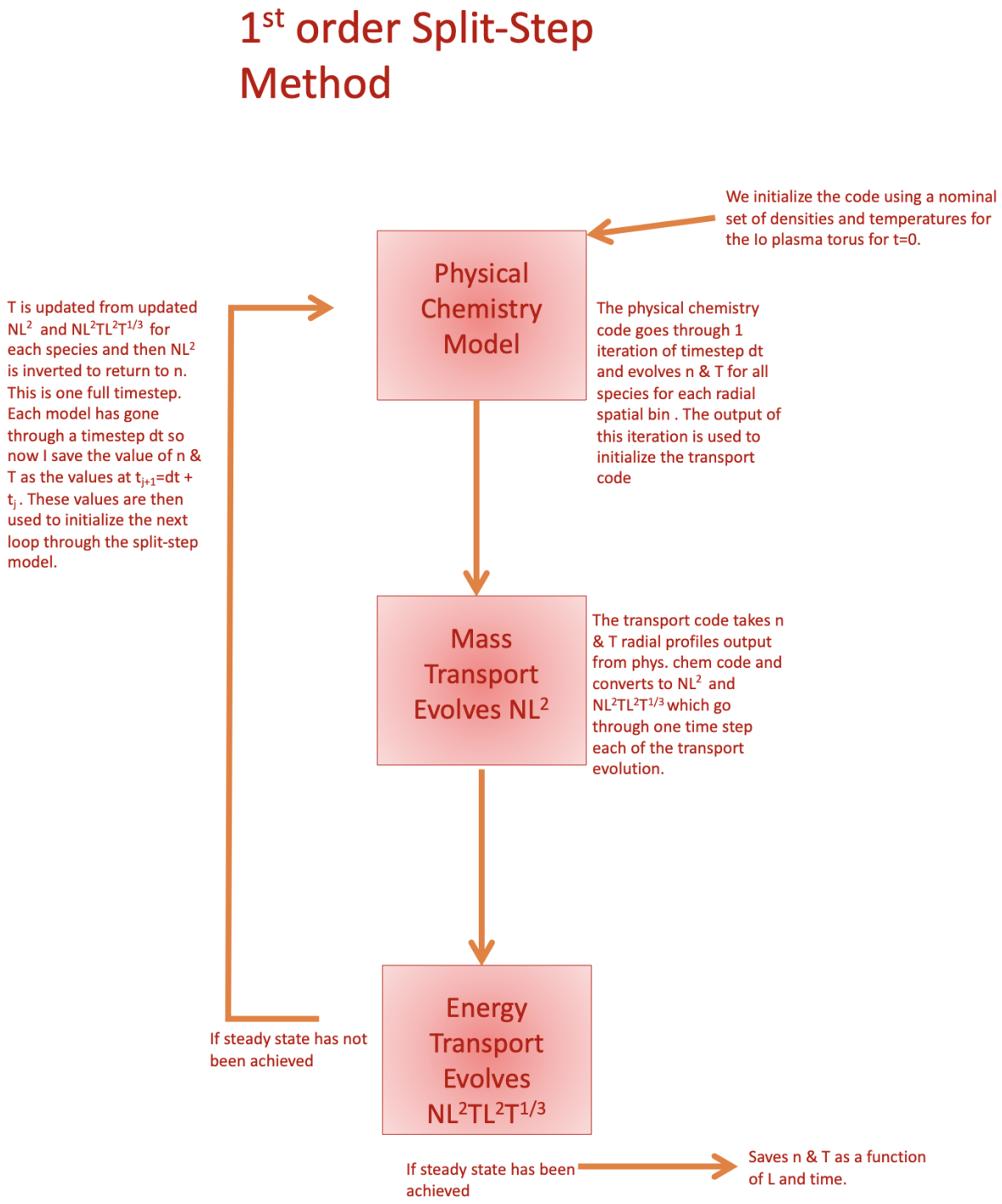

Figure 5.1: Physical Chemistry Split Step method

Each step is of the form

$$\hat{D}A(t) = \dot{A}(t) \tag{5.18}$$

The formal solution of the above equation is given by

$$A(t) = e^{t\hat{D}}A(t=0) \tag{5.19}$$

In a sense, we are applying the operator $e^{t\hat{D}}$ to the initial conditions to find a solution sometime in the future. Though we may have no idea what the operator $\hat{D}$ is for our numerical simulations.

If instead, we have two models to evolve the system simultaneously they can be thought of as two different linear operators being applied to the initial conditions. Or

$$A(t) = e^{t\left(\hat{D}_1+\hat{D}_2\right)}A(t=0) \tag{5.20}$$

The Baker–Campbell–Hausdorff expansion gives us an formula to write down $e^{t\left(\hat{D}_1+\hat{D}_2\right)}$. From Wikipedia:

The Zassenhaus formula [edit]

A related combinatoric expansion that is useful in dual[16] applications is

$$e^{t(X+Y)} = e^{tX}\ e^{tY}\ e^{-\frac{t^2}{2}[X,Y]}\ e^{\frac{t^3}{6}(2[Y,[X,Y]]+[X,[X,Y]])}\ e^{\frac{-t^4}{24}(([[[X,Y],X],X]+3[[[X,Y],X],Y]+3[[[X,Y],Y],Y])}\ \ldots$$

So to first order

$$A(t) = e^{t\left(\hat{D}_1+\hat{D}_2\right)}A(0) \approx e^{t\hat{D}_1}e^{t\hat{D}_2}A(0) \tag{5.21}$$

Related is the Lie product formula.

In mathematics, the **Lie product formula**,

$$e^{A+B} = \lim_{N\to\infty} \left(e^{A/N} e^{B/N}\right)^N,$$

Instead, we have 3 models to evolve the system in time so to first order we have

$$A\left(t\right) = e^{t\left(\hat{D}_1+\hat{D}_2+\hat{D}_3\right)} A\left(0\right) \approx e^{t\hat{D}_1} e^{t\hat{D}_2} e^{t\hat{D}_3} A\left(0\right) \tag{5.22}$$

This can be interpreted as split steps where we evolve the initial conditions using each model separately in steps before applying the next. If we evolve each model for a time-step dt then equivalently

$$A\left(dt\right) = e^{dt\left(\hat{D}_1+\hat{D}_2+\hat{D}_3\right)} A\left(0\right) \approx e^{dt\hat{D}_1} e^{dt\hat{D}_2} e^{dt\hat{D}_3} A\left(0\right) \tag{5.23}$$

So if we step through each model by a time-step of dt then we have evolved the entire system by dt to first order.

In the next 3 sections, I show multiple cases of modeling the warm and cold torus. A summary of the cases are shown in table 5.1.

5.5 Warm Torus Solutions

The combined warm torus model is based on the code of Copper et al. (2016) and Delamere et al. (2005) [33][40]. It is written in fortran90 and uses mpi to parallelize the code. This work utilized the Summit supercomputer, which is supported by the National Science Foundation (awards ACI-1532235 and ACI-1532236), the University of Colorado Boulder, and Colorado State University. The Summit supercomputer is a joint effort of the University of Colorado Boulder and Colorado State University.

Combining all of these pieces together we have many input parameters to explore. The model is initialized with a typical warm torus radial profile of densities and temperatures of all species included in the model. We include neutral atomic sulfur and oxygen as well as S^+, S^{2+}, S^{3+}, O^+,

O^{2+}, and a thermal core electron and hot electron population. We make 1 iteration of physical chemistry in each spatial bin of the model. This updates the temperature and densities. Then we convert these densities to flux-tube mass content NL^2 for each ion species as well as flux-tube energy content $NL^2TL^2T^{1/3}$ of each ion species and apply 1 iteration of the radial Fokker Planck nonlinear diffusion equation then update the temperatures and densities of each species. The model is run to a steady state to predict spatial profiles of densities and temperatures.

The main model "knobs" we focused on are the neutral source rate of atomic sulfur and oxygen, the oxygen-to-sulfur ratio of the neutral source, the diffusion coefficient, the fraction of hot electrons (and their temperature), as well as how these vary in space. Following Copper et al. (2016) and Delamere et al. (2005) [33][40] we adopt power-law radial profiles for the neutral source rate S_n, the fraction of hot electrons F_{eh}, and diffusion coefficient D_{LL}. With the source decreasing away from the orbit of Io, the fraction of hot electrons increasing with radial distance, and the diffusion coefficient also increasing with radial distance. We assume the hot electron temperature is a constant at 269 eV consistent with Voyager electron analysis of Sitter and Strobel (1987) [128]. Though our model output is not sensitive to the hot electron temperature (T_{eh}) above 40 eV due to the flattening of ionization and emission rates above this temperature (Delamere et al. 2003 [39]). We also assume a constant O/S ratio of 2 of the neutral source consistent with dissociation of SO_2 from the ultimate source of volcanism on Io. The neutral source rate used by each cubic cm is in units of $\frac{dn}{dt}$ as it evolves the neutral sulfur and oxygen species in time. The given particles per second of the neutral source rate quoted in Copper et al. (2016) requires an effective volume for each spatial bin to divide the source by to get a volumetric source rate. This volume is determined by the spatial bins area times the neutral scale height.

The radial diffusion equation requires boundary conditions in NL^2 and $NL^2TL^2T^{1/3}$. We applied a zero derivative in NL^2 for each ion species at L=6 in other words $\left.\frac{d\left(NL^2\right)}{dL}\right|_{L=6} = 0$. This was done to match the fact that the flux tube content peaks near there [47] [5]. We then fix the NL^2 value at L=10 to match the values from Bagenal (1994) [5]. These values can be found in Table 1 of Copper et al. (2016) [33]. The finite difference numerical scheme used to update

NL^2 and $NL^2TL^2T^{1/3}$ can be found in equation 2 of Copper et al. (2016) [33]. For the warm torus modeling, we use a timestep of dt=1000 seconds, a radial spatial step of dL=0.1 R_J, and latitudinally we go from -30 to 30 degrees latitude with 1 degree stepsizes corresponding to 0.1 R_J spatial bins along the field lines for computing NL^2 and applying the latitudinal averaging schemes.

We can match solutions from Copper et al. (2016) [33] for uniform system III hot electrons (only a radial variation in F_{eh}) with no subcorotation profile resulting in an n=2 mode due to neutral cloud peak density intersecting plasma at 2 longitudes due to offset tilt. This output is shown in figure 5.2 These are the equivalent of figures 5, 6, and 7 from Copper et al. (2016) [33]. We also successfully recreated Copper's output with the addition of a System III & System IV modulation of hot electrons consistent with Steffl et al. (2008) [136].

Focusing on radial variations, we average over longitude and compare with previously determined composition and find decent agreement.

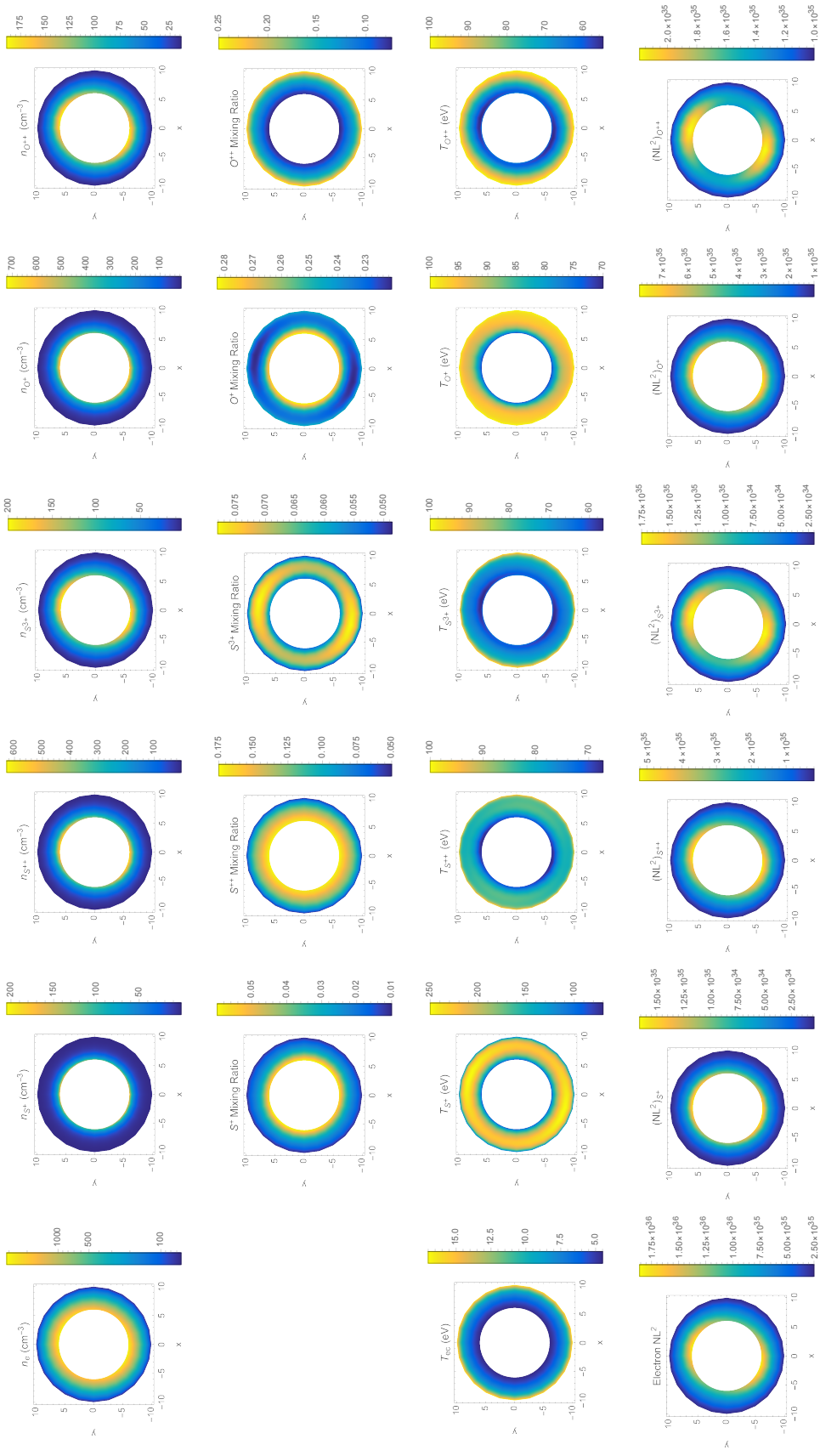

Figure 5.2: 2D Model Output Matching Copper et al. (2016) [33]

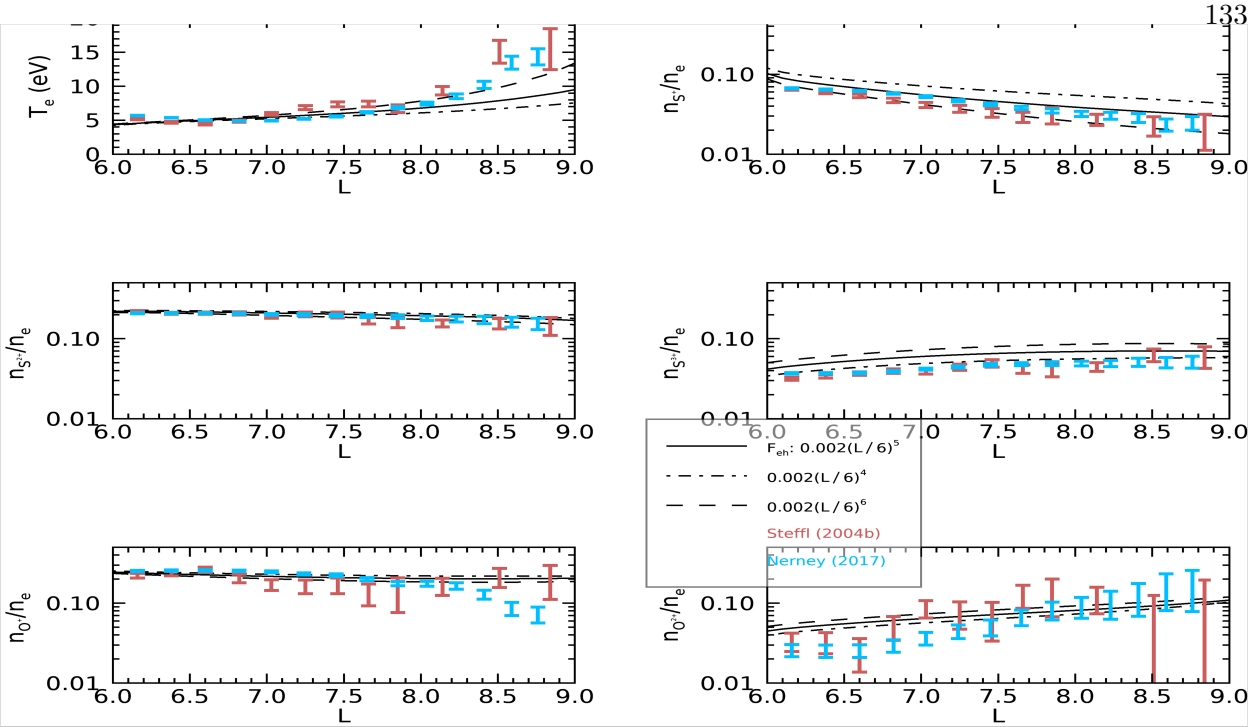

Figure 5.3: Model Output radial profiles Matching Copper et al. (2016) [33] varying F_{eh} power law exponent

In figure 5.3 we explore differing power law exponents for the fraction of hot electrons and their effect on model output. While holding the value of 0.2% constant at L=6. The L^6 power law we found fit the core electron temperatures better from the Cassini epoch [96] [137]. This is in contrast to the L^5 power law Copper found and $L^{4.4}$ that Delamere et al. (2005)[40] found. I believe this is because they were trying to fit mixing ratios and absolute densities more than the electron temperature in the region beyond L=7 though I actually get a better fit outside there for S^+ mixing ratios though worse for S^{3+} for the L^6 model run. In addition, we are using the CHIANTI atomic database v9 emission rates instead of version 4 which changes the electron energy loss terms and model output electron temperatures modestly. In figure 5.4 we show the electron density profile for these parameter ranges which correspond to the mixing ratios and electron temperatures shown in figure 5.3. So for our nominal case, we take the L^6 case for F_{eh}.

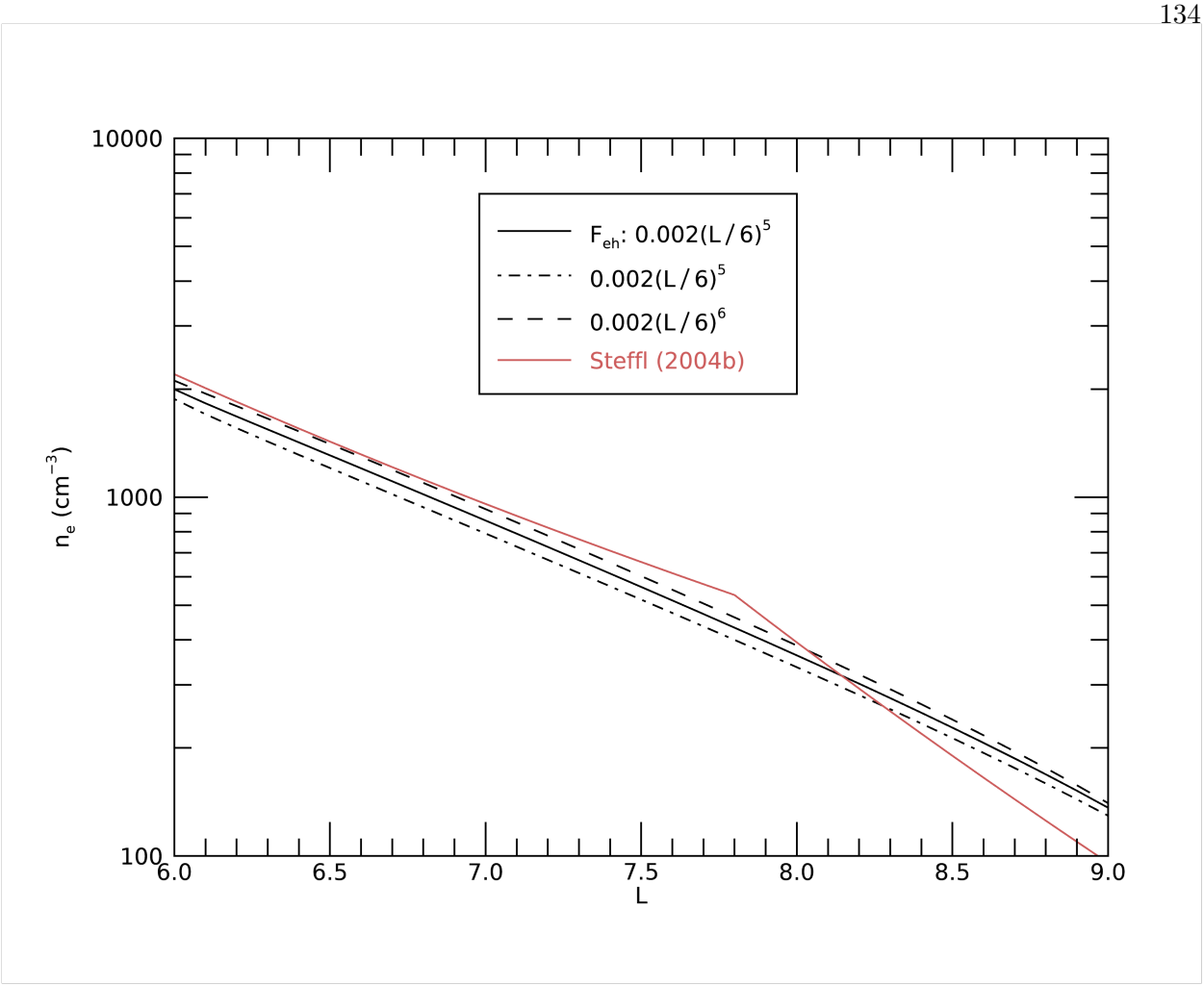

Figure 5.4: Radial Warm torus Model Output n_e, Varying F_{eh} power law exponent.

In figures 5.5 and 5.6 and we explore differing power law exponents for the neutral source rate S_n and their effect on model output. While holding the value constant at L=6.

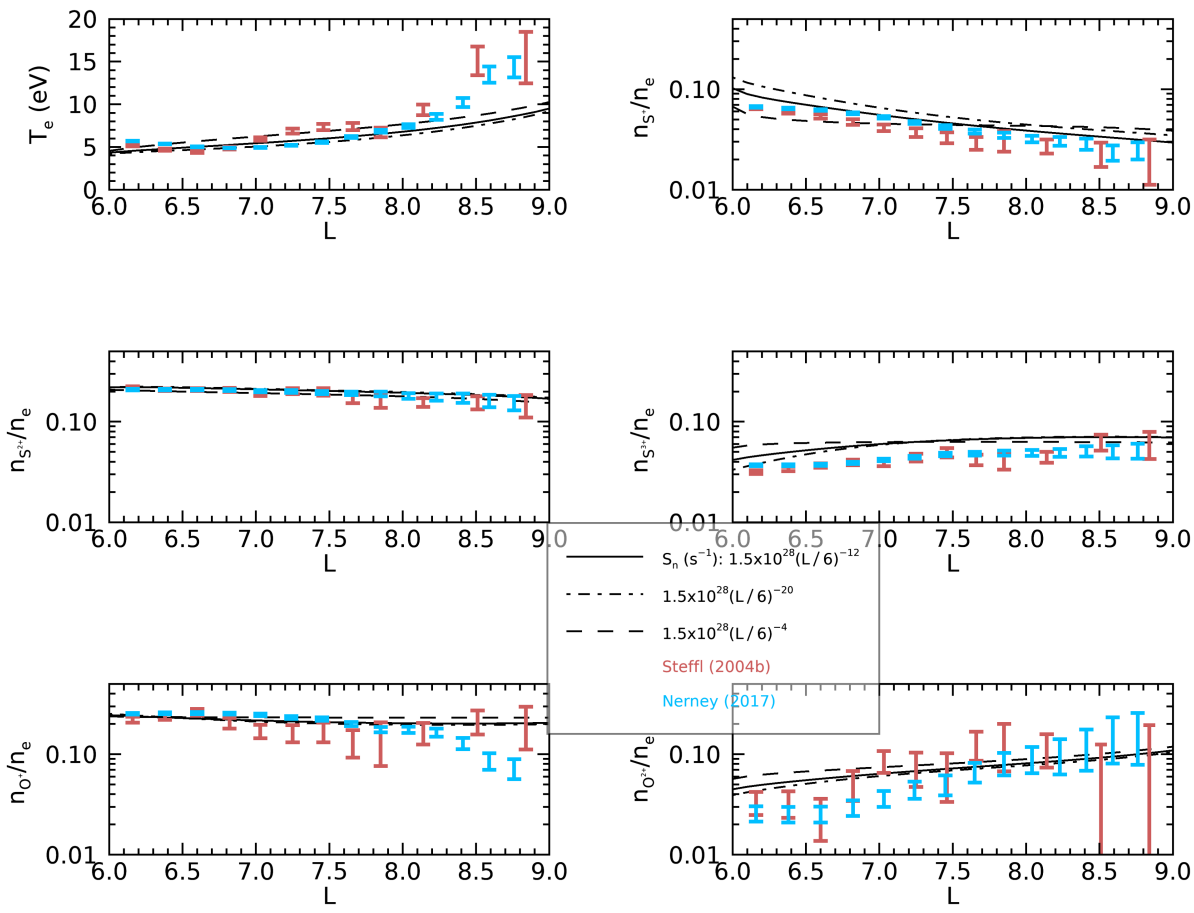

Figure 5.5: Radial Warm torus Model Output, Varying S_n power law exponent.

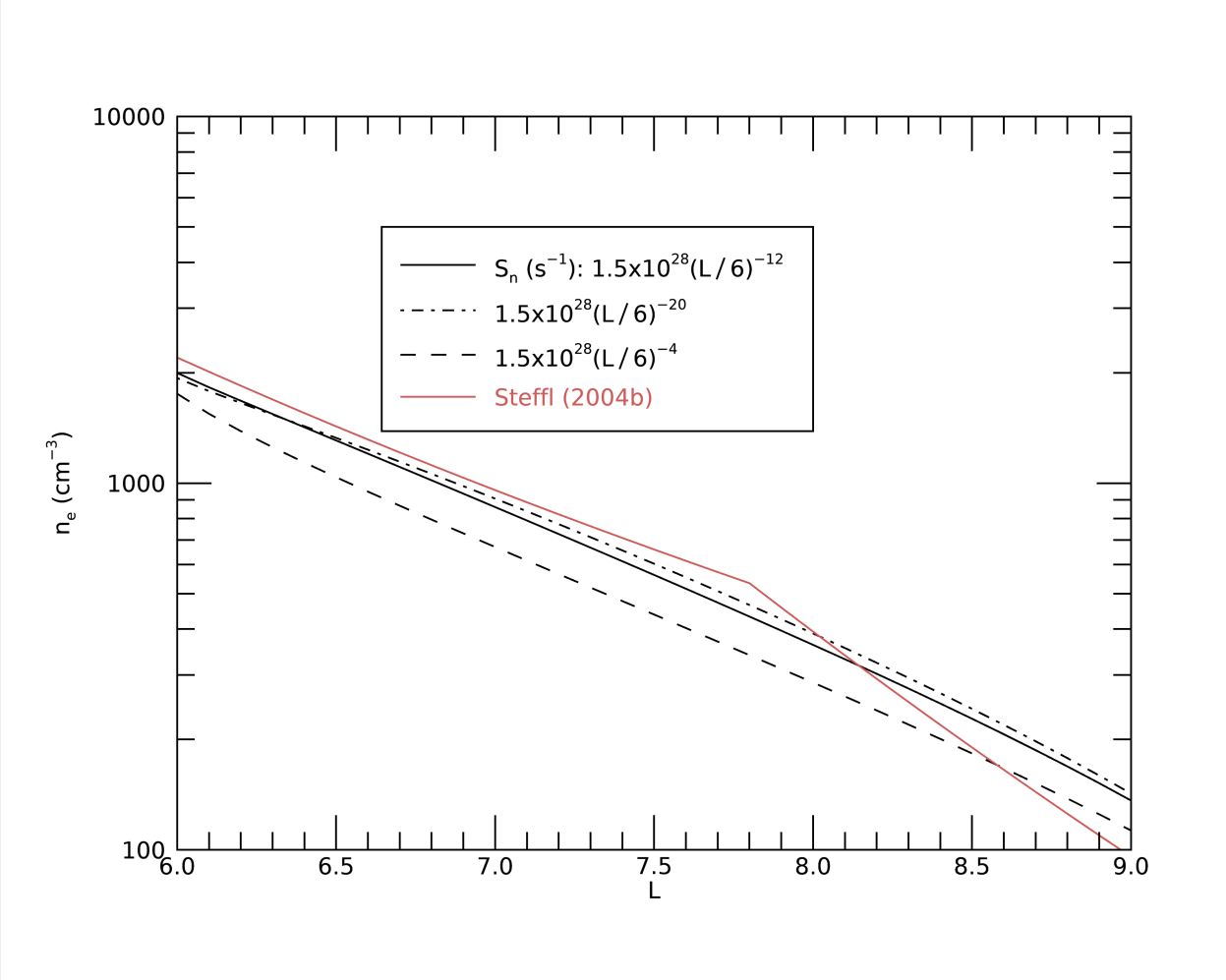

Figure 5.6: Radial Warm torus Model Output n_e, Varying S_n power law exponent.

In figures 5.7 and 5.8 and we explore differing power law exponents for the diffusion coefficient D_{LL} and their effect on model output. While holding the value constant at L=6.

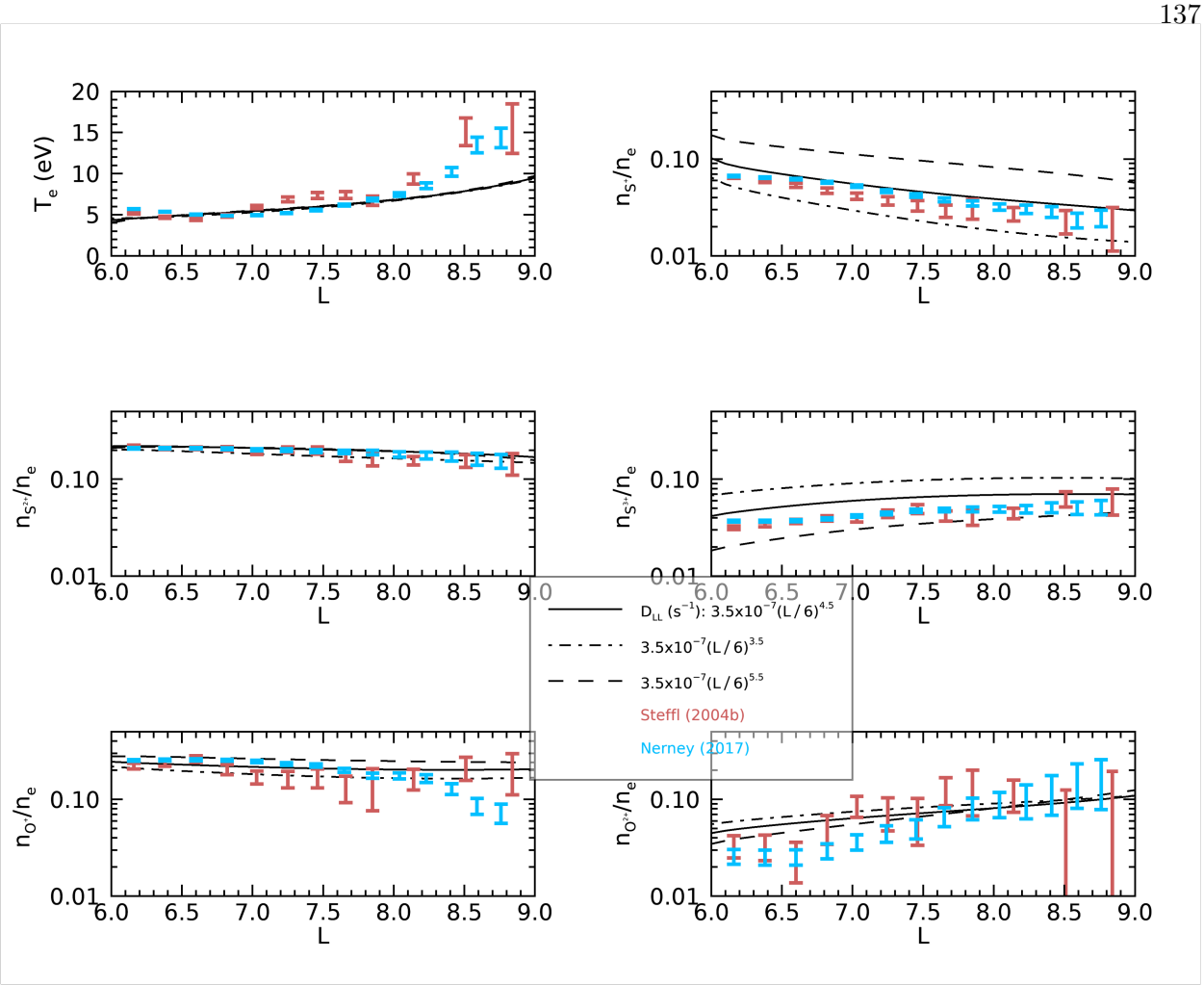

Figure 5.7: Radial Warm torus Model Output, Varying D_{LL} power law exponent.

Siscoe and Summers (1981) [127] showed that flux-tube interchange was unstable under the centrifugal force when $\frac{\partial NL^2}{\partial L} < 0$. Further, they showed that for centrifugally driven interchange the form of the diffusion coefficient was $D_{LL} = kL^m$. Brice and McDonough (1973) [17] previously showed this form for other flux-tube driven interchange motion. In Goertz et al. (1979) [58] they derived a power law exponent value of m=3 for atmospherically driven diffusion. Following Siscoe et al. (1981) [127] and Delamere et al. (2005) [40] we adopt an m value of 4.5 which matches the slope in NL^2 for the Ledge (L=5.7 to 7 R_J) and ignore the required m values of 12 and 4 to match the now considered transient nature of the Voyager NL^2 profile for $L > 7.1$ for the "Ramp" and

"Disk" region (Delamere et al. 2005) [40]. It is thought that outside of L=5.7 centrifugal-driven flux-tube interchange occurs and inside there it is due to ionospheric coupling which is encoded in a drop in the diffusion coefficient by a factor of 50 (Richardson et al. 1980) [106] which we will explore in the next section of our cold torus modeling.

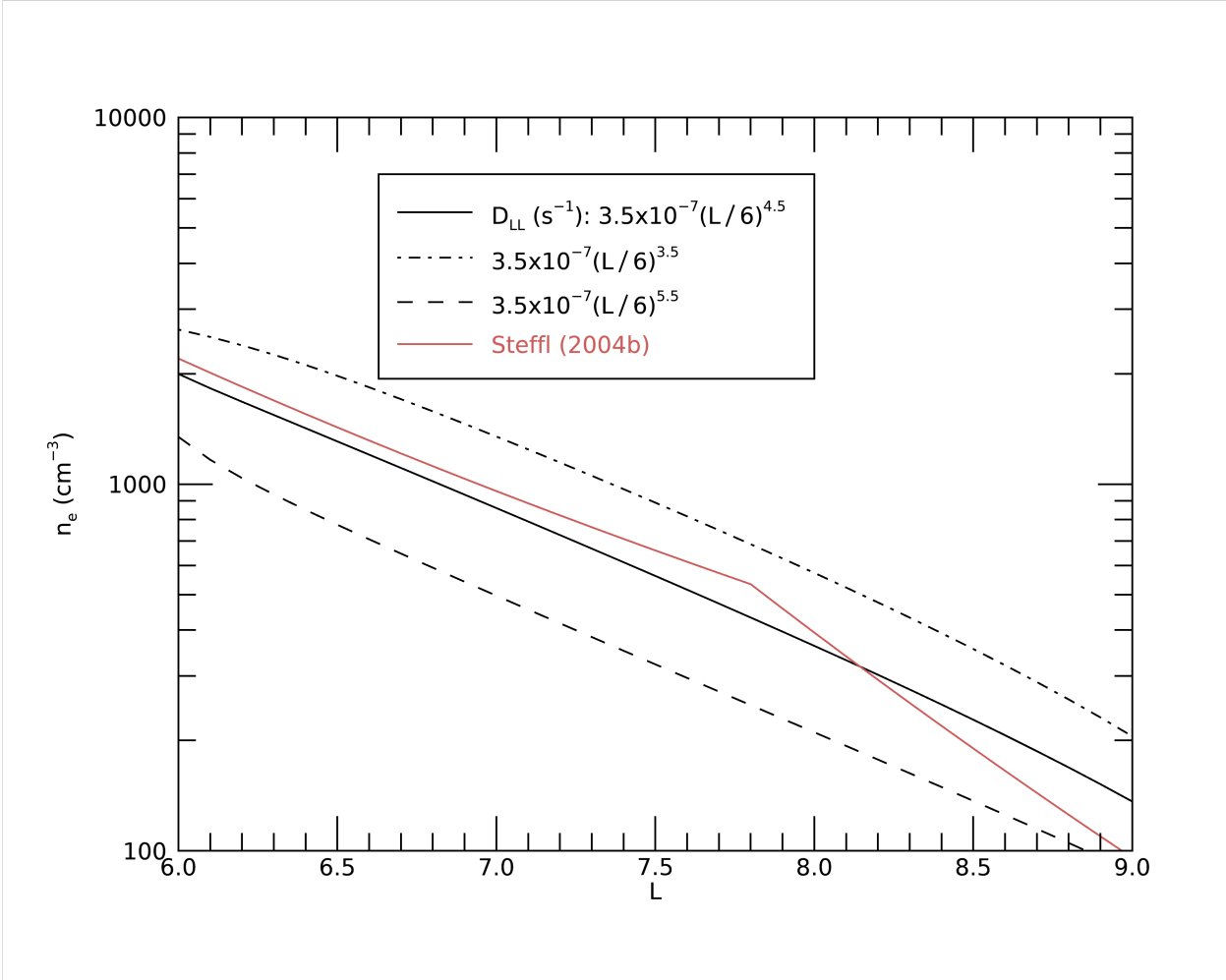

Figure 5.8: Radial Warm torus Model Output n_e, Varying D_{LL} power law exponent.

Likewise, in figures 5.9 and 5.10 we explored the effect of ion temperature boundary conditions and found little effect on output composition. Though of course, this did affect output ion temperature profiles significantly.

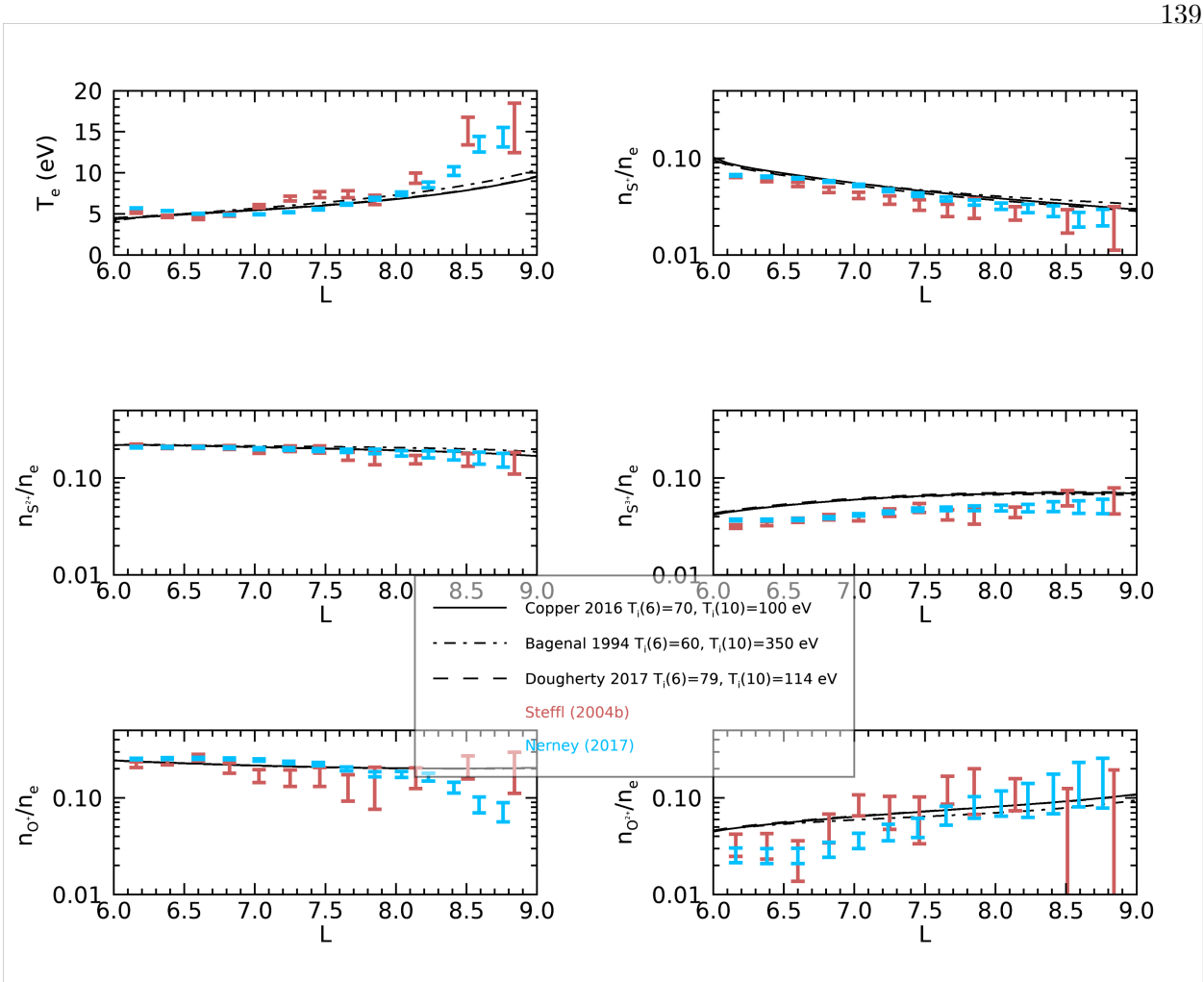

Figure 5.9: Radial Warm torus Model Output, Varying Ion temperature boundary conditions output composition radial profiles.

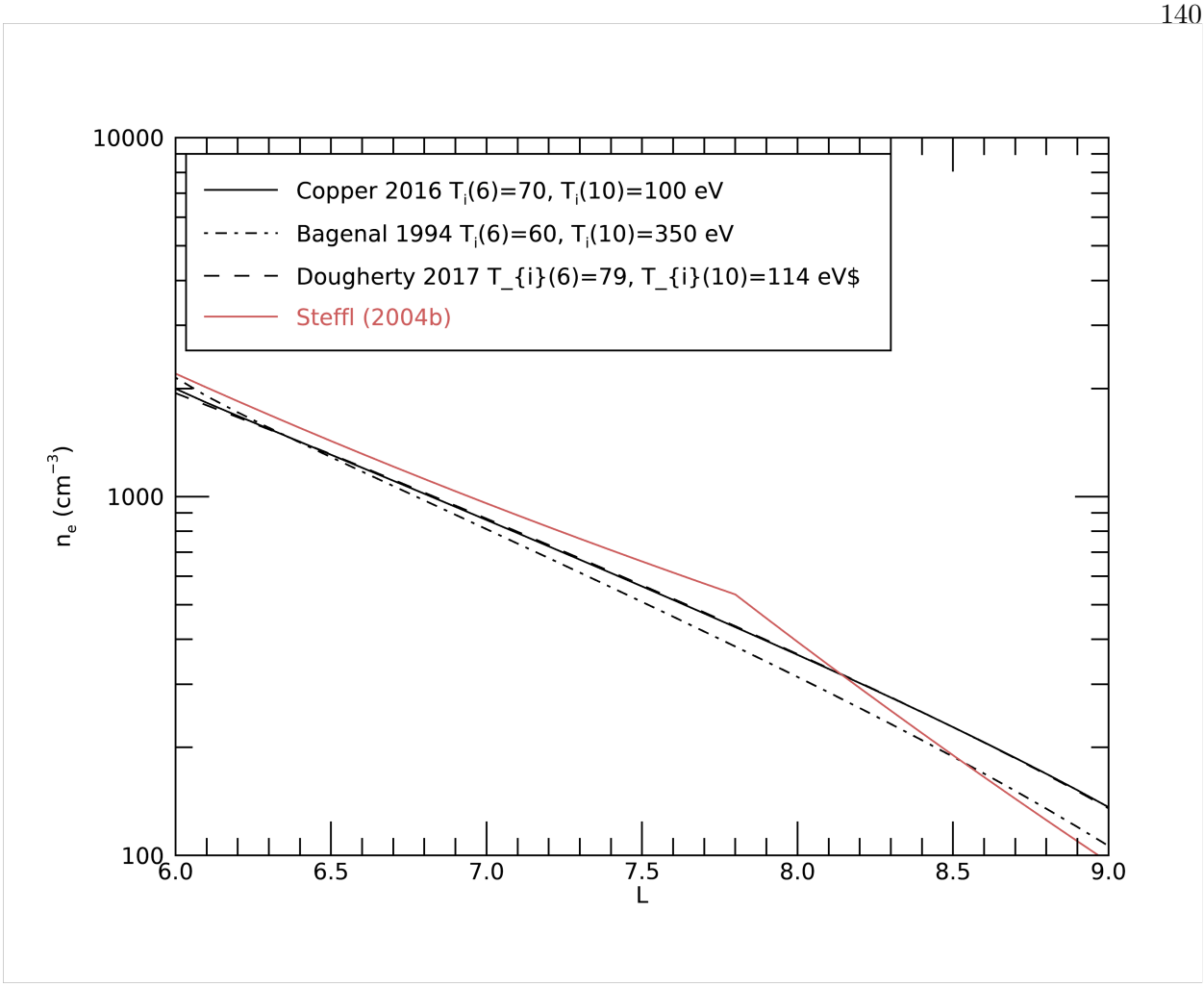

Figure 5.10: Radial Warm torus Model Output, Varying Ion temperature boundary conditions output electron density radial profile.

Taking our nominal case for the warm torus to be Copper et al. (2016) [33] inputs except for the fraction of hot electrons we adopt the power law exponent of 6 which better matches the core electron temperature profile. Plotting model output steady-state radial profiles of local densities, mixing ratios (n_i/n_e), temperatures, and NL^2 this gives us the following output in figure 5.11 (Case A in table 5.1). The ion temperatures have boundary conditions of 60 eV at L=6 and 100 eV at L=10 consistent with Copper. The ion boundary condition at L=10 drives the ion temperatures near the outer boundary at L=10. The fluxtube content is fixed at L=10 and given by a 0 boundary

condition at L=6.

Overall we find decent agreement between our model results and the previous model output of Copper et al. (2016) and Delamere et al. (2005). The output is not perfect of course but demonstrates the basic concept and capability of the model. In addition, we find our model output consistent with Cassini UVIS determined ion composition and electron temperatures of the warm Io plasma torus as determined by Steffl et al. (2004b) [137] and our reanalysis in Nerney et al. (2017) [96] as shown in chapter 2.

5.6 Cold Torus Only Modeling

Starting with a cold torus only model between 5-5.7 R_J we attempt to match the overall shape of the ribbon, gap region, and cold torus peak. We first apply a zero derivative in NL^2 at L=5.7 and fixed values at L=5. The true peak in the flux-tube mass contant from Voyager was at 5.7 R_J which is where the zero should be applied, but Delamere et al. (2005) [40] applied them at L=6 in order to compare with the Steffl et al. (2004b) radial profile between 6-9 R_J. Limiting the choice of the model to this range of interest meant that forcing the peak to be at L=6 required this condition to be set there. But now that we wish to move into the cold torus we apply it at L=5.7. With ion temperatures fixed to 1 eV at L=5 and 60 eV at L=5.7. We find that it is a delicate balance between too much source resulting in too high of temperatures and thus too high of scale heights to produce a cold torus peak. All model output has total fluxtube content monotonically increasing to L=5.7, but if the ion temperatures don't fall fast enough then the scale heights are too large, and the densities don't show a cold torus peak. But if there is too little source then the temperatures plummet to sub eV values inconsistent with reality. We tried having a narrow source function near L=5.7 so as to provide enough input of energy due to pickup from charge exchange and ionization of neutrals. The other competing factor is diffusion of mass and energy which allows the energy from pickup to diffuse inside the radial value where it is sourced. We impose power law source and diffusion coefficients and set the additional energy input from hot electrons to 0 ($F_{eh} = 0$) in this region consistent with thermalization and Sittler et al. (1987) [128]. We set

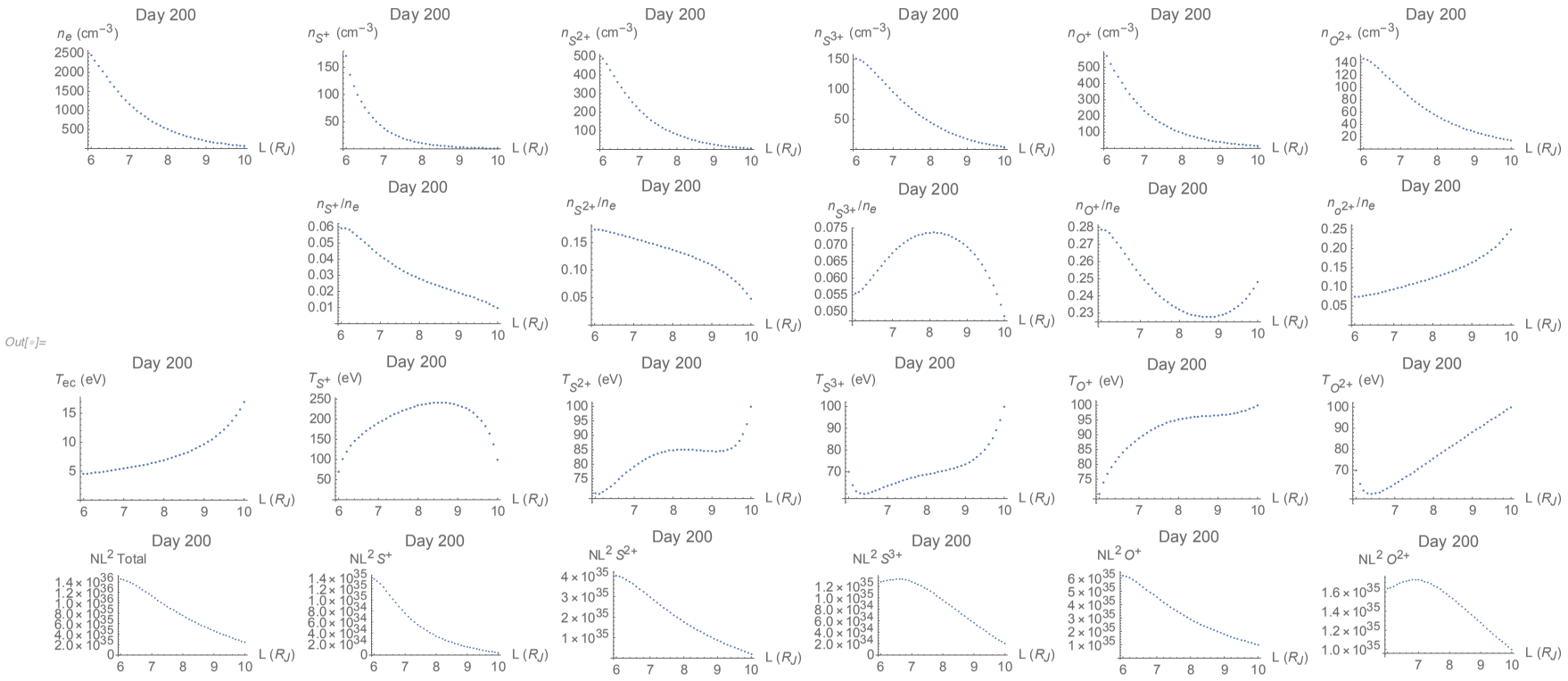

Figure 5.11: All standard model output for our nominal case for the warm torus with Copper et al. (2016) [33] inputs except for the fraction of hot electrons where we adopt the power law exponent of 6 which better matches the core electron temperature profile. (Case A in table 5.1)

the diffusion coefficient a factor of 50 lower than the warm torus consistent with a change in the flux-tube interchange process from centrifugally driven instability for $L > 5.7$ and for ionospheric driven inwards (Richardson et al. 1980, Siscoe and Summers (1981), and Goertz (1979)) [106] [127] [58]. With the same 4.5 power law of D_{LL} in. We used the same peak source profile from the warm torus but used a positive power law exponent to have it decrease inwards of Io. This led to either too much energy from the source or not enough density. It was a fine balance exacerbated by the nonlinear nature of the system.

We found we were able to create a gap region and cold torus peak in S^+ and O^+ by getting rid of the source entirely and setting the higher charge states to the flux-tube equivalent of 1 cm^3. Also instead of a zero derivative condition, we instead set the NL^2 values at L=5.7 of S^+ and O^+ with Bagenal (1994) [5]. Doing the same including the higher charge states did not allow us to create a cold torus. This allowed the mass and energy to diffuse inwards from the peak. It gave us the proper overall shape of NL^2 along with a gap region and cold torus peak in NL^2. The total NL^2 values monotonically decreased from the peak, but the ion temperatures and therefore scale heights fell from 60 to 1 eV faster resulting in such small scale heights that the mass piled up on the centrifugal equator as can be seen in figure 5.12 (Case B in table 5.1) where we vary the D_{LL} power law exponents. We find varying the D_{LL} power law exponent shifts the location of the cold torus peak in and out.

In figure 5.12 (Case B in table 5.1) we find that a cold torus and gap region solution is possible without a source which is instead provided by the fixed boundary flux-tube content at L=5.7 though this case has limited application due to our neglect of the higher charge states and lack of course profile. Nonetheless, we see that there is a fine line between too much pick-up energy, too little, and too much mass being added to the system. In addition, we see that the required condition to generate the gap is the ion and electron temperatures at first falling slower than the NL^2 profile. This means the scale heights are falling slower than the flux-tube mass content, so the local density decreases. Then in the cold torus peak region, we need the opposite to occur. We need the flux-tube mass content (NL^2) of each ion to fall slower than the scale heights $\left(\sqrt{T}\right)$ falls to

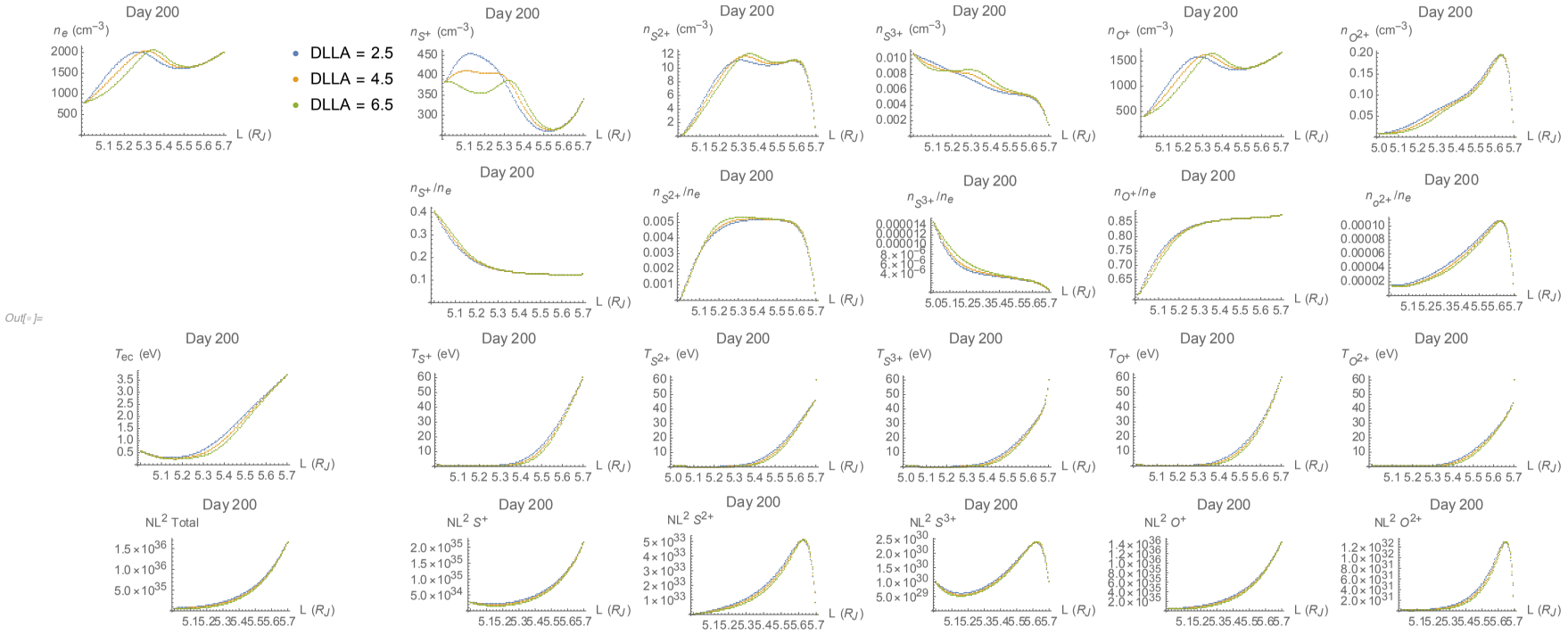

Figure 5.12: Vary DLL power law exponent cold torus only output (Case B in table 5.1) allows us to create a ribbon, gap region, and cold torus peak.

cause the local density to peak even though the total flux-tube mass content is still monotonically decreasing. We see that by varying the diffusion coefficient power law exponent, we can shift the location of the cold torus peak in and out which can be used to match observations and would imply a different diffusion coefficient profile required to match the dawn and dusk radial profiles from ground-based observations.

For the cold torus modeling we had to change our model resolution significantly due to numerical instabilities (due to finite differencing) and physics happening on smaller spatial scales than our model was resolving. In the cold torus modeling, we use a timestep of dt=10-50 seconds (depending on if the code crashed at 50), a radial spatial step of dL=0.005 to 0.025 R_J, and latitudinally we go from -30 to 30 degrees latitude with 0.1-degree stepsizes corresponding to 0.01 R_J spatial bins along the field lines for computing NL^2 and applying the latitudinal averaging schemes. The smaller timesteps from the warm torus by up to a factor of 100 were necessary due to instabilities in the diffusion finite differencing scheme. At larger timesteps, the code would become unstable. The scale heights for ions in the cold torus with temperatures of 1 eV are on the order of 0.1 R_J as opposed to the almost 1 R_J values found in the warm torus which is why the NL^2 calculations and latitudinal averaging scheme required this to properly resolve the ion distributions along the field lines. This additional resolution unfortunately significantly increases the time required to run the model to equilibrium. Without access to CU Boulder's supercomputing cluster to run the code at high resolution in time and space this work would not have been possible.

5.7 Cold Torus, Ribbon, and Warm Torus Self-Consistent Coupled Physical Chemistry Model

Moving the model in to include the cold torus and warm torus we move our inner boundary of the model in to L=5 and keep our outer boundary at L=10. Instead of having a 0 derivative in NL^2 for each ion at L=6 like we did near the peak we instead specify the values of NL^2 at L=5 and fix our ion temperatures at L=5 to 1 eV. These are consistent with the voyager analysis of Dougherty et al. (2017) and Bagenal (1994) [47] [5]. We keep the ion boundary conditions at L=10

consistent with Copper et al. (2016).

Following Richardson et al. (1980) and (1983) [106][105] we impose a discontinuity in D_{LL} of a factor of 50 at the Voyager observed peak in NL^2 at L=5.7. This forces the peak in NL^2 to occur here. Outwards of this peak, we have plasma and energy diffusing outwards, and inwards of this peak, we have plasma and energy diffusing inwards on average. I use a D_{LL} power law exponent of m=4.5 in both regions for our starting case consistent with Copper et al. (2016) [33] and similar to the value of m=3 used by Richardson et al. (1980) [106]. I take the fraction of hot electron (F_{eh}) increasing with radial distance with a power law exponent of 6 (which best match the Cassini core electron temperature as shown in figure 5.4) with a value of 0.2% at L=6 at 269 eV consistent with Copper et al. (2016) [33]. I force the fraction of hot electrons to 0 inside of L=5.7 consistent with thermalization.

We found that by cutting off the source at L=5.55, L=5.65, or 5.7 and trying many variable S_n profiles peaking at L=5.9 (the orbital radius of Io) and power laws decreasing in and out from this peak gave good results in the warm torus but resulted in a buildup of too much neutral oxygen and sulfur in the cold torus which resulted in ion temperatures far too high from continuous pickup to result in realistic ion and electron temperatures which need to drop to 1 eV in the cold torus. So instead we switched to a constant neutral density profile consistent with Koga et al. (2018b) [79] and modeling from Smith et al. (2022) [129] instead of a dynamically sourced profile. We applied a neutral density ratio of 3.8 to specify the neutral sulfur density profile as only neutral O was found from Koga et al. (2018b) [79]. Though the neutral source O/S ratio is 2 the output neutral steady-state ratio of densities of O to S was 4.1 and varied from 3-5 for typical conditions for a single cubic cm model at L=6 from our paper Nerney et al. (2020) [95]. We chose 3.8 arbitrarily to match the $\frac{n_{O^+}}{n_{S^+}}$ at L=5.7 of the ribbon.

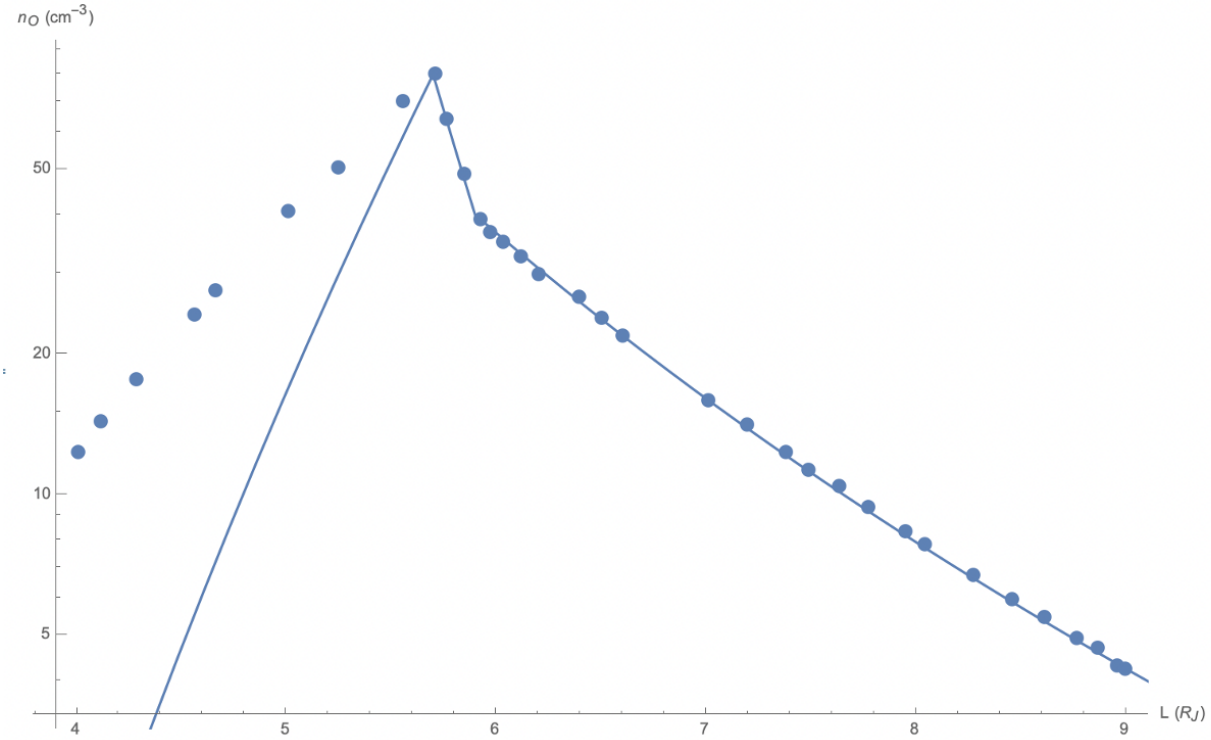

Figure 5.13: Constant Neutral Density Input Used Based on Koga et al. (2018b) [79]. The dots are the values from Koga et al. (2018b) [79] and the line is my adopted profile

Trying to use this Koga et al. (2018b) [79] profile resulted in too high ion temperatures inside 5.6 R_J. We think this is due to issues with projection effects in their modeling and in reality the neutral cloud falls off much faster. Koga's profile peaks at L=5.7 and falls off inside as a power law with an exponent of about 5.3. We switch this to a power law of 20 inside 5.7 for the constant neutral density profile used as shown in figure 5.13 and find much better results which are shown in figure 5.14. This implies to me that Koga overestimated the amount of neutral oxygen inside the peak at L=5.7 due to line-of-sight projection effects.

In figure 5.14 (Case C in table 5.1) we vary the discontinuity in D_{LL} applied at L=5.7 to be 25, 50, and 100 times lower inside L=5.7 but with the same power law exponent of 4.5 for all cases. As can be seen in the total flux tube content (NL^2) this forces the peak at L=5.7 and drives transport in and out from there. We still have a bit too much pickup energy piling up near the

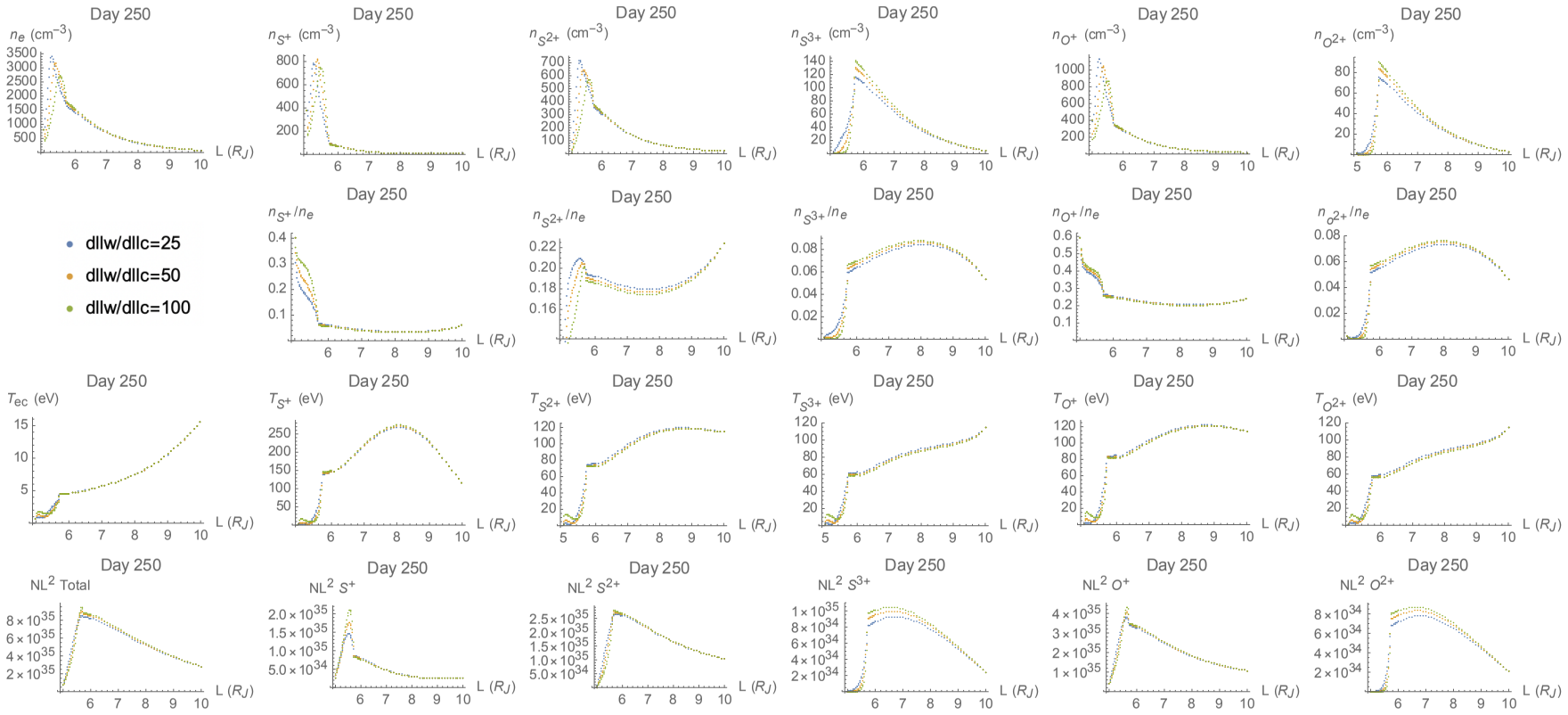

Figure 5.14: Vary DLL discontinuity Whole Torus Fixed Koga Neutral Profile With +12 Power Law inside L=5.7 (Case C in table 5.1)

inner boundary causing a rebound in temperatures. A further reduction in the neutral density profile inside 5.55 would help this. The same issues can be seen in figure 5.15 where we hold the discontinuity constant at 50 and vary the power law exponents between 2.5, 4.5, and 6.5.

In figures 5.14 and 5.15 (cases C and D in table 5.1) where we couple the warm and cold torus together we get a good overall fit to the warm torus profiles still. By placing the discontinuity in D_{LL} at L=5.7 we force the peak in flux-tube mass content to occur there. We observe no gap region because of the ion and electron temperatures and therefore the scale height $\left(\propto \sqrt{T_i}\right)$ always falls faster than the flux-tube mass content $\left(NL^2\right)$. So the local density continues to increase inwards of the peak in flux-tube mass content until it peaks in the cold torus and then decreases all the while the flux-tube content is dropping or the total number of ions on a field line. Likewise, we see a modest change in the peak local density and location by varying the power law exponent for a given discontinuity in the absolute value of the diffusion coefficient at L=5.7. By changing the value of the D_{LL} profile in the gap region we can make the flux-tube mass content fall faster in the gap region, but we also need slightly more pickup energy in this region to prevent the ion temperatures from falling quite as fast too. But it is a fine line between too much and too little in this inherently nonlinear system. This leads us to consider the next case where we look at trying to do just that.

Following Taylor (1996) [142] success in generating a cold torus peak with 2 separate discontinuities in D_{LL} we will now try the same instead of a single discontinuity at L=5.7 that Richardson and Siscoe (1980) [106] used. This strange behavior is also corroborated by modeling done by Herbert et al. (1996) [61] and effective diffusion coefficient values derived in Herbert and Sandel (1995) [64].

Taylor (1996) [142] found similar profiles to what I did in figures 5.14 (Case C in table 5.1) and 5.15 (Case D in table 5.1) with a single discontinuity in D_{LL} as can be seen in their figure 6.2. In my figure 5.16 I show Taylor's figure 6.3 you can see their derived profile of ion density, temperature, and NL^2. They had only a single effective ion species and no separate energy diffusion equation but instead simply determined the mean energy per ion in each radial bin as NL^2 diffused.

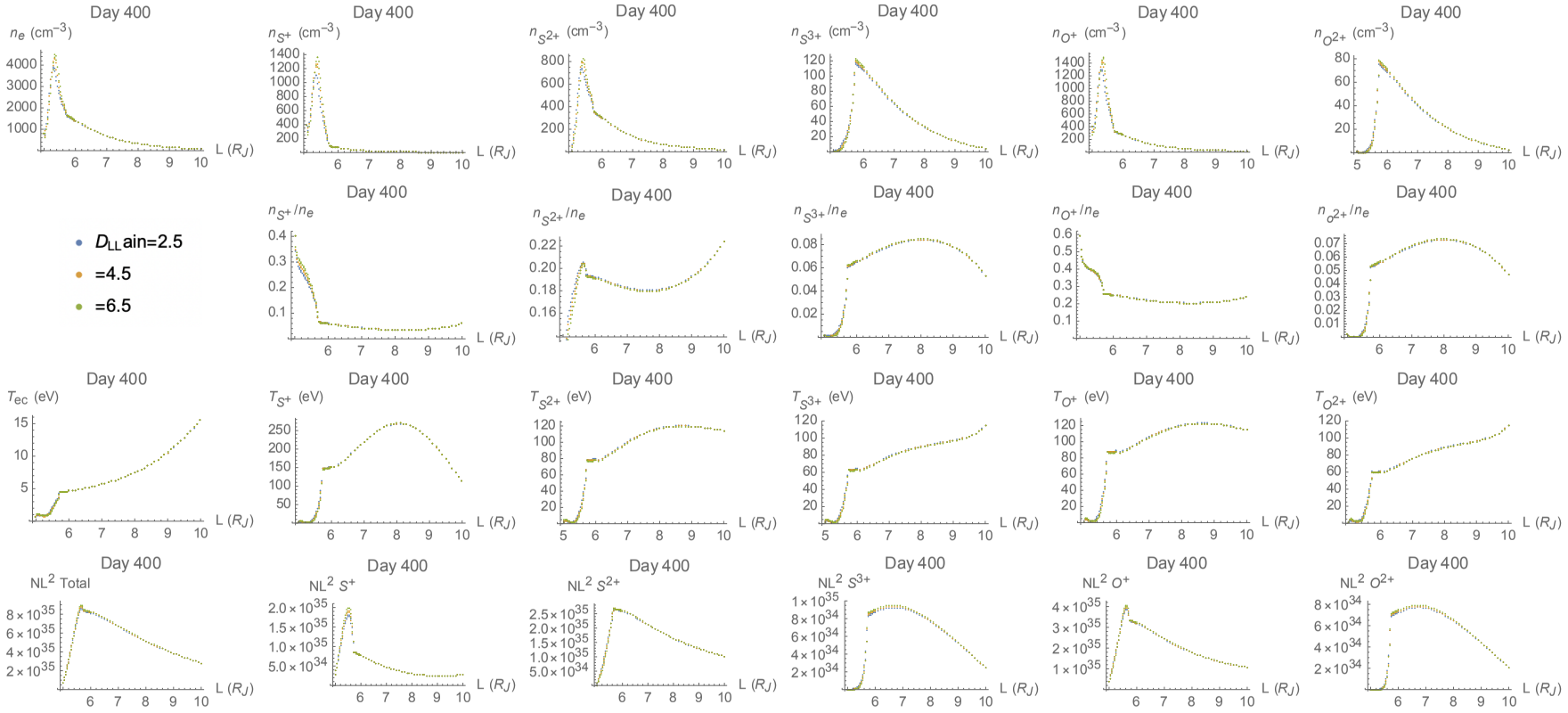

Figure 5.15: Vary DLL exponent in cold torus Whole Torus output Fixed Koga Neutral Profile With +12 Power Law inside L=5.7 (Case D in table 5.1)

Further, they applied a source to that single ion NL^2 diffusion equation not to the local neutrals as we did in the warm torus and tried in the cold torus. Their source shape came from Brown (1994) [23] and arbitrarily cut it off at L=5.5 which I agree with as necessary to prevent too much pickup energy from keeping the ions too warm inside L=5.5. They assumed a constant pickup velocity of 57 km/s which is true at Io's orbit but not as a function of L assuming corotation. We apply the pickup velocity and therefore temperature given by the difference in corotation to the orbital velocity at a given L shell. They also did not include any loss except in the boundaries. Taylor did not evolve the electron temperature in time and instead held the electron temperature constant given by the Voyager empirical profile and coupled it to the ion temperature via Coulomb collisions. They also used a simple scale height approximation to convert between NL^2 and local density. As a result of all of these differences between our models, it will be hard to make a direct comparison.

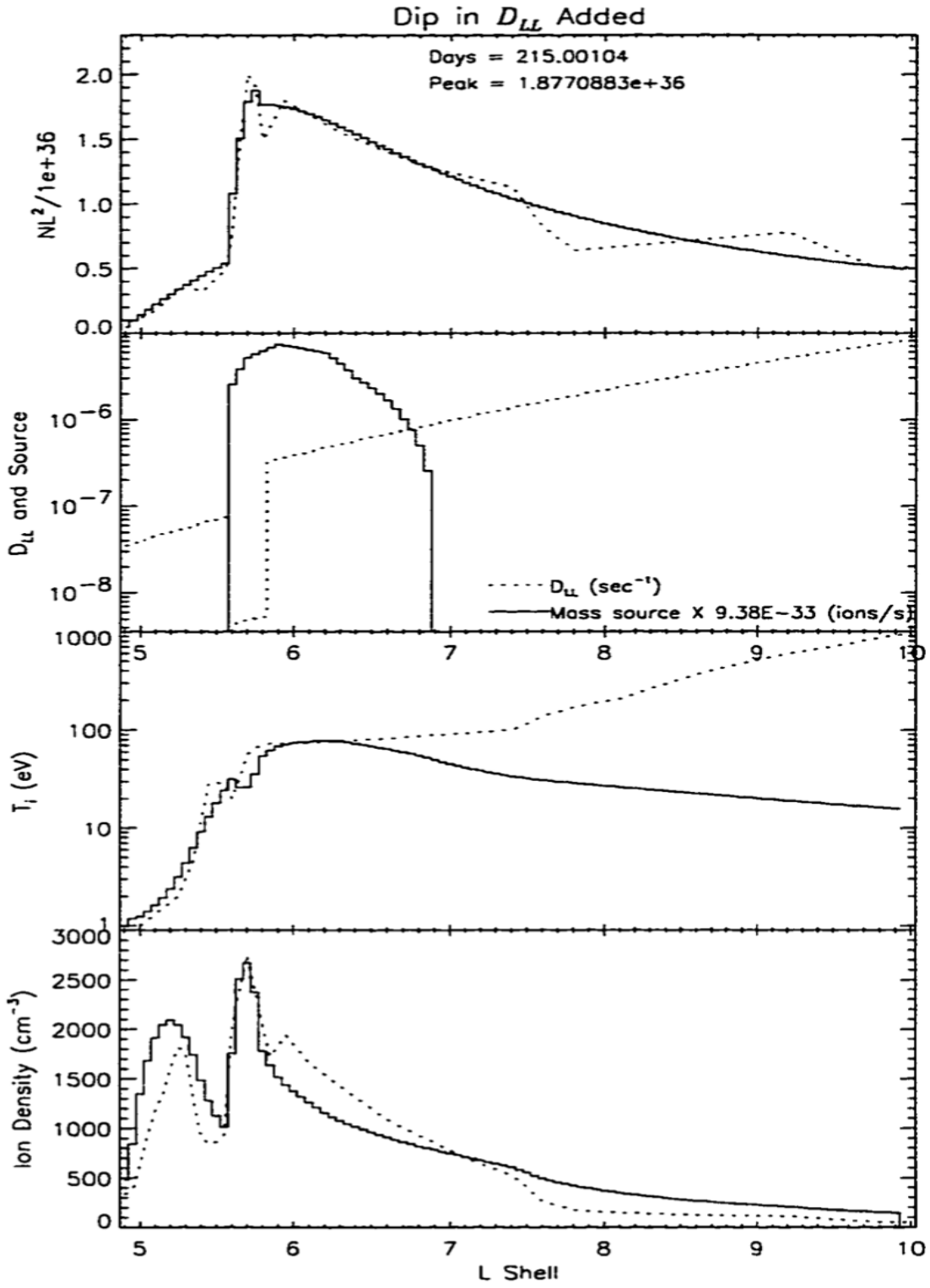

Figure 5.16: Figure 6.3 from Taylor (1996) showing their model output single ion NL^2, density, temperature, and input radial source profile source function from Brown (1994)[23] and input D_{LL} profile.

There are pros and cons to the added complexity of my model. I believe we are closer to the reality of the physical situation, but as a result of that added complexity we have a much larger parameter space to explore, and due to the nonlinear nature of the system this has led to great hardship in matching their results.

In figure 5.17 I show our whole torus piecewise continuous D_{LL} profile that I use to match the general shape of what Taylor et al. (1996) [142] used, but we scale it at L=6 to the value of Copper et al. (2016) [33] to keep the warm torus as unchanged as possible. We use Taylor's [142] m value of the diffusion coefficients power law exponent of m=6 in the ribbon and cold torus region for $L < 5.75$ but Copper's [33] value of 4.5 outward of there. Taylor had approximately a discontinuity of a factor of 60 drop inwards of L=5.75 and an increase of 20 at L=5.55, so we do the same experiment, scaled appropriately.

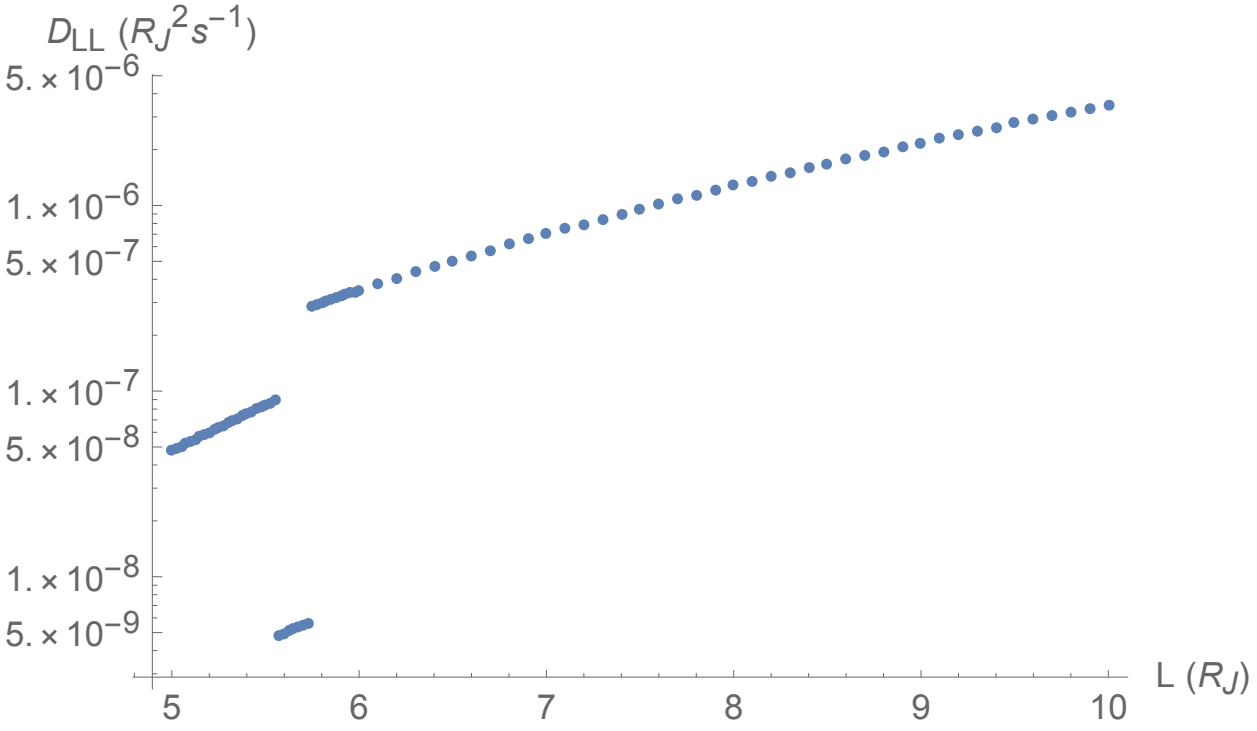

Figure 5.17: Taylor et al. (1996) [142] Scaled to Copper et al. (2016) [33] D_{LL} profile used.

I first again try to use a neutral source profile S_n with the D_{LL} shown in 5.17 with S_n given by power laws peaking at L=5.9 (the orbit of Io). The power law of -12 for $L > 5.9$ again does a great job matching the overall warm torus profile but a power law of +12, +15, and +20 still led to a build-up of too much pickup energy and temperatures remaining too high to result in a collapse of ion densities to the centrifugal equator. This time following Taylor et al. (1996) and Herbert et al. (1996) [142][61] we cut off our neutral source around L=5.5. We tried cutting it off at L=5.5, 5.55, 5.6, and 5.65 for various source exponents inside 5.9 but still had the same issues. We also varied the overall source value up and down from the nominal value of 1.5×10^{28} neutrals/s. In figure 5.18 (Case E in table 5.1) we show model output given figure 5.17's D_{LL} profile with a power law of +15 inwards of 5.9 and -12 outwards for a peak value of 1.5×10^{28} neutrals/s with an O/S of the neutral source of 2 consistent with dissociation of SO_2. We also tried a Gaussian source profile of various FWHM and had similar issues of either having too little ion temperature inside L=5.6 or too high, and no cold torus peak was found.

Instead, we again switch to a constant neutral atomic O and S radial profile throughout the model run and run the model to steady state. We adopt the Koga et al. (2018b) [79] profile but again with the power law of 12 inside L=5.7 as shown in figure 5.13 with $n_O/n_S = 3.8$ but this time cut off both neutral densities to 0 inside 5.65. The overall peak electron density given by neutrality at L$\approx$ 5.7 was found to be too low at 1400 cm^{-3} wanting to get this up to near 3100 cm^{-3} we increased the overall neutral profiles by a factor of $\sqrt{3100/1400} \approx 1.5$ which gave us modest cold torus peak and our best profile yet to match the overall character of the warm torus, cold torus, and gap region. Increasing this factor further gave a better cold torus peak but the overall peak electron density found was far too high. This model output is shown below in figure 5.19 (Case F in table 5.1).

Showing one last model run I take the Herbert (1996) [61] D_{LL} and "Mass Loading profile" which are shown in their figure 1 in terms of relative values. No absolute values are given. I assumed his ion mass loading rate was directly proportional to our neutral source rate S_n and scaled it up to a peak value of 1.5×10^{28} neutrals/s at L=5.9. I likewise scaled their D_{LL} profile up to Copper

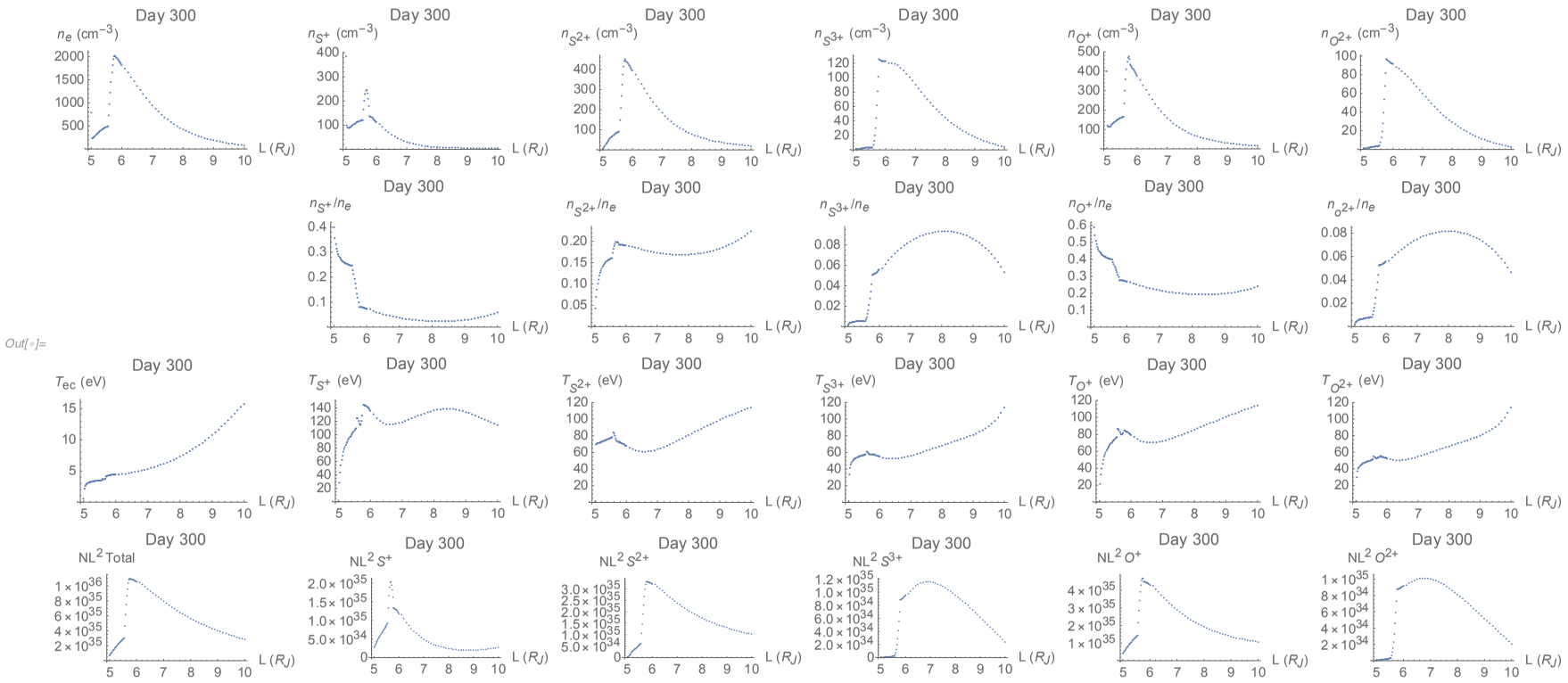

Figure 5.18: Model Output for Taylor Scaled DLL profile with S_n power law of 15 inside 5.9 and -12 outside with a cutoff of the source at L=5.6. The value of the peak source at L=5.9 was 1.5×10^{28} neutrals/s at O/S=2. (Case E in table 5.1)

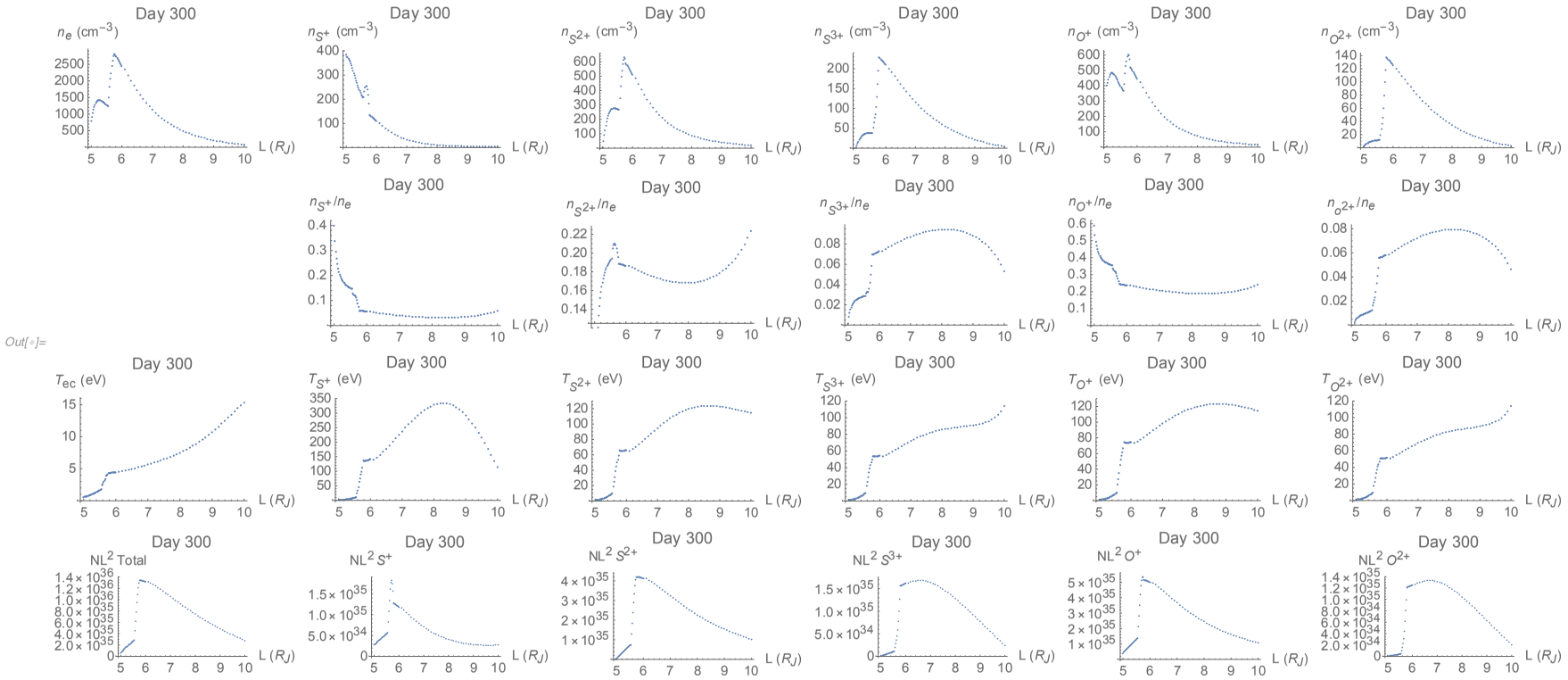

Figure 5.19: Model Output for Taylor (2016) [142] Scaled D_{LL} profile to Copper et al. (2016) [33] value at L=6 with Koga et al. (2018b) [79] neutral scaled up uniformly by a factor of 1.5 assuming $n_O/n_S = 3.8$ with +12 power law inside and a 5.7 neutral density cutoff at 5.65 (Case F in table 5.1)

et al. (2016) [33] D_{LL} value at L=6 of 3.5×10^{-7} $R_J^2 s^{-1}$. These profiles can be seen in figure 5.20

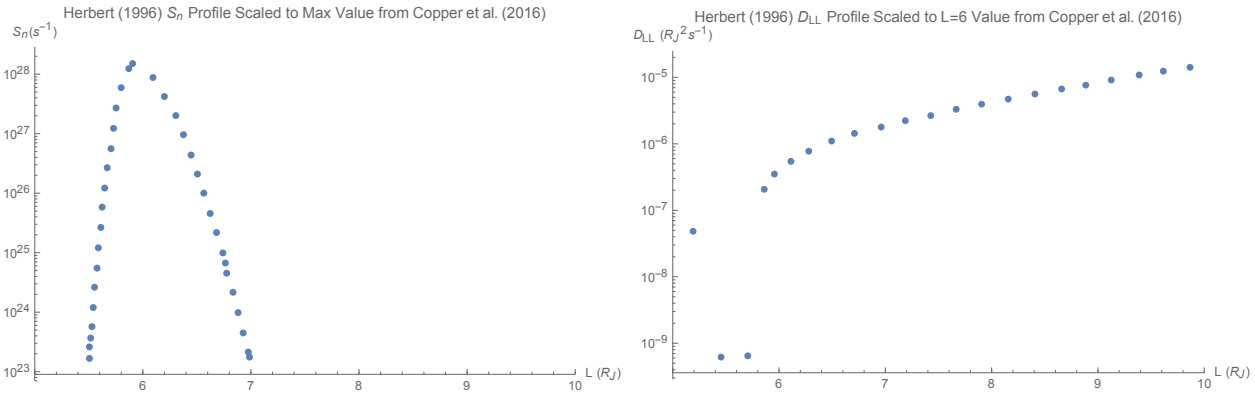

Figure 5.20: D_{LL} and S_n profile used from Herbert (1996) Scaled to Copper values. Values shown were interpolated to the spatial grid we used for our model

In figure 5.21 (Case G in table 5.1) shown above I plot the model output assuming the D_{LL} and S_n shown in figure 5.20 with an O/S=2 of the neutral source. This source profile is insufficient to provide enough pickup energy to keep the ion and core electron temperatures from falling to sub-eV values. This rapid collapse inward of L=5.7 is inconsistent with the Voyager-derived ion and electron temperatures (Bagenal (1994) and Dougherty et al. (2017)) [5][47] which require a more gradual descent to 1 eV at L=5, not sub-eV values inside L=5.7. Moreover, this rapid collapse results in only a single peak in local density with no gap region able to develop between the ribbon and cold torus local density peak. The peak in electron density in figure 5.21 is at L=5.4 R_J. So in a sense, there was a ribbon peak and a cold torus peak at L=5.4, but no gap region was able to develop because this requires the slope in NL^2 to be larger in the gap region than the scale height slope so that the plasma is able to spread out along a field line. To get a cold torus peak, we then need the NL^2 gradient inwards of L=5.55 to be shallower than the scale height gradient so that even as the total flux-tube content is still monotonically decreasing the scale height is dropping faster in this region resulting in a collapse of the plasma to the centrifugal equator.

In table 5.1 I show a summary of cases A-G in which I show the model input parameters

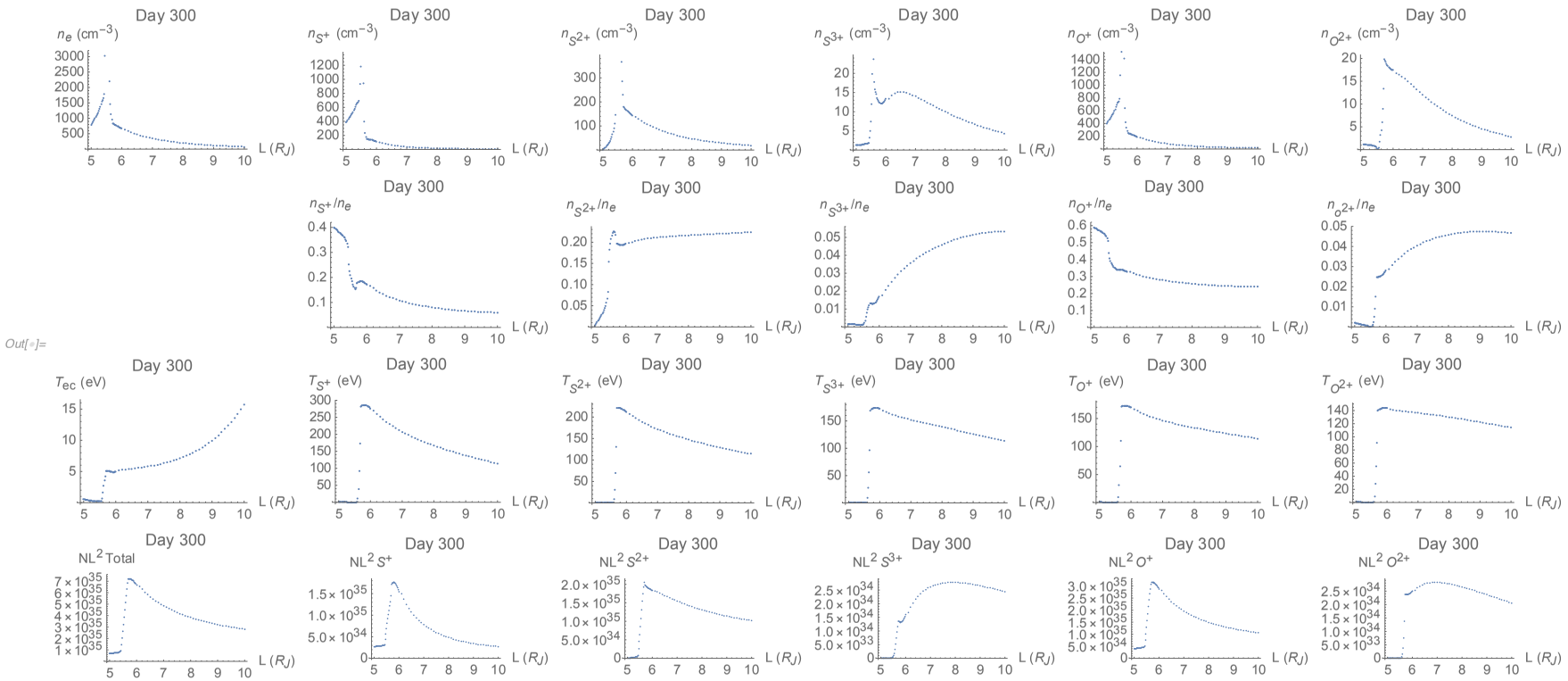

Figure 5.21: Model Output For Herbert (1996) D_{LL} and Mass Loading profile scaled to Copper et al. (2016)'s D_{LL} value at L=6 and peak S_n value of 1.5×10^{28} neutrals/s with O/S=2 of the neutral source (Case G in table 5.1)

varied, things that worked, things that didn't work, and lessons learned.

Case	Input Parameters	Things that worked	Things that didn't work	Lessons Learned
A	$S_n = 1.5x10^{28}(L/6)^{-12}$, $D_{LL} = 3.5x10^{-7}(L/6)^{4.5}$, $F_{eh}=0.002(L/6)^6$, T_{eh}=270 eV Warm 6-10 R_J Model, Copper Boundary Conditions (B.C.)	We can match warm torus composition and temperatures	N/A	Reproduce Copper et al. (2016) Model output for warm torus
B	No Source, $D_{LL} = 7x10^{-9}(L/6)^{4.5}$, No hot electrons Cold 5-5.7 R_J Model, Bag (1994) values Fixed NL^2 at only S^+ and O^+ ions B.C. T_i= 1 eV and 60 eV B.C.	We found a cold torus peak, gap region, and ribbon for our 5-5.7 model	Adding in higher charge states. Using a source profile and 0 deriv. at 5.7 instead of a fixed values	By changing the D_{LL} profile we could move the cold torus peak.
C	Fixed neutrals given by Koga et al. (2018b) profile but falling off at +12 exp inside 5.7 n_o/n_s=3.8 $D_{LL} = 3.5x10^{-7}(L/6)^{4.5}$, for L≥5.7 $7x10^{-9}(L/6)^{4.5}$, for L< 5.7 for middle case of 50 drop. Drop varied between 25,50,100. L>5.7 D_{LL} kept same along with all other inputs $F_{eh}=0.002(L/6)^6$ for L≥5.7, T_{eh}=270 eV F_{eh}=0 for L<5.7 5-10 R_J Model, Fixed conditions both ends Bag (1994) values Fixed NL^2 T_i= 1 eV and 100 eV B.C.	NL^2 profiles match the Voyager profiles, and overall temperature profiles look right. Discontinuity in D_{LL} at L=5.7 gives peak in NL^2 at L=5.7. Warm torus solution looks right overall	No gap region found and cold torus peak too high rising straight from ribbon. T falls off too fast in this region and stays flat resulting in local density continuing to increase from 5.7 to cold torus peak. Inwards of 5.3 the neutral density is still too high and provides too much energy from pickup pulling up temps.	Changing Discontinuity in D_{LL} value peak in local density in and out. Warm torus solution preserved overall but no gap region produced as temperatures fell off too rapidly but then near inner boundary came up due to. Neutral density must go to 0 inside 5.55 but Koga neutral density slope of 5.3 inside 5.7 still too shallow as resulting temperatures to high in that case
D	Fixed neutrals given by Koga et al. (2018b) profile but falling off at +12 exp inside 5.7 n_o/n_s=3.8 $D_{LL} = 3.5x10^{-7}(L/6)^{4.5}$, for L≥5.7 $7x10^{-9}(L/6)^{4.5}$, for L< 5.7 for middle case of 4.5 exp. exp varied between 2.5, 4.5, 6.5 L>5.7 D_{LL} kept same along with all other inputs $F_{eh}=0.002(L/6)^6$ for L≥5.7, T_{eh}=270 eV F_{eh}=0 for L<5.7 5-10 R_J Model, Fixed conditions both ends Bag (1994) values Fixed NL^2 T_i= 1 eV and 100 eV B.C.	NL^2 profiles match the Voyager profiles, and overall temperature profiles look right. Discontinuity in D_{LL} at L=5.7 gives peak in NL^2 at L=5.7. Warm torus solution looks right overall.	No gap region found and cold torus peak too high rising straight from ribbon. T falls off too fast in this region and stays flat resulting in local density continuing to increase from 5.7 to cold torus peak. Inwards of 5.3 the neutral density is still too high and provides too much energy from pickup pulling up temps.	Changing D_{LL} exponent (exp) inside L=5.7 changed absolute values of peak density and shifted the peaks in and out slightly. Overall the profiles are more sensitive to the absolute value of D_{LL} as shown in case C than the exps we changed in this case. Neutral density must go to 0 inside 5.55. but Koga neutral density slope of 5.3 inside 5.7 too shallow as resulting temps too high in that case

E	$S_n = 1.5x10^{28}(L/6)^{-12}$ for $L \geq 5.9$ $= 1.5x10^{28}(L/6)^{12}$ for $5.6 \leq L < 5.9$ $= 0$ for for $L < 5.6$ Notched Taylor (1996) D_{LL} used with factor 60 drop at 5.7 and 20 increase at 5.55 scaled to Case C value outside 5.7 with exp=6 inside 5.7 and 4.5 outside to match warm torus $F_{eh}=0.002(L/6)^6$ for $L \geq 5.7$, $T_{eh}=270$ eV, $F_{eh} = 0$ for $L < 5.7$ 5-10 R_J Model, Fixed conditions both ends Bag (1994) values Fixed NL^2 T_i= 1 eV and 100 eV B.C.	NL^2 profiles match the Voyager profiles with a steeper slope between 5.55 and 5.7. Warm torus solution looks right overall.	Temperatures stayed too high so the peak in density was at L=5.7 and no gap region or cold torus peak form.	Cutting off the source at 5.6 still resulted in too much pickup energy coming into smaller L values resulting in the scale heights staying too high to collapse to the equator. However overall shape of NL^2 profiles is right and matches Voyager profiles including slope between 5.55-5.7. Notched D_{LL} is the way to achieve this.
F	Fixed neutrals given by 1.5x Koga et al. (2018b) profile but falling off at +12 exp $L < 5.7$ $n_o/n_s=3.8$ cutoff to 0 neutrals for $L < 5.65$ Notched Taylor (1996) D_{LL} used with factor 60 drop at 5.7 and 20 increase at 5.55 scaled to Case C value outside 5.7 with exp=6 inside 5.7 and 4.5 outside to match warm torus $F_{eh}=0.002(L/6)^6$ for $L \geq 5.7$, $T_{eh}=270$ eV, $F_{eh} = 0$ for $L < 5.7$ 5-10 R_J Model, Fixed conditions both ends Bag (1994) values Fixed NL^2 T_i= 1 eV and 100 eV B.C.	We get a cold torus peak, and gap region in O^+ and electrons and the NL^2 profiles match the Voyager profiles with a steeper slope between 5.55 and 5.7 Overall temperature profiles look right. Warm torus region looks right overall.	No gap region in S^+ found and density continues to increase to inner boundary at L=5. S^+ temperatures fell too quickly preventing gap region from forming.	Notched D_{LL} profile achieves correct NL^2 profiles including slope between L= 5.55-5.7. Cutting off neutrals at 5.65 allows enough energy to diffuse in to 5.55 but then fall off inside there. Total S^+ density wasn't high enough and temperatures fell off too quickly requiring higher source of neutral S and smaller ratio of n_o/n_s for given Koga n_o profile in cold torus.
G	Herbert (1996) S_n and D_{LL} shape used scaled to Case C peak S_n and D_{LL} value at L=6, $F_{eh}=0.002(L/6)^6$ for $L \geq 5.7$,$T_{eh}=270$eV $F_{eh} = 0$ for $L < 5.7$ 5-10 R_J Model, Fixed conditions both ends Bag (1994) values Fixed NL^2 T_i= 1 eV and 100 eV B.C.	Overall shape of NL^2 is right using Herbert notched and scaled D_{LL} profile. Including slope between 5.7-5.55. Mixing ratios in warm torus are still correct overall.	Temperatures in cold torus fall off too quickly resulting in no gap region and local densities. Overall densities in warm torus too low.	The Gaussian shaped neutral source profile does not provide enough energy for the cold torus or enough density for the warm torus. However, the overall NL^2 looks right given the scaled notched shape of D_{LL}. Need more source between 5.55-5.7 and more extended source outside 6

Table 5.1: Table of Physical Chemistry Model runs for Cases A-G

5.8 Radial Transport Timescales

In chapter 3 [95] we explored the parameter space of a cubic cm physical chemistry model located at L=6. One of the input parameters of this model was an effective transport timescale which was a loss term for mass and energy from the system. At each iteration, the model density loss term for each ion species (α) was $\frac{n_\alpha}{\tau}$ and the energy loss term was $\frac{3n_\alpha T_\alpha}{2\tau}$. We found our best fit to match Cassini-derived composition was 72 days though there was a range of values between 40 - 72 days that had similar best fits due to the anti-correlation between the radial transport timescale and neutral source rate shown in figure 3.7 and table 3.4. In Bagenal and Delamere (2011) [6] they showed that the radial transport time to go from L=6 to L=10 took between 11 and 60 days. This corresponded to radial plasma mass transport rates of 1.4 tonnes/s and 0.26 tonnes/s respectively. They determined these timescales by mass conservation and empirical radial density scale height profiles.

In Delamere et al. (2005) and Copper et al. (2016) [40] [33] following Cheng (1986) [29] and Schreier et al. (1998) [117] they estimated the radial transport timescale by integrating the radial transport equation. In Delamere et al. (2005) [40] they found the integrated transport time from L=6 to L= 9 is ranged between 100-200 days with their best fit to the Steffl et al. (2004b) [137] Cassini profiles at 140 days. Copper found a transport time of 40 days [33] though we now believe there was an error in their code calculating the transport timescale and the Delamere group now gets more like 120 days using Copper's model with standard inputs from Copper et al. (2016)[33] (D.A. Coffin Personal communication 2022). The error did not change any other model output. The method they used that we will also employ is as follows. Taking the radial Fokker Planck equation and approximating the time derivative as a $-\frac{NL^2}{\tau}$ gives us

$$L^2 \frac{d}{dL}\left(\frac{D_{LL}}{L^2}\frac{d\left(NL^2\right)}{dL}\right) \approx -\frac{NL^2}{\tau} \tag{5.24}$$

τ_i is calculated in each spatial bin i of width ΔL. In the limit that $\Delta L \to 0$, N/τ_i is a constant.

Integrating both sides with respect to L over a given bin with the above assumption gives us

$$\int -\frac{N}{\tau} dL \approx -\frac{N}{\tau}\Delta L = \int \frac{d}{dL}\left(\frac{D_{LL}}{L^2}\frac{d\left(NL^2\right)}{dL}\right)dL = \frac{D_{LL}}{L^2}\frac{d\left(NL^2\right)}{dL} \tag{5.25}$$

This gives us the approximate solution for τ_i as a function of L in each bin i of width ΔL

$$\tau_i \approx -\left(\frac{NL^2\Delta L}{D_{LL}\frac{d\left(NL^2\right)}{dL}}\right)_i \tag{5.26}$$

We numerically determine the righthand side of equation 5.26. Then we sum this from the peak in NL^2 outwards to the outer boundary at $L = 10$ or inwards to the inner boundary at $L = 5$.

That is the "integrated" transport timescale or ITT is

$$ITT = \sum_i \tau_i \tag{5.27}$$

This can be done for each ion species separately to get separate timescales for each dependent on their respective NL^2 profiles but following Delamere et al. (2005) [40] and Copper et al. (2016) [33] we instead do this for the total NL^2 profile which is the sum of each which instead gives us an effective radial transport timescale.

Taking our nominal warm torus (6-10 R_J) D_{LL} and NL^2 profile from figure 5.11 we find that ITT is about 130 days as shown in figure 5.22

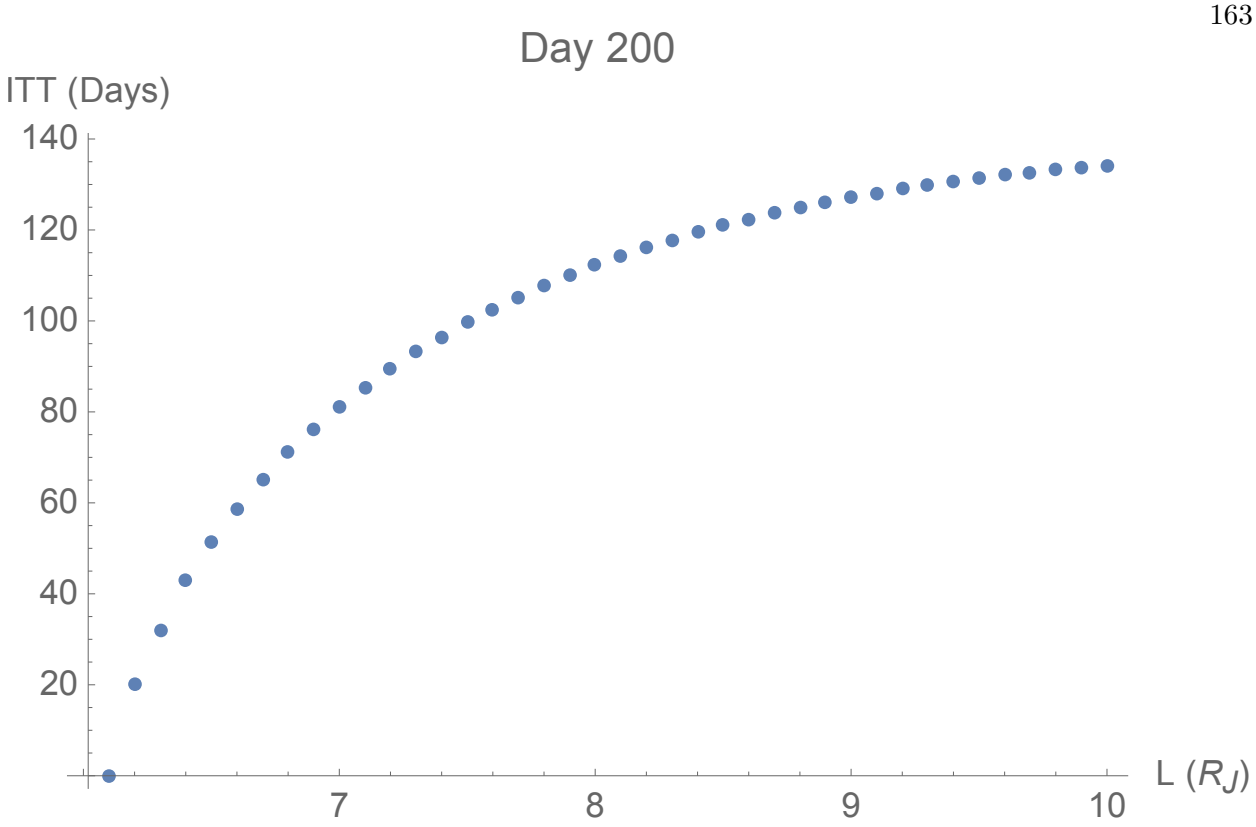

Figure 5.22: Our Nominal Warm Torus Integrated Transport Timescale from 6-10 R_J.

We find our value of 130 days much more consistent with Delamere's [40] value of 140 days instead of Copper's [33] 40 days. Doing the same for our nominal cold torus only model from figure 5.12 gives us about 500 days as shown in figure 5.23.

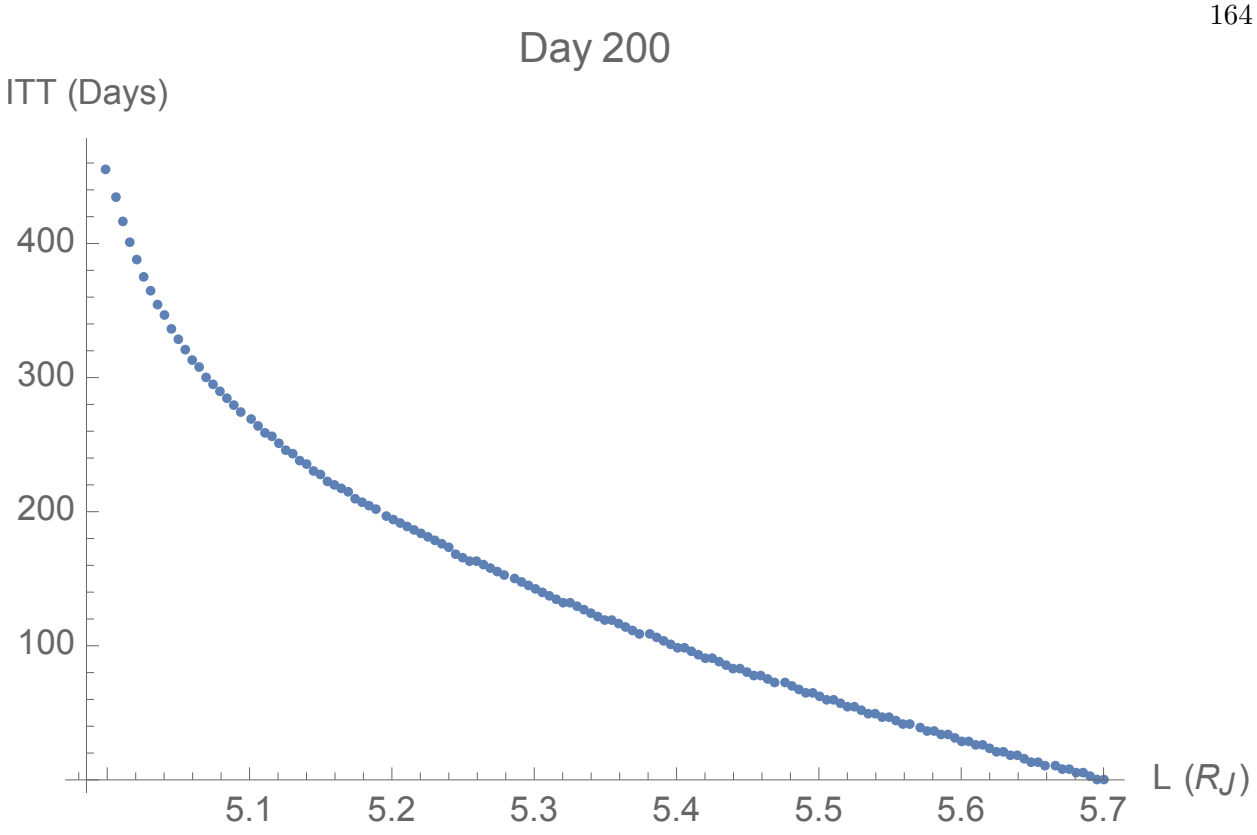

Figure 5.23: Our Nominal Cold Torus Only Integrated Transport Timescale from 5.7-5.0 R_J.

Again we do the same for the coupled whole torus model (5-10 R_J) corresponding to the middle case from figures 5.14 and 5.15 we find 800 days to get from 5.7 to 5 and 400 days to get from 5.7 to 10 as shown in figure 5.24. It should be stressed though that this case wasn't a great match overall but is used as an instructive case to show the corresponding model integrated transport timescales which are highly dependent on output model NL^2 total profiles and the input D_{LL} profile.

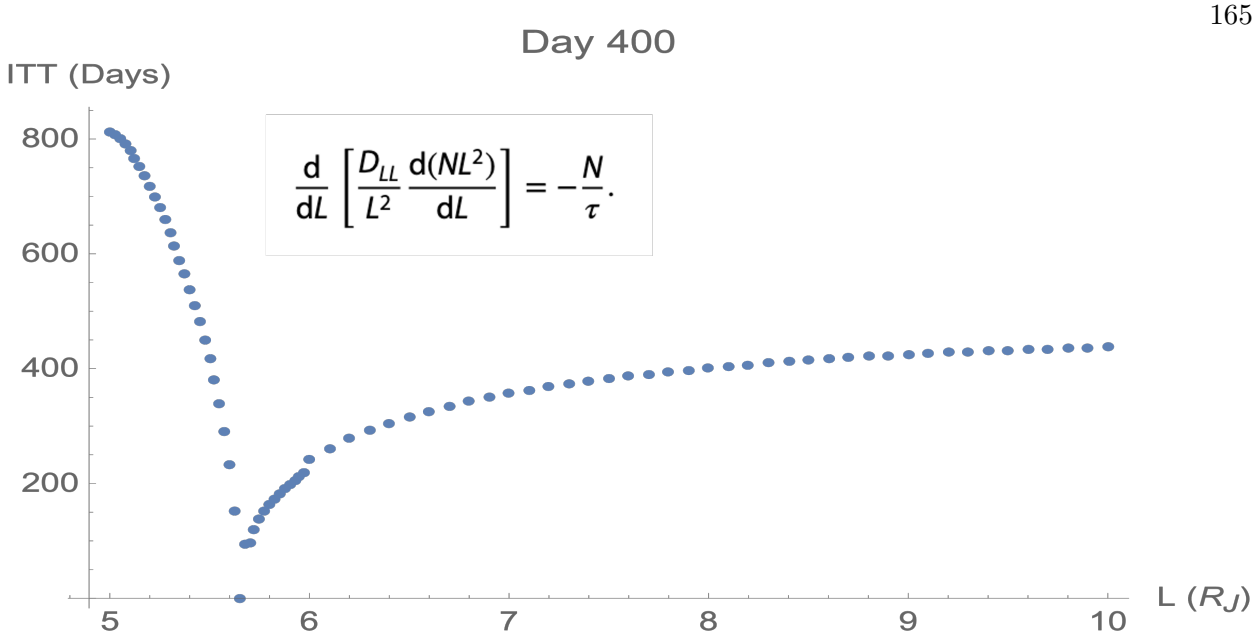

Figure 5.24: Our Whole torus Integrated transport timescale corresponding to torus output from figures 5.14 and 5.15

Using a linear fit to the Bagenal (1994) [5] NL^2 profile between L=6 and L=7 and extending that fit to L=10 (ignoring the "Ramp" and "Disk") and using our nominal warm torus power law exponent D_{LL} profile of $3.5 \times 10^{-7} (L/6)^{4.5}$ $\left(R_J^2 s^{-1}\right)$ I find an integrated transport timescale of 110 days.

An important question to ask ourselves is what is meant by the integrated transport timescale. It is often used to estimate the time for a perturbation such as a volcanic eruption at Io to move through the torus and affect other locations. In appendix A I derive an analytic separable transient solution to the transport equation in the absence of chemistry. I find that the separation constant is proportional to τ and the same equation for τ gives the time dependence of the transient as $e^{-t/\tau}$ as one would find for the linear diffusion equation transient solution. This result leads me to recommend instead we think about the integrated transport timescale as an effective transient e-folding time for a perturbation moving through the system which would be longer than the perturbation merely making it to a location.

Going a step further I apply boundary conditions to a warm torus only and separately a cold torus only transient radial solution in Appendix A. Trying to match the Voyager NL^2 total profile [5] requires tuning the τ parameter and for the warm torus I surprisingly find the best fit for $\tau =$ 90 days of the order the same value we found with the integrated transport timescale method in the warm torus. Likewise doing the same for the cold torus separately I find $\tau = 600$ days again of order what we found in the cold torus for the integrated transport timescale.

But what does it mean to match a steady state profile with a transient profile? At first thought, it might be said that what I have done is nonsense, but I propose that this transient profile (in the absence of chemistry) is being balanced exactly by sources and losses from the physical chemistry. This can be seen by the fact that the steady-state NL^2 profile that I also derive in appendix A for separate warm and cold torus profiles (with 0 derivative conditions at one end and a fixed value at the other) are merely constant values given by the fixed values at either end. Furthermore, once the system reaches steady state (with chemistry) the sources and losses can be thought of as only a function of L, and if we perturb the system the sources/losses would be approximately still constant in time and the separable transient solution in time would still be approximately $\propto e^{-t/\tau}$ but with a more complicated radial profile. In this sense propose again that the integrated transport timescale is not the time for a perturbation to make it to a location but an effective e-folding time for a transient moving through the system.

5.8.1 Numerically Derived Radial Timescale for Transport via Perturbing Steady State

If instead, we wish to know the time for a perturbation to move through the system F.J. Crary (Personal Communication (2022)) proposed that I instead do a numerical experiment to determine just that. I take our nominal warm torus steady state solution for L=6-10 R_J to initialize a model run with the same set of model inputs and then perturb the density of one species at $L = 6$ and watch the perturbation move through the system in NL^2 for that species. I change nothing else for each run. I did this for all model ion species, each separately. I varied the perturbation from

+20% to +70% of the steady state density at L=6 and didn't find significantly different results though for the smaller perturbation the perturbations were lost in the numerical noise. I take a nominal perturbation of +50% from L=6 and find that looking at just the NL^2 radial profile as a function of time it is hard to see much of anything after the first day as it has all been smeared out already as diffusion equations do. Instead, I plot $\frac{\left(NL^2\right)_{j+1}}{\left(NL^2\right)_j}$ as a function of L and watch how that progresses in time plotting the value every day (though the model time step is still 1000 seconds). Where j is the time index in days so for j=0 $\left(NL^2\right)_j$ are our initial perturbed steady state radial profile and $\left(NL^2\right)_{j+1}$ is our profile at day 1 of model run time.

For the major warm torus species S^{2+} and O^+ and the minor warm torus species S^{3+} I find about the same timescale of approximately 30 days. For the minor species S^+ I find a timescale of about 20 days. For the minor species O^{2+} I find a timescale of about 35 days. The individual timescales depend on the individual steady-state profiles and their gradients all with a common D_{LL} profile, so it is not surprising that there is a bit of variability among species.

To illustrate the numerical experiment I show the case of perturbing the O^+ density at t=0 and L=6 by 50% from its L=6 steady-state value and show radial profiles of $\frac{\left(NL^2\right)_{j+1}}{\left(NL^2\right)_j}$ at various times in figure 5.25. I estimate the perturbation has made it to L=10 when the maximum in $\frac{\left(NL^2\right)_{j+1}}{\left(NL^2\right)_j}$ is found at L=10. The boundary condition of a fixed NL^2 value at L=10 means this value is always 1 there and as a result gets in the way of our result and we should really track the perturbation to say L=9 and then propagate it from there to L=10 at its average radial velocity at that time, but we save that analysis for future work, and this is good enough to first order to get an estimation of how long a perturbation originating at L=6 would take to get to L=10 for nominal warm torus conditions. It should also be appreciated that if one was tracking an individual perturbed ion at L=6, it is not clear to me this is the timescale for it to be transported to L=10. I have only shown that this is the time for the perturbation to get there as we are not tracking individual particles.

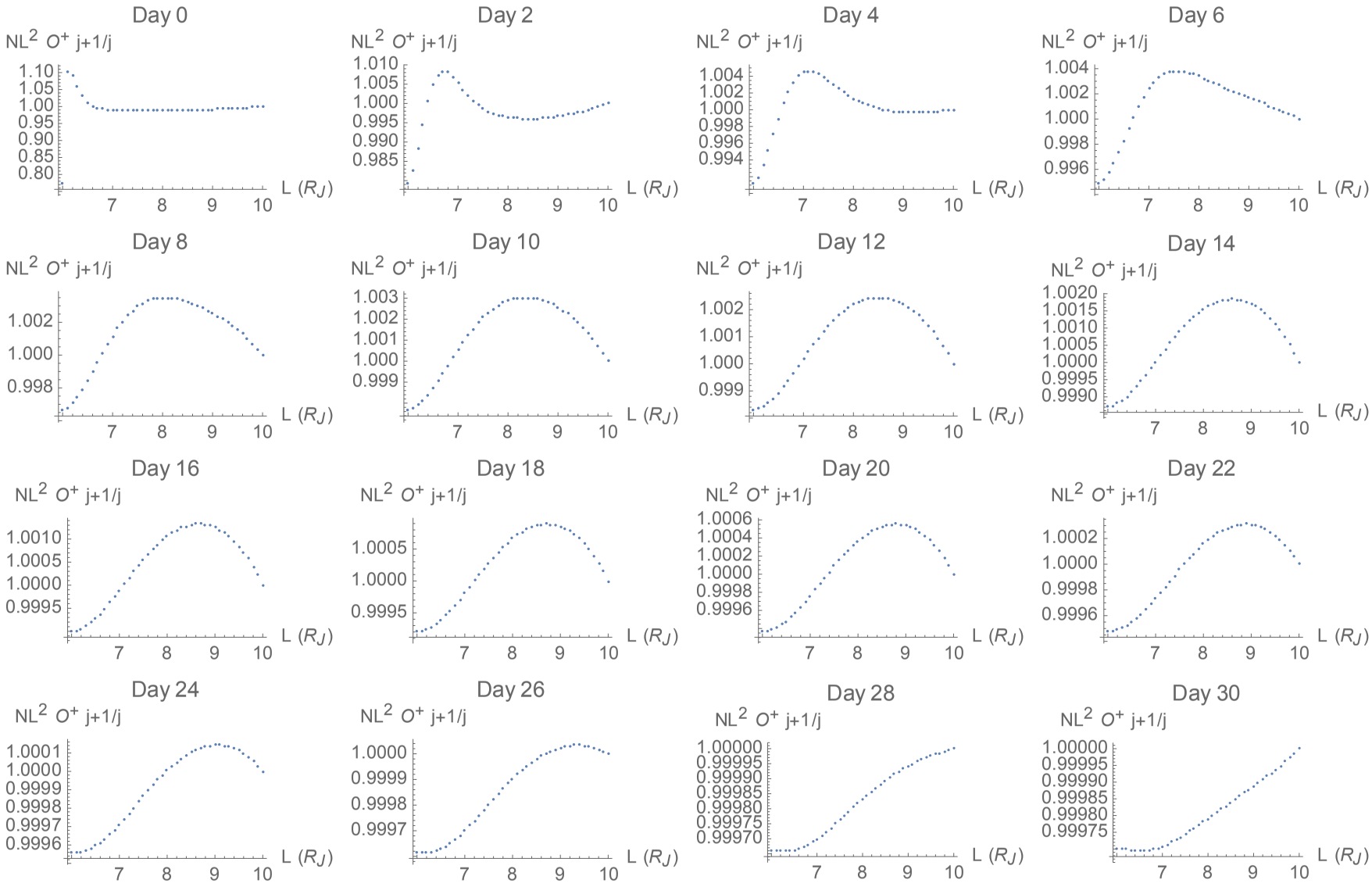

Figure 5.25: Radial Profile as a function of time of $\frac{(NL^2)_{j+1}}{(NL^2)_j}$ of O^+ in Warm Torus to find numerical radial transport timescale via perturbing the steady state n_{O^+} by 50% at t=0.

5.9 Conclusions

In section 5.1 we defined our "cubic centimeter" physical chemistry model. We outlined the different sources and losses of mass and energy. We then went through the latitudinal averaging scheme employed for taking into account the chemistry happening along a magnetic field line. We then described the radial transport model used to move mass through the system in L given a nonlinear diffusion coefficient radial profile. In the next section, we described the split-step method used to couple the different components together. We then coupled all 3 of these models together and produced model output for the warm torus and in doing so reproduced the Copper et al. (2016)[33] model output. Then shifting our attention to the cold torus we focused on modeling from 5 to 5.7 R_J. Finally putting everything together we built a model that went from 5-10 R_J trying to reproduce the warm torus, ribbon, gap region, and cold torus peak self consistently. We had limited success. By following Taylor (1996) [142] we imposed a "notched" D_{LL} profile which gave us the required shape of the flux-tube mass content but we had issues reproducing the cold torus peak except in 1 case where it was localized in only O^+ local density profile but not in the S^+ profile. The nonlinear system is extremely sensitive to the input neutral source profile or fixed neutral density profile depending on the model used. Likewise, it is extremely sensitive to the diffusion coefficient profile in the cold torus. Our model with 5 separate ion species, a separate energy diffusion equation, a consistent electron temperature profile, and the additional chemistry we include makes our model significantly more complicated than Taylor's and we have a much larger parameter space to explore. However, I do believe we are extremely close to our desired solution.

In the cold torus, closer to Jupiter, the higher order moments of the magnetic field become more important, and small differences in the field have a larger effect on the latitudinal distribution due to the smaller scale heights (Dougherty et al. (2017)[47]). Due to this, we believe in the future we should apply a diffusive equilibrium model to better describe the plasma distribution. In addition, we should use the new Juno-derived magnetic field model (Connerney et al. 2022)[32].

Further, an accurate description of the extended neutral cloud coupled with the local interaction is exceedingly important. We plan to take Dols et al. (2008), (2012), (2022) [44][46][45] model of the local interaction and couple it to Smith et al. (2019) [130] and (2022)[129] model of the extended neutral cloud to produce an accurate description of the extended neutral clouds for this exact purpose. In Dols and Johnson (2022)[45] they include the velocity dependence of charge exchange reactions and the additional chemistry from ion/molecule interactions necessary for understanding the local interaction where the flow velocity and ion temperatures are drastically reduced. In addition, it may be advantageous to continue to model the cold and warm torus separately due to their drastically different processes and timescales. Further modeling will benefit from additional observational constraints on the neutral and plasma distributions specifically in the cold torus and ribbon.

Chapter 6

Conclusions

6.1 Summary & Takeaways

I have modeled the emission coming from the Io plasma torus to determine plasma conditions. I reanalyzed the Voyager UVS data from 1979. Insights from modeling the Cassini UVIS observations that had significantly higher resolution and greater temporal coverage and updated atomic data for emission cross sections using the CHIANTI atomic database have allowed us to determine that the ion composition and the electron density and temperature from Voyager are consistent with the conditions observed by Cassini in the warm torus. I found ion mixing ratios at the peak brightness around 6 R_J to be $S^+/N_e \approx 5\%$, $S^{++}/N_e \approx 20\%$, $S^{+++}/N_e \approx 5\%$, $O^+/N_e \approx 20\%$, $O^{++}/N_e \approx 3\%$, with 10% protons, and an average oxygen to sulfur charge state ratio of 0.8. The radial profiles in the warm torus between 6-9 R_J of ion mixing ratios and electron temperature and density I determined are well fit by a radial physical chemistry of the torus with an oxygen to sulfur ratio of the neutral source of 2 consistent with dissociation of sulfur dioxide coming from volcanism on Io. The ion composition determined by my spectral analysis has shown much more similarity between the Cassini and Voyager epochs than previously thought. This composition is similar to that derived from Voyager data by Smith and Strobel (1985) [132] and by Herbert and Sandel (2001) [62] but is very different from the Shemansky (1988) [121] analysis that was also reported in the survey of the Io torus by Bagenal (1994) [5]. Shemansky's analysis (Shemansky (1988) [121]) found an O/S ratio of the neutral source of 4 required to match observations whereas we find it to be 2 consistent with dissociation of SO_2. There are plenty of ways I could see it being

less than 2 when including sources from SO, S_2, and other sulfur compounds but it is much harder to explain it being larger than 2.

By using a double Maxwellian distribution where both the core thermal electrons as well as supra-thermal "hot" electron population are assumed to be Maxwellians I have modeled the emission in the UV using the CHIANTI atomic database. The full electron distribution is approximated as a sum of the two Maxwellian functions, and cross-sections are computed using a weighted sum of the two populations. This double Maxwellian model of UV emission spectra when compared with a spectrum from CASSIN UVIS at 6 R_J does not well constrain the fraction of hot electrons.

Consequently, I turned to models of the physical chemistry of the Io plasma torus to determine the fraction of hot electrons. Using the spectral emission model to match UV spectra to constrain the fraction of hot electrons leads to a similar "goodness of fit" for a range of values of the core electron temperature in the range of 5.6–6.6 eV and a fraction of hot electrons between 0.25% - 5.5%. As a result, it was necessary to constrain the fraction of hot electrons (F_{eh}) with a physical chemistry model. This showed that to match the observed ion and electron densities and temperatures with the "cubic-cm" (0-D) physical chemistry model the fraction of hot electrons must be less than 0.01 or 1%. Additional physics from energy constraints from the physical chemistry modeling allows us to determine that for nominal warm torus plasma parameters the fraction of hot electrons is more likely 0.25% than 1% at 6 R_J. I have successfully modeled the flow of mass and energy through the system for this corresponding result by balancing the sources and losses of mass and energy for each species to show the dominant chemical pathways in the Io plasma torus.

This result is particularly important due to the abundance of recent spectral analyses of UV data from Hisaki. JAXA's Hisaki UV spectrometer has been monitoring the Jupiter system (from Earth's orbit) since its launch in 2013 (Yoshikawa et al., 2014, 2016) [162][161]. Spectral analysis of the Hisaki observations has found fractions of hot electrons on the order of a few percent (Yoshioka et al. (2014); Tsuchiya et al. (2015)) [163][150] inconsistent with our model and previous results. Previous physical chemistry models have found the fraction of hot electrons in the Io plasma torus to be a fraction of a percent (Delamere & Bagenal, 2003; Delamere et al., 2005) [39][40]. In situ

observations from Voyager PLS put the fraction of hot electrons at 0.2% at about 300 eV at the orbit of Io (Sittler & Strobel, 1987) [128]. More recent work from Yoshioka et al. (2017) [165] and Hikida et al. (2020) [69] have found values for the fraction of hot electrons (less than 1%) from spectral analysis at the orbit of Io more consistent with our physical chemistry modeling for steady state Io plasma torus conditions. Hikida et al. (2020) [69] in their recent paper show evidence for an enhancement of the fraction of hot electrons during transient times possibly due to volcanic eruptions on Io.

I have built an emission model using the CHIANTI atomic database that given a 3D model of Io plasma torus densities, temperatures, and observation geometry determines the line of sight of an emission. Given a spatial step size it numerically integrates over the determined line of sight and produces a simulated output spectrum in the wavelength range desired given by electron impact excitation of the ions. I have shown model output for a variety of geometries as well as wavelength ranges. I have summed over various wavelength ranges to produce pictures of intensity and slices through this to compare with observations and to be used as a planning tool for future missions and observations of the plasma torus. We produce output simulated spectra in units of Raylieghs/Å as well as by applying effective area curves for UVS instruments on NASA's future mission Europa Clipper and ESA's JUICE mission to Jupiter I simulate expected counts for given observations. I have dubbed this emission model the Colorado Io Torus Emission package 2 or CITEP 2 to pay homage to CITEP created by Taylor (1996) [142]. I found that using a Cassini-based density model (Steffl et al. (2004b); Nerney et al. (2017))[137][96] from using a "Cubic centimeter" spectral emission model and plugging this model into CITEP 2 resulted in a deficit in emission in the UV. I had to increase the peak electron density from 2200 cm^{-3} to 3000 cm^{-3} at 6 R_J to match the observed brightness from CASSINI UVIS. I believe this was due to assumptions about emission over the line of sight while using the "Cubic centimeter" spectral emission model. Further, my predictions of visible emission (particularly S^+ 6731 and 6716 Å) in the ribbon and cold torus based on a Voyager model (Bagenal 1994) [5] are higher than what has been observed by Schmidt et al. (2018) [111] and peak at smaller radial values.

By taking a physical chemistry model developed by Delamere et al. (2005) [40] and Copper et al. (2016) [33] as a starting point I have corroborated their results and adapted the model for my own purposes. I have moved the model in from the warm torus to simulate the cold torus, gap region, ribbon, and warm torus. The model couples a model of the local physical chemistry (Delamere et al. 2003) [39], with a latitudinal averaging scheme, and a radial transport model for mass and energy. I am able to reproduce the work of Copper et al. (2016) [33] in the warm torus with great success. I am able to produce the ribbon and a peak in flux-tube content at L=5.7 by applying a discontinuity in the D_{LL} in that region consistent with a change in flux-tube interchange processes.

The cold torus and gap region simulations have been more elusive with only limited success due to the complex nonlinear nature of the system and large parameter space to explore in addition to the high spatial and temporal resolution required to resolve the desired features and to avoid numerical instabilities inherent to solving a diffusion equation with an explicit finite difference scheme. By applying the "notched" D_{LL} profile that Taylor (1996) [142] used for a few model runs I was able to produce a cold torus peak and gap region by fixing the neutral density profiles to the Koga et al. (2018b) [79] scaled up by a factor of 1.5 but with a fast power law fall of +20 and cutting it off inside 5.65 R_J. I found that if I didn't have the neutral densities fall off much steeper than the Koga et al. (2018b) [79] implied power law of +12 inside 5.7 than my electron and ion temperatures would stay far too high due to pickup energy. This implies that inside the peak in neutral density at 5.7 R_J Koga et al. (2018b) [79] was overestimating densities due to line of sight projection effects.

I found radial transport timescales ranging between tens of days to hundreds of days in the warm torus depending on the method used and many hundreds of days to a thousand days in cold torus. The output timescales are highly dependent on the input D_{LL} profiles and gradients in the steady state NL^2 profiles. I found a separable transient solution to the radial Fokker-Planck equation I have never seen applied to Jupiter for flux-tube interchange motion. I found an e-folding timescale for the transient separable solution exactly the same as what is used as a radial transport

timescale in the literature and found similar values for this e-folding timescale to match the torus profiles as is found using the integrated transport timescale formulation. I performed a numerical experiment to determine the time for a perturbation to move through the warm torus. By taking our nominal steady-state output in the warm torus and perturbing the solution at L=6 we find shorter timescales for the perturbation to reach L=10 of about 30 days as opposed to around 100 days for the integrated transport timescale. This is consistent as an effective e-folding time for perturbations in the system would be longer than the time for the perturbation to merely move through the system.

The notched D_{LL} profile reproduces the Voyager slope in the flux-tube content in the cold torus. The steep NL^2 profile in the gap region falls off faster than the effective ion scale heights creating the gap in density and emission. In the cold torus region, the slope becomes shallower, and the ion temperatures and therefore scale heights are steeper than the flux-tube content here allowing for a rapid collapse to the centrifugal equator leading to the creation of a cold torus even though the total NL^2 profile is monotonically decreasing and does not show this peak in my model output.

6.2 Future Work

In the future, I plan to apply my emission model to more observations of the Io plasma torus. Juno UVS has recently acquired observations of the Io plasma torus that would be a good test of my model. Juno will also help to constrain my modeling with in-situ observations of the electron and plasma distributions and composition specifically in the cold torus. There is also a data set from New Horizon's Alice UVS instrument that needs to be analyzed. Hisaki, an Earth-orbiting Japanese satellite, has years of UV observations of the Io torus to pour over. I will also explore ground-based optical observations of the Io plasma torus in order to understand the plasma composition and variability. NASA's Juno mission is now beginning to cross through the equator near the orbit of Europa and its equatorial crossings will continue to precess to smaller radial values and into the main Io plasma torus and will provide in-situ observations of the plasma environment

perfect for comparison with my model of the physical chemistry during its extended mission between 2023-2026.

In the future, my emission model will be put in "observer coordinates" for ease of comparison with observations not at the centrifugal equator by properly applying the distribution along a field line. Currently, CITEP 2 works for any 3D model of densities and temperatures and observer location and pointing, but so far I have only applied it in centrifugal coordinates with a scale height distribution as a function of z. This distance z is the distance along a field line, not the cartesian z coordinate as plotted in chapter 4. I will also apply Phipps et al. (2021) [102] model of the centrifugal equator along with ConNerney et al. (2022)'s [32] Juno-based magnetic field model to model the distribution along a field line using the "diffusive equilibrium" approach.

I will further explore parameter space using the physical chemistry model of the Io plasma torus coupling the cold torus, ribbon, and warm torus together. I will explore the tipping point of inward vs. outward radial transport of plasma and determine timescales for diffusion. I will explore the time variability of the torus via looking at the transient model output for a source with a gaussian uptick in time to model an eruption from Io. The boundary at L=5 for the torus is perhaps too close to the cold torus peak and is driven too strongly by the boundary conditions, and I should move this into 4.5. Further work will include coupling my physical chemistry model to a model of the local interaction (Dols et al. 2008, 2012) [44][46], to a model of the neutral cloud (Smith et al. 2019, 2022) [130][129]. I will extend the previous work of (Delamere et al. 2005) [40] to incorporate a Europa source to model the variability in the vicinity of Europa in anticipation of the Europa Clipper mission to Jupiter.

6.3 Open Questions

There are many open questions left to be answered in the Io plasma torus.

- The temporal and spatial modulations of the Io plasma torus are still not well understood. What is their origin?

- Conservation of the 1st adiabatic invariant would imply that the plasma would cool as it moved out into an area of a weaker magnetic field. Why does it heat up instead?
- Where do the hot electrons come from? Are they produced locally or do they come in from the outer magnetosphere? The answer is probably some combination of the two.
- Io is the most volcanically active body in the solar system and is constantly erupting, but the Io plasma torus is in a fairly steady state. With some noted exceptions with increases in brightness and inferred density. What types of eruptions and what geometry of the eruptions is required to produce modulations in the emission and therefore density of the plasma?
- Where is the tipping point for inwards vs. outwards radial transport in the torus and what processes determine the diffusion coefficient?

These are questions to be addressed in the extended mission of Juno, future missions to Jupiter by JUICE & Europa Clipper, and by further modeling work.

Appendix A

Analytic Solutions to the Radial Transport Equation

A.1 Steady State Solution in the absence of Chemistry

The radial Fokker-Planck equation is

$$\frac{\partial Y}{\partial t} = L^2 \frac{\partial}{\partial L}\left(\frac{D_{LL}}{L^2}\frac{\partial Y}{\partial L}\right) \tag{A.1}$$

From Copper et al. (2016) [33] L is the radial coordinate (L = R/R_J where R_J is the planetary radius) and Y is any conserved quantity during flux tube interchange motion. The conserved quantity for mass is $Y = NL^2$ or the total number of ions per unit of magnetic flux. For energy, the conserved quantity for a centrifugally confined plasma is $Y = NL^2TL^2T^{1/3}$ following Richardson and Siscoe (1983) [105]

For steady-state $\frac{\partial Y}{\partial t} = 0$ and therefore Y is only a function of L, and partial derivatives can be replaced by full derivatives.

So we have

$$L^2 \frac{d}{dL}\left(\frac{D_{LL}}{L^2}\frac{dY}{dL}\right) = 0 \tag{A.2}$$

Or

$$\frac{D_{LL}}{L^2}\frac{dY}{dL} = C_1 = \text{Constant} \tag{A.3}$$

For $D_{LL} = K\left(\frac{L}{L_0}\right)^m$ we can use separation of variables and find

$$\int C_1 \frac{L^2}{D_{LL}} dL = \int \frac{C_1}{L_0^m} L^{2-m} dL = \int dY = Y + C_2 \tag{A.4}$$

For $m \neq 3$ we have $\boxed{Y = C_3 L^{3-m} + C_4}$ where we have lumped our old constants into new constants $C_3 = \frac{C_1}{L_0^m (3-m)}$ and $C_4 = -C_2$ to be determined by boundary conditions.

For $m = 3$ then we have $\int \frac{C_1}{L_0^m} \frac{dL}{L} = \frac{C_1}{L_0^m} \ln(L)$ which gives $\boxed{Y = C_5 \ln(L) + C_4}$ where $C_5 = \frac{C_1}{L_0^m}$ and again the constants are determined by boundary conditions.

Applying boundary conditions for mass $Y = NL^2$ we have $\left.\frac{dY}{dL}\right|_{L=6} = 0$ and $Y(L = 10) = A$ where A is a given constant value.

For $m \neq 3$ we have $\left.\frac{dY}{dL}\right|_{L=6} = C_3 (3-m) 6^{2-m} = 0$. For finite m and $m \neq 3$ this means $C_3 = 0$. We also have $Y(L = 10) = C_4 = A$. So this steady state solution is just a constant given by the outer boundary condition, and there is no L dependence $Y = A$.

For these boundary conditions and $m = 3$, we also find $Y = A$ or a constant value for the steady-state solution.

For energy transport $Y = NL^2 TL^2 T^{1/3}$ we have the boundary conditions $Y(L = 6) = E$ and $Y(L = 10) = F$ or that they are just given there. For $m \neq 3$ we have $Y(L = 6) = C_3 6^{3-m} + C_4 = E$ which gives $C_3 = \frac{(E - C_4)}{6^{3-m}}$ and $Y(L = 10) = C_3 10^{3-m} + C_4 = F$ which gives $C_3 = \frac{(F - C_4)}{10^{3-m}}$ which implies $\frac{(F - C_4)}{10^{3-m}} = \frac{(E - C_4)}{6^{3-m}}$ which implies $C_4 = \frac{E - F\left(\frac{3}{5}\right)^{3-m}}{1 - \left(\frac{3}{5}\right)^{3-m}}$ and $C_3 = \frac{F - C_4}{10^{3-m}}$.

A.1.1 Predicting Steady State Temperatures in the absence of Chemistry

We are using m=4.5 consistent with Copper et al. (2016) [33], so we can use the solution for $m \neq 3$

For $Y_m = NL^2$ the boundary conditions are $\left.\frac{d(NL^2)}{dL}\right|_{L=6} = 0$ and $NL^2(L = 10) = A$ which is a constant.

We have seen from above that the steady state $Y_m = A$ or is just a constant for all L.

For temperature we have $T_i(L=6) = 70$ eV, $T_e(L=6) = 5$ eV and $T_i(L=10) = 100$ eV, $T_e\,(L=10) = 30$ eV

This implies for $Y_E = \left(NL^2\right) L^2 T^{4/3}$ that the steady state boundary conditions are $Y_E(L = 6) = 36A\,(T(L=6))^{4/3}$ and $Y_E\,(L=10) = 100A\,(T(L=10))^{4/3}$ for ion or electron temperature boundary conditions. Using these and the above solutions for $Y_E\,(L) = C_3 L^{3-m} + C_4$ we have $E = 36A\,(T(L=6))^{4/3}$ and $F = 100A\,(T(L=10))^{4/3}$ with $C_4 = \dfrac{E - F\left(\dfrac{3}{5}\right)^{3-m}}{1 - \left(\dfrac{3}{5}\right)^{3-m}}$ and $C_3 = \dfrac{F - C_4}{10^{3-m}}$.

We would expect the steady state temperature to follow $T = \left(\dfrac{Y_E}{AL^2}\right)^{3/4} = \left(\dfrac{C_3 L^{3-m} + C_4}{AL^2}\right)^{3/4}$

I ran the model without physical chemistry and only transport and found the following output which matches my predictions perfectly for all species. The predictions are solid lines, and the model output is the dots.

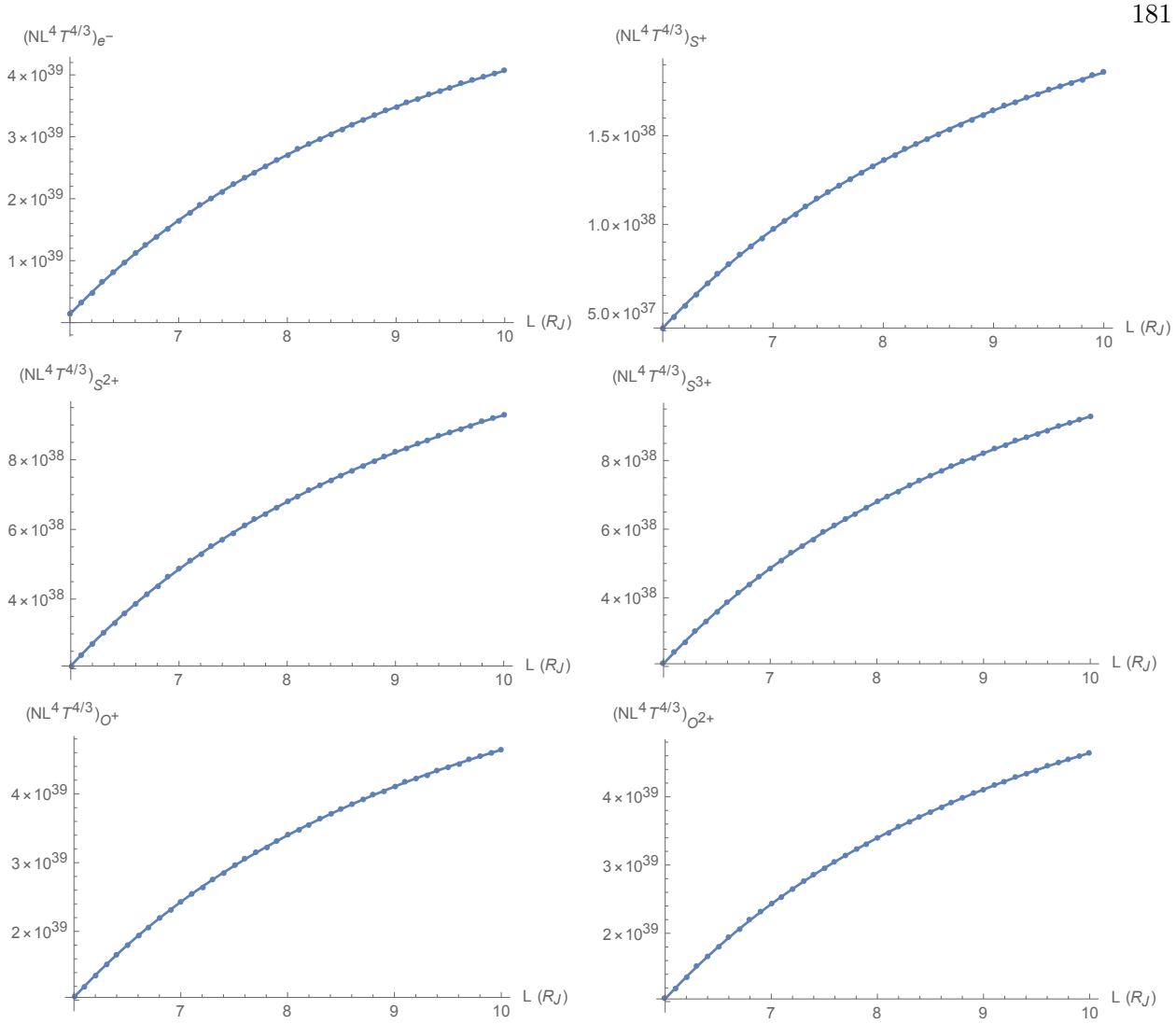

Figure A.1: Steady State prediction vs model Output For Energy Conserved Quantity

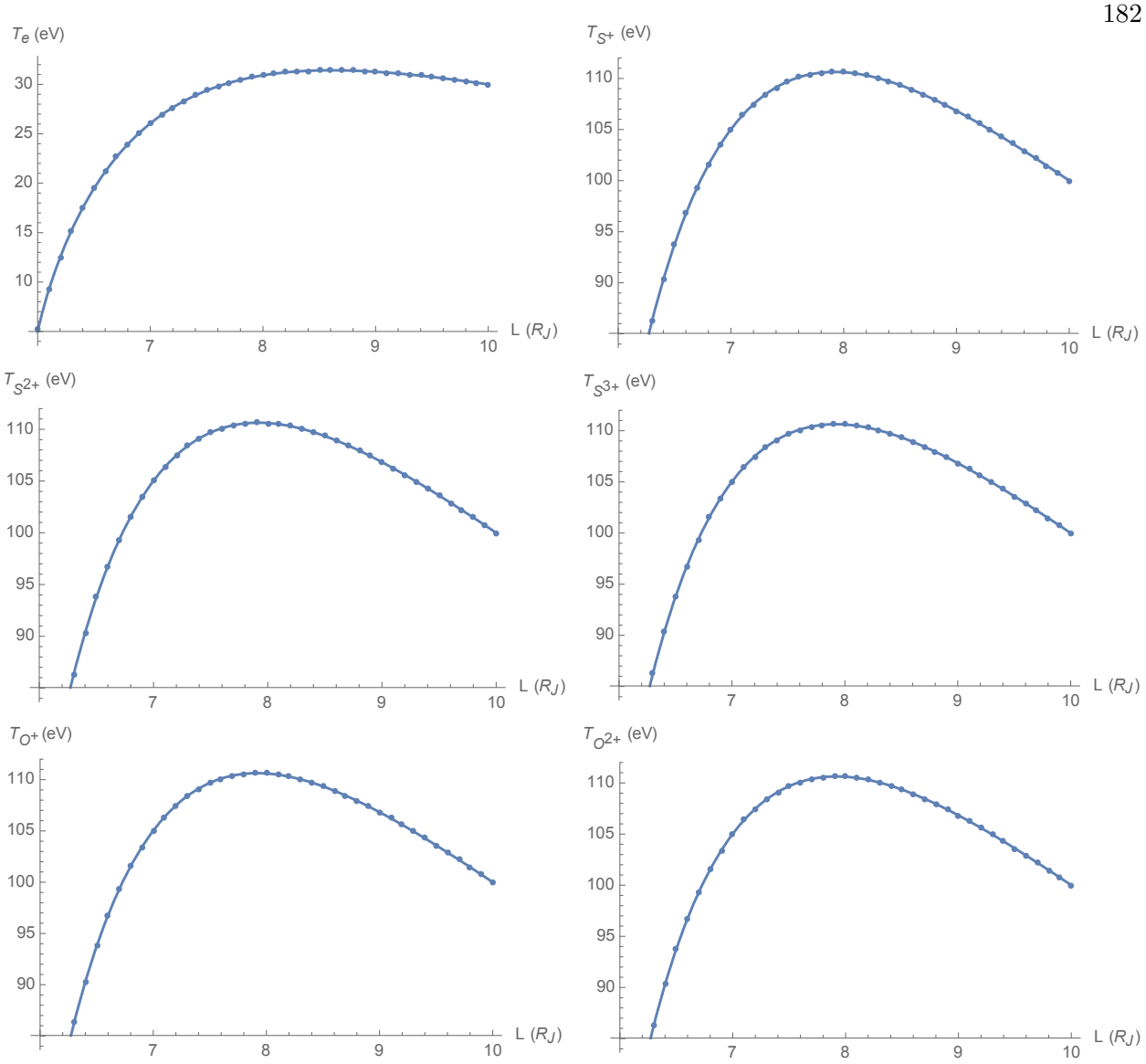

Figure A.2: Steady State prediction vs model Output For Temperatures

A.1.2 Steady State with a General Source and Loss function

We choose to handle the chemistry locally because we believe these to be local processes. One can equivalently think about the sources and loss functions in terms of NL^2 instead of local n or equivalently in terms of the energy quantities ($NL^2TL^2T^{1/3}$). In that case we have

$$\frac{\partial Y}{\partial t} = L^2 \frac{\partial}{\partial L}\left(\frac{D_{LL}}{L^2}\frac{\partial Y}{\partial L}\right) + S\left(L,t\right) - L\left(L,t\right) \tag{A.5}$$

During steady state we define $f\left(L\right) = -\lim_{t\to\infty}\left[S\left(L,t\right) - L\left(L,t\right)\right]$ and integrating twice we find

$$Y\left(L\right) = \frac{L_0^m}{K}\int L^{2-m}\left(\int \frac{f\left(L\right)}{L^2}dL\right)dL + K_1\int L^{2-m}dL + K_2 \tag{A.6}$$

Where K_1 and K_2 are constants of integration to be determined by two boundary conditions. Where the 2nd term on the right is the same we found without sources or losses and for $m \neq 3$ we found it is $\frac{K_1}{3-m}L^{3-m}$ and for m=3 it is $K_1 \ln\left(L\right)$.

For future work, I will take the output numerically determined source minus loss functions at steady state as a function of L in terms of density and integrate along a field line to get the equivalent fluxtube terms source and loss terms and then integrate that once more to determine the steady state solution including source and loss terms.

A.2 Separable Analytic Transient Solution to Transport Equation

$$\frac{\partial Y}{\partial t} = L^2 \frac{\partial}{\partial L}\left(\frac{D_{LL}}{L^2}\frac{\partial Y}{\partial L}\right) \tag{A.7}$$

With $D_{LL} = k\left(\frac{L}{L_0}\right)^m = CL^m$ gives

$$\frac{\partial Y}{\partial t} = CL^2 \frac{\partial}{\partial L}\left(L^{m-2}\frac{\partial Y}{\partial L}\right) \tag{A.8}$$

Assuming a separable solution we have $Y\left(L,t\right) = R\left(L\right)T\left(t\right)$. Plugging this in and dividing both sides by $Y\left(L,t\right) = R\left(L\right)T\left(t\right)$ we find

$$\frac{1}{T}\frac{dT}{dt} = \frac{CL^2}{R}\frac{d}{dL}\left(L^{m-2}\frac{dR}{dL}\right) \tag{A.9}$$

Where R is only a function of L and T is only a function of t so we rewrote our partial differential equations as ordinary differential equations.

The only way for this statement to be true for all of space and time is for both sides to be equal to a constant. The same constant we will call α

$$\alpha = \frac{1}{T}\frac{dT}{dt} = \frac{CL^2}{R}\frac{d}{dL}\left(L^{m-2}\frac{dR}{dL}\right) \tag{A.10}$$

Solving the time ODE by integrating both sides with respect to time and solving for $T(t)$

$$\alpha = \frac{1}{T}\frac{dT}{dt} = \frac{d(\ln T)}{dt} \implies T(t) = C_1 e^{\alpha t} \tag{A.11}$$

Where C_1 is an integration constant given by initial conditions. For a physical nontrivial solution $\alpha < 0$ so we define a new constant that is positive.

$$\alpha = \frac{-1}{\tau} = \frac{1}{T}\frac{dT}{dt} = \frac{CL^2}{R}\frac{d}{dL}\left(L^{m-2}\frac{dR}{dL}\right) = \frac{L^2}{Y}\frac{\partial}{\partial L}\left(\frac{D_{LL}}{L^2}\frac{\partial Y}{\partial L}\right) \tag{A.12}$$

Which gives us

$$T(t) = C_1 e^{-t/\tau} \tag{A.13}$$

Where clearly we see that this constant is the transport transient timescale or e-folding time, This is the same timescale as defined in Copper et al. (2016) [**?**] [33], Delamere et al. (2005) [40], Schreir et al. (1998) [117], and Cheng (1986) [29].

We also have the nonlinear radial equation to solve

$$\frac{1}{C\tau} = \frac{1}{\beta} = -\frac{L^2}{R}\frac{d}{dL}\left(L^{m-2}\frac{dR}{dL}\right) \tag{A.14}$$

With $\beta = C\tau = \dfrac{k\tau}{L_0^m}$

Plugging this into DSolve in Mathematica, assuming $\tau > 0$, $C > 0$ ($\implies \beta > 0$), and $m > 0$. I get the following horrendous solution in terms of Bessel and Gamma functions

$$R(L) = (2-m)^{\frac{1}{m-2}-1} (L^m)^{-\frac{m-3}{2m}} \beta^{-\frac{m-3}{2(m-2)}} \left[C_2 \Gamma\left(2 + \frac{1}{2-m}\right) J_{\frac{m-3}{m-2}}\left(-\frac{2(L^m)^{1/m}}{(m-2)\sqrt{L^m \beta}}\right) \right. \quad \text{(A.15)}$$

$$\left. + C_3 \Gamma\left(\frac{1}{m-2}\right) J_{\frac{1}{m-2}-1}\left(-\frac{2(L^m)^{1/m}}{(m-2)\sqrt{L^m \beta}}\right) \right] \quad \text{(A.16)}$$

Where C_2 and C_3 are constants to be determined by boundary conditions.

By applying the boundary conditions we should be able to determine the allowed value/values of τ.

Plugging in the boundary conditions $R'(L = L_0 = 6) = 0$ and $R(L = 10) = A$ with $A > 0$, $m = 4.5$, $L > 0$,

$$R(L) = \frac{-5.62341A \left(J_{-0.4}\left(-\frac{0.0851924}{\sqrt{\beta}}\right) J_{-0.6}\left(-\frac{0.8}{L^{1.25}\sqrt{\beta}}\right) + J_{0.4}\left(-\frac{0.0851924}{\sqrt{\beta}}\right) J_{0.6}\left(-\frac{0.8}{L^{1.25}\sqrt{\beta}}\right) \right)}{L^{0.75} \left(J_{-0.6}\left(\frac{0.0449873}{\sqrt{\beta}}\right) J_{-0.4}\left(\frac{0.0851924}{\sqrt{\beta}}\right) + J_{0.4}\left(\frac{0.0851924}{\sqrt{\beta}}\right) J_{0.6}\left(\frac{0.0449873}{\sqrt{\beta}}\right) \right)} \quad \text{(A.17)}$$

Trying to also match the value of $R(L = L_0 = 6) = 2 \times 10^{36}$ with $A = 4.5 \times 10^{35}$ and $k = 3.5 \times 10^{-7}\ s^{-1}$ I find decent agreement for $\tau \approx 90$ days

In reality, the total solution is a sum of the transient and the steady state. In this case, the steady state for NL^2 in the absence of source or loss terms is a constant value for a 0 derivative and given value at one end such as a separate cold and separate warm torus model. Thus the solution applied to these boundary conditions is only shifted by a constant factor and the determination of the τ values and ability to get a general fit to the global warm and cold torus trends in order to estimate the transient timescale.

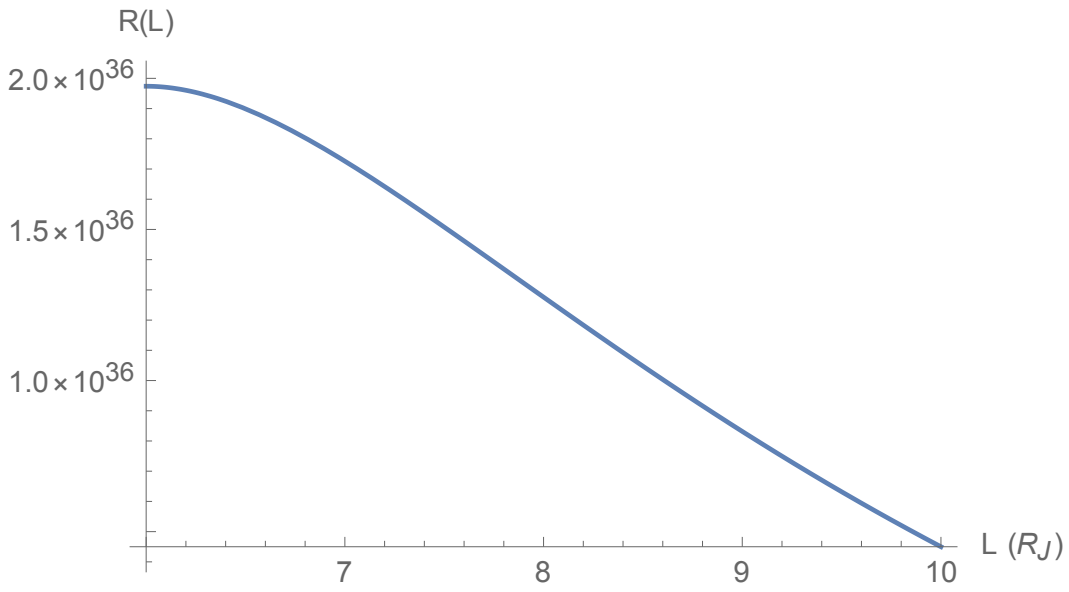

Figure A.3: Warm Torus Separable Transient R(L) matching Voyager total NL^2 profile.

The same can also be done for the cold torus. We instead impose the boundary conditions $R'(L=5.7)=0$ and $R(L=5.0)=A=10^{35}$, $m=4.5$, $L>0$ and also trying match the value of $R(L=5.7)=2\times10^{36}$ with $k=5\times10^{-9}\ s^{-1}$ (factor of 50 lower than in warm) I find decent agreement for $\tau\approx600$ days. Plugging these in gives β= 0.00011431 which gives R(L) as

$$R(L)=\frac{2.03086\times10^{37}J_{0.6}\left(\frac{74.8254}{L^{5/4}}\right)-1.33606\times10^{37}J_{-0.6}\left(\frac{74.8254}{L^{5/4}}\right)}{L^{3/4}} \tag{A.18}$$

Plotting this gives

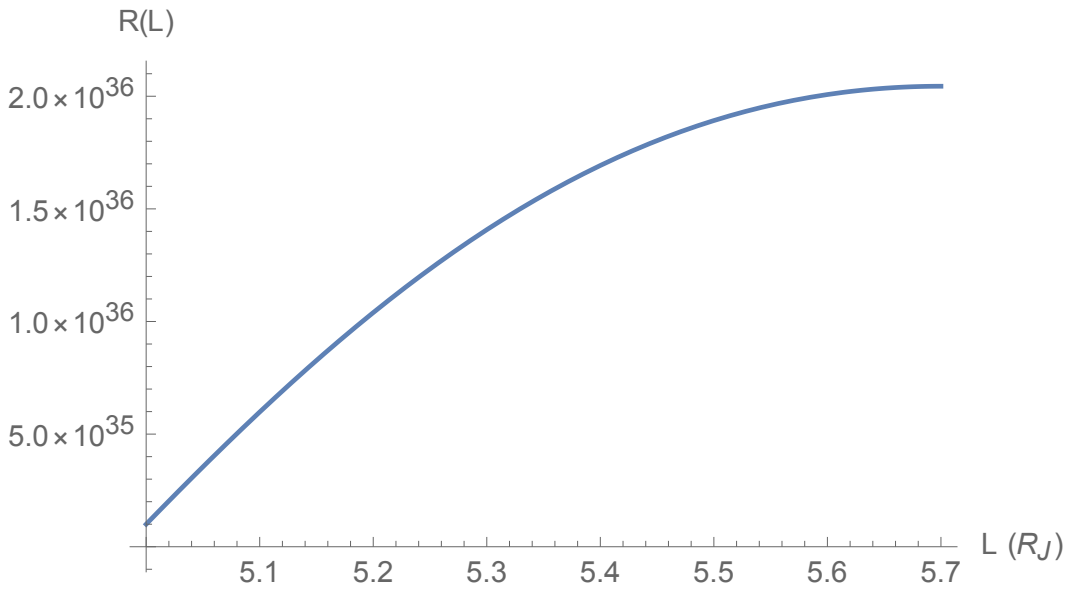

Figure A.4: Cold Torus Separable Transient R(L) matching Voyager total NL^2 profile.

Plotting both profiles over the Bagenal (1994) [5] NL^2 total profile gives

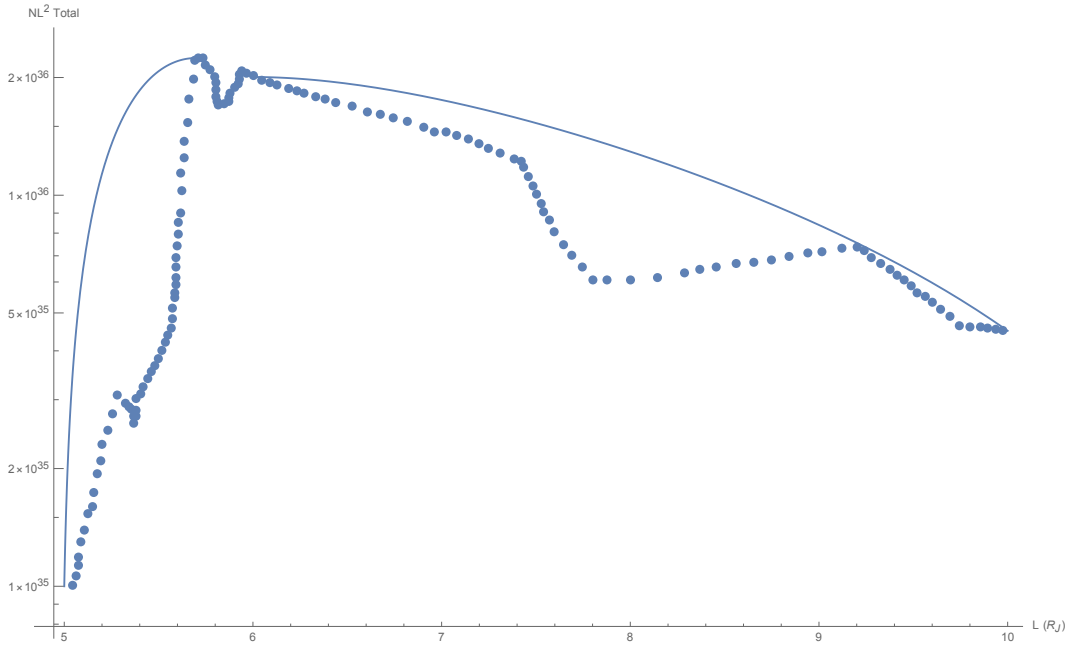

Figure A.5: Comparing NL^2 total to transient radial profile for the warm and cold torus.

My work in appendix A has shown that I can determine an analytic steady-state solution to

the nonlinear radial transport (radial Fokker Planck) diffusion equation in the absence of chemistry. Further, I showed the general form of the solution when sources and sinks are included by integrating the general source and loss terms. Then I showed an analytic separable solution in the absence of sources and sinks that had a transient e-folding timescale that had the exact definition as that our radial transport timescale we use to numerically integrate from the peak in flux-tube mass content to get an estimate of transport timescales. As a result, we have postulated that this numerical estimate is instead a measure of the transient e-folding timescale in the event of a perturbation added to the system, not just the time required for the perturbation to travel through the system. In The previous section, we performed a numerical experiment by perturbing the steady-state warm torus solution and found a shorter timescale of 30 days (instead of 100 for ITT) for the perturbation to move through the system. This is consistent my suggested definition as one would expect the e-folding timescale to be longer than the timescale for the perturbation to merely get there. For a small transient perturbation, I would expect the sources and sinks to still be mostly constant in time, and only the flux-tube mass content would be perturbed and thus the time part of the solution would still go as $e^{-t/\tau}$. Further, by tuning our radial solution in the cold and warm torus to match the Voyager Bagenal (1994) NL^2 profile, I find similar timescales as our integrated transport timescales for the cold and warm torus. ,

Bibliography

[1] F. Bagenal, A. Adriani, F. Allegrini, S. J. Bolton, B. Bonfond, E. J. Bunce, J. E. P. Connerney, S. W. H. Cowley, R. W. Ebert, G. R. Gladstone, C. J. Hansen, W. S. Kurth, S. M. Levin, B. H. Mauk, D. J. McComas, C. P. Paranicas, D. Santos-Costa, R. M. Thorne, P. Valek, J. H. Waite, and P. Zarka. Magnetospheric science objectives of the Juno mission. Space Science Reviews, 213(1):219–287, Nov 2017.

[2] F Bagenal, LP Dougherty, KM Bodisch, JD Richardson, and JM Belcher. Survey of voyager plasma science ions at jupiter: 1. analysis method. Journal of Geophysical Research: Space Physics, 122(8):8241–8256, 2017.

[3] F. Bagenal, D. E. Shemansky, R. L. McNutt Jr., R. Schreier, and A. Eviatar. The abundance of O^{++} in the jovian magnetosphere. Geophysical Research Letters, 19(2):79–82, 1992.

[4] Fran Bagenal. Plasma conditions inside Io's orbit: Voyager measurements. Journal of Geophysical Research: Space Physics, 90(A1):311–324, 1985.

[5] Fran Bagenal. Empirical model of the io plasma torus: Voyager measurements. Journal of Geophysical Research: Space Physics, 99(A6):11043–11062, 1994.

[6] Fran Bagenal and Peter A Delamere. Flow of mass and energy in the magnetospheres of jupiter and saturn. Journal of Geophysical Research: Space Physics, 116(A5), 2011.

[7] Fran Bagenal and Vincent Dols. The space environment of io and europa. Journal of Geophysical Research: Space Physics, 125(5):e2019JA027485, 2020.

[8] Fran Bagenal and James D. Sullivan. Direct plasma measurements in the io torus and inner magnetosphere of jupiter. Journal of Geophysical Research: Space Physics, 86(A10):8447–8466, 1981.

[9] Fran Bagenal, Robert J. Wilson, Scott Siler, William R. Paterson, and William S. Kurth. Survey of galileo plasma observations in jupiter's plasma sheet. Journal of Geophysical Research: Planets, 121(5):871–894, 2016.

[10] D. D. Barbosa. Neutral Cloud Theory of the Jovian Nebula: Anomalous Ionization Effect of Superthermal Electrons. , 430:376, July 1994.

[11] D. D. Barbosa and M. A. Moreno. A comprehensive model of ion diffusion and charge exchange in the cold io torus. Journal of Geophysical Research: Space Physics, 93(A2):823–836, 1988.

[12] DD Barbosa, FV Coroniti, and A Eviatar. Coulomb thermal properties and stability of the io plasma torus. The Astrophysical Journal, 274:429–442, 1983.

[13] DD Barbosa and MG Kivelson. Dawn-dusk electric field asymmetry of the io plasma torus. Geophysical Research Letters, 10(3):210–213, 1983.

[14] Charles A Barth. Planetary ultraviolet spectroscopy. Applied optics, 8(7):1295–1304, 1969.

[15] X. Blanco-Cano. Wave generation in moon–satellite interactions. Advances in Space Research, 33(11):2078–2091, 2004. Comparative Magnetospheres.

[16] KM Bodisch, LP Dougherty, and F Bagenal. Survey of voyager plasma science ions at jupiter: 3. protons and minor ions. Journal of Geophysical Research: Space Physics, 122(8):8277–8294, 2017.

[17] Neil Brice and Thomas R Mcdonough. Jupiter's radiation belts. Icarus, 18(2):206–219, 1973.

[18] HS Bridge, JW Belcher, AJ Lazarus, JD Sullivan, RL McNutt, F Bagenal, JD Scudder, EC Sittler, GL Siscoe, VM Vasyliunas, et al. Plasma observations near jupiter: Initial results from voyager 1. Science, 204(4396):987–991, 1979.

[19] A. L. Broadfoot, M. J. S. Belton, P. Z. Takacs, B. R. Sandel, D. E. Shemansky, J. B. Holberg, J. M. Ajello, S. K. Atreya, T. M. Donahue, H. W. Moos, J. L. Bertaux, J. E. Blamont, D. F. Strobel, J. C. McConnell, A. Dalgarno, R. Goody, and M. B. McElroy. Extreme ultraviolet observations from voyager 1 encounter with jupiter. Science, 204(4396):979–982, 1979.

[20] A. L. Broadfoot, B. R. Sandel, D. E. Shemansky, S. K. Atreya, T. M. Donahue, H. W. Moos, J. L. Bertaux, J. E. Blamont, J. M. Ajello, D. F. Strobel, J. C. McConnell, A. Dalgarno, R. Goody, M. B. McElroy, and Y. L. Yung. Ultraviolet spectrometer experiment for the voyager mission. Space Science Reviews, 21(2):183–205, Nov 1977.

[21] A. L. Broadfoot, B. R. Sandel, D. E Shemansky, J. C. McConnell, G. R. Smith, J. B. Holberg, S. K. Atreya, T. M. Donahue, D. F. Strobel, and J. L. Bertaux. Overview of the voyager ultraviolet spectrometry results through jupiter encounter. Journal of Geophysical Research: Space Physics, 86(A10):8259–8284, 1981.

[22] Michael E. Brown and Antonin H. Bouchez. The response of jupiter's magnetosphere to an outburst on io. Science, 278(5336):268–271, 1997.

[23] Michael Edwards Brown. The structure and variability of the io plasma torus. Ph. D. Thesis, 1994.

[24] R. A. Brown and D. E. Shemansky. On the nature of S II emission from Jupiter's hot plasma torus. , 263:433–442, December 1982.

[25] R. A. Brown, D. E. Shemansky, and R. E. Johnson. A deficiency of O III in the Io plasma torus. , 264:309–323, January 1983.

[26] R. A. Brown and Y. L. Yung. Io, its atmosphere and optical emissions. Jupiter: studies of the interior, atmosphere, magnetosphere, and satellites, pages 1102–1145, 1976.

[27] Matthew H Burger and Robert E Johnson. Europa's neutral cloud: morphology and comparisons to io. Icarus, 171(2):557–560, 2004.

[28] Matthew Howard Burger. Io's neutral clouds: From the atmosphere to the plasma torus. University of Colorado at Boulder, 2003.

[29] Andrew F Cheng. Radial diffusion and ion partitioning in the io torus. Geophysical research letters, 13(6):517–520, 1986.

[30] Drew Coffin, Peter Damiano, Peter Delamere, Jay Johnson, and Chung-Sang Ng. Broadband energization of superthermal electrons in jupiter's inner magnetosphere. Journal of Geophysical Research: Space Physics, 127(8):e2022JA030528, 2022.

[31] Drew A Coffin and Peter A Delamere. Modeling the evolution of the system iv period of the io torus. In AGU Fall Meeting Abstracts, volume 2017, pages SM33C–2671, 2017.

[32] JEP Connerney, S Timmins, RJ Oliversen, JR Espley, JL Joergensen, S Kotsiaros, PS Joergensen, JMG Merayo, M Herceg, J Bloxham, et al. A new model of jupiter's magnetic field at the completion of juno's prime mission. Journal of Geophysical Research: Planets, 127(2):e2021JE007055, 2022.

[33] M. Copper, P. A. Delamere, and K. Overcast-Howe. Modeling physical chemistry of the io plasma torus in two dimensions. Journal of Geophysical Research: Space Physics, 121(7):6602–6619, 2016.

[34] FJ Crary, F Bagenal, LA Frank, and WR Paterson. Galileo plasma spectrometer measurements of composition and temperature in the io plasma torus. Journal of Geophysical Research: Space Physics, 103(A12):29359–29370, 1998.

[35] Michael W. Davis, G. Randall Gladstone, Rohini S. Giles, Thomas K. Greathouse, Philippa M. Molyneux, Ujjwal Raut, Kurt D. Retherford, Sue Baldor, Maarten H. Versteeg, Matthew Freeman, Kristian Persson, and Steven C. Persyn. Ground calibration results of the JUICE ultraviolet spectrograph. In Jan-Willem A. den Herder, Shouleh Nikzad, and Kazuhiro Nakazawa, editors, Space Telescopes and Instrumentation 2020: Ultraviolet to Gamma Ray, volume 11444, page 1144404. International Society for Optics and Photonics, SPIE, 2020.

[36] Michael W. Davis, Kurt D. Retherford, Philippa M. Molyneux, G. Randall Gladstone, Noel Eloriaga, Rohini S. Giles, Thomas K. Greathouse, Ujjwal Raut, Todd J. Veach, Sue Ferrell, Maarten H. Versteeg, Matthew A. Freeman, and Kristian B. Persson. Europa clipper ultraviolet spectrograph: ground calibration results. In Jan-Willem A. den Herder, Shouleh Nikzad, and Kazuhiro Nakazawa, editors, Space Telescopes and Instrumentation 2022: Ultraviolet to Gamma Ray, volume 12181, page 1218138. International Society for Optics and Photonics, SPIE, 2022.

[37] G. Del Zanna and N. R. Badnell. Atomic data and density diagnostics for S iv. Monthly Notices of the Royal Astronomical Society, 456(4):3720–3728, 01 2016.

[38] Del Zanna, G., Dere, K. P., Young, P. R., Landi, E., and Mason, H. E. Chianti - an atomic database for emission lines. version 8. A&A, 582:A56, 2015.

[39] P. A. Delamere and F. Bagenal. Modeling variability of plasma conditions in the io torus. Journal of Geophysical Research: Space Physics, 108(A7), 2003.

[40] P. A. Delamere, F. Bagenal, and A. Steffl. Radial variations in the io plasma torus during the cassini era. Journal of Geophysical Research: Space Physics, 110(A12), 2005.

[41] P. A. Delamere, A. Steffl, and F. Bagenal. Modeling temporal variability of plasma conditions in the io torus during the cassini era. Journal of Geophysical Research: Space Physics, 109(A10), 2004.

[42] Kenneth P Dere, Giulio Del Zanna, Peter R Young, Enrico Landi, and Ralph S Sutherland. Chianti—an atomic database for emission lines. xv. version 9, improvements for the x-ray satellite lines. The Astrophysical Journal Supplement Series, 241(2):22, 2019.

[43] Dere, K. P., Landi, E., Mason, H. E., Monsignori Fossi, B. C., and Young, P. R. CHIANTI - an atomic database for emission lines* - I. Wavelengths greater than 50 Å. Astron. Astrophys. Suppl. Ser., 125(1):149–173, 1997.

[44] V Dols, PA Delamere, and F Bagenal. A multispecies chemistry model of io's local interaction with the plasma torus. Journal of Geophysical Research: Space Physics, 113(A9), 2008.

[45] V. Dols and R.E. Johnson. Ion-molecule charge exchange in io's extended atmosphere: Velocity dependence. Icarus, 2022.

[46] Vincent Dols, Peter A Delamere, Fran Bagenal, William S Kurth, and William R Paterson. Asymmetry of io's outer atmosphere: Constraints from five galileo flybys. Journal of Geophysical Research: Planets, 117(E10), 2012.

[47] LP Dougherty, KM Bodisch, and F Bagenal. Survey of voyager plasma science ions at jupiter: 2. heavy ions. Journal of Geophysical Research: Space Physics, 122(8):8257–8276, 2017.

[48] JW Dungey. Effects of the electromagnetic perturbations on particles trapped in the radiation belts. Space Science Reviews, 4:199–222, 1965.

[49] S. T. Durrance, P. D. Feldman, and H. A. Weaver. Rocket detection of ultraviolet emission from neutral oxygen and sulfur in the IO Torus. , 267:L125–L129, April 1983.

[50] Larry W. Esposito, Charles A. Barth, Joshua E. Colwell, George M. Lawrence, William E. McClintock, A. I. A. N. F. Stewart, H. Uwe Keller, Axel Korth, Hans Lauche, Michel C. Festou, Arthur L. Lane, Candice J. Hansen, Justin N. Maki, Robert A. West, Herbert Jahn, Ralf Reulke, Kerstin Warlich, Donald E. Shemansky, and Yuk L. Yung. The Cassini Ultraviolet Imaging Spectrograph Investigation, pages 299–361. Springer Netherlands, Dordrecht, 2004.

[51] Carl-Gunne Fälthammar. Radial diffusion by violation of the third adiabatic invariant. Earth's particles and fields, page 157, 1968.

[52] Paul D. Feldman, Thomas B. Ake, Alice F. Berman, H. Warren Moos, David J. Sahnow, Darrell F. Strobel, Harold A. Weaver, and Peter R. Young. Detection of chlorine ions in the [ITAL]far ultraviolet spectroscopic explorer[/ITAL] spectrum of the io plasma torus. The Astrophysical Journal, 554(1):L123–L126, jun 2001.

[53] Paul D. Feldman, Darrell F. Strobel, H. Warren Moos, and Harold A. Weaver. The far-ultraviolet spectrum of the io plasma torus. The Astrophysical Journal, 601(1):583–591, jan 2004.

[54] L. A. Frank and W. R. Paterson. Observations of plasmas in the io torus with the galileo spacecraft. Journal of Geophysical Research: Space Physics, 105(A7):16017–16034, 2000.

[55] LA Frank and WR Paterson. Return to io by the galileo spacecraft: Plasma observations (paper 1999ja000460). Journal of Geophysical Research-All Series-, 105(11):25–363, 2000.

[56] G. Randall Gladstone and Doyle T. Hall. Recent results from EUVE observations of the io plasma torus and jupiter. Journal of Geophysical Research: Planets, 103(E9):19927–19933, 1998.

[57] GR Gladstone. Solar oi 1304-å triplet line profiles. Journal of Geophysical Research: Space Physics, 97(A12):19519–19525, 1992.

[58] CK Goertz, James Alfred Van Allen, and Michelle F Thomsen. Further observational support for the lossy radial diffusion model of the inner jovian magnetosphere. Journal of Geophysical Research: Space Physics, 84(A1):87–92, 1979.

[59] D. T. Hall, G. R. Gladstone, F. Herbert, R. Lieu, and N. Thomas. Io torus EUV emissions during the comet Shoemaker-Levy/9 impacts. Geophysical Research Letters, 22(24):3441–3444, 1995.

[60] D. T. Hall, G. R. Gladstone, H. W. Moos, F. Bagenal, J. T. Clarke, P. D. Feldman, M. A. McGrath, N. M. Schneider, D. E. Shemansky, D. F. Strobel, and J. H. Waite. Extreme Ultraviolet Explorer Satellite Observation of Jupiter's Io Plasma Torus. , 426:L51, May 1994.

[61] Floyd Herbert. A simple transport model for the io plasma torus "ribbon". Geophysical Research Letters, 23(21):2875–2878, 1996.

[62] Floyd Herbert, G. Randall Gladstone, and Gilda E. Ballester. Extreme ultraviolet explorer spectra of the io plasma torus: Improved spectral resolution and new results. Journal of Geophysical Research: Space Physics, 106(A11):26293–26309, 2001.

[63] Floyd Herbert and Doyle T. Hall. Disentangling electron temperature and density in the io plasma torus. Journal of Geophysical Research: Planets, 103(E9):19915–19925, 1998.

[64] Floyd Herbert and B. R. Sandel. Radial profiles of ion density and parallel temperature in the io plasma torus during the voyager 1 encounter. Journal of Geophysical Research: Space Physics, 100(A10):19513–19529, 1995.

[65] Floyd Herbert and Bill R. Sandel. Azimuthal variation of ion density and electron temperature in the io plasma torus. Journal of Geophysical Research: Space Physics, 105(A7):16035–16052, 2000.

[66] Floyd Herbert, Nicholas M Schneider, and AJ Dessler. New description of io's cold plasma torus. Journal of Geophysical Research: Space Physics, 113(A1), 2008.

[67] Floyd Herbert, Nicholas M. Schneider, Amanda R. Hendrix, and Fran Bagenal. Hubble space telescope observations of sulfur ions in the io plasma torus: New constraints on the plasma distribution. Journal of Geophysical Research: Space Physics, 108(A5), 2003.

[68] S. L. G. Hess, P. A. Delamere, F. Bagenal, N. Schneider, and A. J. Steffl. Longitudinal modulation of hot electrons in the io plasma torus. Journal of Geophysical Research: Space Physics, 116(A11), 2011.

[69] R Hikida, K Yoshioka, F Tsuchiya, M Kagitani, T Kimura, F Bagenal, N Schneider, G Murakami, A Yamazaki, H Kita, et al. Spatially asymmetric increase in hot electron fraction in the io plasma torus during volcanically active period revealed by observations by hisaki/exceed from november 2014 to may 2015. Journal of Geophysical Research: Space Physics, 125(3):e2019JA027100, 2020.

[70] TW Hill, AJ Dessler, and LJ Maher. Corotating magnetospheric convection. Journal of Geophysical Research: Space Physics, 86(A11):9020–9028, 1981.

[71] TW Hill, AJ Dessler, and FC Michel. Configuration of the jovian magnetosphere. Geophysical Research Letters, 1(1):3–6, 1974.

[72] TW Hill and FC Michel. Heavy ions from the galilean satellites and the centrifugal distortion of the jovian magnetosphere. Journal of Geophysical Research, 81(25):4561–4565, 1976.

[73] PC Hinton, F Bagenal, and Bertrand Bonfond. Alfvén wave propagation in the io plasma torus. Geophysical Research Letters, 46(3):1242–1249, 2019.

[74] C. W. Hord, W. E. McClintock, A. I. F. Stewart, C. A. Barth, L. W. Esposito, G. E. Thomas, B. R. Sandel, D. M. Hunten, A. L. Broadfoot, D. E. Shemansky, J. M. Ajello, A. L. Lane, and R. A. West. Galileo ultraviolet spectrometer experiment. Space Science Reviews, 60(1):503–530, May 1992.

[75] R. E. Johnson and D. F. Strobel. Charge exchange in the io torus and exosphere. Journal of Geophysical Research: Space Physics, 87(A12):10385–10393, 1982.

[76] Tomoki Kimura, Y Hiraki, Chihiro Tao, Fuminori Tsuchiya, PA Delamere, Kazuo Yoshioka, Go Murakami, Atsushi Yamazaki, Hajime Kita, Sarah V Badman, et al. Response of jupiter's aurora to plasma mass loading rate monitored by the hisaki satellite during volcanic eruptions at io. Journal of Geophysical Research: Space Physics, 123(3):1885–1899, 2018.

[77] R Koga, F Tsuchiya, M Kagitani, T Sakanoi, K Yoshioka, I Yoshikawa, T Kimura, G Murakami, A Yamazaki, HT Smith, et al. Volcanic change of io's neutral oxygen cloud and plasma torus observed by hisaki. J. Geophys. Res, 124, 2019.

[78] Ryoichi Koga, Fuminori Tsuchiya, Masato Kagitani, Takeshi Sakanoi, Mizuki Yoneda, Kazuo Yoshioka, Tomoki Kimura, Go Murakami, Atsushi Yamazaki, Ichiro Yoshikawa, et al. The time variation of atomic oxygen emission around io during a volcanic event observed with hisaki/exceed. Icarus, 299:300–307, 2018.

[79] Ryoichi Koga, Fuminori Tsuchiya, Masato Kagitani, Takeshi Sakanoi, Mizuki Yoneda, Kazuo Yoshioka, Ichiro Yoshikawa, Tomoki Kimura, Go Murakami, Atsushi Yamazaki, H. Todd Smith, and Fran Bagenal. Spatial distribution of io's neutral oxygen cloud observed by hisaki. Journal of Geophysical Research: Space Physics, 123(5):3764–3776, 2018.

[80] H. Krüger, P. Geissler, M. Horányi, A. L. Graps, S. Kempf, R. Srama, G. Moragas-Klostermeyer, R. Moissl, T. V. Johnson, and E. Grün. Jovian dust streams: A monitor of io's volcanic plume activity. Geophysical Research Letters, 30(21), 2003.

[81] I Kupo, Yu Mekler, Y Mekler, and A Eviatar. Detection of ionized sulfur in the jovian magnetosphere. The Astrophysical Journal, 205:L51–L53, 1976.

[82] G. Lichtenberg, N. Thomas, and T. Fouchet. Detection of s (iv) 10.51 m emission from the io plasma torus. Journal of Geophysical Research: Space Physics, 106(A12):29899–29910, 2001.

[83] P Mazzotta, G Mazzitelli, S Colafrancesco, and N Vittorio. Ionization balance for optically thin plasmas: Rate coefficients for all atoms and ions of the elements h to ni. Astronomy and Astrophysics Supplement Series, 133(3):403–409, 1998.

[84] M. A. McGrath, P. D. Feldman, D. F. Strobel, H. W. Moos, and G. E. Ballester. Detection of [O ii] lambda 2471 from the Io Plasma Torus. , 415:L55, September 1993.

[85] M. A. McGrath and R. E. Johnson. Charge exchange cross sections for the io plasma torus. Journal of Geophysical Research: Space Physics, 94(A3):2677–2683, 1989.

[86] Ralph L. McNutt Jr. Possible in situ detection of k2+ in the jovian magnetosphere. Journal of Geophysical Research: Space Physics, 98(A12):21221–21229, 1993.

[87] Gilbert D Mead. The effect of jupiter's satellites on the diffusion of protons. In JPL Proc. of the Jupiter Radiation Belt Workshop, 1972.

[88] Michael Mendillo, Jeffrey Baumgardner, Brian Flynn, and W Jeffrey Hughes. The extended sodium nebula of jupiter. Nature, 348(6299):312–314, 1990.

[89] H. W. Moos, S. T. Durrance, T. E. Skinner, P. D. Feldman, J. L. Bertaux, and M. C. Festou. IUE spectrum of the IO torus - Identification of the 5S2-3P2,1 transition of S III. , 275:L19–L23, December 1983.

[90] H. W. Moos, P. D. Feldman, S. T. Durrance, W. P. Blair, C. W. Bowers, A. F. Davidsen, W. V. Dixon, H. C. Ferguson, R. C. Henry, R. A. Kimble, G. A. Kriss, J. W. Kruk, K. S. Long, and O. Vancura. Determination of Ionic Abundances in the Io Torus Using the Hopkins Ultraviolet Telescope. , 382:L105, December 1991.

[91] Miguel A. Moreno, William I. Newman, and Margaret G. Kivelson. Ion partitioning in the hot io torus: The influence of s2 outgassing. Journal of Geophysical Research: Space Physics, 90(A12):12065–12072, 1985.

[92] SN Nahar. Vizier online data catalog: Iron project vii. feii radiative transitions (nahar, 1995). VizieR Online Data Catalog, pages J–A+, 1995.

[93] Sultana N Nahar. Total electron-ion recombination of fe i i i. Physical Review A, 53(4):2417, 1996.

[94] Sultana N Nahar. Electron-ion recombination rate coefficients, photoionization cross sections, and ionization fractions for astrophysically abundant elements. ii. oxygen ions. The Astrophysical Journal Supplement Series, 120(1):131, 1999.

[95] Edward G. Nerney and Fran Bagenal. Combining UV spectra and physical chemistry to constrain the hot electron fraction in the Io plasma torus. Journal of Geophysical Research: Space Physics, 125(4):e2019JA027458, 2020. e2019JA027458 2019JA027458.

[96] Edward G. Nerney, Fran Bagenal, and Andrew J. Steffl. Io plasma torus ion composition: Voyager, Galileo, and Cassini. Journal of Geophysical Research: Space Physics, 122(1):727–744, 2017.

[97] H. Nozawa, H. Misawa, S. Takahashi, A. Morioka, S. Okano, and R. Sood. Long-term variability of [sii] emissions from the io plasma torus between 1997 and 2000. Journal of Geophysical Research: Space Physics, 109(A7), 2004.

[98] H. Nozawa, H. Misawa, S. Takahashi, A. Morioka, S. Okano, and R. Sood. Relationship between the jovian magnetospheric plasma density and io torus emission. Geophysical Research Letters, 32(11), 2005.

[99] Donald E Osterbrock and Gary J Ferland. Astrophysics Of Gas Nebulae and Active Galactic Nuclei. University science books, 2006.

[100] Stanton J Peale, P Cassen, and Ray T Reynolds. Melting of io by tidal dissipation. Science, 203(4383):892–894, 1979.

[101] D Péquignot, P Petitjean, and C Boisson. Total and effective radiative recombination coefficients. Astronomy and Astrophysics, 251:680–688, 1991.

[102] Phillip Phipps and Fran Bagenal. Centrifugal equator in jupiter's plasma sheet. Journal of Geophysical Research: Space Physics, 126(1):e2020JA028713, 2021.

[103] Andrew S Richardson. 2019 nrl plasma formulary. Technical report, US Naval Research Laboratory, 2019.

[104] Andrew S Richardson. 2019 nrl plasma formulary. Technical report, US Naval Research Laboratory, 2019.

[105] John D Richardson and George L Siscoe. The problem of cooling the cold io torus. Journal of Geophysical Research: Space Physics, 88(A3):2001–2009, 1983.

[106] John D. Richardson, George L. Siscoe, F. Bagenal, and James D. Sullivan. Time dependent plasma injection by io. Geophysical Research Letters, 7(1):37–40, 1980.

[107] C.T. Russell, X. Blanco-Cano, Y.L. Wang, and M.G. Kivelson. Ion cyclotron waves at io: implications for the temporal variation of io's atmosphere. Planetary and Space Science, 51(14):937–944, 2003. Surfaces and Atmospheres of the Outer Planets their Satellites and Ring Systems.

[108] B. R. Sandel, D. E. Shemansky, A. L. Broadfoot, J. L. Bertaux, J. E. Blamont, M. J. S. Belton, J. M. Ajello, J. B. Holberg, S. K. Atreya, T. M. Donahue, H. W. Moos, D. F. Strobel, J. C. McConnell, A. Dalgarno, R. Goody, M. B. McElroy, and P. Z. Takacs. Extreme ultraviolet observations from voyager 2 encounter with jupiter. Science, 206(4421):962–966, 1979.

[109] BR Sandel and AL Broadfoot. Discovery of an io-correlated energy source for io's hot plasma torus. Journal of Geophysical Research: Space Physics, 87(A4):2231–2240, 1982.

[110] BR Sandel and AL Broadfoot. Io's hot plasma torus—a synoptic view from voyager. Journal of Geophysical Research: Space Physics, 87(A1):212–218, 1982.

[111] C Schmidt, N Schneider, François Leblanc, C Gray, J Morgenthaler, J Turner, and C Grava. A survey of visible s+ emission in io's plasma torus during the hisaki epoch. Journal of Geophysical Research: Space Physics, 123(7):5610–5624, 2018.

[112] Nicholas M Schneider and Fran Bagenal. Io's neutral clouds, plasma torus, magnetospheric interaction. In Io After Galileo, pages 265–286. Springer, 2007.

[113] Nicholas M Schneider, Martin H Taylor, Frank J Crary, and John T Trauger. On the nature of the λiii brightness asymmetry in the io torus. Journal of Geophysical Research: Space Physics, 102(A9):19823–19833, 1997.

[114] Nicholas M Schneider and John T Trauger. The structure of the io torus. The Astrophysical Journal, 450:450, 1995.

[115] Nicholas M Schneider, John T Trauger, Jody K Wilson, David I Brown, Robin W Evans, and Donald E Shemansky. Molecular origin of io's fast sodium. Science, 253(5026):1394–1397, 1991.

[116] NM Schneider, WH Smyth, and MA McGrath. Io's atmosphere and neutral clouds. NASA Special Publication, 494, 1989.

[117] Ron Schreier, Aharon Eviatar, and Vytenis M. Vasyliūnas. A two-dimensional model of plasma transport and chemistry in the jovian magnetosphere. Journal of Geophysical Research: Planets, 103(E9):19901–19913, 1998.

[118] J. D. Scudder, E. C. Sittler Jr., and H. S. Bridge. A survey of the plasma electron environment of jupiter: A view from voyager. Journal of Geophysical Research: Space Physics, 86(A10):8157–8179, 1981.

[119] D. E. Shemansky. Mass-loading and diffusion-loss rates of the Io plasma torus. , 242:1266–1277, December 1980.

[120] D. E. Shemansky. Radiative cooling efficiencies and predicted spectra of species of the Io plasma torus. , 236:1043–1054, March 1980.

[121] D. E. Shemansky. Energy branching in the io plasma torus: The failure of neutral cloud theory. Journal of Geophysical Research: Space Physics, 93(A3):1773–1784, 1988.

[122] D. E. Shemansky and B. R. Sandel. The injection of energy into the io plasma torus. Journal of Geophysical Research: Space Physics, 87(A1):219–229, 1982.

[123] D. E. Shemansky and Gerald R. Smith. The voyager 1 euv spectrum of the io plasma torus. Journal of Geophysical Research: Space Physics, 86(A11):9179–9192, 1981.

[124] D. E. Shemansky, Y. L. Yung, X. Liu, J. Yoshii, C. J. Hansen, A. R. Hendrix, and L. W. Esposito. A New Understanding of thee Europa Atmosphere and limits on geophysical activity. The Astrophysical Journal, 797(2):84, dec 2014.

[125] Donald E. Shemansky. Ratio of oxygen to sulfur in the io plasma torus. Journal of Geophysical Research: Space Physics, 92(A6):6141–6146, 1987.

[126] J Michael Shull and Michael Van Steenberg. The ionization equilibrium of astrophysically abundant elements. The Astrophysical Journal Supplement Series, 48:95–107, 1982.

[127] George L Siscoe and Danny Summers. Centrifugally driven diffusion of iogenic plasma. Journal of Geophysical Research: Space Physics, 86(A10):8471–8479, 1981.

[128] E. C. Sittler Jr. and Darrell F. Strobel. Io plasma torus electrons: Voyager 1. Journal of Geophysical Research: Space Physics, 92(A6):5741–5762, 1987.

[129] H. T. Smith, R. Koga, F. Tsuchiya, and V. J. Dols. Insight into io enabled by characterization of its neutral oxygen torus. Journal of Geophysical Research: Space Physics, 127(8):e2022JA030581, 2022. e2022JA030581 2022JA030581.

[130] Howard Todd Smith, Donald G Mitchell, Robert E Johnson, Barry H Mauk, and Jacob E Smith. Europa neutral torus confirmation and characterization based on observations and modeling. The Astrophysical Journal, 871(1):69, 2019.

[131] Robert A. Smith, Fran Bagenal, Andrew F. Cheng, and Darrell F. Strobel. On the energy crisis in the io plasma torus. Geophysical Research Letters, 15(6):545–548, 1988.

[132] Robert A. Smith and Darrell F. Strobel. Energy partitioning in the io plasma torus. Journal of Geophysical Research: Space Physics, 90(A10):9469–9493, 1985.

[133] William H. Smyth and M.L. Marconi. Nature of the iogenic plasma source in jupiter's magnetosphere: Ii. near-io distribution. Icarus, 176(1):138–154, 2005.

[134] William H Smyth and Donald E Shemansky. Escape and ionization of atomic oxygen from io. The Astrophysical Journal, 271:865–875, 1983.

[135] AJ Steffl, PA Delamere, and F Bagenal. Cassini uvis observations of the io plasma torus: Iii. observations of temporal and azimuthal variability. Icarus, 180(1):124–140, 2006.

[136] AJ Steffl, PA Delamere, and F Bagenal. Cassini uvis observations of the io plasma torus: Iv. modeling temporal and azimuthal variability. Icarus, 194(1):153–165, 2008.

[137] Andrew J. Steffl, Fran Bagenal, and A.Ian F. Stewart. Cassini uvis observations of the io plasma torus: Ii. radial variations. Icarus, 172(1):91–103, 2004. Special Issue: Cassini-Huygens at Jupiter.

[138] Andrew J. Steffl, A.Ian F. Stewart, and Fran Bagenal. Cassini uvis observations of the io plasma torus: I. initial results. Icarus, 172(1):78–90, 2004. Special Issue: Cassini-Huygens at Jupiter.

[139] EJ Stone and EC Zipf. Electron-impact excitation of the 3 s 0 and 5 s 0 states of atomic oxygen. The Journal of Chemical Physics, 60(11):4237–4243, 1974.

[140] D. F. Strobel. Energetics, Luminosity, and Spectroscopy of Io's Torus. In NASA Special Publication, volume 494, pages 183–195. 1989.

[141] DF Strobel and J Davis. Properties of the io plasma torus inferred from voyager euv data. The Astrophysical Journal, 238:L49–L52, 1980.

[142] Martin Hayward Taylor. Modeling emissions from the Io plasma torus. University of Colorado at Boulder, 1996.

[143] N. Thomas, F. Bagenal, T. W. Hill, and J. K. Wilson. The Io neutral clouds and plasma torus. In Fran Bagenal, Timothy E. Dowling, and William B. McKinnon, editors, Jupiter. The Planet, Satellites and Magnetosphere, volume 1, pages 561–591. 2004.

[144] Nicolas Thomas. Optical observations of io's neutral clouds and plasma torus. Surveys in Geophysics, 13(2):91–164, 1992.

[145] Nicolas Thomas. The variability of the io plasma torus. Journal of Geophysical Research: Planets, 98(E10):18737–18750, 1993.

[146] Nicolas Thomas, G. Lichtenberg, and M. Scotto. High-resolution spectroscopy of the io plasma torus during the galileo mission. Journal of Geophysical Research: Space Physics, 106(A11):26277–26291, 2001.

[147] RM Thorne. Jovian auroral secondary electrons and their influence on the io plasma torus. Geophysical Research Letters, 8(5):509–512, 1981.

[148] Constantino Tsallis, RenioS Mendes, and Anel R Plastino. The role of constraints within generalized nonextensive statistics. Physica A: Statistical Mechanics and its Applications, 261(3-4):534–554, 1998.

[149] Fuminori Tsuchiya, Ryo Arakawa, Hiroaki Misawa, Masato Kagitani, Ryoichi Koga, Fumiharu Suzuki, Reina Hikida, Kazuo Yoshioka, A Steffl, F Bagenal, et al. Azimuthal variation in the io plasma torus observed by the hisaki satellite from 2013 to 2016. Journal of Geophysical Research: Space Physics, 124(5):3236–3254, 2019.

[150] Fuminori Tsuchiya, Masato Kagitani, Kazuo Yoshioka, Tomoki Kimura, Go Murakami, Atsushi Yamazaki, Hiromasa Nozawa, Yasumasa Kasaba, Takeshi Sakanoi, Kazunori Uemizu, et al. Local electron heating in the io plasma torus associated with io from hisaki satellite observation. Journal of Geophysical Research: Space Physics, 120(12):10–317, 2015.

[151] Fuminori Tsuchiya, Kazuo Yoshioka, Tomoki Kimura, Ryoichi Koga, Go Murakami, Atsushi Yamazaki, Masato Kagitani, Chihiro Tao, Fumiharu Suzuki, Reina Hikida, et al. Enhancement of the jovian magnetospheric plasma circulation caused by the change in plasma supply from the satellite io. Journal of Geophysical Research: Space Physics, 123(8):6514–6532, 2018.

[152] Vytenis M Vasyliunas. A survey of low-energy electrons in the evening sector of the magnetosphere with ogo 1 and ogo 3. Journal of Geophysical Research, 73(9):2839–2884, 1968.

[153] DA Verner and Gary J Ferland. Atomic data for astrophysics. i. radiative recombination rates for h-like, he-like, li-like and na-like ions over a broad range of temperature. arXiv preprint astro-ph/9509083, 1995.

[154] GS Voronov. A practical fit formula for ionization rate coefficients of atoms and ions by electron impact: Z= 1–28. Atomic Data and Nuclear Data Tables, 65(1):1–35, 1997.

[155] RJ Wilson. Error analysis for numerical estimates of space plasma parameters. Earth and Space Science, 2(6):201–222, 2015.

[156] Thomas N Woods and Gary Rottman. Xuv photometer system (xps): Solar variations during the sorce mission. In The Solar Radiation and Climate Experiment (SORCE), pages 375–387. Springer, 2005.

[157] M Yoneda, M Kagitani, F Tsuchiya, T Sakanoi, and S Okano. Brightening event seen in observations of jupiter's extended sodium nebula. Icarus, 261:31–33, 2015.

[158] M Yoneda, H Nozawa, H Misawa, M Kagitani, and S Okano. Jupiter's magnetospheric change by io's volcanoes. Geophysical research letters, 37(11), 2010.

[159] I Yoshikawa, F Suzuki, R Hikida, K Yoshioka, G Murakami, F Tsuchiya, C Tao, and M Fujimoto. Volcanic activity on io and its influence on the dynamics of the jovian magnetosphere observed by exceed. Hisaki in, page 110, 2015.

[160] Ichiro Yoshikawa, Fumiharu Suzuki, Reina Hikida, Kazuo Yoshioka, Go Murakami, Fuminori Tsuchiya, Chihiro Tao, Atsushi Yamazaki, Tomoki Kimura, Hajime Kita, et al. Volcanic activity on io and its influence on the dynamics of the jovian magnetosphere observed by exceed/hisaki in 2015. Earth, Planets and Space, 69(1):1–11, 2017.

[161] Ichiro Yoshikawa, Kazuo Yoshioka, Go Murakami, Fumiharu Suzuki, Reina Hikida, Atsushi Yamazaki, Tomoki Kimura, Fuminori Tsuchiya, Masato Kagitani, Takeshi Sakanoi, et al. Properties of hot electrons in the jovian inner magnetosphere deduced from extended observations of the io plasma torus. Geophysical Research Letters, 43(22):11–552, 2016.

[162] Ichiro Yoshikawa, Kazuo Yoshioka, Go Murakami, Atsushi Yamazaki, Fuminori Tsuchiya, Masato Kagitani, Takeshi Sakanoi, Naoki Terada, Tomoki Kimura, Masaki Kuwabara, et al. Extreme ultraviolet radiation measurement for planetary atmospheres/magnetospheres from the earth-orbiting spacecraft (extreme ultraviolet spectroscope for exospheric dynamics: Exceed). Space Science Reviews, 184(1):237–258, 2014.

[163] K Yoshioka, G Murakami, A Yamazaki, F Tsuchiya, T Kimura, M Kagitani, T Sakanoi, K Uemizu, Y Kasaba, I Yoshikawa, et al. Evidence for global electron transportation into the jovian inner magnetosphere. Science, 345(6204):1581–1584, 2014.

[164] K Yoshioka, I Yoshikawa, F Tsuchiya, M Kagitani, and G Murakami. Hot electron component in the io plasma torus confirmed through euv spectral analysis. Journal of Geophysical Research: Space Physics, 116(A9), 2011.

[165] Kazuo Yoshioka, Fuminori Tsuchiya, Tomoki Kimura, Masato Kagitani, Go Murakami, Atsushi Yamazaki, Masaki Kuwabara, Fumiharu Suzuki, Reina Hikida, Ichiro Yoshikawa, et al. Radial variation of sulfur and oxygen ions in the io plasma torus as deduced from remote observations by hisaki. Journal of Geophysical Research: Space Physics, 122(3):2999–3012, 2017.